

Improving fMRI analysis methods for the measurement of cerebrovascular function



Ryan Anthony Beckerleg

Supervisor: Prof. Kevin Murphy

School of Physics and Astronomy
Cardiff University

This dissertation is submitted for the degree of
Doctor of Philosophy

Acknowledgements

Throughout my PhD, I have been supported by many people and I would like to thank them all for their support. Firstly, I'm enormously grateful for the support and guidance I received from my primary supervisor, Kevin Murphy. Without whom, I'm not sure I'd have made it to the end of my PhD. He inspired loads of interesting scientific discussion which shaped the research I've presented in this thesis. Our weekly meetings were always great (even when Ireland did beat Wales in the rugby) and I'll definitely miss these. Kevin has really helped me to develop as a scientist and I feel indebted to him for this.

Secondly, I'd like to thank the wonderful people in our research lab. Of whom, a few people stand out. My secondary supervisor, Leandro Beltrachini, for his encouragement, guidance and willingness to help wherever he could. Joe, who in the early years of my PhD felt like my third supervisor. He helped me to collect data and was always there when I needed a hand with analysis. Hannah, who has been a big emotional support throughout and has always been there to help me with research questions. Kajal, who was always there to listen to me grumble about issues with analysis. Finally, the rest of our lab, who have always been there when I needed their help and advice. I'd also like to thank the other friends I've made throughout my PhD for their friendship, moral support, and company at lunch time. Namely, Kajal, Lars, Elisa, Alix, Katya, Matt and Luke. All of these people have made CUBRIC such a wonderful place to study and work and for that I am very grateful.

Next, I'd like to thank my close friends, especially, Cobi, Jaydn and Liz. They've been there for me throughout this journey to provide emotional and moral support, as well as laughter and advice. I'd also like to thank the other friends I've made throughout my years in Cardiff who I've shared many good memories with.

My family have always been there for me and I'd like to thank them for their unwavering support in everything I do. Without them, I'm not sure I'd have ever taken up the opportunity to do this PhD. They have always encouraged me to be the best I can be, even when I didn't believe I could. So, a big thank you to my parents, Roz and Darryl, and to my sister and her partner, Rhian and Rupert. I'd also love to thank my little nephew, Macsen.

Finally, I'd like to thank Will. You have been my rock over the past couple of months. You have always been there when I needed you most and always manage to make me smile. For that I will always be grateful.

Abstract

This work endeavoured to improve current methods of investigating cerebrovascular function using functional magnetic resonance imaging (fMRI). The main areas identified for improvement were retrospective motion correction (Chapter 3) and data-based quantification of cardiac pulsatility and heart rate variability (Chapters 4 and 5).

Chapter 3 demonstrated that conventional motion correction techniques result in erroneous motion estimates in scans of cerebrovascular function. The severity of this was investigated using an external camera and novel methods were introduced to improve motion estimates. The ICA-based method more accurately estimated motion when compared with the other methods. However, this didn't work for multi-PLD pseudo-continuous ASL scans. Additionally, the ICA-based methods performed the best when quantifying measures of cerebrovascular function. Therefore, I would recommend the use of an ICA in the calculation of motion parameters for scans of cerebrovascular function.

Chapter 4 aimed to develop data-based methods to quantify cardiac pulsatility using resting-state fMRI (rfMRI). Ultimately, these methods failed because the cardiac signal was aliased and could not be accurately located. This chapter also showed that a regression-based approach using cardiac-related components as regressors would be better in the estimation of cardiac pulsatility.

In Chapter 5, two novel methods of estimating cardiac pulsatility were introduced. Both methods created training datasets by isolating independent components that were cardiac-related. These were then used to train FSL's ICA-based Xnoisifier (FIX). The first method (HRV method) used quality physiological traces to achieve this. Whereas the second method (Frequency method) used only the frequency data. Then, FIX was used to isolate cardiac components for all rfMRI datasets. Estimates of cardiac pulsatility were produced and compared to a gold standard. Results showed that both methods correlated highly with this gold standard. The HRV method showed slightly higher correlations than the Frequency method and is the recommended method.

Table of contents

List of figures	xiii
Symbols	xvii
1 Introduction to fMRI	1
1.1 Chapter Overview	1
1.2 Nuclear Magnetic Resonance	2
1.2.1 Spin	2
1.2.2 Precession, Excitation and Relaxation	3
1.3 Basic MR Signals	6
1.3.1 Echo Creation	7
1.4 Image Formation	9
1.4.1 K-space	9
1.4.1.1 Gradients	9
1.5 EPI Imaging	12
1.5.1 Aliasing	13
1.6 Acceleration & Parallel Imaging	14
1.6.1 Generalized autocalibrating partially parallel acquisitions (GRAPPA)	16
1.6.2 Sensitivity Encoding for Fast MRI (SENSE)	17
1.6.3 Multi-band	18
1.7 Functional Imaging & BOLD	18
1.7.1 Neurovascular Coupling	18
1.7.1.1 The Haemodynamic Response	18
1.7.2 Spatial and Temporal Resolution of BOLD	19
1.7.3 Analysis of fMRI data	20
1.7.3.1 Preprocessing of fMRI data	20
1.7.4 Statistical Analysis	21
1.8 Arterial Spin Labelling (ASL)	22
1.9 Summary	23

2	Introduction to Cerebral Physiology	25
2.1	Chapter Overview	25
2.2	Anatomy of the Cerebrovasculature	25
2.2.1	Blood Vessels	25
2.2.2	Circle of Willis	26
2.3	Regulation of Blood Flow	28
2.3.1	Autoregulation	28
2.4	Effects of Ageing on Vessel Health	28
2.4.1	Arterial Stiffness	28
2.4.2	Arterial Compliance	29
2.4.3	Pulsatility	29
2.4.4	Heart Rate Variability (HRV)	29
2.5	Quantifying Cerebrovascular Physiology	31
2.5.1	Quantification of Cerebrovascular Reactivity (CVR)	31
2.5.2	Quantification of Cerebral Blood Flow (CBF)	32
2.5.3	Quantification of the Cerebral Metabolic Rate of Oxygen Consumption (CMRO ₂) and Oxygen Extraction Fraction (OEF)	33
2.6	Overview of Algorithms	35
2.6.1	Volume Registration Algorithm (VRA)	35
2.6.2	Volume Regression	36
2.6.3	Independent Components Analysis (ICA)	36
2.6.4	FMRIB's ICA-based X-noiseifier (FIX)	36
2.6.5	Human Connectome Project datasets	37
2.6.6	Global Intensity Changes	37
2.7	Summary	38
2.8	Outline of Experimental Chapters	39
3	Correcting motion registration errors caused by Global Intensity Changes (GICs)	41
3.1	Chapter Overview	41
3.2	Introduction	41
3.3	Methods	45
3.3.1	Data Collection	45
3.3.1.1	Overview of Scanner Protocols	45
3.3.1.2	Overview of External Motion tracking system	47
3.3.2	Data Analysis	48
3.3.2.1	Volume Registration Algorithm (VRA) based correction	49
3.3.2.2	Camera-based correction & the issues associated with it	49
3.3.3	Independent Component Analysis (ICA) based correction	53
3.3.4	Erosion-based correction	53

3.3.4.1	Erosion-based ‘doughnut’ masks	53
3.3.5	Hybrid Independent Component Analysis (ICA) & Erosion-based correction	53
3.3.6	Boundary Based Registration (BBR)	54
3.3.7	Registration & Regression analysis	54
3.3.8	Analysis of Motion Parameters	55
3.3.9	Quantification of Cerebrovascular Physiology	55
3.3.9.1	Connectivity analysis	55
3.3.9.2	CBF Quantification	56
3.3.9.3	CVR Quantification	56
3.3.9.4	CMRO ₂ Quantification	57
3.3.10	Grey Matter Segmentation	57
3.4	Results	58
3.4.1	Volume Registration Algorithm (VRA) based correction	58
3.4.2	Camera-based correction	58
3.4.3	Independent Component Analysis (ICA) based correction	61
3.4.4	Erosion-based correction	63
3.4.5	Quantification of Cerebrovascular Physiology	63
3.4.5.1	Connectivity analysis	63
3.4.5.2	CBF Quantification	64
3.4.5.3	CVR Quantification	66
3.4.5.4	CMRO ₂ & OEF Quantification	69
3.5	Discussion	71
3.5.1	Volume Registration Algorithm (VRA) based correction	71
3.5.2	Camera-based correction	72
3.5.3	Independent Component Analysis (ICA) based correction	72
3.5.4	Erosion-based correction	73
3.5.5	Quantification of Cerebrovascular Physiology	73
3.5.5.1	Connectivity analysis	74
3.5.5.2	CBF Quantification	74
3.5.5.3	CVR Quantification	75
3.5.5.4	CMRO ₂ & OEF Quantification	76
3.6	Conclusion/Summary	76
4	Data-driven methods for collecting cardiac information from functional MRI scans	79
4.1	Overview of the following two Chapters	79
4.2	Chapter 4	81
4.2.1	Introduction	81
4.3	Methods	81

4.3.1	HCP data	81
4.3.2	Processing of rfMRI Data	82
4.3.3	Processing of Structural T1w Data	82
4.3.4	Processing of ICA components	83
4.3.5	Generation of Brain Masks	83
4.3.6	Processing of Cardiac Data	83
4.3.7	Frequency Method 60-100 BPM & 50-100 BPM	83
4.3.8	Frequency Method 100-400 Samples	84
4.3.8.1	Definition of the Cardiac Window	84
4.3.8.2	Stage One of Classification	85
4.3.8.3	Stage Two of Classification	85
4.3.8.4	Stage Three of Classification	85
4.3.8.5	Calculation of Heart Rates	88
4.3.8.6	Regression Method	88
4.3.8.7	Fast Fourier Transform (FFT) Method	88
4.3.8.8	Bandpass Method	89
4.3.9	Generation of Pulsatility	89
4.3.10	Correlation with physiological measures	89
4.4	Results	90
4.4.0.1	Classification of Components	90
4.4.0.2	Calculation of Heart Rates	91
4.4.0.3	Verification of Classification	92
4.4.0.4	Generating Pulsatility - Comparison between methods	92
4.4.0.5	Correlation with physiological information	93
4.4.0.6	Iteration Problem	94
4.5	Discussion	95
4.5.1	Generating Pulsatility - Comparison between methods	95
4.6	Conclusion/Summary	96
5	Novel Methods for quantifying cardiac pulsatility in resting state functional images	97
5.1	Chapter Overview	97
5.2	Introduction	97
5.3	Methods	98
5.3.1	HCP data	98
5.3.2	Processing of Cardiac Data	98
5.3.3	Processing of rfMRI Data	98
5.3.4	Processing of Structural T1w Data	99
5.3.5	Processing of ICA components	99
5.3.6	Generation of Brain Masks	99

5.3.7	Classification of ICA Components - HRV Method	99
5.3.7.1	Correlation of ICA & Cardiac data	100
5.3.7.2	Calculation of Pulsatility	100
5.3.7.3	The relationship between HRV and Pulsatility	102
5.3.8	Classification of ICA components - Frequency Method	103
5.3.8.1	Calculation of Pulsatility	105
5.3.9	Cardiac Regressors	105
5.3.10	Verification of pulsatility values	105
5.3.11	Correlation with Physiological measures	105
5.4	Results	106
5.4.1	Verification of method accuracy - HRV method	106
5.4.2	Verification of method accuracy - Frequency Method	107
5.4.3	"True" Pulsatility correlations with physiological information	108
5.4.4	HRV Method Pulsatility correlations with physiological information	108
5.4.5	Frequency Method Pulsatility correlations with physiological information	109
5.4.6	Comparisons across methods	110
5.4.7	Averaged pulsatility maps	113
5.4.8	HRV Method	113
5.4.9	Frequency Method	114
5.4.10	"True" Pulsatility	116
5.5	Discussion	116
5.6	Conclusion	119
6	Discussion	121
	References	135
	Appendix A Additional Figures and Tables	147

List of figures

1.1	Representation of spin alignment before and after an external magnetic field is applied	3
1.2	Representation of precession for an individual proton in the presence of an external magnetic field	4
1.3	Schematic diagram showing the steps required to generate an MR signal	6
1.4	A simulation of free induction decay (FID)	6
1.5	A description of the spin echo with two consecutive 90° pulses (taken from (Hahn, 1950b))	7
1.6	A simulation of multiple spin echoes	8
1.7	A simulation of inversion recovery	9
1.8	A representation of the effect each gradient field has on the magnetic field . . .	11
1.9	A representation of a pulse sequence and its corresponding k-space	12
1.10	A representation of an EPI pulse sequence and its corresponding k-space	13
1.11	Aliasing example showing wrap around of the nose (highlighted with the arrow). This image was taken from (Pusey et al., 1988)	14
1.12	An example image representing parallel imaging and the magnitude of signal detected by receiver coils	15
1.13	A representation of cartesian sampling of k-space	15
1.14	A representation of an accelerated k-space acquisition using GRAPPA	16
1.15	A SENSE reconstructed image before correction	17
1.16	The haemodynamic response function	19
1.17	An example of the ASL signal	22
1.18	A representation of the differences in labelling schemes between PCASL, CASL and PASL	23
2.1	The anatomy of vessels within the brain viewed from the front	27
2.2	The anatomy of vessels in the brain viewed from the side	27
2.3	An example of a photoplethysmograph (PPG) trace	30
2.4	A schematic diagram showing the close relationship between heart rate variability (HRV) and pulsatility	31
2.5	An example of volume registration showing the rotation of a brain volume . . .	35

2.6	A diagrammatic representation of the signal change in two scenarios, one with motion and one with a global intensity change (GIC)	38
3.1	A schematic diagram showing the spin history effect	43
3.2	Motion parameters derived from a volume registration algorithm during a CO ₂ gases challenge with ASL tagging	45
3.3	A representation of the 3D surface collected during external motion tracking . .	47
3.4	An example of the calibration between a structural (MPRAGE) image and the surface generated by the Tracoline system	48
3.5	Translational motion parameters derived from the camera-based method	50
3.6	Rotational motion parameters derived from the camera-based method	50
3.7	Translational motion parameters derived from the VRA-based method	51
3.8	Rotational motion parameters derived from the VRA-based method	51
3.9	An FFT of camera-derived motion parameters	52
3.10	An FFT of camera-derived motion parameters with the problematic frequency range filtered out	52
3.11	R ² variance values showing the amount of variance explained in the global (average) signal for each correction method	59
3.12	R ² variance values showing the amount of variance explained in the signal driving the GIC for each correction method	60
3.13	R ² variance values showing the amount of variance explained in the VRA-based motion parameter estimates for each correction method	62
3.14	Connectivity values generated from resting state scans	64
3.15	Connectivity values generated from resting state scans with additional motion .	64
3.16	CBF values generated from multi-PLD PCASL scans	65
3.17	CBF values generated from Dual-excitation pCASL scans	66
3.18	CVR values generated from BOLD data collected as part of Dual-excitation pCASL scans	67
3.19	CVR values generated from Dual-excitation pCASL scans	68
3.20	CVR values generated from BOLD scans with a breath hold challenge	69
3.21	CMRO ₂ values generated from Dual-excitation pCASL scans	70
3.22	OEF values generated from Dual-excitation pCASL scans	71
4.1	A schematic diagram detailing the classification steps using in the 100-400 samples classifier	87
4.2	An example of stage two of the 100-400 samples classification algorithm	90
4.3	An example of components that survived all three stages of the 100-400 samples classification algorithm	91
4.4	Plots showing the heart rate values calculated from the 100-400 samples classifier	91

4.5	Plots comparing the heart rate values calculated using the 100-400 samples classifier and the true heart rate	92
4.6	A correlation matrix comparing the three methods used to generate pulsatility .	93
4.7	A correlation matrix showing the correlation between each method of generating pulsatility and physiological parameters	94
4.8	Plots showing the optimum number of iterations to calculate an accurate p -value for the permutation analysis	95
5.1	A schematic diagram outlining the classification process for the HRV method of classification	101
5.2	A schematic diagram showing the close relationship between heart rate variability (HRV) and pulsatility	102
5.3	A schematic diagram detailing the classification steps using in the 100-400 samples classifier	104
5.4	A correlation matrix comparing the "true" pulsatility values with the different HRV training datasets	106
5.5	A correlation matrix comparing the "true" pulsatility values with the different Frequency method training datasets	107
5.6	A bar chart showing percentage differences in gradients for scatter graphs . . .	107
5.7	A correlation matrix comparing the "true" GM pulsatility values with the different physiological parameters	108
5.8	A correlation matrix comparing the HRV generated GM pulsatility values with physiological parameters	109
5.9	A correlation matrix comparing the Frequency method generated GM pulsatility values with physiological parameters	110
5.10	A correlation matrix comparing the GM pulsatility values generated from both methods	111
5.11	A bar chart showing the number of runs analysed for each method of generating pulsatility	112
5.12	A bar chart showing the number of participants analysed for each method of generating pulsatility	112
5.13	Average Pulsatility maps for the HRV method	113
5.14	A bar chart showing the estimated pulsatility value in different tissue types using the HRV method	114
5.15	Average Pulsatility maps for the Frequency method	115
5.16	A bar chart showing the estimated pulsatility value in different tissue types using the Frequency method	115
5.17	A Bar chart showing the estimated pulsatility value in different tissue types using the HRV trace ("true" pulsatility)	116

A.1	Scatter graphs showing relationship between HRV pulsatility estimates and the ‘true’ pulsatility	147
A.2	Scatter graphs showing relationship between Frequency method pulsatility estimates and the ‘true’ pulsatility	148
A.3	Tables showing the correlation and p -values for the comparison between the HRV method estimates and the ‘true’ pulsatility	148
A.4	Tables showing the correlation and p -values for the comparison between the Frequency method estimates and the ‘true’ pulsatility	149
A.5	Tables showing the correlation and p -values for the comparison between the ‘true’ pulsatility and different physiological parameters	150
A.6	Tables showing the correlation and p -values for the comparison between the HRV method estimates of pulsatility and different physiological parameters . . .	151
A.7	Tables showing the correlation and p -values for the comparison between the Frequency method estimates of pulsatility and different physiological parameters	152
A.8	Tables showing the correlation and p -values for the comparison between the HRV estimates of pulsatility and the Frequency estimates of pulsatility	153

Symbols

Roman Symbols

A Field-dependent Constant

B_0 Magnetic Field Strength, T

ΔP Change in Pressure

ΔV Change in Volume

E Energy, J

f_{alias} Aliasing Frequency, Hz

f_N Nyquist Frequency, Hz

f_s Sampling Frequency, Hz

f_{true} True Frequency, Hz

\hbar A reduced form of Plancks constant $\simeq (1.055 \times 10^{-34} Js)$

k Boltzmann Constant ($\simeq 1.38 \times 10^{-23} kgm^2s^{-2}K^{-1}$)

L Vessel Length, m

M Maximum Possible BOLD Signal Change

M_0 Net magnetisation vector, T

$M_{0,a}$ Magnetisation of Arterial Blood

$M_{0,CSF}$ Magnetisation of Tissue (CSF in this case)

$M_x(t)$ x-component of the net magnetisation vector over time, T

$M_{xy}(t)$ Transverse component of the net magnetisation vector over time, T

$M_y(t)$ y-component of the net magnetisation vector over time, T

$M_z(t)$	z-component of the net magnetisation vector over time, T
n	Harmonic Number, H_z
N^+	Number of Anti-Parallel Spins
N^-	Number of Parallel Spins
PaO_2	Partial Pressure of Oxygen in Arterial Blood
R	Cerebrovascular Resistance
r	Vessel Radius, m
\vec{S}	Spin, kgm^2s^{-1}
SaO_2	Arterial Oxygen Saturation
$\frac{\Delta S}{S_0}$	Fractional BOLD Signal Change
T	Temperature, K
t	Time, s
T_1	Longitudinal relaxation time constant, s
$T_{1,blood}$	Longitudinal Relaxation Time of Blood, s
T_2	Natural transverse relaxation time constant, s
T_2'	Transverse relaxation time constant due to field inhomogeneities, s
T_2^*	Observed transverse relaxation time constant, s
$T_{2,a}^*$	Transverse Relaxation Time of Arterial Blood
$T_{2,CSF}^*$	Transverse Relaxation Time of Tissue
X	Regressors (as part of General linear model)
Y	Data (as part of General linear model)
Greek Symbols	
α	ASL Labelling Efficiency
β	Constant Depending on Vessel Size and Geometry
β_0	Mean Offset Over Time

ε	Coefficient of Solubility of Oxygen in Blood
ε	Residuals (as part of General linear model)
γ	Gyromagnetic Ratio of a Hydrogen atom ($\simeq 4.258 \times 10^7 \text{ HzT}^{-1}$)
λ	Brain/Blood Partition Coefficient, mlg^{-1}
μ	Blood Viscosity, Pas
$\vec{\mu}$	Magnetic Dipole Moment, NmT^{-1}
ν	Frequency of Precession, Hz
ϕ	O_2 Carrying Capacity of Haemoglobin, $\text{gHbdl}^{-1}\text{blood}$
$\phi]$	O_2 Carrying Capacity of Haemoglobin
τ	ASL Label Duration, s

Acronyms / Abbreviations

AAT Arterial Arrival Time

AC Arterial Compliance

ACFF_{Cardiac} Amplitude of Cardiac Frequency Fluctuations (across cardiac window)

ACFF_{Whole} Amplitude of Cardiac Frequency Fluctuations (across whole spectrum)

ANS Autonomic Nervous System

ASL Arterial Spin Labelling

BBB Blood Brain Barrier

BBR Boundary Based Registration

BH Breath Hold

BOLD Blood Oxygenation Level Dependent Effect

BPM Beats per Minute

BV Brain Volume

CaO₂ Concentration of Arterial Oxygen

CASL Continuous ASL

- CBF* Cerebral Blood Flow, ($ml100g^{-1}min^{-1}$)
- CBF₀* Baseline Cerebral Blood Flow
- CBV* BOLD-relevant Blood Volume
- CBV₀* BOLD-relevant Baseline Blood Volume
- CMRO₂* Cerebral Metabolic Rate of Oxygen Consumption, $\mu moles(100g)^{-1}min^{-1}$
- corr_{rand}* Correlation Value from the Random Permutation
- corr_{true}* Actual Correlation Value
- CPP* Cerebral Perfusion Pressure
- CVR* Cerebrovascular Reactivity
- dHb* Deoxyhaemoglobin
- dHb* Concentration of deoxyhaemoglobin
- dHb₀* Concentration of deoxyhaemoglobin at baseline
- DIA* Diastolic Blood Pressure
- DSC* Dynamic Susceptibility Contrast
- EEG* Electroencephalography
- EPI* Echo-Planar Imaging
- ETCO₂* End-tidal Carbon Dioxide, *mmHg*
- fACFF* Fractional Amplitude of Cardiac Frequency Fluctuations
- FD* Framewise Displacement
- FFT* Fast Fourier Transform
- FID* Free Induction Decay
- FIX* FMRIB's ICA-based X-noiseifier
- fMRI* Functional MRI
- GIC* Global Intensity Change
- GM* Grey Matter

<i>Hb</i>	Haemoglobin
<i>HCP</i>	Human Connectome Project
<i>HRV</i>	Heart Rate Variability
<i>IC</i>	Independent Component
<i>ICA</i>	Independent Component Analysis
<i>IR</i>	Inversion Recovery
<i>LFFs</i>	Low Frequency Fluctuations
<i>MAP</i>	Mean Arterial Pressure
<i>MEG</i>	Magnetoencephalography
<i>MR</i>	Magnetic Resonance
<i>MRI</i>	Magnetic Resonance Imaging
<i>NMR</i>	Nuclear Magnetic Resonance
<i>OEF</i>	Oxygen Extraction Fraction
<i>pCASL</i>	Pseudo-Continuous ASL
<i>PASL</i>	Pulsed ASL
<i>PNS</i>	Parasympathetic Nervous System
<i>PPG</i>	Photoplethysmograph
<i>p – value</i>	Probability Value
<i>RF</i>	Radio Frequency (pulse)
<i>rfMRI</i>	Resting-state fMRI
<i>RSN</i>	Resting State Network
<i>SE</i>	Spin Echo
<i>SI_{control}</i>	Time averaged Signal Intensity in Control Image
<i>ST_{PD}</i>	Signal Intensity of Proton Density Weighted Image
<i>SNR</i>	Signal-to-Noise Ratio

SNS Sympathetic Nervous System

SI_{tag} Time averaged Signal Intensity in Tag Image

SYS Systolic Blood Pressure

TE Echo Time

TI Inversion Time

TR Repetition Time

VRA Volume Registration Analysis

WB Whole Brain

WM White Matter

Chapter 1

Introduction to fMRI

1.1 Chapter Overview

Functional Magnetic Resonance Imaging (fMRI) is widely used to map brain function. It is thought to be a superior method of mapping brain function due to its relatively high spatial resolution. The majority of fMRI experiments make use of the Blood Oxygenation Level Dependent (BOLD) effect, first described by Ogawa and colleagues in 1990 (Ogawa et al., 1990). They showed that by using the BOLD technique, signals from the brain micro-vasculature could be measured. In 1992, the first detections of the BOLD effect were reported by three separate labs (Bandettini et al., 1992; Kwong et al., 1992; Ogawa et al., 1992). Since then, BOLD fMRI has been used extensively by cognitive neuroscientists to investigate the relationship between behaviour and the brain (Jezzard et al., 2003). While many fMRI studies use tasks to activate areas of the brain, resting-state fMRI (rfMRI) uses the ongoing fluctuations of neural activity to infer connections between different regions (Lee et al., 2013; Smith et al., 2013; Van Essen et al., 2013). Additionally, rfMRI can be used to identify resting-state networks (RSNs), disparate regions of the brain connected together to support functional processing (Lee et al., 2013; Smith et al., 2013; Van Essen et al., 2013). During an rfMRI experiment, participants are instructed to not perform any cognitive tasks so that the resting brain can be measured. Biswal and colleagues (Biswal et al., 1995) performed the first rfMRI experiment and detected spontaneous low frequency fluctuations (LFFs) within the BOLD signal. The authors also noted that these LFFs showed a high correlation with the left and right motor cortex at rest (Biswal et al., 1995). There is evidence suggesting that rfMRI can be used in surgical planning (Bettus et al., 2010; Kokkonen et al., 2009; Liu et al., 2009; Shimony et al., 2009), in the detection of patients with Alzheimer's Disease (Dai et al., 2012; Koch et al., 2012; Supekar et al., 2008) and in the detection of patients with autism (Anderson et al., 2011). Since BOLD-fMRI is derived from a vascular signal, conclusions related to the health of the cerebrovasculature can also be drawn from it.

Perfusion imaging measures brain perfusion, the rate of blood delivery to a particular region, which when combined with other measures can lead to the quantification of cerebral blood flow

(CBF) (Alsop et al., 2015; Buxton et al., 1998; Chen et al., 2008), cerebrovascular resistance (CVR) (Fierstra et al., 2013) and the cerebral metabolic rate of oxygen consumption ($CMRO_2$) (Davis et al., 1998; Germuska et al., 2019; Hoge et al., 1999a; Merola et al., 2016; Wise et al., 2013). These metrics allow us to understand the cerebrovasculature much better. Typically, perfusion imaging can be performed in one of two ways, using an exogenous contrast agent in a process known as Dynamic Susceptibility Contrast, or using arterial spin labelling (ASL) which will be covered in detail in a further section in this chapter. From here on when referring to perfusion imaging I will be talking about ASL.

In this chapter, I will introduce the basic concepts that enable functional imaging, including spin, precession, echo creation and k-space (among other fundamental concepts), as well as introduce and explain the BOLD effect and ASL imaging methods.

1.2 Nuclear Magnetic Resonance

1.2.1 Spin

Functional Magnetic Resonance Imaging (fMRI) is an adapted version of Magnetic Resonance Imaging (MRI), an imaging technique that uses the principles of Nuclear Magnetic Resonance (NMR), to explore the functional aspects of the brain. To fully understand the principles of fMRI, one must understand the principles of NMR. NMR was initially discovered in 1938 when researchers used a beam of lithium chloride, an electromagnet and a hairpin coil to measure the resonance of peaks of lithium and chlorine (Rabi et al., 1938). This was taken further in the 1940s when two separate groups demonstrated NMR in condensed matter (Bloch et al., 1946; Purcell et al., 1946). The protons and neutrons that make up matter have an intrinsic quantum mechanical property known as spin which is a quantum mechanical form of angular momentum (Buxton, 2009). Many believe that spin can be likened to a ball spinning, which is implied by the name spin. However, this is not the case as spin is an intrinsic characteristic of the protons and neutrons and its values occur in specific quantized values (Jezzard et al., 2003). Protons (and neutrons) that make up a nucleus do so in pairs of opposite spin (Buxton, 2009). This results in elements with even numbers of protons and neutrons having no net spin and those with odd numbers having a net spin. Elements with no net spin have no NMR signal associated with them and thus cannot be measured in this way (Jezzard et al., 2003). The magnetic dipole moment is a property closely related to spin and it is this property that makes protons slightly magnetic. The relationship between the magnetic dipole moment and the spin angular momentum is shown in equation 1.1, where $\vec{\mu}$ is the magnetic dipole moment, γ is the gyromagnetic ratio (for a hydrogen atom this is $4.258 \times 10^7 \text{ HzT}^{-1}$) and \vec{S} is the spin. MRI is an adapted version of NMR that produces images of the inside of a human body, which contains an abundance of hydrogen atoms. Hydrogen has only one proton within its nucleus and so has a net spin. This coupled with its abundance in the human body makes hydrogen an important part of MRI experiments.

$$\vec{\mu} = \gamma \vec{S} \quad (1.1)$$

1.2.2 Precession, Excitation and Relaxation

In the presence of a uniform external magnetic field, a torque will be exerted on the protons causing the magnetic dipole moment to align either parallel (low energy state) or anti-parallel (high energy state) (Figure 1.1) to the magnetic field (Huettel et al., 2014). The ratio of parallel to anti-parallel alignment can be calculated from equation 1.2, where N^+ is the number of anti-parallel spins, N^- is the number of parallel spins, E is energy, k is the Boltzmann Constant and T is the temperature. The energy variable can be calculated using equation 1.3, where \hbar is the reduced Planck Constant and B_0 is the Magnetic Field Strength. Assuming a 3T scanner and a temperature of 37° C (average human body temperature) the ratio of parallel spins to anti-parallel spins is equal to 1.00003.

$$\frac{N^+}{N^-} = e^{-\frac{E}{kT}} \quad (1.2)$$

$$E = \gamma \hbar B_0 \quad (1.3)$$

The percentage of spins aligning parallel can be determined from equation 1.4. This was calculated to be $\sim 50.00008\%$ and so the percentage aligning anti-parallel is $\sim 49.99992\%$. Therefore, the majority of the proton's magnetic dipole moments will align parallel to the field as this is a lower energy state (although the difference in those aligning parallel and those aligning anti-parallel is small $\sim 0.00016\%$). This causes a net magnetisation, M_0 , to occur in the direction parallel to the B_0 field.

$$\%N^- = \frac{N^-}{N^- + N^+} \cdot 100 \quad (1.4)$$

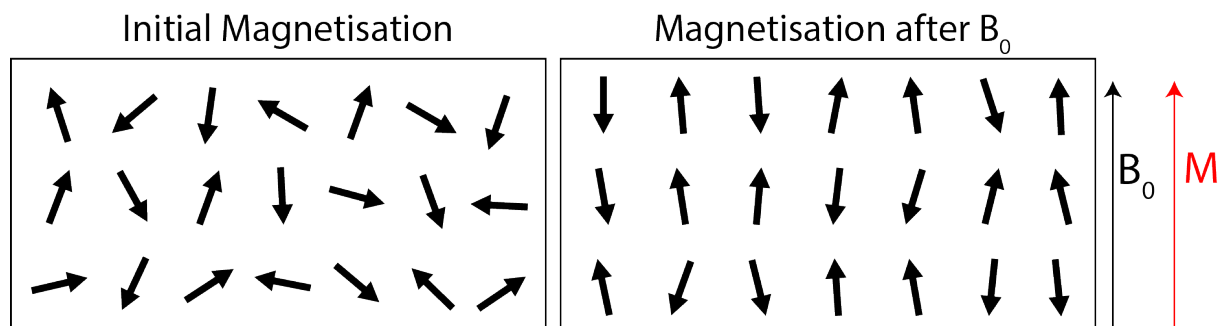


Fig. 1.1 Magnetisation before and after alignment with an external magnetic field. Initially, the magnetic moments will be orientated in a random direction, but in the presence of an external magnetic field, they will align parallel (or anti-parallel) to the field.

In the presence of this B_0 field, a torque will be exerted on the magnetic dipole moments causing them to precess around the direction of the magnetic field (Buxton, 2009). The frequency of precession, ν , is known as the Larmor frequency and is directly proportional to the strength of the magnetic field. It can be calculated using equation 1.5. Figure 1.2 diagrammatically represents precession for an individual proton.

$$\nu = \gamma B_0 \quad (1.5)$$

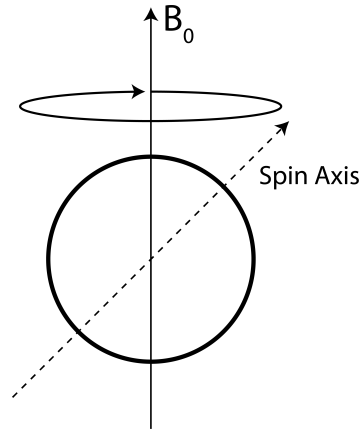


Fig. 1.2 Diagrammatic representation of precession for an individual proton when in the presence of an external magnetic field (B_0). The spin axis will precess around the B_0 field as depicted by the circular arrow with frequency ν

The sum of all the individual proton's magnetic dipole moments is called the net magnetisation vector (M_0) and this quantity is zero in the absence of an external magnetic field. When aligned with the B_0 field, the value of M_0 is substantially smaller than that of B_0 . To measure an MR signal, the net magnetisation vector needs to be perturbed so that it has a transverse component associated with it (Jezzard et al., 2003). This is achieved using the transmit radiofrequency (RF) coils. Within these coils, an oscillating current produces an oscillating magnetic field known as the B_1 field. If the oscillation frequency is at the Larmor frequency for which resonance occurs, the magnetisation is tipped towards the transverse plane. The angle of perturbation is known as the flip angle (α). While the magnetic field is oscillating, M_0 will move towards the transverse plane. As noted by Bloch, the M_0 vector can be resolved into three components, $M_x(t)$, $M_y(t)$, and $M_z(t)$ (Bloch, 1946). $M_z(t)$ is defined as the longitudinal component and $M_x(t)$ and $M_y(t)$ are known as the transverse components, which together in the rotating frame are called $M_{xy}(t)$. Once the magnetisation is tipped away from the longitudinal z-direction, the transverse component of the $M(t)$ will precess in the x-y plane and will induce an oscillating voltage in the RF receiver coils. This oscillating voltage can be converted into a digital signal which is the MR signal. The precession caused by the B_1 field continues after it is switched off and $M(t)$ will begin to realign with B_0 in a process known as relaxation. During relaxation the transverse components of $M(t)$ will reduce in magnitude and the longitudinal component will increase.

The precession of the transverse components of $M(t)$ will induce an oscillating voltage in the RF receive coils and therefore an MR signal is generated during relaxation. The longitudinal and transverse magnetisations are defined in equations 1.6 and 1.7, where t is time, T_1 is the longitudinal relaxation time constant and T_2 is the transverse relaxation time constant.

$$M_z(t) = M_0(1 - e^{-\frac{t}{T_1}}) \quad (1.6)$$

Longitudinal relaxation is characterised by the time constant T_1 whereas transverse relaxation is characterised by the time constant T_2 .

$$M_{xy} = M_0 e^{-\frac{t}{T_2}} \quad (1.7)$$

In reality, the decay of the transverse magnetisation is much quicker than its theoretical decay. This is due to local and external magnetic field inhomogeneities that interact with the individual spins, causing them to move out of phase with each other (dephase) much quicker. This is called T_2^* decay and is represented in equation 1.8, where T_2' is the relaxation rate contribution from the field inhomogeneities.

$$\frac{1}{T_2^*} = \frac{1}{T_2} + \frac{1}{T_2'} \quad (1.8)$$

These principles form the basis of any MRI experiment. A patient is placed into the static B_0 field, and the M_0 of the protons within their water molecules align with it. A B_1 field oscillating at the Larmor frequency is used to perturb M_0 and rotate the magnetisation towards the transverse plane. During this, the magnetisation will precess around B_0 . This precession continues even when the B_1 field is switched off, however $M(t)$ will begin to relax and re-align with B_0 . The precession of $M(t)$ produces RF signal which can be detected in the RF receiver coils. This is the MR signal. Figure 1.3 demonstrates these steps diagrammatically.

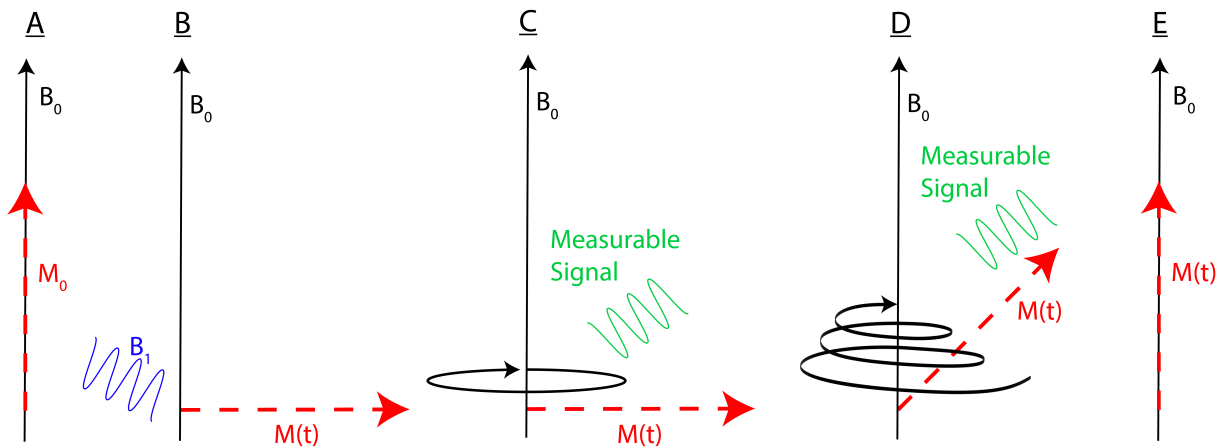


Fig. 1.3 The generation of an MR signal. A. The initial magnetisation is aligned with the B_0 field. B. A B_1 field is used to perturb the system (in this case a 90° flip angle was used). C. While the signal is perturbed, $M(t)$ precesses in the x-y plane and a measurable signal can be detected. D. Once the B_1 field is switched off, the magnetisation relaxes back into alignment with the B_0 field. During which, a measurable signal can be detected. E. B_0 and $M(t)$ are back in alignment.

1.3 Basic MR Signals

The most basic MR signal that can be acquired is called free induction decay (FID) which is collected by perturbing the net magnetisation and recording the signal received. FID was first detected by Hahn in the 1950s (Hahn, 1950a) and a simulation of FID is shown in Figure 1.4. T_2^* weighted signal can be obtained from FID as this is the raw signal which includes dephasing information described by T_2^* .

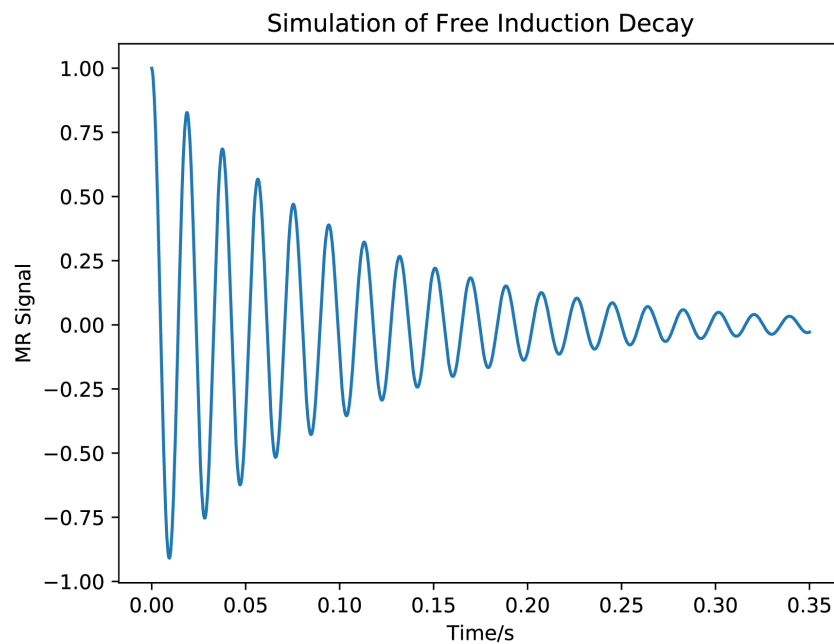


Fig. 1.4 A simulated example of the free induction decay (FID) signal. The signal oscillates at the Larmour frequency and is dampened by T_2^* decay. A T_2^* weighted signal can be measured from FID. The parameters used in this simulation this were; $T_1=0.6$ s, $T_2=0.1$ s.

1.3.1 Echo Creation

FID alone is unable to measure T_2 weighted signal and another technique must be used to achieve this. This technique makes use of echo creation. Individual proton spins dephase more quickly than expected due to magnetic field inhomogeneities and this is characterised by T_2^* . If the inhomogeneous dephasing could be removed then one could measure T_2 weighted signal. In the 1950s Hahn discovered that the proton spins could be refocused by use of a pair of consecutive 90° RF pulses separated by time period, τ (Hahn, 1950b). This refocusing resulted in the reversal of some dephasing allowing $M(t)$ to regrow to a measurable value. The regrowth of $M(t)$ is called an echo. In the paper where Hahn first described the spin echo, the initial 90° pulse was used to move the spins into the transverse plane, and the second 90° pulse was used to move the spins back into the longitudinal plane. The x-component of the spins will still precess and, after some time, refocus to produce an echo (Figure 1.5).

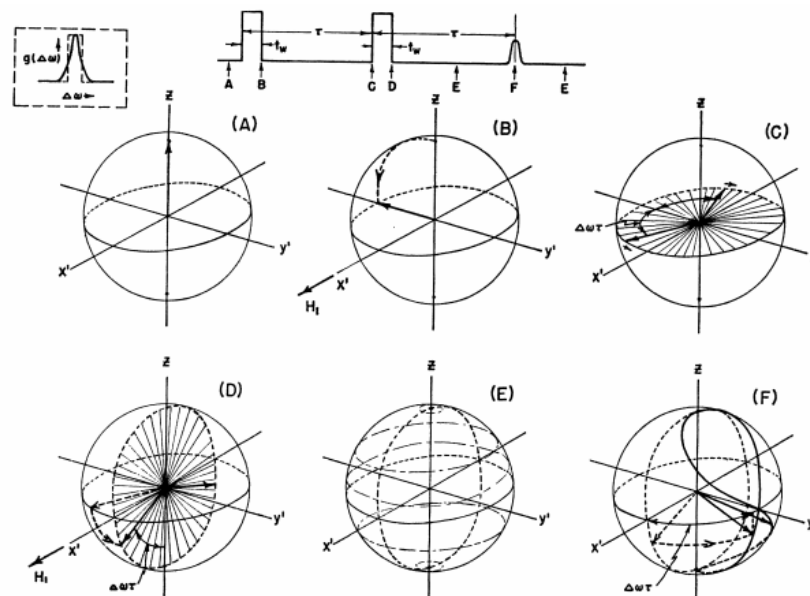


Fig. 1.5 Figure describing Spin Echo with two consecutive 90° pulse (taken from (Hahn, 1950b)). A. Spins are all precessing in the longitudinal plane. B. A 90° RF pulse is applied to move the spins into the transverse plane. C. Spins precess in the transverse plane at different frequencies. D. A second 90° pulse is applied and the spins are moved into the longitudinal plane. E. The z-component of these spins will be static and in alignment with M_z . The x-component will precess around the x-y plane. F. After a time period (2τ from the start of the experiment) the spins precessing in the x-y plane will refocus forming an echo.

This sequence was further modified by Carr and Purcell who proposed the use of an initial 90° RF pulse, to move the spins into the transverse plane. Following this, a 180° RF pulse (applied at time τ after the 90° pulse) was used to invert the spins and cause them to refocus instead of two 90° pulses (Carr and Purcell, 1954). By doing this the signal regrows back to the T_2 curve. Repeating this process multiple times enables the measurement of the T_2 decay curve. This process is simulated in Figure 1.6.

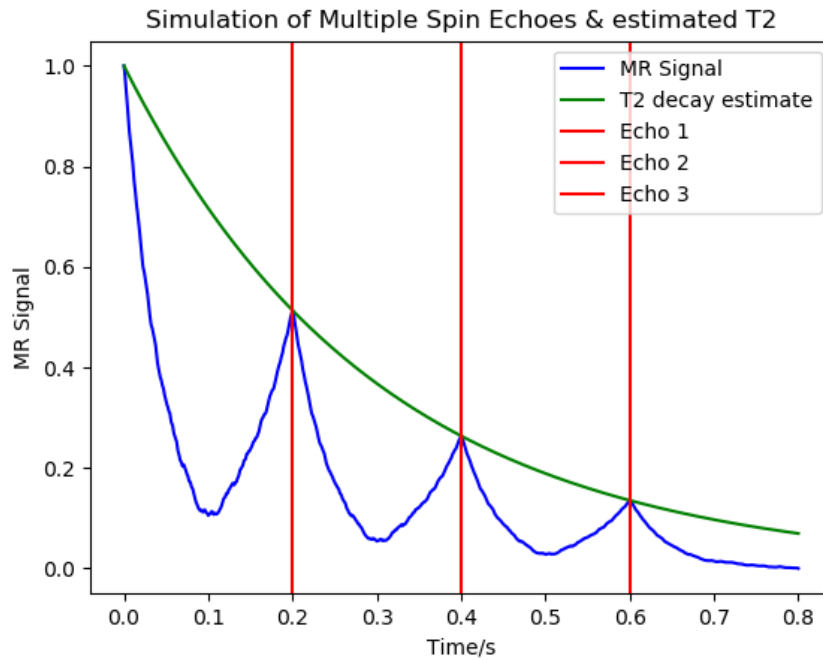


Fig. 1.6 A simulated example of a multiple spin echo sequence used to estimate T_2 decay. The blue line represents the MR signal which initially decays and is then regrown after the refocusing pulse is turned on. The green line represents the estimated T_2 decay curve. The red lines represent the spin echoes. In this simulation 3 echoes were used with parameters; $T_1=0.6$ s, $T_2=0.1$ s.

Another method of generating an echo that doesn't require the use of another RF pulse is called a gradient echo which is T_2^* dependent. This method works by initially using a negative gradient to dephase the spins and causes them to precess in a frequency dependent pattern (Elster, 1993). Then a positive gradient is used to rephase the spins and generates a gradient echo.

The longitudinal magnetisation ($M_z(t)$) is very small in comparison to the B_0 field and, as such, its characteristic time constant, T_1 , is also difficult to measure. The accepted method of measuring T_1 is called Inversion Recovery (IR) and uses an initial 180° RF pulse to flip M_0 so that it points in the opposite direction to B_0 . Following this 180° RF pulse, the magnetisation is allowed to evolve for a time period known as the inversion time (TI) and then a 90° pulse is used to flip the resulting longitudinal magnetisation into the transverse plane. During the inversion time, the individual spins will relax back to alignment with the B_0 field at a rate determined by their T_1 relaxation value (Jezzard et al., 2003). Different tissues in the body will relax at different T_1 rates and those with shorter T_1 values will relax quicker than those with longer T_1 values, therefore defining different tissue types. A simulation of inversion recovery is shown in Figure 1.7.

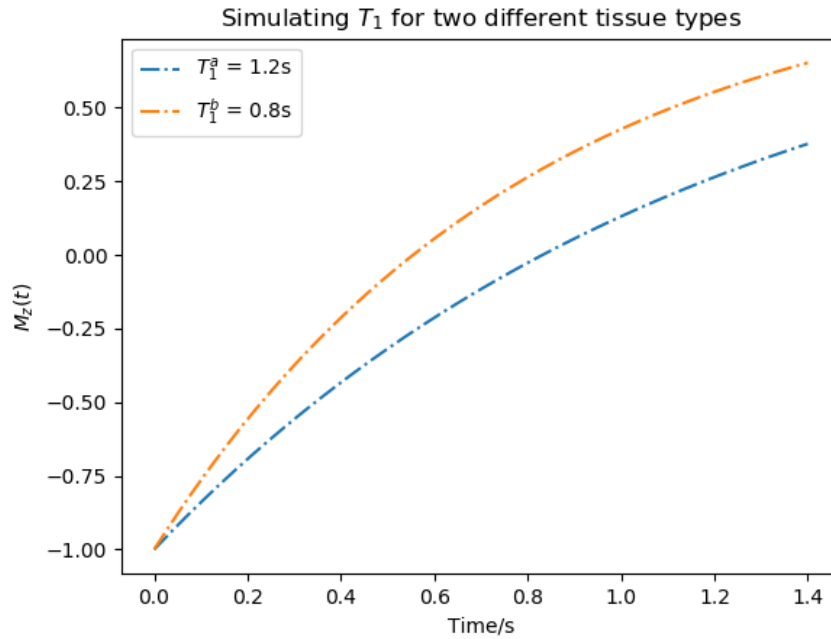


Fig. 1.7 Simulation of Inversion Recovery to determine T_1 curves for two different tissue types. The two dotted lines represent each of the estimated T_1 curves. The magnetisation is tipped into the $-z$ direction with a 180° RF pulse and then relaxes back to the $+z$ direction at a rate of T_1

1.4 Image Formation

1.4.1 K-space

The signal detected by the receiver coils is not an image, instead, it is a mixture of signals which are contained within k-space. From Fourier theory, we know that a 2D image can be represented by a set of sine and cosine terms that differ by their frequency and amplitude. The information collected by the receiver coils is in this form and the signals are known as spatial frequencies. An inverse Fourier transform must be used to convert these spatial frequencies into an image. Equation 1.9 shows the discrete Fourier transform used to convert between k-space and image space for a 1-dimensional signal.

$$X_j = \sum_{k=0}^{N-1} x_k e^{-\frac{2\pi i k j}{N}}, \quad j = 0, 1, \dots, N-1 \quad (1.9)$$

Before an image can be generated, enough of k-space must be sampled to ensure good data quality. Sampling of k-space can be achieved through many different methods, one of these is Echo Planar Imaging, which will be discussed further in section 1.5.

1.4.1.1 Gradients

Magnetic field gradients are used to vary the precession frequency of the magnetisation M at different points in space to localise the source of the MR signal. These gradients are generated in gradient coils and there are three different types. Each gradient works to vary the magnetic

field in each of the three spatial directions (x , y , z). To select an axial slice, a gradient is applied in the z -direction with the magnetic field gradient causing spins to precess at different rates depending on their position in the z direction. This leads to spins with position dependent resonant frequencies. An RF pulse with frequency matching the resonant frequency of spins in the desired slice will excite only the spins within that slice, thus selecting it. Equation 1.10, which is a variation of equation 1.5, describes the effect of the linearly varying magnetic field on the resonant frequency of spins along the z -direction. As before ν is the precessional frequency as a function of z , γ is the gyromagnetic ratio and B_0 is the magnetic field strength as a function of z .

$$\nu(z) = \gamma B_0(z) \quad (1.10)$$

The x -direction is normally denoted the frequency encoding direction. Gradients applied in this direction result in a linear series of frequencies representing spatial locations along the x -axis. This results in spins that precess slower where the gradient is weakest and faster where the gradient is strongest. In the y -direction, magnetic field gradients applied momentarily alter the phase of precession of the spins in the y -direction for a given frequency in the x -direction. This process is called phase encoding. For this explanation, frequency encoding was chosen to work in the x -direction and phase encoding was chosen to work in the y -direction, however the choice of the direction of the x , y , z coordinate system is arbitrary. Figure 1.8 shows the effect of the different magnetic field gradients on the magnetic field.

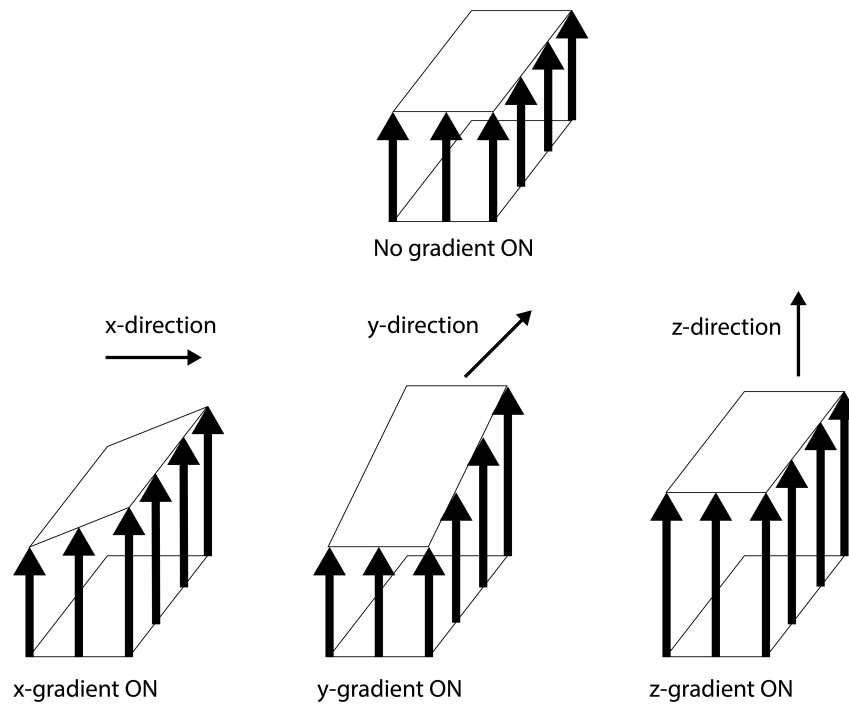


Fig. 1.8 A representation of the effect each gradient field has on the magnetic field. For example, when the x-gradient is on, the frequency of the proton precession is altered in the x-direction. In addition an example where there is no gradient field is included. This figure is adapted from the figure found here: <https://www.mriquestions.com/gradient-coils.html>

In k-space, the frequency encoding gradient corresponds to the sampling of a single line of k-space in one direction (the k_x -direction in this example), whereas the phase encoding gradient alters the position that this line of k-space is sampled in the k_y direction.

A typical MR experiment follows a complex pulse sequence that dictates when each RF pulse and gradient field are used. By repeating the sequence and only changing the phase encoding gradient one can cycle through k-space and collect a full image (or slice). Each repetition of the sequence would encode one line of k-space and the time between each repeat is the repetition time (TR). To collect an image of the whole brain, multiple slices must be acquired by changing the slice select gradient and then traversing k-space as outlined earlier in this section. An example of a pulse sequence used to acquire a slice and its corresponding k-space is shown in Figure 1.9.

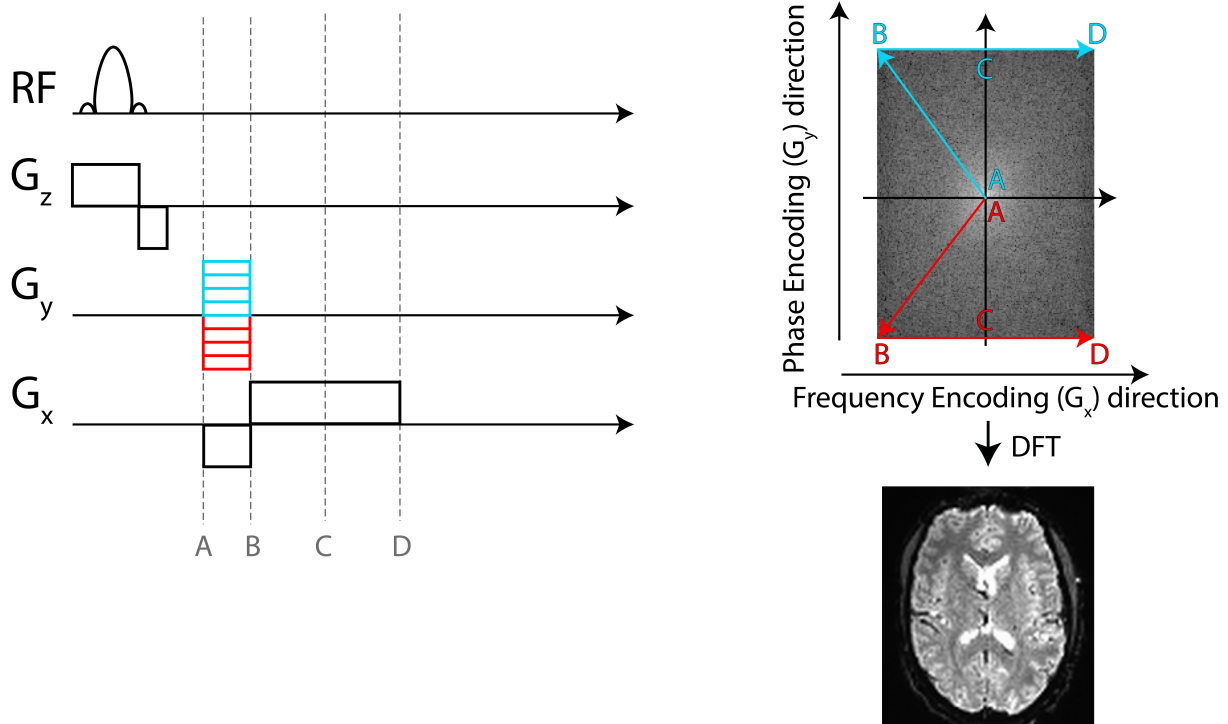


Fig. 1.9 A pulse sequence and its corresponding k-space acquisition. Each letter (A, B, C & D) represents the different parts of the pulse sequence on the k-space image. Each repetition of this sequence would acquire a different part of k-space by changing G_y (the phase encoding direction) only. Finally, after all spatial areas of k-space are acquired a discrete Fourier transform can be used to convert the data into image space.

1.5 EPI Imaging

As explained in the previous section, an image is formed by using magnetic field gradients to navigate k-space, and each repeat of the experiment will encode a different line of k-space. This is inefficient as the collection of one slice would take a large amount of time. Echo Planar Imaging (EPI) significantly reduces this acquisition time by navigating the whole of k-space with one excitation pulse. This is achieved by rapidly switching the frequency encoding gradient so that it traverses back and forth through the entirety of k-space. As well as changing the frequency encoding gradient, the phase encoding gradient is used as a series of 'blips' which enable a slight movement in the y-direction for each k-space line acquired in the x-direction. This is shown in Figure 1.10.

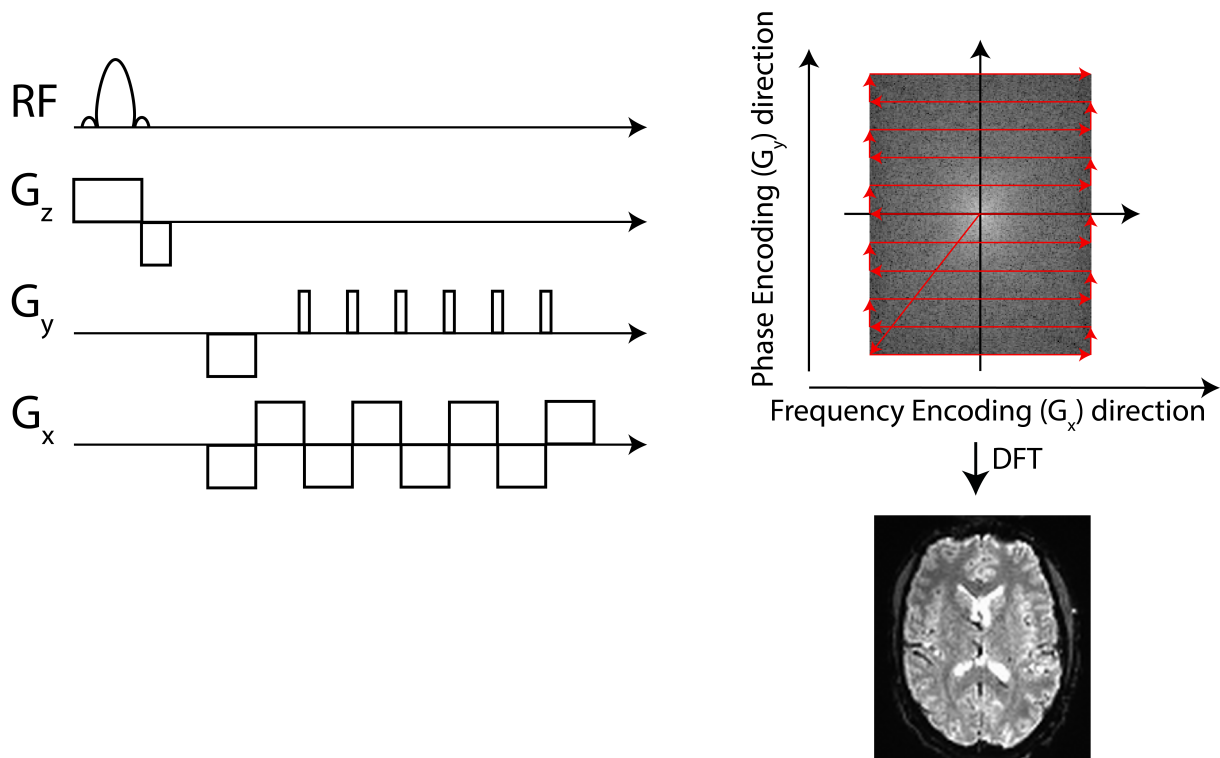


Fig. 1.10 A pulse sequence showing an EPI acquisition and its associated k-space. Instead of starting from the centre and acquiring one line of k-space at a time, EPI captures the whole of k-space by ‘blipping’ through the G_y (phase encode) direction.

1.5.1 Aliasing

When sampling a signal, it is important to ensure that samples are collected fast enough, as under sampling will result in an incorrect reconstruction of the original signal. The Nyquist theorem states that the sampling frequency must be equal or higher than two times the highest frequency present in the data. This is described by equation 1.11 where f_s is the sampling frequency and f_N is the Nyquist frequency, or the highest frequency present in the data.

$$f_s = 2f_N \quad (1.11)$$

In MR, aliasing can be detrimental to the output image. These effects cause signal wrap around, resulting in parts of the image to be misplaced in space. An example of this wrap around artefact is shown in Figure 1.11, which was taken from (Pusey et al., 1988). Aside from causing issues in the image itself, aliasing can cause issues with frequency related data. An example of this is discussed in detail in Chapter 4, where frequency data related to the cardiac cycle is aliased to another location on the frequency spectrum.

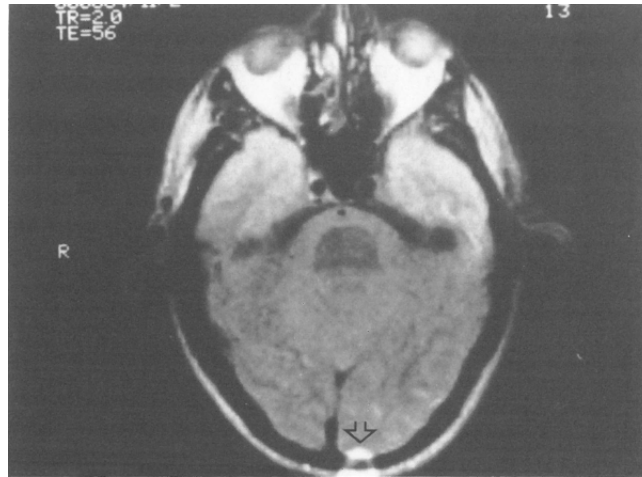


Fig. 1.11 Aliasing example showing wrap around of the nose (highlighted with the arrow). This image was taken from (Pusey et al., 1988)

1.6 Acceleration & Parallel Imaging

When designing a pulse sequence, a trade-off must be made between the speed of k-space sampling and the data quality. The more of k-space that is sampled, the better the data quality will be. However fully sampling k-space is a lengthy procedure that may not dramatically increase data quality. Additionally, because the MR signal will decay over time, it is important to sample k-space before the signal is no longer measurable.

Parallel imaging techniques can be used to accelerate the imaging process. These techniques make use of receiver coil placements and sensitivities to aid in spatial encoding. This information allows for a reduction in the number of required phase encoding steps which is used to accelerate the scan time. Reducing the number of phase encoding steps is the same as undersampling k-space.

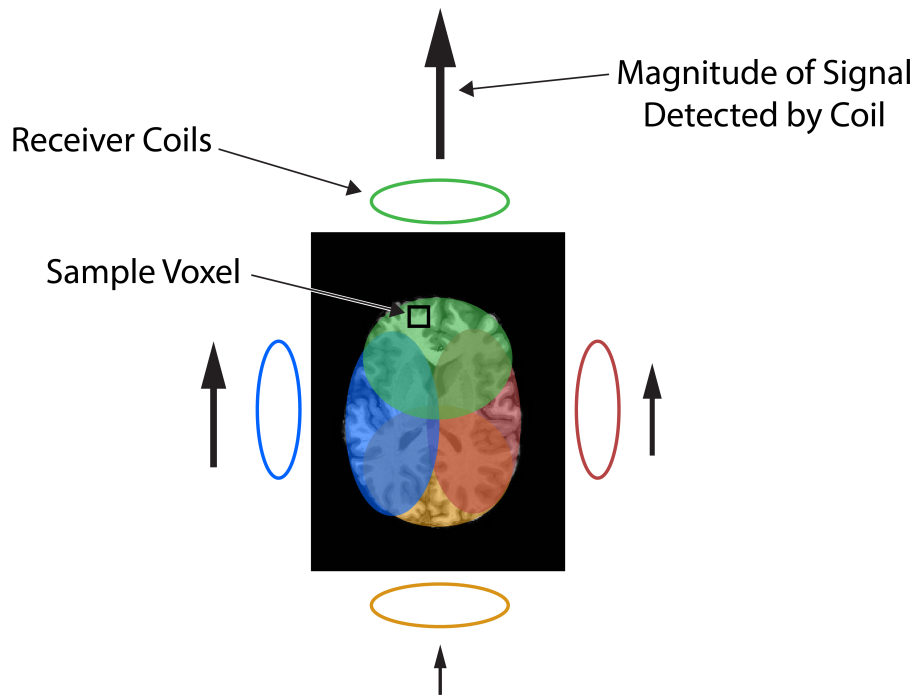


Fig. 1.12 An example figure showing that different receiver coils will detect a different magnitude of signal depending on where they are in relation to the voxel being sampled. In this example, the green ellipses represent the receiver coils, the square represents the sampling voxel and the arrows represent the magnitude of the signal. Notice that the arrows closest to the sampling voxel are much thicker and longer. This figure is an adapted version of a figure found here: <https://mriquestions.com/what-is-pi.html>

Two examples of parallel imaging methods which will be explained in this section include GRAPPA and SENSE. Additionally, I will introduce multi-band imaging, which is not a parallel imaging method but can be used to achieve accelerated scan times by acquiring multiple slices simultaneously. In a non-accelerated pulse sequence, the majority of k-space will be sampled as shown in Figure 1.13.

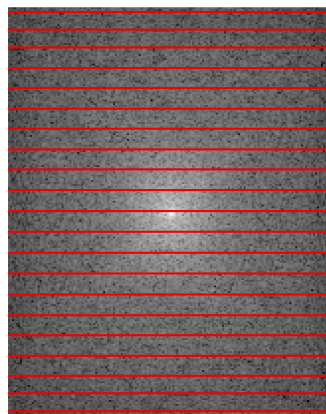


Fig. 1.13 An example of cartesian sampling of k-space in non-accelerated pulse sequences. The red lines represent the lines of k-space that are collected.

1.6.1 Generalized autocalibrating partially parallel acquisitions (GRAPPA)

In 2002 Griswold and colleagues introduced an acceleration technique known as the Generalized autocalibrating partially parallel acquisitions (GRAPPA) (Griswold et al., 2002). This purposefully undersamples k-space by increasing the distance between sampled k-space lines. However, the centre of k-space is fully sampled and this makes the autocalibration region. This is repeated for all of the receive coils and results in a k-space matrix for each coil. Before an image can be generated, GRAPPA must estimate the k-space lines that were missed. GRAPPA uses an interpolation algorithm that takes in information from 3 dimensions. These dimensions are: the frequency encode direction, the phase encode direction and the k-space information from the other coils. It calculates weighting factors from the autocalibration region which determine the amount of distortion, displacement and shear each coil has on the spatial frequencies within k-space. This is shown in Figure 1.14.

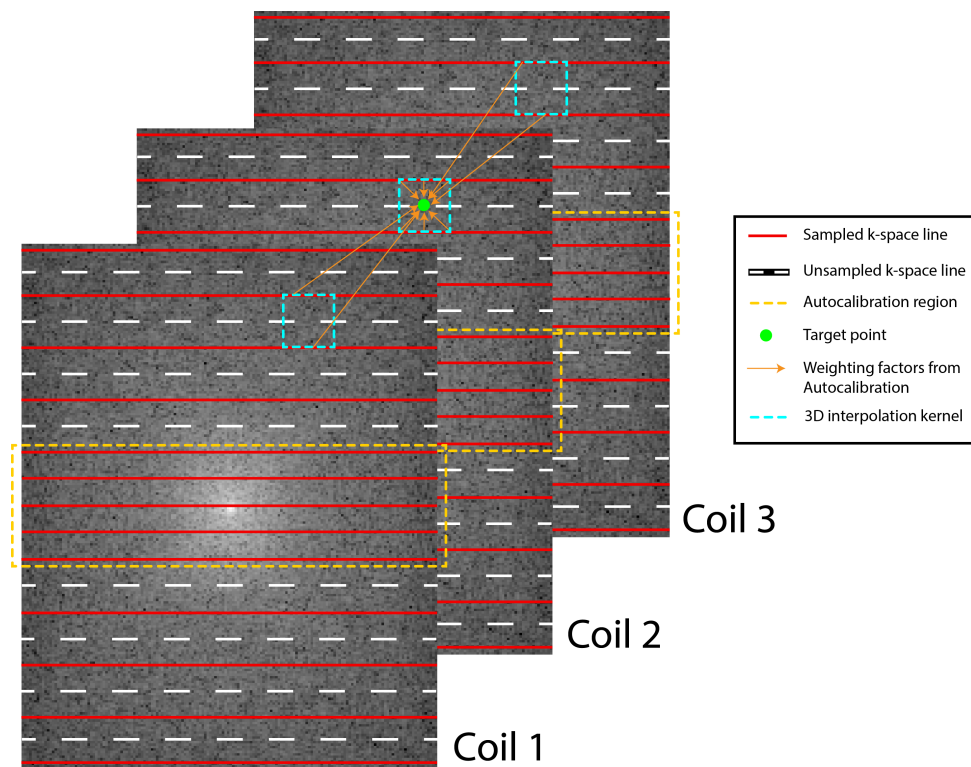


Fig. 1.14 Estimation of k-space lines for undersampled k-space using the GRAPPA method. In this example, the red lines represent the sampled lines of k-space, the dashed white line represents lines of k-space that are unsampled, the yellow dashed line represents the autocalibration region, the green dot represents that target location, the orange arrows represent the weighting factors from the autocalibration and the blue dashed line represents the 3D interpolation kernel. GRAPPA purposefully undersamples k-space. The centre of k-space is fully sampled and this makes up the autocalibration region. There is an autocalibration region for each receiver coil. Then the undersampled lines of k-space can be estimated using the autocalibration region using an interpolation algorithm.

Following the estimation of the missing k-space lines, an inverse Fourier transform is used to generate an image for each coil and these can be combined using a sum-of-squares combination (or any array reconstruction method) to generate a whole image (Griswold et al., 2002).

1.6.2 Sensitivity Encoding for Fast MRI (SENSE)

GRAPPA works to estimate missing k-space lines before performing an inverse Fourier transform. Another acceleration technique works in a similar way to GRAPPA but performs image reconstruction before estimating the missing data. This method, known as Sensitivity Encoding for Fast MRI (SENSE) was first described by Pruessmann and colleagues in 1999 (Pruessmann et al., 1999). The initial step that SENSE performs is to generate coil sensitivity maps which determine the spatial sensitivity distribution for each receiver coil. Once coil sensitivity maps have been generated, undersampling of k-space is performed for each coil. This results in an image containing aliasing with a 'wrap around' artefact, an example of which is shown in Figure 1.15.

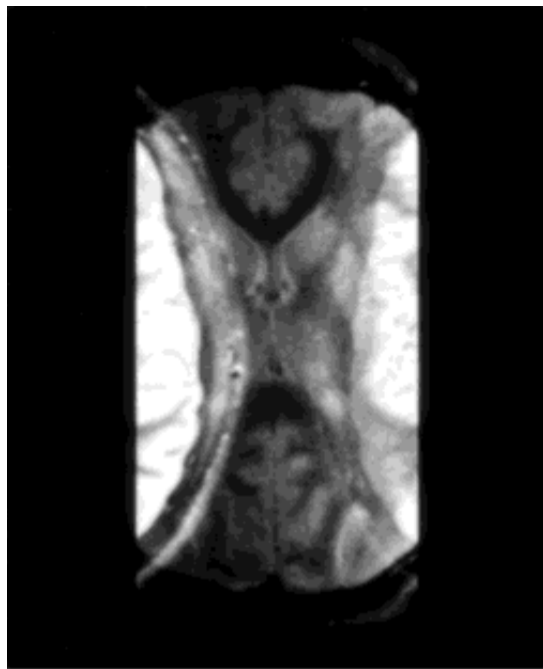


Fig. 1.15 SENSE reconstructed image before correction. This image shows the aliasing and wrap around artefact. SENSE 'unwraps' the image by using coil sensitivity maps that were generated prior to sampling k-space. This image was taken from (Pruessmann et al., 1999).

Using the coil sensitivity data collected before image acquisition, an unfolding matrix is calculated and used to separate the images and unfold the image. This procedure is repeated for each pixel resulting in an unaliased image (Pruessmann et al., 1999).

1.6.3 Multi-band

In both non-accelerated and accelerated MRI acquisitions, slice select gradients are used to select a slice of interest within which k-space is sampled, resulting in a 2D image. This is repeated for every slice to generate a whole brain image. Multi-band imaging accelerates image acquisition by allowing multiple slices to be excited at once. A complex RF pulse is used which is the sum of multiple RF waveforms (Barth et al., 2015), each of which has a resonant frequency able to excite a specific slice. Following the excitation step, accelerated acquisition/reconstruction techniques such as GRAPPA or SENSE can be used to generate an image.

1.7 Functional Imaging & BOLD

In an ideal world, fMRI would be capable of detecting neural activity in the brain directly by measuring the magnetic signals associated with the electrical activity in those neurons. However, these magnetic fields are very weak and difficult to detect with current MR techniques (Huettel et al., 2014). Instead, fMRI relies on measuring the haemodynamic effects associated with neural activity which typically occur within a few seconds of neural activation.

1.7.1 Neurovascular Coupling

Changes in local neural activity cause changes in local blood flow. This process is known as neurovascular coupling (Phillips et al., 2016). However, the mechanisms underlying the blood flow response are not fully understood. Changes in local blood flow result in changes in blood oxygenation and differences in blood oxygenation allow for the blood oxygenation level dependent (BOLD) signal to be collected. The BOLD effect was first described in 1990 (Ogawa et al., 1990) and it exploits the differences in magnetic susceptibility of oxyhaemoglobin (oHb), which is diamagnetic, and deoxyhaemoglobin (dHb), which is paramagnetic. Paramagnetic materials cause inhomogeneities to be introduced to the local magnetic field which in turn causes the spins to dephase more quickly. So, a larger concentration of dHb would cause a reduction in MR signal. During neural activity, neurons consume more oxygen which results in a slight localised increase in the concentration of dHb. Due to neurovascular coupling, local blood flow increases but at a greater rate than needed for the increased oxygen consumption (Davis et al., 1998; Hoge et al., 1999b) resulting in an oversupply of oHb. Consequently, the concentration of dHb is decreased and the MR signal (or BOLD signal) is increased. Therefore, local fMRI signals increase as local neural activity increases.

1.7.1.1 The Haemodynamic Response

The haemodynamic response typically occurs within a few seconds of neural activation and typically peaks between 5 and 10 seconds (see Figure 1.16) following a stimulus. The signal returns

to a baseline level after around 12 seconds following the initial stimulus delivery. Following this, the signal undergoes a "post-stimulus undershoot" which typically lasts around 10-20 seconds. The reason for this post-stimulus undershoot has been debated by scientists for the lifetime of fMRI (van Zijl et al., 2012), but is thought to be neuronally modulated (Mullinger et al., 2013).

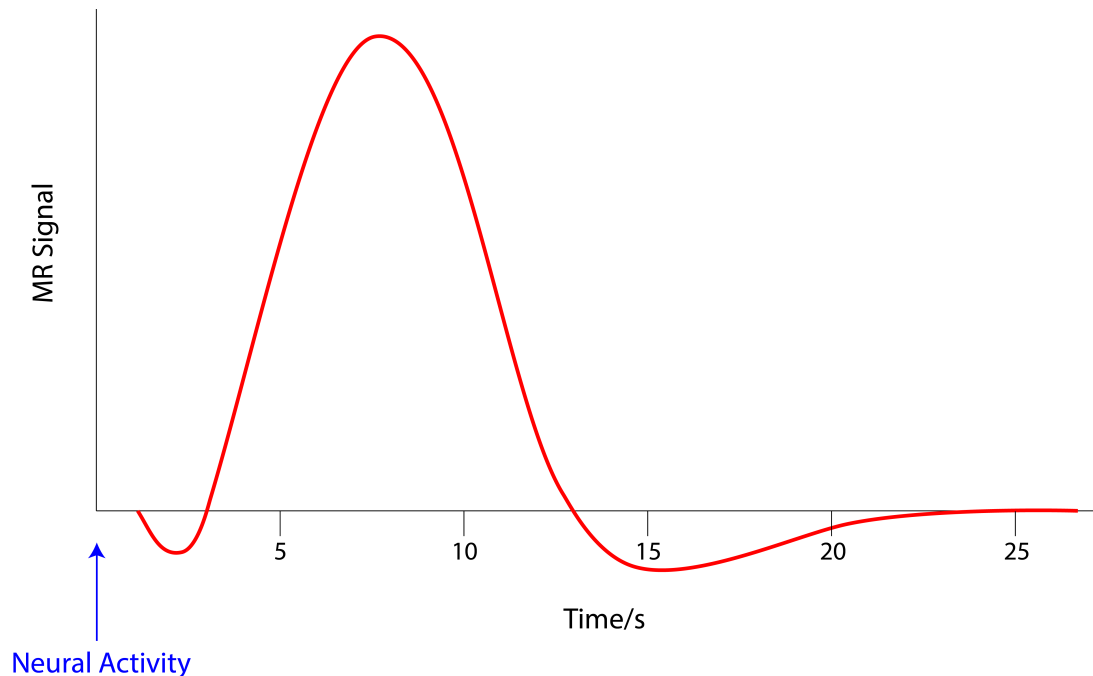


Fig. 1.16 The haemodynamic response function. Typically it occurs within a few seconds of neural activation (Blue arrow) and peaks between 5 and 10 seconds. The signal then undergoes a 'post-stimulus undershoot' which lasts around 10-20 seconds.

1.7.2 Spatial and Temporal Resolution of BOLD

The BOLD effect is a result of the haemodynamic response of blood vessels to neural activity. These effects are not instantaneous, and following a stimulus, the haemodynamic changes are not observable for around 1-2 s (Huettel et al., 2014). This leads to fMRI having a low temporal resolution as it is reliant on this haemodynamic response. It has been noted that the haemodynamic response is faster in subcortical structures than in the cortex at 7 T (Lewis et al., 2018). On the other hand, fMRI has quite a high spatial resolution in comparison with other methods (such as MEG and EEG) with a typical value of $< 3 \text{ mm}^3$ (Glover, 2011). Spatial resolution as high as 0.5 mm has been demonstrated in layer fMRI (Finn et al., 2021). Spatial resolution is dependent on the field-of-view (FOV), matrix size, slice thickness and number of slices. Higher spatial resolution will result in more noise associated with the signal and a lower SNR. SNR is proportional to the voxel volume (Scouten et al., 2006). So when deciding on the optimal MR sequence a trade-off must be made between a higher resolution and a high SNR.

1.7.3 Analysis of fMRI data

Some fMRI studies make use of different stimuli to investigate their effects on the brain. For example, a simple study to map the visual cortex would use flashing checkerboards that cause a strong BOLD response in the visual cortex (DeYoe and Raut, 2014).

1.7.3.1 Preprocessing of fMRI data

Typical preprocessing steps in fMRI include slice timing correction, motion correction, distortion correction, temporal filtering, and spatial filtering/smoothing. Each of these steps aims to improve the image and time-series information acquired by the scanner.

Since fMRI slices are collected at different times, slice time correction is required so that further analysis methods can assume the slices were collected simultaneously (Jezzard et al., 2003). Slice time correction is achieved by aligning each slice to a reference slice (Henson et al., 1999; Sladky et al., 2011; Soares et al., 2016). Another method to achieve this correction uses multiple regression. This method includes additional regressors to the general linear model (introduced in section 1.7.4). These regressors can be the temporal derivatives of the expected HRF or regressors which are shifted in time to account for the time delay and are dependent on the slice (Henson et al., 1999; Sladky et al., 2011). Sladky and colleagues investigated slice timing effects on fMRI datasets and found no adverse effects when including slice time correction (Sladky et al., 2011). Their results showed that the addition of slice time correction improved the accuracy of fMRI data and recommend it as a preprocessing step in fMRI analysis (Sladky et al., 2011).

Motion correction is a key preprocessing step and will be discussed in detail in Chapters 3 and 4 of this thesis. As a brief introduction, fMRI is very susceptible to motion effects due to the long acquisition times associated with MR imaging. These effects can influence fMRI results by introducing motion artefacts into the data.

Distortion correction is used to reduce the effects of geometric distortions that affect fMRI images. These distortions are usually a result of magnetic field inhomogeneities and in severe cases can cause signal loss (Huettel et al., 2014). Distortion correction is usually performed by generating a field map which represents the magnetic field intensity throughout the image. This can then be used to correct the image of inhomogeneities (Jezzard and Balaban, 1995). Another method involves collecting the data twice with different phase encoding directions (Andersson et al., 2003).

Spatial filtering/smoothing aims to reduce noise effects in the fMRI image and increase the overall signal-to-noise ratio (SNR) (Huettel et al., 2014; Lowe and Sorenson, 1997). However as the SNR increases using smoothing, the resolution of the image will decrease. Therefore, there is a trade-off between increasing the SNR and losing spatial resolution. Spatial filtering is usually performed using a Gaussian filter of a specific width which averages signals between adjacent voxels (Huettel et al., 2014; Soares et al., 2016). The width of the filter used is important as it

determines the amount of smoothing that will be applied (Soares et al., 2016). Determining the width of the filter is a difficult task due to the trade-off between SNR and spatial resolution, as mentioned earlier.

Temporal filtering works similarly to spatial filtering but acts on the time series rather than individual volumes. It aims to increase the SNR of the data and remove components of the time series that are not of interest (noise) (Jezzard et al., 2003). Typically, fMRI data contains information related to the cardiac and respiratory cycles as well as slow scanner drifts and these are usually regarded as noise. Thus, temporal filtering aims to remove the effects of these from the time series while having a minimal effect on the signal of interest. Temporal filtering usually makes use of highpass and bandpass filters to perform the filtering (Soares et al., 2016). It has been shown that relevant functional information can be determined from high frequencies (Chen and Glover, 2015; Gohel and Biswal, 2015), so highpass filters will leave only those signals of interest. However, Biswal and colleagues determined that spontaneous low frequency fluctuations are functionally relevant and represent neural activity (Biswal et al., 1995). Therefore, it is important to include these low frequencies in fMRI analysis and a bandpass filter can achieve this.

1.7.4 Statistical Analysis

The general linear model (GLM) is a statistical tool used in most fMRI research. It can be used to model fMRI signals in terms of other variables known as regressors (Jenkinson et al., 2020). The GLM can be described by equation 1.12 where Y represents the data, X represents the regressor, β represents the scaling parameter (also known as beta weights) and ϵ represents the error (otherwise known as residuals).

$$Y = X\beta_{0,1} + \epsilon \quad (1.12)$$

Equation 1.12 represents a GLM with only one regressor. In the case of most fMRI analyses, multiple regressors are used. In this case, each regressor will have its own scaling parameter as shown in equation 1.13 (Jenkinson et al., 2020).

$$Y = X_1\beta_1 + X_2\beta_2 + X_3\beta_3 + X_4\beta_4 + \epsilon \quad (1.13)$$

In addition to statistical testing, the GLM can be used to remove nuisance parameters from fMRI datasets. Using the nuisance time series as individual regressors in the model will allow the residual time series to contain everything not related to these nuisance regressors. This results in a dataset that has been stripped of noise.

1.8 Arterial Spin Labelling (ASL)

Dynamic susceptibility contrast (DSC) MRI is a form of perfusion imaging that uses a bolus of gadolinium, injected intravenously, which results in a loss of T_2^* weighted signal. Measurement of the signal intensity can lead to the calculation of different perfusion parameters. The use of gadolinium is considered generally safe but can bring risks of adverse effects related to the bolus (Essig et al., 2013). An alternative to DSC was developed in 1992 (Williams et al., 1992) which used arterial blood water as an endogenous tracer. This method removes the need for intravenous injections of gadolinium and is known as arterial spin labelling (ASL). In ASL, the magnetisation of blood in the labelling plane, or slab, (usually the neck) is inverted using a 180° RF pulse. Then, after waiting a short amount of time for the labelled blood to reach the imaging plane, images are acquired. This is interleaved with control images where no blood is labelled, and the difference in both the tag and control images is proportional to the amount of blood that was delivered to the tissue by perfusion (Alsop et al., 2015). This difference image is known as the ASL difference image, or simply the ASL image (Wong, 2014). When the tagged blood reaches the target tissue it causes the overall magnetisation to decrease. This is due to the inverted spins associated with the tagged blood (these spins are flipped by 180° at the beginning of the tag). This results in a 'zig-zag' pattern when plotting the ASL signal, an example of which is shown in Figure 1.17.

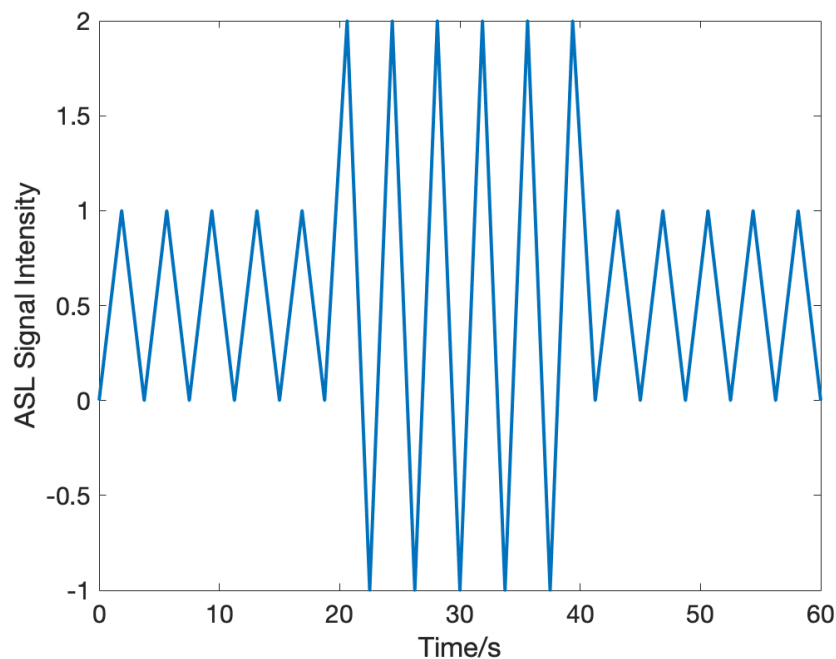


Fig. 1.17 An example of the 'zig-zag' pattern seen when plotting the ASL signal. At around 20s the intensity of the ASL signal is increased as shown by the increase in size of the 'zig-zag' pattern. This intensity then decreases to the baseline level at around 40s.

There are three different forms of ASL, continuous ASL (CASL), pulsed ASL (PASL) and pseudo-continuous ASL (pCASL). CASL uses a continuous RF pulse applied in the labelling

slice to continuously invert blood flowing through this slice (Borogovac and Asllani, 2012; Wong, 2014). A continuous gradient is applied in the z-direction (the direction of flow) which allows for the selection of the labelling slice by creating a gradient of spins precessing at different frequencies. Then, the continuous RF pulse is applied at the labelling slice, with frequency equal to the Larmour frequency (Wong, 2014). The inversion of blood happens due to a process called adiabatic inversion and this results in the 180° inversion of all spins passing through the labelling slice (Borogovac and Asllani, 2012; Wong, 2014). Although CASL has the largest SNR, the continuous pulse of RF energy causes increases in the specific absorption rate (SAR) which could lead to tissue heating. Pulsed ASL (PASL) works slightly differently to CASL. Instead of inverting all spins that flow through the labelling slice, PASL inverts a slab of spins (Alsop et al., 2015). Unlike CASL, PASL achieves this inversion of spins by use of a 180° RF pulse. The SNR of PASL is lower than that of CASL, but the SAR is also much lower. Pseudo-Continuous ASL (pCASL) is a form of CASL and works in a similar way, however instead of a continuous pulse that deposits a large amount of RF energy into the participant, pCASL uses a large number of RF pulses (~ 1000 or more) rapidly applied to the labelling slice (Alsop et al., 2015). The SNR of pCASL is higher than that of PASL but lower than that of CASL. The difference in labelling scheme between PASL, pCASL and CASL is shown in Figure 1.18.

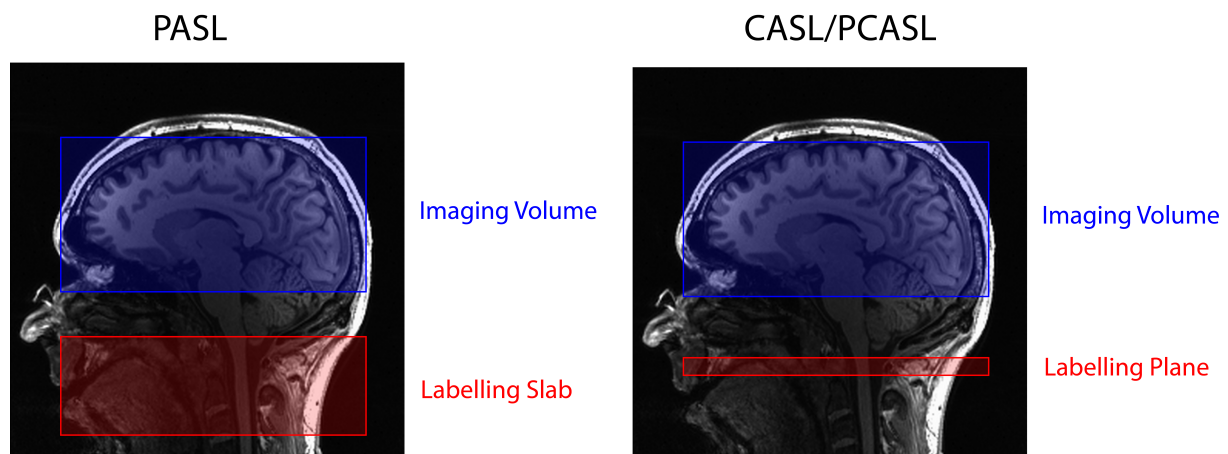


Fig. 1.18 The differences in labelling schemes between PCASL, CASL and PASL. The blue boxes represent the imaging volume and the red boxes represent the labelling slab (PASL) or the labelling plane (CASL/PCASL).

1.9 Summary

The physics underlying MRI is complex and in this chapter, I have summarised the key ideas needed to understand the work conducted within this thesis. The BOLD effect, which is the basis of fMRI, is derived from the NMR signal. This can be described by the quantum mechanical property known as spin. The magnetic dipole moment, a property closely related to spin, causes protons to be slightly magnetic. In the presence of an external magnetic field, the magnetic

dipole moment will align either parallel or anti-parallel to the field. A torque is exerted on the net magnetisation vector causing it to align with the field. However, this does not happen immediately as the proton will precess into alignment. Using RF energy, these protons can be knocked out of alignment with the field and once the RF energy is no longer applied, the protons will precess back into alignment. This process is called relaxation, and the receiver coils can be used to measure it (and generate the MR signal). Gradient fields are used to determine where, in space, the signals originated. This process happens in k-space and a Fourier transform of the information generated in k-space results in the generation of an image. Pulse sequences are used to determine the method of generating and reading the MR signal and variations of these pulse sequences can generate different images. EPI imaging uses a pulse sequence that allows the whole of k-space to be navigated with one excitation pulse. The BOLD effect exploits the difference in magnetic susceptibility of oxyhaemoglobin and deoxyhaemoglobin. When neurons are active they require more oxygen and neurovascular coupling is the process that controls the flow of blood to these active areas. As local neurons become more active, the BOLD effect becomes larger, resulting in a greater fMRI signal. Arterial spin labelling allows for the quantification of cerebral blood flow by inverting the blood flowing into a target tissue. This results in a reduction in the MR signal in the target tissue. By comparing a control image, where no tag is present, and the image where the tag is present, the quantification of CBF is possible. In the next chapter, I will discuss the theory underlying the anatomy and physiology of the cerebrovasculature and the processes that regulate the flow of blood. I will also discuss the effects of ageing on these processes (and vessels) and introduce algorithms and datasets used within this thesis.

Chapter 2

Introduction to Cerebral Physiology

2.1 Chapter Overview

The BOLD effect and its associated haemodynamic response function arise from the need for the human body to transport and utilise blood efficiently. In this chapter, I will introduce the concepts that govern the ability of blood to move around the body. I will discuss how the body is able to regulate blood flow and how this changes with age. I will talk about the methods we currently have to investigate cerebrovascular health including CVR, CBF, CMRO₂ and OEF. Finally, I will discuss some of the pre-defined algorithms and datasets that are later used in the experimental chapters of this thesis.

2.2 Anatomy of the Cerebrovasculature

2.2.1 Blood Vessels

Blood is circulated throughout the human body within blood vessels. There are three main groups of blood vessels: arteries, veins and capillaries. Arteries branch into smaller vessels called arterioles. Arterioles further branch into capillaries which are the site of oxygen exchange. These capillaries then converge into small vessels called venules which further converge into larger veins. Arteries can be split into two groups, elastic and muscular. The former making up the bigger arteries found near the heart, such as the aorta, and the latter making up the anatomically named arteries, such as the femoral artery (Tucker et al., 2017). The role of the arteries is to supply the body with oxygen and nutrients through the medium of blood. The heart pushes blood into the arteries forcefully, meaning arteries are under a large amount of pressure. Arteries have elastic walls which can accommodate the large pressure and stress they experience. The arteries must dampen the high pressure before it reaches the smaller vessels (arterioles and capillaries) (James et al., 2019; London and Pannier, 2010) and their elastic walls allow for this.

Arteries lead to arterioles after continuous bifurcation. Arterioles are surrounded by smooth muscle which allows them to change their diameter by vasoconstriction (narrowing of the vessel

diameter) or by vasodilation (the widening of the vessel diameter). They do this to respond to the oxygen/nutrient needs of the tissue (Tucker et al., 2017). Arterioles further branch until they reach the capillary network. Capillaries are the site where oxygen and nutrients are exchanged between tissue and blood (usually through diffusion). They are thin-walled vessels with porous junctions that make up the blood-brain-barrier (BBB). They connect the arteries in the body to the veins through the arterioles and venules. Venules are smaller blood vessels that converge to the veins. They carry de-oxygenated blood from capillaries after the exchange of oxygen and nutrients has occurred, eventually reaching the veins on its journey back to the heart. They are less elastic than arteries as they are not under the same amount of pressure. The veins have one-way valves contained within them to ensure blood moves in one direction only. Blood moving through the veins will eventually reach the heart where it will begin its journey through the body. Initially, the blood will move through the right chambers of the heart and will be pushed through the pulmonary artery towards the lungs. Blood will move from the pulmonary artery into capillaries within the lungs. The blood will then be oxygenated through diffusion and CO₂ will be exchanged into the lungs. The blood will then move from the capillaries into the pulmonary vein and back into the left chambers of the heart. Then, the blood will be pumped through the aorta and to the rest of the body through the network of arteries, arterioles, capillaries, venules and veins found within the body.

2.2.2 Circle of Willis

The human brain is supplied with blood from four arteries. These are the left and right internal carotid arteries and the left and right vertebral arteries (Cipolla, 2016). The internal carotid artery stems from the bifurcation of the common carotid artery into the internal and external carotid arteries (Snell, 2011). The external carotid artery is responsible for supplying blood to the face and neck while the internal carotid artery mainly supplies blood to the cerebrum.

The vertebral arteries join to form the basilar artery which connects with the internal carotid arteries through the Circle of Willis. This is an anastomotic ring at the base of the brain which is responsible for supplying blood to all areas within the brain (Cipolla, 2016). In theory, the Circle of Willis can supply blood to any area of the brain since it is connected to all four feeding arteries. This is advantageous as it allows perfusion to occur in all areas of the brain in the case of a stenosis or blockage in any part of the Circle or its feeding arteries. The Circle of Willis is made up of the anterior communicating, posterior communicating, anterior cerebral, posterior cerebral, internal carotid and basilar arteries (Snell, 2011). Coming from the Circle of Willis are smaller arteries which are responsible for supplying blood to different sections of the brain. The middle cerebral arteries are also connected to the Circle of Willis. Figures 2.1 and 2.2 show some of these arteries and how they link through the Circle of Willis.

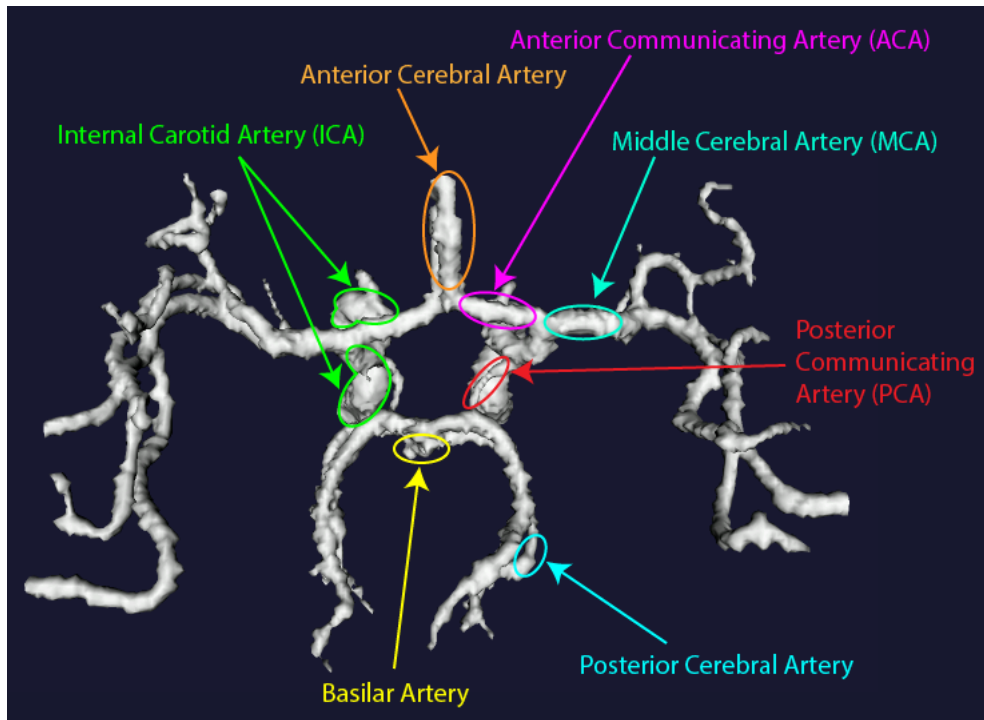


Fig. 2.1 A front on view of the anatomy of the vessels within the brain. The vessels highlighted are: the Internal Carotid Artery (green), the Anterior Cerebral Artery (orange), the Anterior Communicating Artery (pink), the Middle Cerebral Artery (turquoise), the Posterior Communicating Artery (red), the Posterior Cerebral Artery (teal) and the Basilar Artery (yellow).

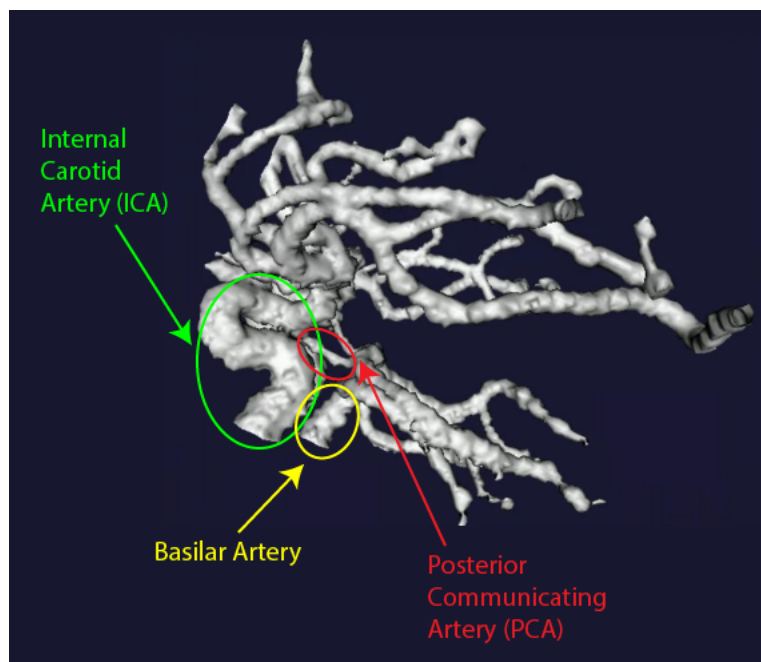


Fig. 2.2 A side view of the anatomy of the vessels within the brain. The vessels highlighted are: the Internal Carotid Artery (green), the Anterior Cerebral Artery (orange), the Anterior Communicating Artery (pink), the Middle Cerebral Artery (turquoise), the Posterior Communicating Artery (red), the Posterior Cerebral Artery (teal) and the Basilar Artery (yellow).

2.3 Regulation of Blood Flow

2.3.1 Autoregulation

Autoregulation is the mechanism by which the brain maintains a constant cerebral blood flow (CBF) in response to changes in cerebral perfusion pressure (CPP) (Powers, 2016). This can be understood using equation 2.1 (Payne, 2016; Powers, 2016).

$$CBF = \frac{CPP}{R} \quad (2.1)$$

As CPP increases, an increase in cerebrovascular resistance (R) is required to maintain a constant CBF. In the opposite scenario, as CPP decreases a decrease in cerebrovascular resistance is required to maintain a constant CBF. The resistance of a single vessel can be calculated by equation 2.2 (Payne, 2016).

$$R = \frac{8\mu L}{\pi r^4} \quad (2.2)$$

Resistance of a blood vessel is therefore dependent on the length of the vessel (L), the viscosity of blood (μ) and the radius of a vessel (r). However, viscosity and length are properties that don't change in time (except in extreme time scales). Therefore, resistance is mainly controlled by changes in vessel radius (Payne, 2016). Equation 2.3 shows that the resistance of a single vessel is inversely proportional to its radius to the fourth power. This means that a small change in vessel radius translates to a large change in vessel resistance (Payne, 2016). Arterioles, the small-diameter vessels that arteries branch into, are comprised of smooth muscle which allows them to change their radius resulting in changes in resistance to maintain a constant CBF.

$$R \propto \frac{1}{r^4} \quad (2.3)$$

2.4 Effects of Ageing on Vessel Health

2.4.1 Arterial Stiffness

As mentioned in section 2.2.1, arteries are made up of vessel walls which are very elastic in order to accommodate the high pressure they experience. Arterial stiffening is the loss of elasticity resulting in arteries with stiffer walls (Oh, 2018; Sun, 2015). Arterial stiffness is more prevalent with age (Sun, 2015) and is much more common in older adults (Palta et al., 2019). Cardiovascular risk factors (such as hypertension, diabetes mellitus and chronic kidney diseases) can increase arterial stiffness (Lacolley et al., 2020). Arterial stiffness has been associated with a decrease in cognitive function (Gorelick et al., 2011; Hanon et al., 2005; Singer et al., 2014),

cerebral small-vessel disease (Singer et al., 2014), microvascular brain damage (Gorelick et al., 2011) and structural brain changes such as white matter hyperintensities (Singer et al., 2014). Therefore, measuring the extent of arterial stiffness may be an early marker to detect and treat potential damage to the cerebrovasculature.

2.4.2 Arterial Compliance

Arterial compliance is defined as the ability of an artery to increase its volume by distending under large amounts of pressure (Papaioannou et al., 2014). As noted in Section 2.2.1, arteries are both under large amounts of pressure and surrounded by elastic tissue that allows them to be compliant. Arterial compliance can be represented by equation 2.4 (Nichols et al., 2011; Papaioannou et al., 2014), where AC is arterial compliance, ΔV represents a change in volume and ΔP represents a change in pressure. Arterial compliance is the inverse of arterial stiffness and so the stiffer an artery becomes, the less compliant it will be (Nichols et al., 2011; Papaioannou et al., 2014). The compliance of an artery determines how well it will dampen the pressure before it reaches micro-vessels. This is important since large pressure waves reaching the microvasculature could cause damage.

$$AC = \frac{\Delta V}{\Delta P} \quad (2.4)$$

2.4.3 Pulsatility

The flow of blood within arteries is pulsatile in nature. This is because the blood flowing from the heart into the arteries does so in a pulsatile way (i.e. the heartbeat). The compliance of arteries allows them to expand and account for the pulsatile nature of the flow, dampening the changes in pressure. Pulsatility is therefore an important metric related to stiffness and compliance that may indicate potential damage to the microvasculature. This could open avenues for tracking, prevention and treatment of related diseases. As arterial stiffness correlates highly with age, the arteries in older people will be less compliant and unable to dampen the pulsatile flow. Therefore, this increase in pulsatile flow could cause damage to the microvasculature and may be a contributing factor in age-related deterioration of brain health. Chapters 4 and 5 develop methods to measure cardiac-related information in fMRI signals to provide an estimate of pulsatility. These will allow researchers to track deterioration in cerebrovascular function/health.

2.4.4 Heart Rate Variability (HRV)

The heart is responsible for moving blood throughout the body and achieves this with a pumping action. The term used to describe this pumping action is a beat and the number of times the heart beats per minute is called the heart rate (measured in beats per minute - *BPM*). Typically,

the heart rate is measured using a photoplethysmograph (PPG) during MRI experiments. An example of a PPG trace is shown in Figure 2.3.

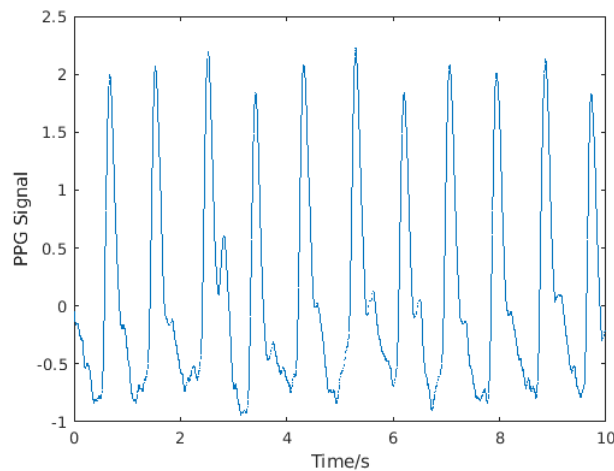


Fig. 2.3 An example of a PPG trace as taken from work completed in Chapters 4 and 5. The PPG trace was collected by (Kassinopoulos and Mitsis, 2020).

A PPG records the variation in blood volume which is synchronous to heart rate. The time interval between heart beats can be variable and this variation is called heart rate variability (HRV). HRV is an important measure of overall cardiac health. It reflects how well the autonomic nervous system (ANS), responsible for regulating cardiac activity, is working (Rajendra Acharya et al., 2006). Two branches of the ANS, the sympathetic nervous system (SNS) and parasympathetic nervous system (PNS), balance to control HR (Rajendra Acharya et al., 2006). Variations in HRV could be attributed to changes in the activity of the SNS and the PNS. A decrease in HRV has been observed as we age (Jandackova et al., 2016; Reardon and Malik, 1996). Measurement of HRV and pulsatility from a BOLD signal is difficult due to the lack of samples collected within a single heartbeat. Blood flowing into vessels is pulsatile in nature and this is undersampled by BOLD imaging. In a toy example, if there were no variation in HR the fMRI signal collected would not change. This is shown in part A of Figure 2.4. However, if there was some variation in HR (HRV), then there would be an increase/decrease in one fMRI point reflecting the variability in HR. This is shown in part B of Figure 2.4. This isn't the only situation which could lead to this change in fMRI signal. In the case of a change in pulsatility, there would also be an increase/decrease in the fMRI signal. Therefore, it is difficult to distinguish whether the change is related to HRV or pulsatility. As a result, these two measures are coupled from an fMRI perspective, and voxels that show HRV changes should also show pulsatility changes. This can be seen schematically in parts B and C of Figure 2.4. HRV is used in Chapter 5 as part of a new method to quantify cerebrovascular physiology (and therefore cerebrovascular health).

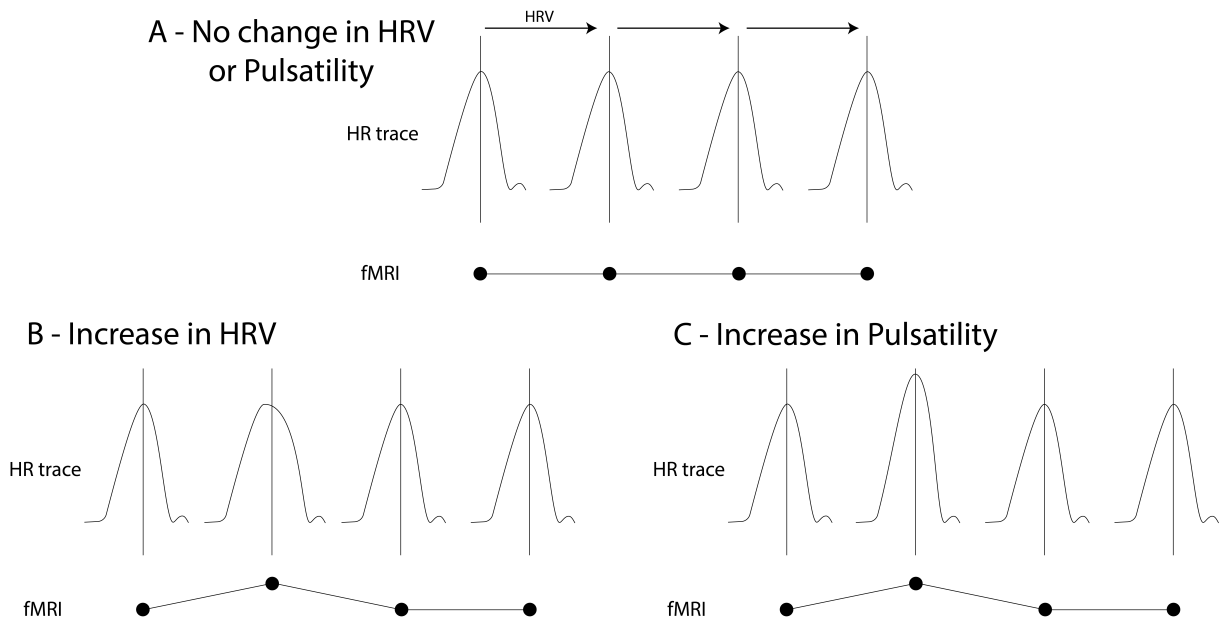


Fig. 2.4 A schematic diagram showing how closely related HRV and Pulsatility are from an fMRI perspective. A change in either HRV or Pulsatility would be reflected by the same change in fMRI and so the ability to distinguish between these two measures is difficult.

2.5 Quantifying Cerebrovascular Physiology

2.5.1 Quantification of Cerebrovascular Reactivity (CVR)

CVR is the change in CBF in response to a vasoactive stimulus (Fierstra et al., 2013). A vasoactive stimulus is a stimulus that causes changes to the radius of blood vessels (and therefore the vessel resistance). CVR can be calculated from BOLD/CBF data in which a vasoactive stimulus is present. In the case of CO_2 administration, CVR can be calculated using a general linear model and the end-tidal CO_2 (EtCO_2) as shown in equation 2.5. To ensure the units of CVR are $\%Signal/mmHg$, the BOLD data must be converted into $\%BOLD$ and the EtCO_2 must be in units of mmHg.

$$MRI_{Signal}(t) = CVR \cdot EtCO_2(t) + \beta_0 + \epsilon(t) \quad (2.5)$$

CVR can be used as an indicator of autoregulation efficiency (Chen, 2018) and early vascular dysfunction (Glodzick et al., 2013). The latter is predominantly due to arterial stiffening. Studies have shown that CVR is impaired in Alzheimer's Disease and people with mild cognitive impairment (Cantin et al., 2011; Glodzick et al., 2013).

Measurement of EtCO_2 can be achieved using a face mask or nasal cannula which records expired breath throughout the scanning session. The vasoactive stimulus required to measure CVR can be administered in different ways. Two of the most common ways make use of CO_2 to cause vasodilation. The first uses inhaled CO_2 and the second increases the concentration of CO_2 by asking participants to hold their breath for extended periods. As the concentration of CO_2

increases, dilation of vessels occurs to increase the relative concentration of oxygen. Inhalation of CO₂ works very well as a vasodilator and inhalation of 5% CO₂ results in an increase in CBF of ~75% (Kety and Schmidt, 1948). Asking participants to hold their breath increases the concentration of CO₂ in the blood due to the lack of exhalation which removes CO₂ from the body. CVR measures obtained through either method have been shown to correlate highly suggesting that either method works to a similar accuracy (Kastrup et al., 2001).

2.5.2 Quantification of Cerebral Blood Flow (CBF)

Cerebral Blood Flow is defined as the volume of blood delivered to 100g of tissue per minute (Buxton, 2005) and is an important metric for determining the health of brain tissue. It can be quantified using ASL techniques (explained in Chapter 1).

$$CBF = 0 \quad 0 < t < AAT \quad (2.6)$$

$$CBF = \frac{\lambda \cdot (SI_{control} - SI_{tag}) \cdot e^{\frac{PLD}{T_1'}} \cdot e^{\frac{AAT}{T_{1,blood}}}}{2 \cdot \alpha \cdot T_1' \cdot SI_{PD} (1 - e^{\frac{\tau}{T_1'}})} \quad \tau + AAT < t \quad (2.7)$$

$$CBF = \frac{\lambda \cdot (SI_{control} - SI_{tag}) \cdot e^{\frac{AAT}{T_{1,blood}}}}{2 \cdot \alpha \cdot T_1' \cdot SI_{PD} \cdot (1 - e^{\frac{-(t-AAT)}{T_1'}})} \quad AAT < t < \tau + AAT \quad (2.8)$$

Equations 2.6, 2.7 and 2.8 can be used to calculate CBF for data acquired using a pseudo-continuous ASL data acquisition (Alsop et al., 2015; Buxton et al., 1998). In these equations, λ is the brain/blood partition coefficient, $SI_{control}$ and SI_{tag} are the time-averaged signal intensities in the control and tag images respectively, $T_{1,blood}$ is the longitudinal relaxation time of blood, α is the labelling efficiency, SI_{PD} is the signal intensity for a proton density weighted image, τ is the label duration, T_1' is the effective T_1 of a voxel which includes the original T_1 plus another component related to the flow of blood into the voxel, AAT is the arterial transit time and PLD is the post labelling delay. The units of CBF derived from these equations are $mlg^{-1}s^{-1}$. The addition of a factor of 6000 in the numerator would allow these units to be converted to $ml100g^{-1}min^{-1}$.

In pCASL, a time period is left to allow the inverted blood to move to the imaging plane after labelling blood. This time period is called the post labelling delay (PLD). In an ideal case, the PLD would be slightly longer than the time it takes for the blood to travel from the labelling plane to the imaging plane (known as the arterial arrival time, ATT). In practice, this is not an achievable feat as the AAT is an unknown variable. If the PLD was just longer than the AAT, all the labelled blood would reach the imaging plane (and target tissue) before images are acquired.

Therefore, the signal would have decayed, resulting in a decreased signal-to-noise ratio (SNR). Aside from SNR concerns, the PLD must also be long enough to ensure a large amount of the labelled blood has reached the target tissue before imaging. AAT varies with age and can be different for different disease states. So, these need to be accounted for when choosing the best PLD. Alsop and colleagues recommend a PLD of 1500ms for a PCASL acquisition in children, 1800ms in healthy adults under the age of 70, 2000ms for healthy adults over the age of 70 and 2000ms for adult clinical patients (Alsop et al., 2015).

Multiple-PLD methods make use of multiple different PLD values. The advantage of this is a more precise quantification of CBF and the ability to collect information about the AAT (Alsop et al., 2015). Methods that make use of multiple-PLD's are more complicated and require more analysis to generate accurate results.

2.5.3 Quantification of the Cerebral Metabolic Rate of Oxygen Consumption ($CMRO_2$) and Oxygen Extraction Fraction (OEF)

The cerebral metabolic rate of oxygen consumption is the rate at which oxygen is consumed by the brain at rest. It is considered a direct indicator of brain health. Quantifying it is a difficult task, however. $CMRO_2$ can be calculated using equation 2.9, where CaO_2 represents the concentration of arterial oxygen, OEF represents the oxygen extraction fraction and CBF represents cerebral blood flow.

$$CMRO_2 = CaO_2 \cdot OEF \cdot CBF \quad (2.9)$$

CaO_2 can be quantified using end-tidal O_2 partial pressure and CBF can be quantified using ASL. OEF can be quantified using equation 2.10, where SvO_2 represents the venous oxygen saturation, ϕ is the oxygen carrying capacity of haemoglobin and $[Hb]$ is the concentration of haemoglobin.

$$OEF = \frac{CaO_2 - SvO_2 \phi [Hb]}{CaO_2} \quad (2.10)$$

It is useful to rearrange equation 2.9 so that it is in terms of SvO_2 and this can be achieved using equation 2.10. This results in equation 2.11 which shows that the estimation of SvO_2 leads to the calculation of $CMRO_2$.

$$CMRO_2 = (CaO_2 - SvO_2 \phi [Hb]) \cdot CBF \quad (2.11)$$

Initial work to estimate $CMRO_2$ was performed by Davis (Davis et al., 1998) and Hoge (Hoge et al., 1999a). Their model took into account hypercapnia to calculate M (the BOLD signal change if total elimination of deoxyhaemoglobin in the image voxel was achieved). Then, the model could be used to calculate task-related changes in $CMRO_2$. Wise and colleagues modified this model to include hyperoxia and the modified model is described by equation 2.12

(Wise et al., 2013). In this equation, CBV is the BOLD-relevant blood volume, $[dHb]$ is the concentration of deoxyhaemoglobin, and β is a constant that is dependent on the vessel size, geometry and magnetic field strength. The parameters with the subscript '0' indicate baseline conditions.

$$\frac{\Delta S}{S_0} = M \left\{ 1 - \left(\frac{CBV}{CBV_0} \right) \left(\frac{[dHb]}{[dHb_0]} \right)^\beta \right\} \quad (2.12)$$

The $\frac{CBV}{CBV_0}$ term can be described in terms of CBF via the use of equation 2.13, resulting in equation 2.14. In these equations, α is the Grubb exponent (Grubb et al., 1974).

$$\left(\frac{CBV}{CBV_0} \right) = \left(\frac{CBF}{CBF_0} \right)^\alpha \quad (2.13)$$

$$\frac{\Delta S}{S_0} = M \left\{ 1 - \left(\frac{CBF}{CBF_0} \right)^\alpha \left(\frac{[dHb]}{[dHb_0]} \right)^\beta \right\} \quad (2.14)$$

In equation 2.14, M and $[dHb]_0$ are unknown values and their estimation is necessary to calculate $CMRO_2$. M can be calculated using equation 2.15, but is dependent on $[dHb]_0$. In this equation TE represents the echo time and A is a constant dependent on the field.

$$M = TE \cdot A \cdot CBV_0 \cdot [dHb]_0^\beta \quad (2.15)$$

The estimation of $[dHb]_0$ can be achieved using equation 2.16 leaving the unknown variables M and SVO_2 .

$$[dHb]_0 = 1 - SvO_2|_0 [Hb] \quad (2.16)$$

During the experiment proposed by Wise and colleagues (Wise et al., 2013), periods of hypercapnia and hyperoxia were interleaved which allowed variables such as the partial pressure of oxygen in arterial blood (PaO_2), the partial pressure of carbon dioxide in arterial blood ($PaCO_2$), the cerebral blood flow (CBF) and the BOLD signal to be measured using both the physiological equipment and the MR data. The measurement of PaO_2 allows for the estimation of CaO_2 .

The $\frac{[dHb]}{[dHb_0]}$ term in equation 2.14 can be replaced with equation 2.17 as per (Wise et al., 2013).

$$\frac{[dHb]}{[dHb_0]} = \frac{CBF_0}{CBF} - \frac{1}{[dHb]_0} \left\{ \frac{1}{\phi} \left(CaO_2 - \left(\frac{CBF_0}{CBF} \right) CaO_2|_0 \right) + [Hb] \left(\frac{CBF_0}{CBF} - 1 \right) \right\} \quad (2.17)$$

In equation 2.17, ϕ was assumed to be $1.34 ml O_2 / g Hb$ and the concentration of haemoglobin ($[Hb]$) was assumed to be $15 g Hb dl^{-1} blood$ (Wise et al., 2013). Then, to estimate the unknown

variables (M and SvO_2), a nonlinear least-squares fitting function (Germuska et al., 2019) can be used. Once these variables have been calculated, $CMRO_2$ can be estimated from equation 2.11.

The assumed values were ϕ , which represents the carrying capacity of haemoglobin, and $[Hb]$, which represents the concentration of haemoglobin. ϕ is not expected to change in ageing and disease unless the haemoglobin is damaged. One disease in which there could be an exception is sickle cell disease. In sickle cell disease, haemoglobin has a decreased oxygen affinity (Safo and Kato, 2014), which could mean that the carrying capacity is also reduced. $[Hb]$ could change in ageing and disease and it is expected to decrease in either of these conditions. For this work $[Hb]$ was assumed, however it is possible to measure this variable by taking a blood sample.

2.6 Overview of Algorithms

2.6.1 Volume Registration Algorithm (VRA)

Volume registration can be used for many different applications. Two of which include motion correction and alignment of functional images to a structural image. The latter ensures spatial correspondence between the functional and structural images. One of its more common uses is in motion correction. In motion correction, volume registration is used to realign each image (or volume) collected as part of a functional MRI data acquisition to a pre-defined image (e.g., the first image acquired). The aim of this is to realign the images to where they would have been acquired in the absence of motion. Typically, volume registration uses 6 degrees of freedom, 3 translational parameters (x - defined as side to side movement in the scanner, y - defined as movement into/out of the bed of the scanner (towards/away from the sky), z - defined as movement into/out of the bore of the scanner) and three rotational parameters (pitch - rotation about x , yaw - rotation about y , roll - rotation about z). An example of volume registration is shown in Figure 2.5.

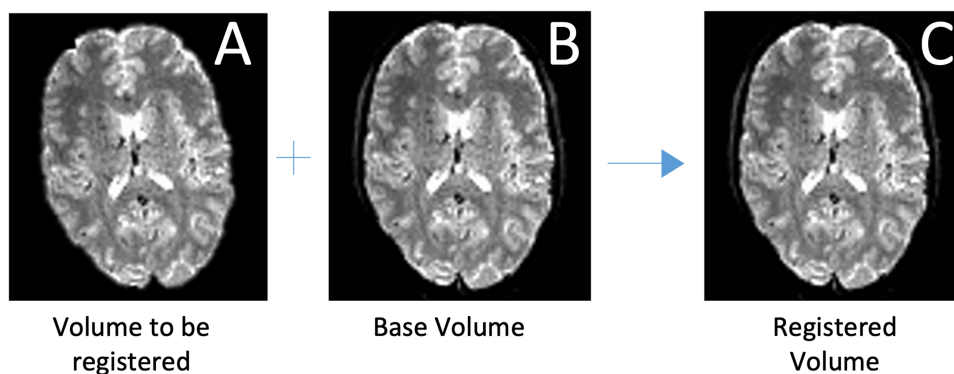


Fig. 2.5 An example of volume registration used to correct motion. A) The volume to be registered. B) The pre-defined image to register to. There is a clear difference between A and B with A needing to be rotated around the z axis (roll). C) The registered volume after its rotation about z .

2.6.2 Volume Regression

Volume registration is the first step of motion correction in fMRI. However, it does not remove motion effects from the time series. Volume regression accounts for this by removing motion regressors from time series data. The 6 motion parameter estimates (as explained in section 2.6.1) are included as regressors in a general linear model to remove their related variance. This is further explained in chapter 3.

2.6.3 Independent Components Analysis (ICA)

Data generated from an fMRI scan contains a mix of different signals pertaining to different sources of information. For example, a typical fMRI dataset will contain signals related to head motion, respiratory information, cardiac information, neural signal and scanner artefacts. To analyse this data effectively it may be desirable to separate these mixed signals into their constituent parts using an independent components analysis (ICA). An ICA works by assuming that these different processes can be represented by one or more spatially-independent components or maps (McKeown et al., 1998). The maps are spatial in nature as there are not enough time-points sampled in order to generate temporal components. The ICA results in spatial maps and an associated time-course which can be classified as different source signals (head noise, scanner artefacts, cardiac pulsation). This classification can be performed by hand (Griffanti et al., 2017) or by use of an automatic classifier (Salimi-Khorshidi et al., 2014). Hand-classification requires skilled researchers who are able to identify features from within the spatial maps and associated time-courses to correctly classify the components. Automatic classification tries to avoid the potential for human error by performing statistical tests on the time-course in order to classify the components. Automatic classification is covered in depth in Chapters 4 and 5.

2.6.4 FMRIB's ICA-based X-noiseifier (FIX)

FMRIB's ICA-based X-noiseifier (FIX) is an automatic classification algorithm that can distinguish 'good' and 'bad' components from within an ICA decomposition. It is part of the FSL software package. FIX is predominantly used for denoising of fMRI data. It is used to distinguish components related to neural activity from components related to various noise sources (such as head motion, physiological noise, scanner artefacts, etc). From the ICA decomposition, FIX is able to generate spatial and temporal features for each ICA component. These features are then fed into a multi-level classifier (Salimi-Khorshidi et al., 2014). For the classifier to work it must first be trained with training datasets containing components that have been labelled as 'good' or 'bad' components. FSL recommend that at least 10 training datasets are required to enable an accurate classification by FIX, however, in the paper introducing FIX the authors used 100 datasets (Salimi-Khorshidi et al., 2014). The authors also suggested that the training datasets contain a list of hand-labelled components determining which components are 'good' or 'bad'.

After FIX is trained, it is able to generate a list of ‘good’ and ‘bad’ components for any dataset passed to it (assuming the dataset is collected with the same parameters as those which provided the training). After determining which components are ‘good’ and which are ‘bad’ a linear regression can be used to regress the ‘bad’ components from the dataset leaving only those of interest. In their initial investigation of FIX, Salimi-Khorshidi and colleagues (Salimi-Khorshidi et al., 2014) reported that FIX achieved a 95% overall accuracy when working on conventional resting-state data, and over 99% accuracy when working on high-quality resting-state data from the Human Connectome Project. It is possible to train FIX on a dataset that classifies other features as ‘good’ instead of neural activity. Chapter 5 looks at using FIX to classify components related to cardiac data as ‘good’ components, removing the other signals from the dataset.

2.6.5 Human Connectome Project datasets

The Human Connectome Project (HCP) aims to study brain connectivity and function in healthy adults (age range - 22-35) (Van Essen et al., 2012, 2013). In the 1200 release, ~1200 subjects underwent brain scans through four different imaging modalities, structural MRI, resting-state functional MRI, task-based fMRI and diffusion MRI (Van Essen et al., 2013). All subjects were scanned at 3 T, with a subset (200 subjects) repeating the scanning protocols at 7 T. Additionally, 100 subjects were scanned with MEG/EEG (Van Essen et al., 2013). A range of behavioural and genetic tests were also conducted (Van Essen et al., 2012, 2013). During functional scanning, cardiac, respiratory and head motion information was acquired. Chapters 4 and 5 make use of the resting-state datasets collected by the HCP to develop methods of measuring HRV and pulsatility. Each resting-state fMRI scan was completed four times, two of which were performed on day one with opposite phase encode orientations (LR then RL) and the other two collected on day two (again with different phase encode orientations). Each raw rfMRI scan was around 1 GB in size equating to around 4 GB of storage per subject. This large amount of data posed new challenges during analysis, most of which related to storage capacity and quotas. Improved efficiency of scripts overcame this issue.

2.6.6 Global Intensity Changes

Global Intensity Changes (GICs) describe a global change in MR signal intensity. This change in global signal can arise for many different reasons. An example of this is a global increase in CBF caused by an increase in the concentration of CO₂ in the blood. The larger the concentration of CO₂, the larger the BOLD signal change. This effect is especially prevalent in edge voxels as the biggest signal change is detected here. ASL sequences cause GICs too. These occur due to the reduction in MR signal in the imaging plane after the labelled blood has reached this plane. The labelled blood has an inverted magnetisation and will result in a reduction in the overall MR signal. Many VRA algorithms use a least squares approach to determine the magnitude of signal within the voxels in the brain, with a specific focus on edge voxels. Edge voxels represent

the biggest signal change during motion, CO_2 changes and ASL tagging. These GICs can look like motion to the VRA and this can cause signal loss when performing motion correction. As a participant moves their head, the magnetisation signal that was previously collected in one voxel can change intensity dramatically as the head moves into/out of the voxel. This is especially true for voxels that did not contain any brain tissue prior to the movement, as the intensity of the signal in this voxel will increase by a large amount. Figure 2.6 diagrammatically represents the signal change in two scenarios, one with motion and one with a GIC.

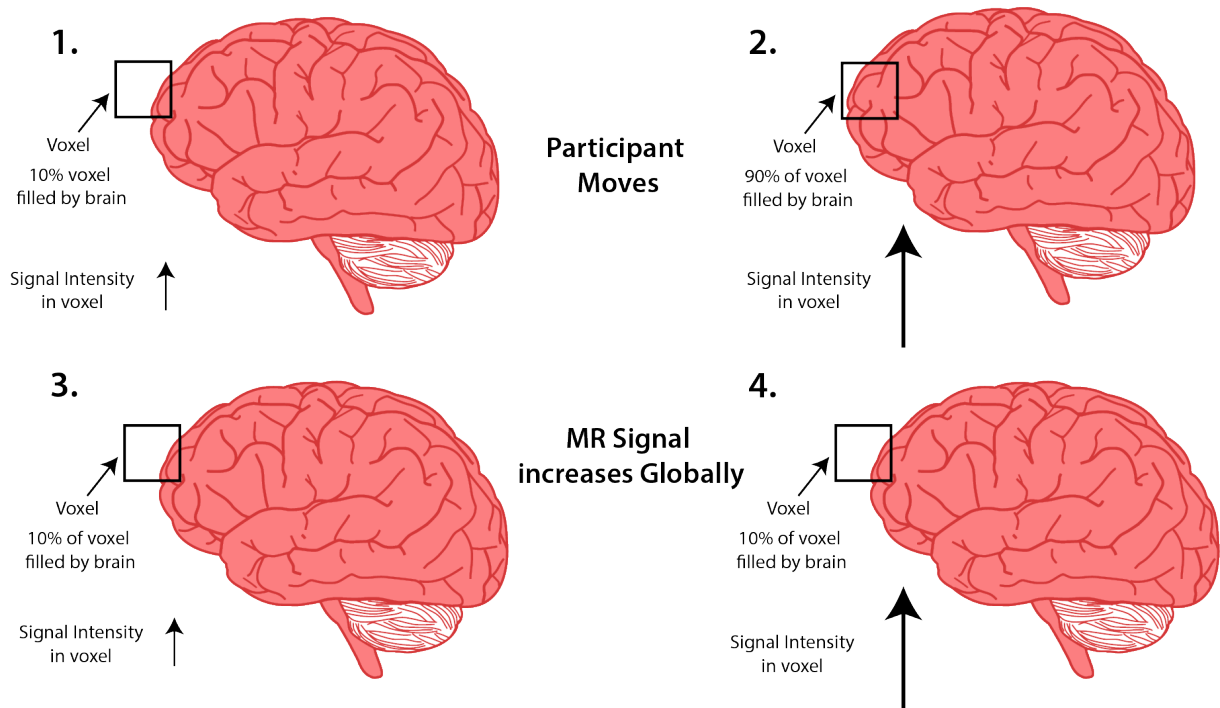


Fig. 2.6 Diagram explaining the hypothesis that the VRA can misrepresent GICs as motion. 1. During a scan a participant's brain fills 10% of an edge voxel. 2. The participant moves so that their brain occupies much more of the voxel (90%) an accompanying signal increase in this edge voxel is seen by the VRA. 3. The same participant in a case where no motion occurred. Their brain occupies 10% of an edge voxel. 4. After a GIC is present the MR signal intensity increases. As there is no motion the brain only occupies 10% of the edge voxel as before. However, the VRA sees the intensity change and misrepresents this as motion.

2.7 Summary

Throughout this chapter, I have introduced some key physiological concepts, including the cerebrovasculature, the role of the Circle of Willis, cerebral autoregulation, arterial stiffness, arterial compliance, pulsatility and heart rate variability. Additionally, I've outlined various algorithms and datasets that are relevant to the experimental chapters of this thesis.

2.8 Outline of Experimental Chapters

This thesis is divided up into three experimental chapters. Each of these chapters aims to improve methods of measuring cerebrovascular physiology and, therefore, cerebrovascular health.

Chapter 3 investigates the current methods used to correct motion in fMRI data and how they may fail in the measurement of cerebrovascular physiology. Correction of motion is important to ensure accurate estimates of cerebrovascular function. The conventional method used (volume registration - Outlined in section 2.6.1) falls short in experiments that make use of Global Intensity Changes to quantify cerebrovascular health. Therefore, it is important to correct the errors derived from VRA-based methods or find a new method to correct for motion. I propose some techniques to achieve this.

Chapters 4 and 5 make use of the Human Connectome Project's 1200 Young Person dataset to derive measures related to cardiac pulsatility and Heart Rate Variability from resting state fMRI information. Chapter 4 outlines some of the initial attempts and highlights why they failed. Chapter 5 outlines the methods that achieved high correlations with a gold standard which could be rolled out to larger datasets.

Chapter 3

Correcting motion registration errors caused by Global Intensity Changes (GICs)

3.1 Chapter Overview

In this chapter, the conventional retrospective motion correction method used in fMRI is investigated since erroneous motion parameter estimates may be calculated using this method. An external, optical motion tracking system was used to generate motion parameters that should avoid this issue. This was compared with the conventional technique. Data-based methods were developed to determine whether the erroneous estimates could be improved. In total, five new motion correction methods were developed (including the camera-based method), and their ability to generate accurate motion parameter estimates was explored. Finally, measures of cerebrovascular function/health were quantified using all of the motion correction techniques to determine the accuracy of these motion correction strategies.

3.2 Introduction

To acquire accurate information about the health of the cerebrovasculature, sources of noise that could otherwise affect the results should be removed. One big source of noise in all fMRI experiments is subject motion. The long scan times required to collect quality BOLD-fMRI images increase the likelihood of subject motion. Such sources of subject motion include involuntary motion of the brain due to cardiac and respiratory motion, coughing and movement in the posterior direction (sinking into the scanner bed), as well as voluntary motion such as fidgeting, shaking of the head, scratching an itch, etc. Subject motion can compromise data quality by affecting M_0 in three different ways: changes to the content of each voxel, changes to the uniformity of the magnetic field and spin history effects. These changes are explored in detail by Murphy and colleagues (Murphy et al., 2013). The main approaches to account for subject motion are prevention and retrospective correction, the former being the most desirable. Making

participants more aware of their movement has been effective in reducing motion during a scan in some cases. It has been shown that using medical sticky tape applied to the participants' forehead and the scanner head coil to introduce tactile feedback significantly reduced translational and rotational motion (Krause et al., 2019). Additionally, multiple memory foam cushions are packed into the head coil, which helps to keep the participant more comfortable and limits the amount of head motion. Even after implementing these methods to reduce motion there is usually some residual motion during the scan. As a result correction of motion is a needed step to ensure good data quality. This is not quite as straightforward as the methods to reduce motion, however.

There are two groups of methods that can reduce noise associated with motion, prospective and retrospective motion correction. Prospective motion correction deals with correcting the effects of motion in real time, usually by measuring motion during a scan and updating scanner gradients to move the imaging slice or volume to compensate (Maclaren et al., 2012; Zahneisen and Ernst, 2016; Zaitsev et al., 2017). On the other hand, retrospective motion correction deals with correction of motion after the experiment. There are many methods of achieving this in fMRI with the most common being image realignment. Image realignment algorithms typically use a rigid body method that assumes the motion can be accounted for by three translational and three rotational parameters. This accounts for six degrees of freedom (Zaitsev et al., 2017). These algorithms then align each volume to a reference volume to determine the six motion parameters.

Retrospective motion correction can be split into two separate steps, motion registration and motion regression. The former deals with the removal of motion from the image, whereas the latter deals with removing the effects of that motion from the time series. Motion affects the time series in various ways. The density of spins in a voxel is directly related to the net magnetisation and so a change of tissue composition within the voxel (i.e the head moves so that the voxel contains grey matter rather than the white matter that it contained before the movement) will affect the net magnetisation (Caballero-Gaudes and Reynolds, 2017). Spin history effects can have a large effect on the fMRI signal. Spin history artefacts arise due to changes in the steady state magnetisation reached in a typical fMRI experiment. Head motion results in a change in timing between the excitations experienced by the spins which causes a shift from a steady state (Caballero-Gaudes and Reynolds, 2017). This shift from a steady state causes the spin history artefact. This is shown schematically in Figure 3.1.

Throughout this chapter, I investigate the use of AFNI's image realignment algorithm referred to as the Volume Registration Algorithm (VRA). The six motion parameters estimated by the VRA are used to generate a motion-registered dataset with the motion removed from the image. The standard regression approach involves regressing the six motion parameters along with their temporal derivatives from the time series data. The addition of the temporal derivatives as regressors is to account for small timing differences. Some studies have even proposed the use of up to 36 regressors. The 36 regressors include 3 initial parameters (mean global time series, white matter and cerebrospinal fluid time series), 6 standard motion parameters, 9 temporal

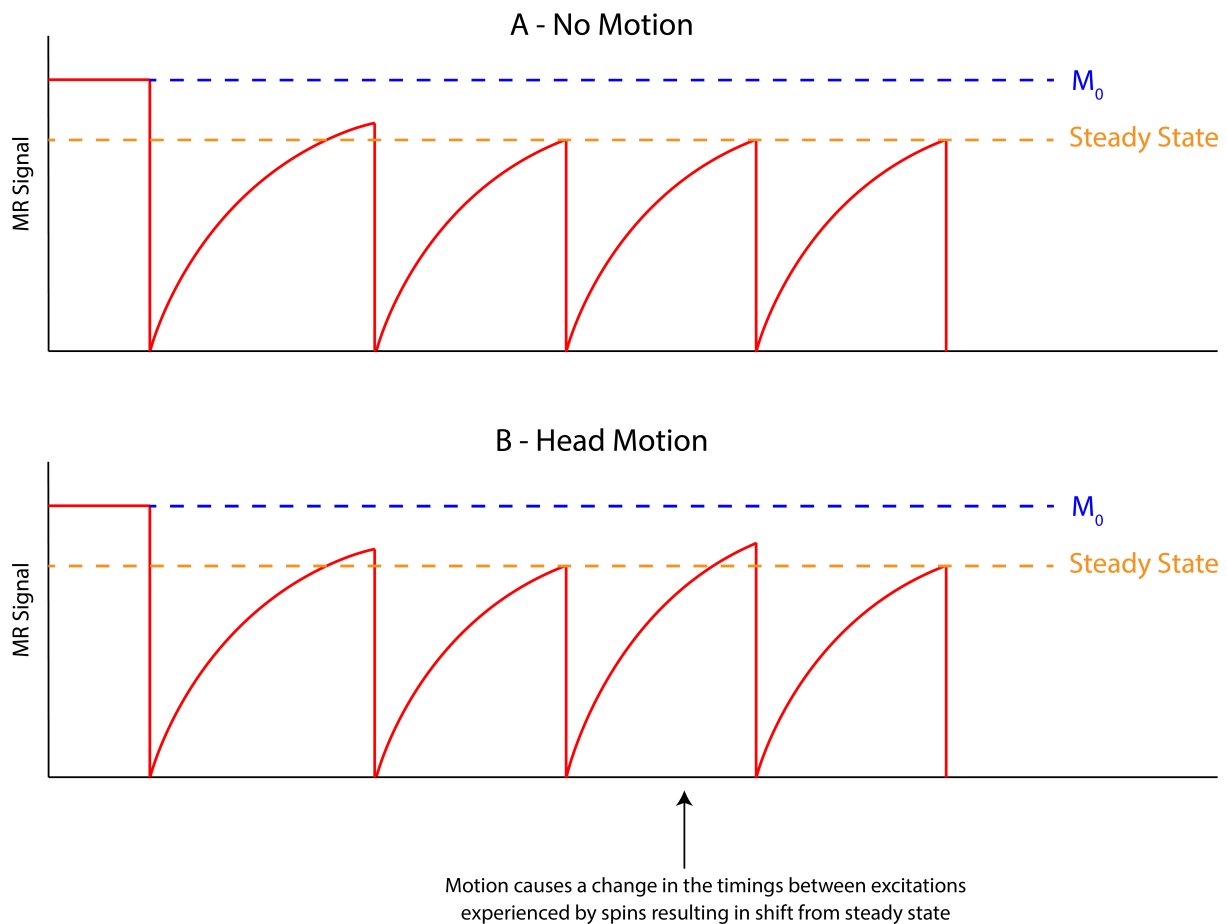


Fig. 3.1 A. A schematic diagram showing the MR signal reaching a steady state. B. Head motion effects cause a change in timing between the excitations experienced by the spins causing a shift from a steady state magnetisation. This is known as the spin history effect.

parameters (the temporal derivatives of the previous 9 parameters) and 18 quadratic parameters (the quadratic terms for all the previous 18 parameters) (Satterthwaite et al., 2013). However, it has been shown that using large numbers of motion regressors is detrimental and could result in a loss of signal (Bright and Murphy, 2015). Therefore, using the six motion parameters as regressors could be more beneficial than including the temporal derivatives as it will avoid the signal loss noted by Bright and Murphy (Bright and Murphy, 2015). As a result, only six regressors were used to generate the motion regression datasets in this study.

Additionally, I considered an external motion detector that uses an external camera mounted to the bed of the MRI scanner. This is a marker-less system that uses infrared light to create a 3D surface on the face of the participants. It provides real-time motion feedback as well as the estimation of translational and rotational motion parameters that can be used in retrospective correction. This system is the Tracoline (TCL) v3.074 motion tracking system (TracInnovations, Bellarup, Denmark) and has been shown to be compatible with both MR and positron emission tomography (PET) scanners (Slipsager et al., 2019). An overview of this system is explained in detail in section 3.3.1.2. The work demonstrated in this chapter focuses on retrospective motion correction which the TCL system is capable of. However, most studies that have used this camera

focus on prospective motion correction (Berglund et al., 2020; Frost et al., 2019; Slipsager et al., 2019). One study compared the system's ability to perform retrospective and prospective motion correction (Slipsager et al., 2021). Slipsager and colleagues determined that the TCL system performed prospective correction far more accurately than retrospective correction when compared visually and quantitatively (Slipsager et al., 2021). The TCL system has been shown to reduce motion artefacts and significantly improve prospective motion estimates in both PET and MR scans (Slipsager et al., 2019). One study found that the median absolute differences between the TCL tracking system and MR image registration were 0.26mm in the y-direction and 0.02° rotation about the y-axis and motion artefacts were significantly reduced when using TCL (Frost et al., 2019).

Measurement of cerebral vascular health can be achieved using physiological challenges that cause vasodilatory responses in the brain. Such challenges include inducing periods of hypercapnia and hyperoxia (Germuska et al., 2016; Wise et al., 2013) and introducing a breath-hold challenge that increases the arterial blood CO_2 level (Cohen and Wang, 2019; Murphy et al., 2011). The use of arterial spin labelling (ASL) has been verified as a non-invasive method of acquiring information about cerebral blood flow (CBF) (Buxton et al., 1998; Fantini et al., 2016a). These methods increase the signal in all areas of the brain ('globally') and are referred to as global intensity changes (GICs) throughout this work. GICs were explained in detail in a previous chapter as part of section 2.6.6.

There are three main hypotheses for this work. The first is that the GIC's cause the misrepresentation of motion in standard motion registration algorithms (the VRA's), contaminating the resulting motion estimates. The second is that the markerless motion tracking system, introduced in this section, will provide a gold standard that can be used to test the misrepresentation of motion. The third is that data-driven approaches to estimate motion will be improved by two approaches: i) using an independent component analysis as part of the motion estimation, ii) using a brain mask that is eroded at the edges to remove edge voxels that may be driving this misrepresentation of motion.

Although motion registration methods are designed to accurately determine motion parameters from the data, they can also contain a large amount of signal that does not pertain to motion in certain circumstances. Figure 3.2, which shows the motion parameters derived from ASL data during a CO_2 gas challenge, displays a clear 'tag-control' pattern and CO_2 signal. Therefore, as mentioned earlier, I propose that the VRA interprets GICs at edge voxels to be motion, and the GICs are represented in the motion parameters – thus causing signal loss when motion regressions using these parameters are performed. Here, I compare VRA-based and external marker-less camera-based correction with novel techniques designed to limit the influence GICs on the estimated motion parameters.

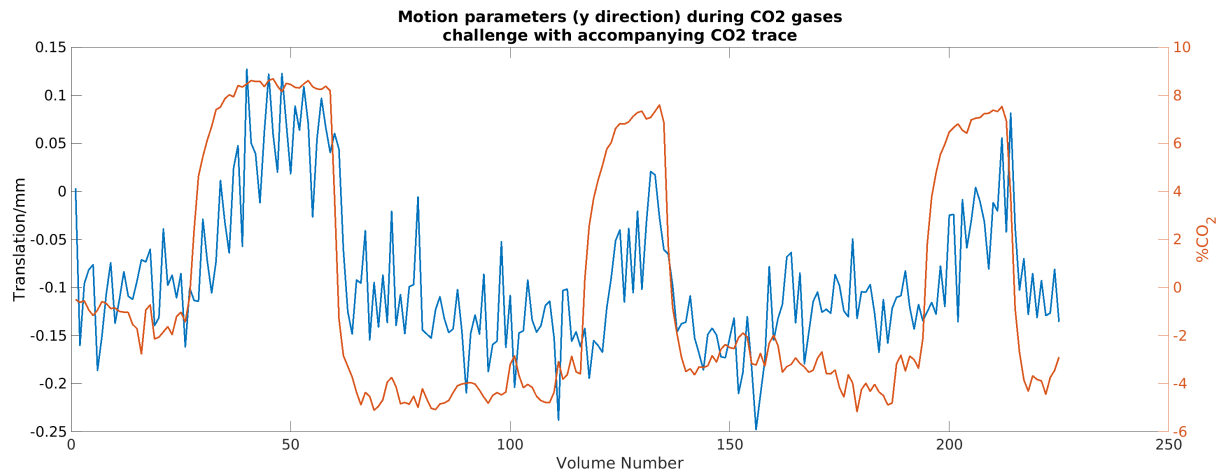


Fig. 3.2 The VRA-derived motion parameters (y-direction) for a CO₂ gases challenge which contained Arterial Spin Labelling (ASL) (blue) and the corresponding CO₂ trace recorded by external physiological equipment during the scan (orange).

3.3 Methods

3.3.1 Data Collection

Healthy participants (19-32 years) were recruited for the study of which, 5 were male and 5 were female. Data were acquired on a Siemens 3T MAGNETOM Prisma scanner using a 64-channel receiver head coil.

3.3.1.1 Overview of Scanner Protocols

To investigate the issue of misrepresenting GICs as motion, multiple different scan types were chosen as part of the scanning protocol. Each scan type enabled a different metric of cerebrovascular health to be quantified. The different scan types can be represented as a resting state scan plus some added task and will be referred to as ‘Rest+task’ throughout this chapter. Firstly, a resting state scan was collected as a sanity check. This scan does not contain a GIC and was expected to produce VRA motion estimates most similar to the camera-based method (and the other novel motion correction methods). Following the resting state scan, a BOLD scan was collected with participants asked to move their head along with a pre-defined movement sequence which introduced severe motion. The reason for this was to consider the accuracy of the motion correction methods in severe motion conditions. Additionally, connectivity measures could be collected from the resting state data. The multi-PLD pCASL scan allowed for the calculation of cerebral blood flow (CBF). This scan type used multiple post-labelling delay (PLD) times in an attempt to improve the accuracy of CBF quantification. The dual-excitation pCASL scan type was used to quantify cerebrovascular reactivity (CVR), cerebral blood flow (CBF), oxygen extraction fraction (OEF) and the cerebral metabolic rate of oxygen consumption (CMRO₂). During this scan, participants underwent periods of hypercapnia and hyperoxia as per (Germuska

et al., 2016; Wise et al., 2013). The breath hold (BH) scan was collected to quantify CVR. End-expiration breath holding causes a rise in end-tidal CO_2 (Moreton et al., 2016) which in turn induces a GIC. BH scans are also very easy to implement and so this was added to the protocol.

The scanning protocols used were as follows:

- Resting state - "*RestOnly*" (TR=2s, TE=30ms, $\alpha=70^\circ$, In-plane=2mm², 64 slices(2mm+0.5mm gap)). An EPI readout was used. This was collected as a control without any GICs. Connectivity measures were quantified. It was expected that motion estimates would perform in a similar way across all motion-correction methods.
- BOLD with applied motion - "*Rest+Motion*". The protocol was identical to the Resting state protocol. An EPI readout was used. Participants were asked to move their heads along with a predefined movement sequence. This was collected to determine how well methods perform in severe motion conditions. Connectivity values were quantified. Expected similar results to that of resting state.
- Dual-excitation pCASL - "*Rest+CO₂+ASLTag & Rest+CO₂*"(TR=1.1/3.8s, TE=11/30ms, $\alpha=90^\circ$, In-plane=3.4mm², 19 slices(6mm+1.2mm gap)). This protocol uses an interleaved BOLD/ASL sequence (Germuska et al., 2019; Schmithorst et al., 2013) in which a BOLD image is collected (TR=1.1s, TE=11ms), followed by an ASL tag image (TR=3.8s, TE=30ms), followed by a BOLD image (TR=1.1s, TE=11ms), followed by an ASL control image (TR=3.8s, TE=30ms). This is repeated for the duration of the sequence. This scan was collected to quantify cerebrovascular reactivity (CVR), cerebral blood flow (CBF), oxygen extraction fraction (OEF) and the cerebral metabolic rate of oxygen consumption (CMRO₂). Participants underwent periods of hypercapnia and hyperoxia during this scanning session as per (Germuska et al., 2016; Wise et al., 2013). It was expected that CO_2 and O_2 increases would drive erroneous motion estimates in the BOLD portion and a mixture of ASL tagging and CO_2 would drive errors in ASL motion estimates.
- Multi-PLD pCASL - "*Rest+ASLTag*" (MaxTR=5.60, MinTR=2.85s, TE=11ms, PLD=250-3000ms in 250ms steps, $\alpha=90^\circ$, In-plane=3.4mm², 20 slices(6mm+1.2mm gap)). This was collected to quantify CBF. It was expected that a PLD-ramp and ASL tagging would drive errors in VRA motion parameter estimates.
- Breath Hold EPI BOLD - "*Rest+CO₂+Motion*" (TR=2s, TE=30ms, $\alpha=70^\circ$, In-plane=2mm², 64 slices(2mm+0.5mm gap)). This was collected to quantify CVR. It was expected that CO_2 would drive errors in motion estimates although it was also expected that large amounts of motion would be present.

3.3.1.2 Overview of External Motion tracking system

As mentioned previously, as well as collecting MR data, motion data was collected using the Tracoline (TCL) motion tracker (TracInnovations, Bellarup, Denmark). The TCL is made up of two units, the camera/light source and the vision probe (Slipsager et al., 2019). The camera sits behind the bore of the MR scanner and the vision probe is mounted to the MR bed using a specially designed mounting arm. The vision probe and camera are attached by 3-meter long fibre optic cables housed within an energy chain cable to protect them from damage (Slipsager et al., 2019). The vision probe is positioned so that it is directly above the participant's face and has a focus of 10-25cm (Slipsager et al., 2019). The TCL system uses Infra-Red light to generate a 3D facial surface at the beginning of the data acquisition and this surface is used as a reference for motion parameter estimation. It does this by projecting the IR light onto the participant's face using the vision probe. The IR light is generated in the camera and transferred to the vision probe using the optical fibres. Throughout the scanning session, the TCL continuously generated 3D facial surfaces known as point clouds. The reference surface can be edited by the operator using the tracsuite software and this is how the eye was cropped from the reference. The system generates 30 point clouds per second and these are registered to the reference surface to generate motion parameter estimates. An example of the point clouds collected and the reference surface can be seen in Figure 3.3 (taken from (Frost et al., 2019)). For retrospective correction, the motion parameter estimates need to be calibrated to a structural MPRAGE image acquired at the beginning of the scanning session. This is to ensure that the motion information from the camera is in the coordinate system of the MR scanner (the isocentre). The surface model of the MPRAGE and the reference point cloud calibration can be seen in Figure 3.4.

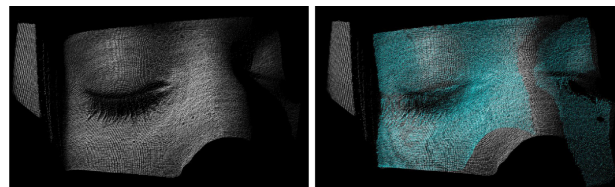


Fig. 3.3 Representation of the 3D surface collected during tracking. The green surface shown is the reference surface that the point clouds were registered to which was used to generate motion parameters. This image was taken from (Frost et al., 2019)

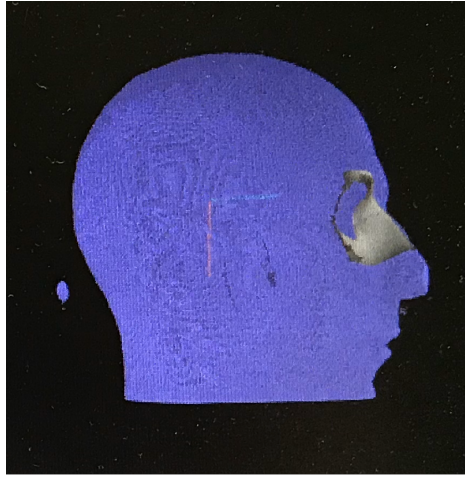


Fig. 3.4 MPRAGE to surface calibration example. The MPRAGE collected at the beginning of the scanning session is shown in purple and the reference surface is shown in grey. The eye was cropped out of the reference surface to prevent corruption of motion estimates by blinking.

3.3.2 Data Analysis

Estimates of motion regressors were calculated in four groups of methods; VRA-based, camera-based, ICA-based and Erosion-based. This project investigated motion parameters in detail and so no preprocessing steps were used. Preprocessing was avoided in case spurious interactions with motion occurred, as these could alter motion parameter estimation. The VRA-based method is the conventional motion correction method. It was included in this analysis in order to draw comparisons with the novel methods. The camera-based method is external to the MR scanner and should not be prone to the misrepresentation error outlined in Figure 3.2. Therefore, it is expected that this will produce accurate estimates of motion. The ICA-based methods isolate the signal expected to drive the error and removed it from the data before calculating motion parameters. This was to generate more precise motion estimates without the erroneous signal. The external influence on the GIC can be identified for each scan type using the table (Table 3.1) The Erosion-based methods used whole brain masks that were eroded at the edges with differing severity's. This was to remove the edge voxels from the estimation in an attempt to improve the motion estimates. The edge voxels would have the largest change in signal intensity and as so it was hypothesised that their removal would improve the estimation of motion.

Table 3.1 A table showing the external influence on the GIC for each scan type analysed in this project

Scan Type	Alternative Name	External influence on GIC
Resting state	RestingOnly	None
BOLD with applied motion	Rest+Motion	None
Multi-PLD pCASL	Rest+ASLTag	PLD ramp/ASL Tagging
Dual-excitation pCASL - BOLD	Rest+CO ₂	CO ₂ + O ₂ challenge
Dual-excitation pCASL - ASL	Rest+CO ₂ +ASLTag	CO ₂ challenge/ASL Tagging
Breath Hold EPI BOLD	Rest+CO ₂ +Motion	CO ₂ breath hold challenge

3.3.2.1 Volume Registration Algorithm (VRA) based correction

The VRA-based method used AFNI's 3dAllineate (Cox, 1996; Cox and Hyde, 1997), a program that performs alignment of a dataset with a pre-defined base dataset, to perform rigid-body volume registration and calculate motion parameters. This has 6 degrees of freedom (3 translational and 3 rotational). The temporal resolution of these motion parameters is one parameter per TR.

3.3.2.2 Camera-based correction & the issues associated with it

The camera motion parameter estimates were calculated with a temporal resolution of 30Hz. However this was downsampled to match the VRA-based method (one parameter per TR).

Initially, it was thought that the camera-based motion parameter estimates should be considered the 'true' motion of the participant throughout the scanning session. This is because the camera is external to the scanner. However, on initial analysis of the motion parameters produced by the TCL motion tracking system, it was clear that there is a large amount of movement and noise within the parameter estimates. This can be seen in the comparison between Figures 3.5, 3.6, 3.7 and 3.8 which shows the parameter estimates for the VRA-based and camera-based methods. The TCL system works by attaching to the scanner bed by an arm. During the scan this arm would vibrate with the vibration of the gradients within the MR scanner and so it was hypothesised that this vibration is driving the added noise. By isolating the frequency of vibration, I tried to remove this added source of noise and improve the accuracy of the camera-based estimates. An FFT was applied to the camera-based motion parameters to determine the frequency range that the vibration occurred in. I determined that the vibration was occurring between 0.2Hz and 0.3Hz and so a bandpass filter was applied with these frequencies as the upper and lower bandpass frequencies. Then, the bandpassed motion parameters were subtracted from the original motion parameters to calculate the filtered motion parameters. Figures 3.9 and Figure 3.10 show the FFT and the bandpassed FFT. The filtered motion parameters were then used to rotate the raw data to generate a camera-based registration file. Unfortunately, the filtered parameters showed a large amount of noise and the registration dataset contained more motion.

As such, this attempt at reducing the noise is not substantial enough to remove noise fully even though a small visual reduction in noise can be seen.

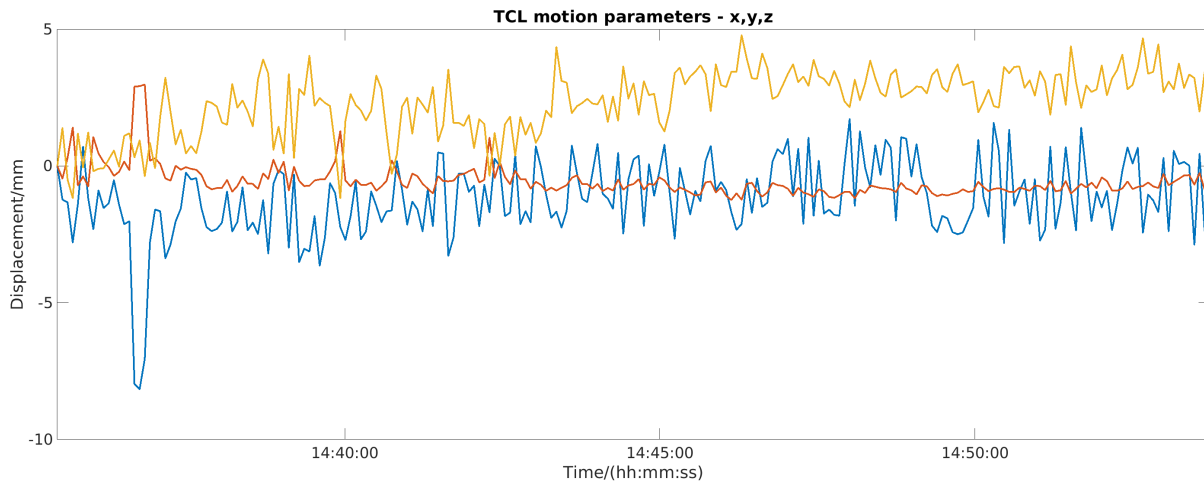


Fig. 3.5 Camera-derived translational (x, y, z) motion parameters for ASL data taken from a dual echo excitation scan. The blue line represents the x parameter, the orange line represents the y parameter and the yellow line represents the z parameter.

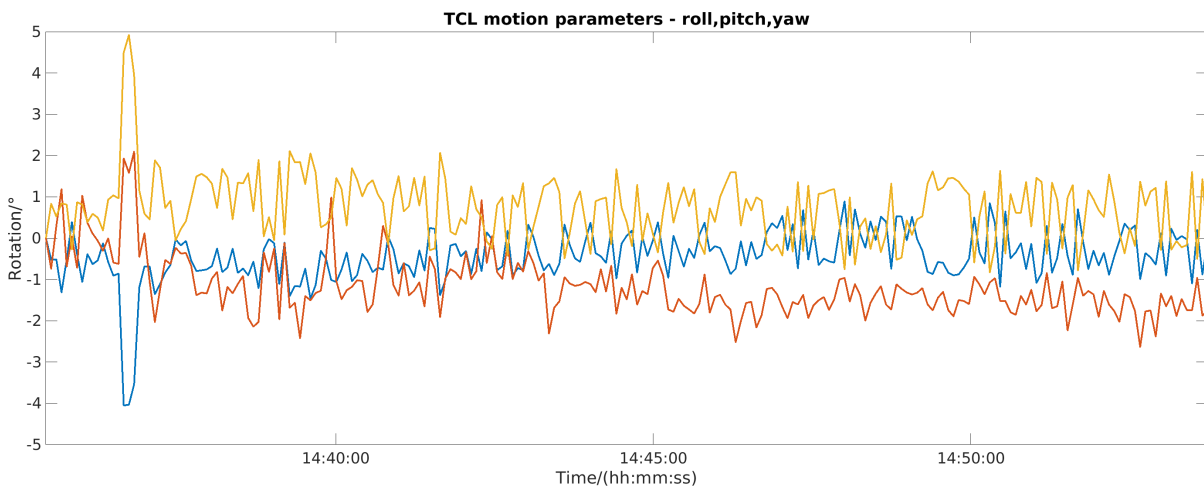


Fig. 3.6 Camera-derived rotational (roll, pitch, yaw) motion parameters for ASL data taken from a dual echo excitation scan. The blue line represents the roll parameter (rotation around z-direction), the orange line represents the pitch parameter (rotation around x-direction) and the yellow line represents the yaw parameter (rotation around y-direction).

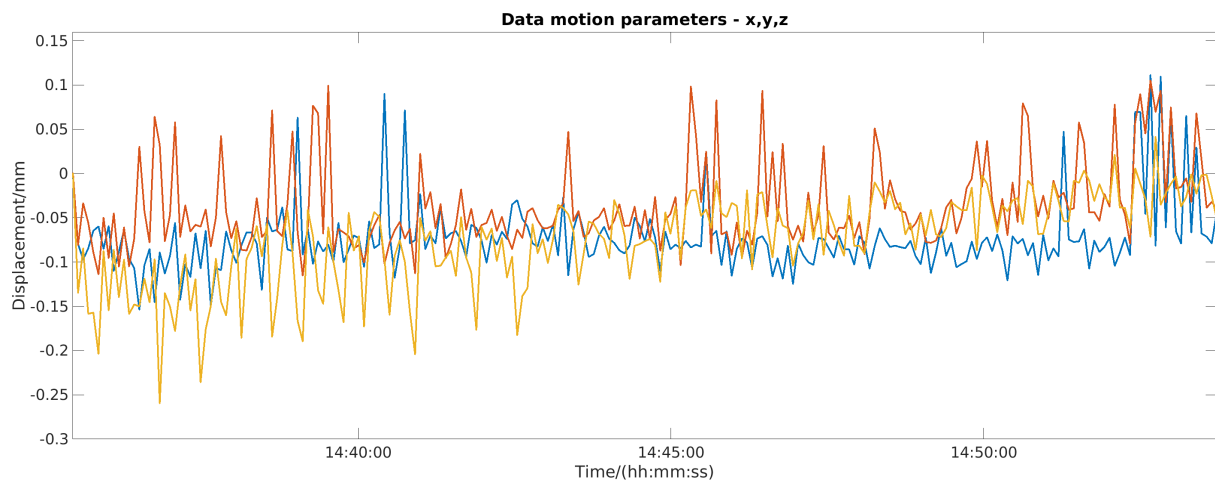


Fig. 3.7 VRA-derived translational (x , y , z) motion parameters for ASL data taken from a dual echo excitation scan. The blue line represents the x parameter, the orange line represents the y parameter and the yellow line represents the z parameter.

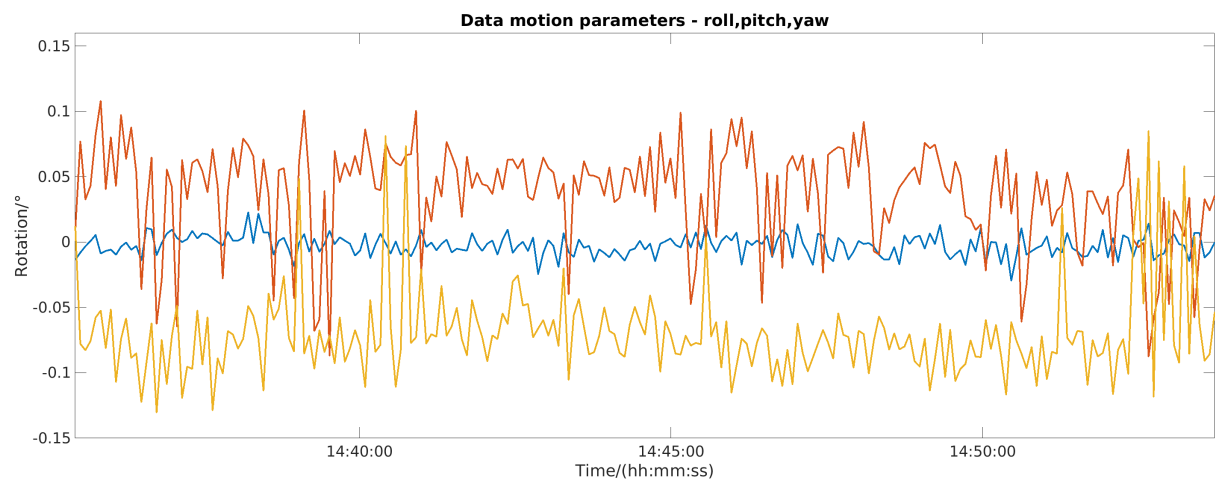


Fig. 3.8 VRA-derived rotational (roll, pitch, yaw) motion parameters for ASL data taken from a dual echo excitation scan. The blue line represents the roll parameter (rotation about the z -direction), the orange line represents the pitch parameter (rotation about the x -direction) and the yellow line represents the yaw parameter (rotation about the y -direction).

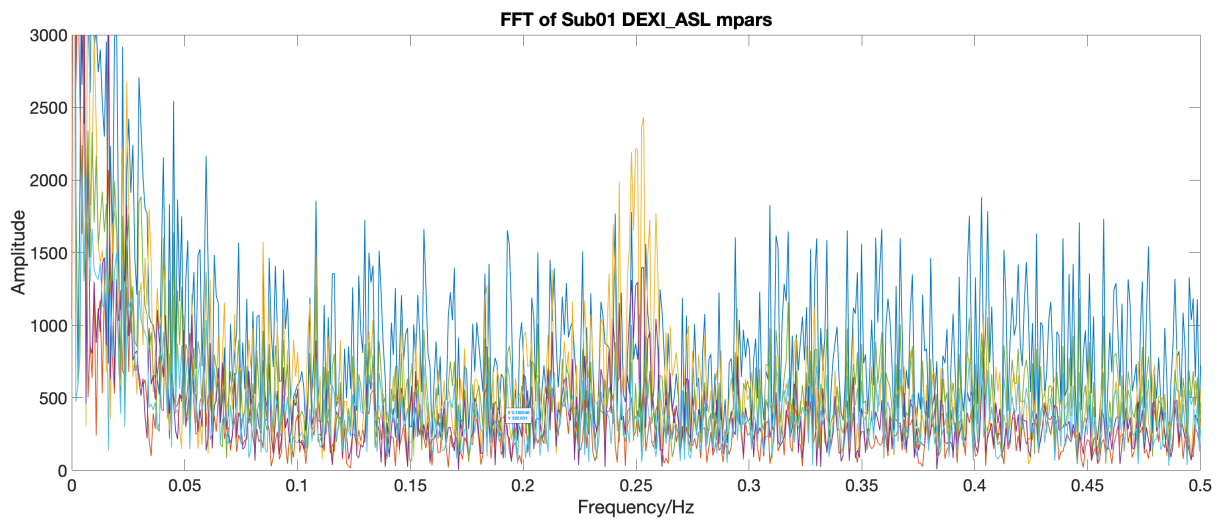


Fig. 3.9 FFT of camera-derived motion parameters from ASL data acquired using a dual echo excitation scan.

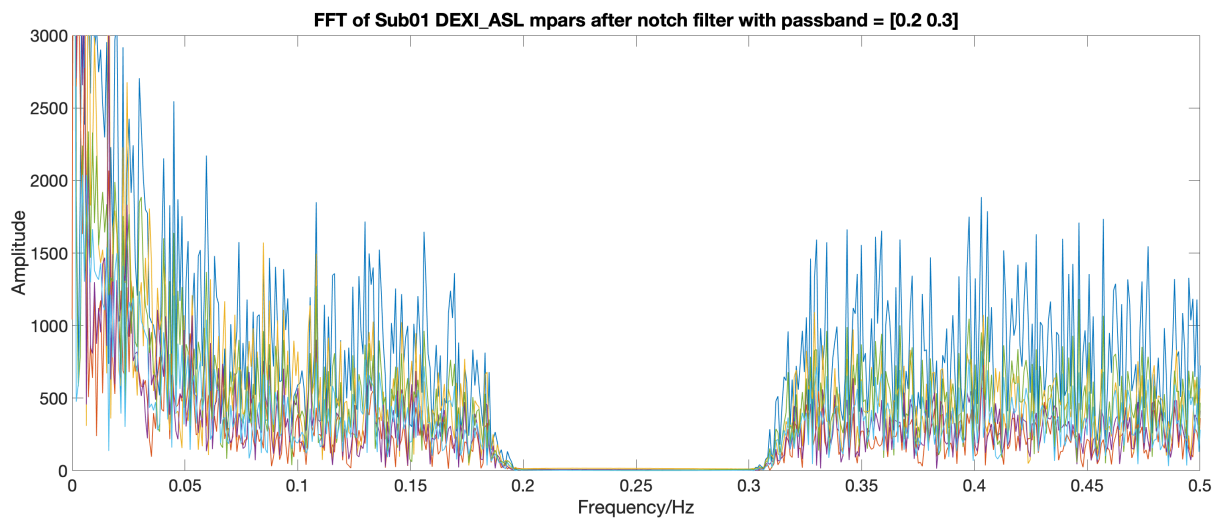


Fig. 3.10 FFT of camera-derived motion parameters with the problematic frequency range bandpass filtered out.

3.3.3 Independent Component Analysis (ICA) based correction

The ICA-based method used FSL's MELODIC to perform an Independent Component Analysis (ICA) (Beckmann and Smith, 2004) to decompose the data into independent components. Then, the external influence on the GIC caused by any CO₂ or tagging-induced global changes along with the ICA decomposition was used to isolate and remove components related to these signals. Data were pre-processed by MELODIC in the following way: masking of non-brain voxels, voxel-wise demeaning of data and normalisation of the voxel-wise variance. The data was then whitened and projected into a 60-dimensional subspace using principal component analysis. Next, the whitened observations were decomposed into sets of vectors which describe the signal variation across the temporal and spatial domains. Finally, the estimated component maps were divided by the standard deviation of the residual noise and thresholded by fitting a mixture model to the histogram of intensity values. Components were removed by regressing them from the data using ordinary least squares regression (part of the MELODIC toolbox). Then, motion parameters were calculated from the datasets that no longer contained the external influences on the GICs using a VRA. The number of components removed was determined by a correlation of the external influence on the GIC with each ICA component. The components with statistically significant p -values ($p < 0.05$ - uncorrected) were removed (*Method 1*). In *Method 2*, a Bonferroni correction accounted for multiple comparisons and statistically significant components were removed.

3.3.4 Erosion-based correction

The Erosion-based method excluded voxels from the VRA using a whole brain mask that had been eroded (from the outer edge) by either 5mm or 20mm.

3.3.4.1 Erosion-based 'doughnut' masks

Masks were created that combined the Erosion-based masks to generate 'doughnut' masks. These masks removed data from the centre of the original Erosion-based masks so that they were 'ring-shaped' (or doughnut shaped). The idea behind this was to isolate the signal originating from the GM. Additionally, the masks were thought to remove any signal from the brain stem which could interfere with the calculation of motion parameters. The results for this method have not been included in this work as initial analyses suggested the method did not work well.

3.3.5 Hybrid Independent Component Analysis (ICA) & Erosion-based correction

A hybrid method that combined the ICA and Erosion methods was used to determine if a mixture of these methods would increase the accuracy of the motion parameter estimates. An ICA was run and the external influence on the GICs was removed from the data as per the ICA-based

method (section 3.3.3). Then, motion parameters were calculated from the data that no longer contained the external influences on the GICs using a VRA. However, in the setup of the VRA, an eroded whole brain mask was used to restrict the registration so that it did not include the edge voxels in its estimate of motion. The results from this method have not been included in this work as initial analyses suggested the method did not work well.

3.3.6 Boundary Based Registration (BBR)

Boundary based registration was used as an alternative data-based method which is independent of the GICs brought on by registering the fMRI volumes with each other. BBR works by mapping the white matter boundaries to the EPI images. This is usually performed with a rigid-body registration with 6 degrees of freedom. FSL's implementation of BBR was used to perform the registration. Initially, the EPI image was averaged and this was registered to the structural image using FSL's epi reg resulting in an initial BBR registration matrix. The next step used the initial BBR matrix and each fMRI volume to register them to the structural image. This produced a BBR matrix and BBR volume for each fMRI volume. The resulting matrix corresponds to the motion between each successive volume. Finally, the BBR volumes were combined to create one BBR dataset corrected of motion. Unfortunately, the initial results for this method showed that it did not work as expected and so have not been added to the results for this work. The conclusion made is that there is not enough information in the fMRI images to allow for an accurate BBR correction of motion.

3.3.7 Registration & Regression analysis

Retrospective motion correction can be achieved in two stages, motion registration and motion regression. The former deals with the correction of motion in the images themselves which is important to remove any rotations/translations that can be seen within the images. The latter deals with the correction of motion within the time series data. This is achieved by using linear regression and the motion parameters (or regressors in this case). The motion parameters are then regressed from the data resulting in a dataset corrected of motion.

Following the creation of motion parameters, a registration dataset was created for each method by rotating and translating the raw data using the motion parameters. For the VRA-based and Erosion-based methods this was an automatic process that formed part of the registration algorithm. For the camera-based and ICA-based methods this was completed manually by using AFNI's 3drotate. The six motion parameters were then used as regressors in a linear regression and regressed from the registration dataset resulting in datasets that were fully corrected of motion. To understand whether the different steps of motion correction affect the misrepresentation of signal, the different stages of motion correction will be presented separately in the results. The data corrected up to the motion registration step will be referred to as *registration only* and the data that is fully corrected of motion will be referred to as *registration + regression*.

3.3.8 Analysis of Motion Parameters

A global signal was created from the raw data acquired directly from the scanner. This was accomplished using AFNI's 3dmaskave function which computed an average of all voxels within the input dataset (the raw data). This was repeated for all scan types and participants.

To determine how much variance GICs add to the motion parameters, linear regression was performed on the global signal with the motion parameters (from each method) used as regressors for each scan and participant. The global signal was then plotted against the model fit created from the linear regression. This was to determine how closely fitting the model fit was to the global signal. R^2 statistics were calculated from the linear regression.

Linear regression was also used to compare the motion parameters for each method to the VRA motion parameters and to compare to the external influence on the GIC that was hypothesised to drive the misrepresentation of signal (explained in Table 3.1). This would indicate how closely the estimates were to the VRA-based estimates as well as the driver of the error. R^2 values were calculated from each regression and paired t-tests were used to estimate the significance when compared to the VRA-based R^2 values.

This analysis was expected to identify which technique performed the best at calculating motion parameters. The graphs that were created by this method show how much variance in the global signal, the expected GIC and the VRA-based estimation each method's estimation of motion explains. This would therefore show which method produces motion estimates that contain the least variance related to the global signal and GIC. It would also demonstrate which method was most similar to the VRA method (which has been found to show erroneous motion parameter estimates). The impact that improved motion correction would have on the calculated physiological parameters would vary for each. It is thought that the values of CVR and CBF would increase where there is a more accurate correction of motion. The expected trend for CMRO₂ and OEF is not as straight forward, however. It is currently unclear whether motion correction would lead to a drop in these measures or an increase. It is expected that measures of connectivity will increase with better motion correction.

3.3.9 Quantification of Cerebrovascular Physiology

Cerebrovascular measures were quantified for each motion correction method. For completeness, these measures were calculated after the *registration only* dataset was created and also after the *registration + regression* dataset was created.

3.3.9.1 Connectivity analysis

Left and right motor cortex masks from the Juleich atlas were registered to subject space. These were combined with participant grey matter masks (explained in section 3.3.10) to generate a left and right motor cortex masks containing only grey matter. These masks were then used to

generate the average BOLD (*RestOnly* or *Rest+Motion*) signal contained within the left and right motor cortex for each of the motion correction types. A correlation was performed between the average BOLD signal in the left and right motor cortex and these correlation values were used as connectivity values. This was repeated for each motion correction type and each participant, considering both *registration only* and *registration + regression*. The average connectivity value across all 10 participants was calculated.

3.3.9.2 CBF Quantification

To calculate CBF it is first necessary to calculate the $M_{0,blood}$ as this will allow for the determination of the amount of magnetisation in the tag and control images that is related to blood. The protocol used a multi-PLD pCASL acquisition with PLD times ranging from 250-3000ms in 250ms steps. CBF values were quantified by fitting all PLD values simultaneously using equations 2.6, 2.7 and 2.8 (as per the method outlined by Buxton (Buxton et al., 1998) - This is described in detail in Chapter 2). Initially a value for the magnetisation of arterial blood ($M_{0,a}$) was calculated using equation 3.1 (Pinto et al., 2019). The parameters used in this equation included the magnetisation of tissue (CSF in this case - $M_{0,CSF}$), echo time ($TE = 11ms$ (Pinto et al., 2019)), the transverse relaxation time of tissue (CSF used as reference tissue - $T_{2,CSF}^* = 400ms$), the transverse relaxation time of arterial blood ($T_{2,a}^* = 48.4ms$) and the blood-brain water partition coefficient $\lambda_t = 1.15$ (Pinto et al., 2019).

Following the calculation of $M_{0,a}$, CBF was calculated using equations 2.6, 2.7 and 2.8. Parameters used within this equation were as follows: $\lambda = 0.9mlg^{-1}$ (Alsop et al., 2015), $\alpha = 0.85$, $\tau = 1.8ms$

$$M_{0,a} = \frac{M_{0,CSF} \cdot e^{TE(\frac{1}{T_{2,CSF}^*} - \frac{1}{T_{2,a}^*})}}{\lambda_t} \quad (3.1)$$

3.3.9.3 CVR Quantification

CVR quantification initially involved the normalisation of the BOLD signal to produce a percentage BOLD dataset. This was achieved using equation 3.2. Then a linear regression was used with the measured CO_2 trace as a regressor. This follows the method outlined in Chapter 2, following equation 2.5. This resulted in the quantification of CVR maps.

$$\%BOLD = \frac{BOLD}{BOLD_{mean}} \cdot 100 \quad (3.2)$$

Additionally, CBF CVR was also generated in this study. Quantification of CBF CVR follows the same method as above however the CO_2 trace is regressed from the CBF data in place of the BOLD data.

3.3.9.4 CMRO₂ Quantification

Quantification of CMRO₂ followed the method described in Chapter 2 using equation 2.9. Calculation of CaO₂ was achieved using equation 3.3 where $\phi = 1.34[ml]O_2([g]Hb)^{-1}$ (the O₂ carrying capacity of haemoglobin), *Hb* is the haemoglobin concentration, SaO₂ is the arterial oxygen saturation, PaO₂ is the partial pressure of oxygen in arterial blood and $\epsilon = 0.000031[ml]O_2([ml]blood[mmHg])^{-1}$ is the coefficient of solubility of oxygen in blood. In this work the value used for *Hb* depended on the gender of the participant as blood samples weren't taken to measure this per participant. For male participants the value used was $0.155[g]Hb([ml]blood)^{-1}$ and for female participants the value used was $0.135[g]Hb([ml]blood)^{-1}$ (Billett, 1990).

$$CaO_2 = \phi \cdot Hb \cdot SaO_2 + PaO_2 \cdot \epsilon \quad (3.3)$$

To use equation 3.3, one must first calculate SaO₂. This can be accomplished using equation 3.4 (Wise et al., 2013). PaO₂ can be measured from the O₂ trace collected as part of the data collection.

$$SaO_2 = \left(\frac{1}{\frac{23400}{(PaO_2)^3 + 150(PaO_2)} + 1} \right) \quad (3.4)$$

The parameters used to calculate CMRO₂ (equation 2.9) follow those outlined in Chapter 2 as well as using equation 3.3 to calculate CaO₂.

3.3.10 Grey Matter Segmentation

Following the creation of maps containing CVR, CBF, CMRO₂ and OEF, the values for each parameter in grey matter (GM) were extracted from the maps using GM masks. These masks were generated from structural T1w images acquired as part of the scanning protocol. Generation of these masks began by running Advanced Normalization Tools (ANTs) cortical thickness pipeline to segment the different tissues within the brain. Then, the segmented GM (T1) image was registered to functional (EPI) space using boundary based registration (epi_reg - part of FSL's FLIRT (Jenkinson et al., 2002; Jenkinson and Smith, 2001)). This resulted in a GM masks in EPI space. The average signal in GM within the CVR, CBF, CMRO₂ and OEF maps was calculated using AFNI's 3dmaskave to generate cerebrovascular measures in GM.

3.4 Results

3.4.1 Volume Registration Algorithm (VRA) based correction

Motion parameter estimates generated by the VRA-based correction method varied across the different scan types collected. The motion estimates for the scans containing a GIC supported my hypothesis that the VRA misrepresents signal as motion in the presence of a GIC. This is demonstrated in both Figure 3.11 and Figure 3.12 where the former represents the effects on the global signal (mean across voxels) and the latter represents the effects on the different GICs that were expected to cause the misrepresentation. It is clear from both Figures that a high R^2 was calculated from the VRA-based estimates in most of those scans that contained a GIC (*Rest+CO₂*, *Rest+ASLTag*, *Rest+CO₂+Motion*, *Rest+CO₂+ASLTag*).

3.4.2 Camera-based correction

Motion parameter estimates generated by the camera-based method showed a large variation across scan types. The lowest values were detected for the *Rest+ASLTag* scans with almost all values of R^2 less than 0.2 (Figure 3.11). In some cases, the R^2 values were similar to that of the VRA-based method which was predominantly the case for the scans that did not contain GICs (*RestOnly* and *Rest+Motion*). Figure 3.13 compared the novel methods of correction to that of the VRA-based method and in most cases the camera-based method showed a large difference to the VRA-based method. This is reflected in the low values of R^2 calculated for the camera-based method in most scan types.

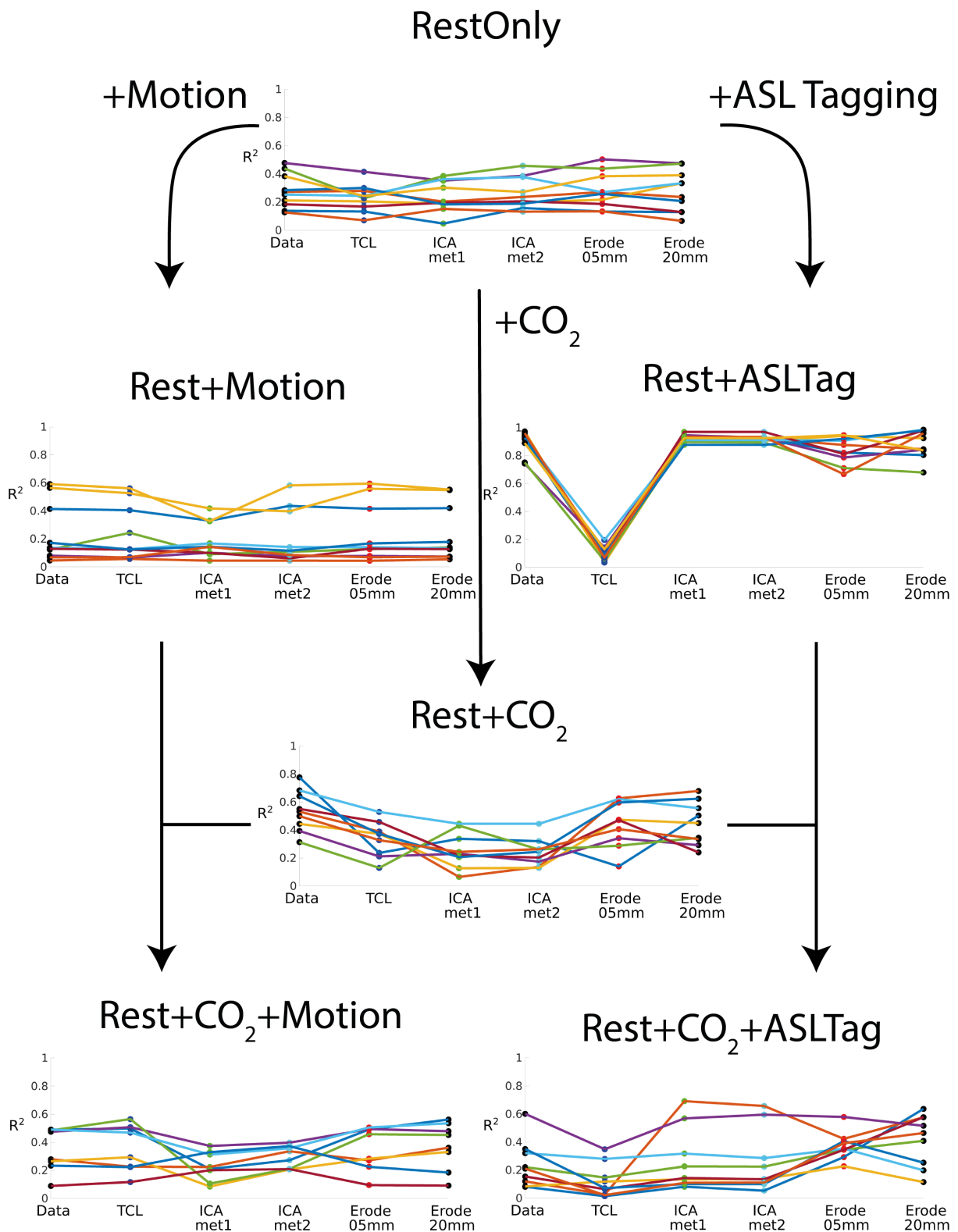


Fig. 3.11 R^2 variance values showing how much variance the motion parameters from each method could explain in the global signal (average over voxels). The lines connecting each method show the deviation between methods and each coloured line represents one participant. The colours of the points represent the method used. For example, all participants have the same coloured point for the data-derived method but a different coloured line connecting the points. At each step in the diagram, the scan type can be represented as a resting-state scan + a task. The lower the R^2 value, the less variance is explained in the global signal by the motion parameters which would suggest the method with the lowest variance is the least problematic method.

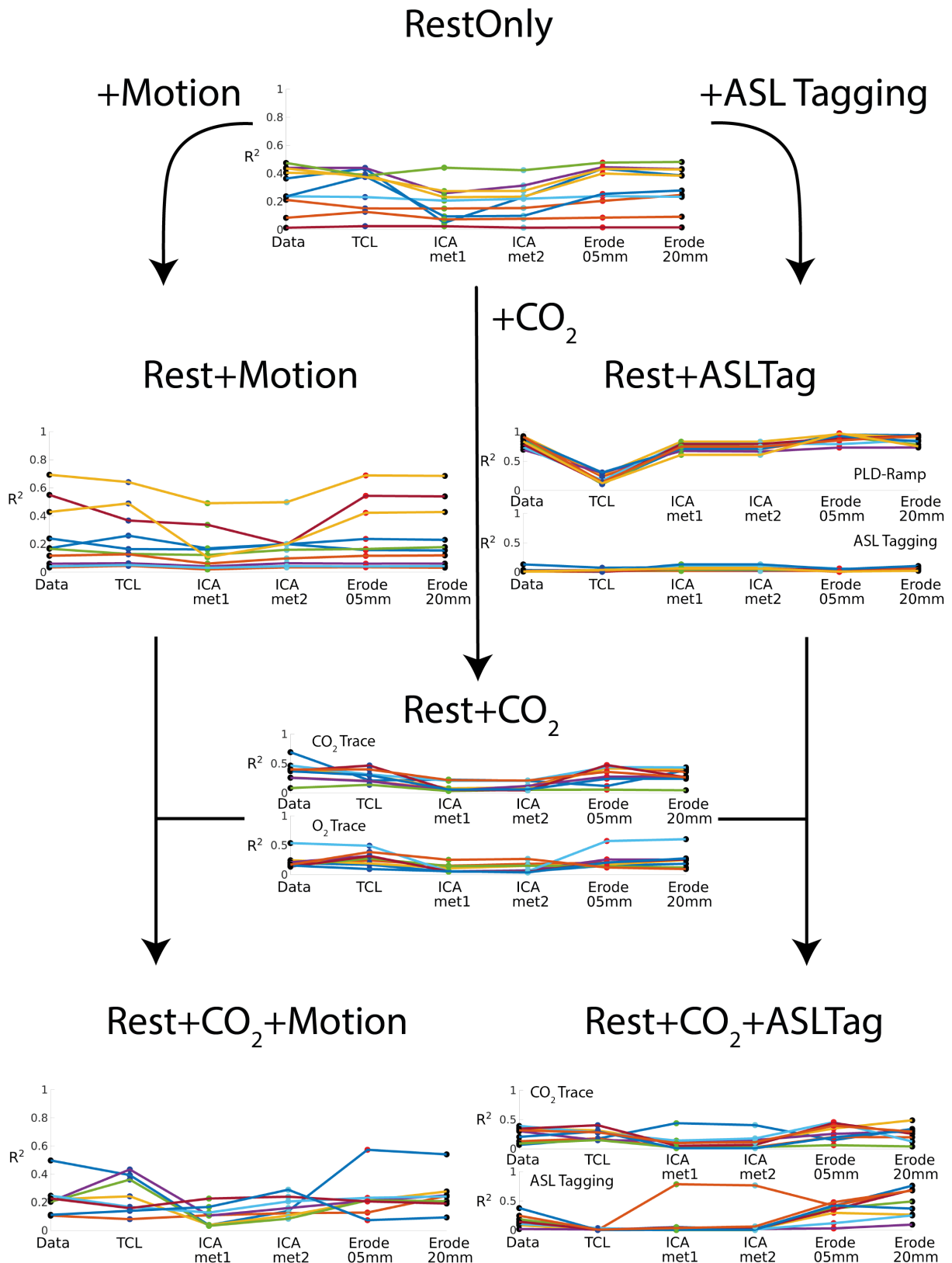


Fig. 3.12 R^2 variance values showing how much variance the motion parameters from each method could explain in the external signal expected to influence the GIC (explained in Table 3.1). The lines connecting each method show the deviation between methods, and each coloured line represents one participant. The colours of the points represent the method used. For example, all participants have the same coloured point for the data-derived method but a different coloured line connecting the points. At each step in the diagram, the scan type can be represented as a resting-state scan + a task. The lower the R^2 value, the less variance is explained in the external signal influencing the GIC by the motion parameters which would suggest the method with the lowest variance is the least problematic method.

3.4.3 Independent Component Analysis (ICA) based correction

Examining Figure 3.11, the ICA-based methods displayed R^2 values that were lower than the VRA-based estimate in some scans that contained a GIC (*Rest+CO₂*, *Rest+CO₂+ASLTag*). The most prominent case was detected for the *Rest+CO₂* scan type with p -values 2.2×10^{-4} (ICA method 1) and 1.6×10^{-4} (ICA method 2). This highlights that the motion parameter estimates calculated by the ICA methods do not show as much R^2 variance as the other methods and so they contain less information related to the GICs.

Examining the results from Figure 3.12, the ICA-based methods showed a lower R^2 in most scan types that contained a GIC (*Rest+CO₂*, *Rest+CO₂+Motion*, *Rest+CO₂+ASLTag*). The greatest difference was detected for the *Rest+CO₂* scan with p -values of 2.1×10^{-4} (ICA method 1) and 5.8×10^{-3} (ICA method 2), when comparing the VRA-based method. A significant difference was found for the *Rest+ASLTag* scan, when compared to the VRA-based method. The PLD-ramp was the predominant GIC causing the misrepresentation of motion (p -vals= 6.6×10^{-3} (ICA method 1), 3.0×10^{-3} (ICA method 2)). ASL tagging showed a significant p -value when compared to the VRA-based estimate also (p -value= 4.0×10^{-2} (ICA method 1), 3.8×10^{-2} (ICA method 2)). Lower R^2 values were calculated for the *RestOnly* scan (p -vals= 7.8×10^{-3} (ICA method 1), 2.6×10^{-3} (ICA method 2)) and the *Rest+Motion* scan (p -vals= 2.2×10^{-2} (ICA method 1) suggesting less signal is misrepresented as motion when using the ICA-based methods.

The ICA-based results showed similarities to that of the VRA-based results in all scan types (Figure 3.13). A bigger spread of R^2 values is present in the scans that contained GICs (*Rest+CO₂*, *Rest+ASLTag*, *Rest+CO₂+Motion*, *Rest+CO₂+ASLTag*) as expected. In most cases, the R^2 values calculated from ICA method 2 were higher than ICA method 1 and thus more similar to those of the VRA-based method.

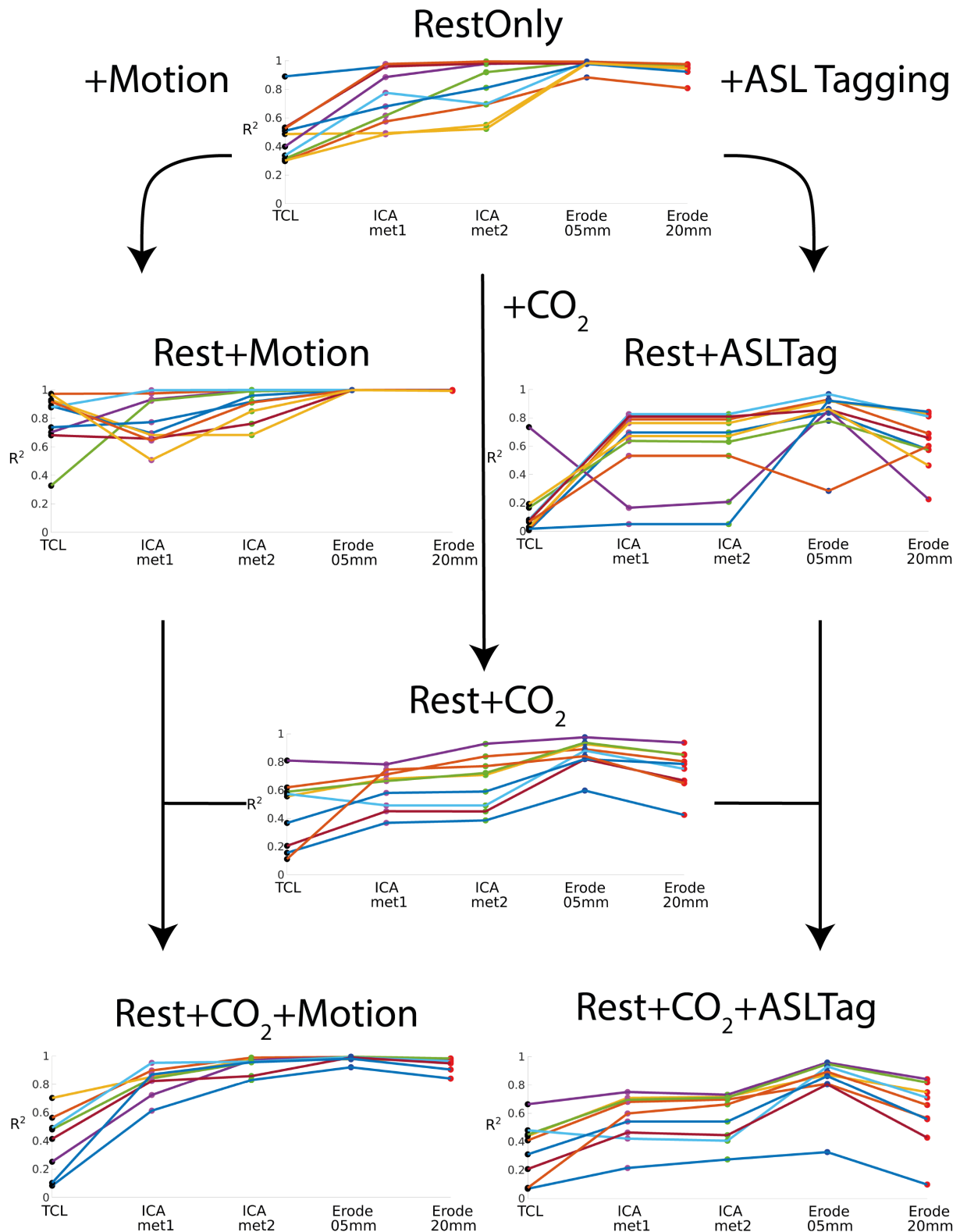


Fig. 3.13 R^2 variance values showing how much variance the motion parameters from each method (TCL, ICAMet1, ICAMet2, Erode05mm, Erode20mm) could explain in the VRA-based motion parameter estimates. The lines connecting each method show the deviation between methods and each coloured line represents one participant. The colours of the points represent the method used. For example, all participants have the same coloured point for the data-derived method but a different coloured line connecting the points. At each step in the diagram, the scan type can be represented as a resting-state scan + a task. The lower the R^2 value, the less variance the motion parameters will explain in the VRA-based motion parameters which would suggest the method with the lowest variance is the least problematic method.

3.4.4 Erosion-based correction

Referring to the similarities to the global signal (Figure 3.11) the Erosion-based methods displayed R^2 values that were consistent with that of the VRA-based estimates in most cases. This differs when looking at the *Rest+ASLTag* scan type where there was a statistical difference observed with p -values of 3.7×10^{-3} (Erosion 05mm) and 7.4×10^{-2} (Erosion 20mm).

On the whole, Erosion-based estimates generated similar results to that of the VRA-based estimates when looking at the effects of the different GICs (Figure 3.12). There were statistical differences between the VRA-based estimate and the Erosion-based estimates in some cases, namely for the *Rest+Motion* scan (p -value= 3.2×10^{-2} (Erosion 05mm)), the *Rest+CO₂+ASLTag* (p -value= 2.03×10^{-3} (Erosion 05mm), p -value= 3.4×10^{-3} (Erosion 20mm)) and the *Rest+ASLTag* (p -value= 9.4×10^{-4} (Erosion 20mm)).

For scans that did not include a GIC (*RestOnly*, *Rest+Motion*), the Erosion-based estimates showed a very high similarity (and therefore R^2 value) to the VRA-based estimates (Figure 3.13). In the scans that did contain a GIC (*Rest+CO₂*, *Rest+ASLTag*, *Rest+CO₂+Motion*, *Rest+CO₂+ASLTag*), there was a large spread in R^2 for the Erosion-based estimates with the erosion 5mm estimates showing less of a spread in similarity.

3.4.5 Quantification of Cerebrovascular Physiology

3.4.5.1 Connectivity analysis

Both the *RestOnly* and *Rest+Motion* scans were used to generate connectivity values for the right and left motor cortex areas. Results are shown in Figures 3.14 and 3.15 with the former showing the results for the *RestOnly* and the latter showing the results for the *Rest+Motion*. The bar plots show the average connectivity values across the participants for that correction method. For the *RestOnly* scan, values of connectivity varied across the different correction methods with most methods showing connectivity values between 0.5 and 1. The average connectivity for each scan type fell between 0.76 and 0.86. The average value for each correction method was quite similar for each correction type. A statistical difference was detected when comparing the *registration only* VRA-based and camera-based methods (p -value= 7.3×10^{-2}) and the *registration + regression* VRA-based and camera-based correction methods (p -value= 8.9×10^{-4}). The *Rest+Motion* scan was more variable with values ranging from -0.1 to 1 across the different methods. *Registration only* methods showed lower values for connectivity than *registration + regression* methods overall. No statistically significant differences were detected for the *registration only* methods when compared to the VRA-based method. The VRA-based method alone showed similar values to those that were data-based with the camera-derived and ICA-based method 1 showing slightly lower values. When comparing the VRA-based *registration + regression* method to the other *registration + regression* methods, a statistically

significant difference was detected for no motion correction (p -value= 7.5×10^{-3}) and for ICA method 1 (p -value= 1.5×10^{-2}).

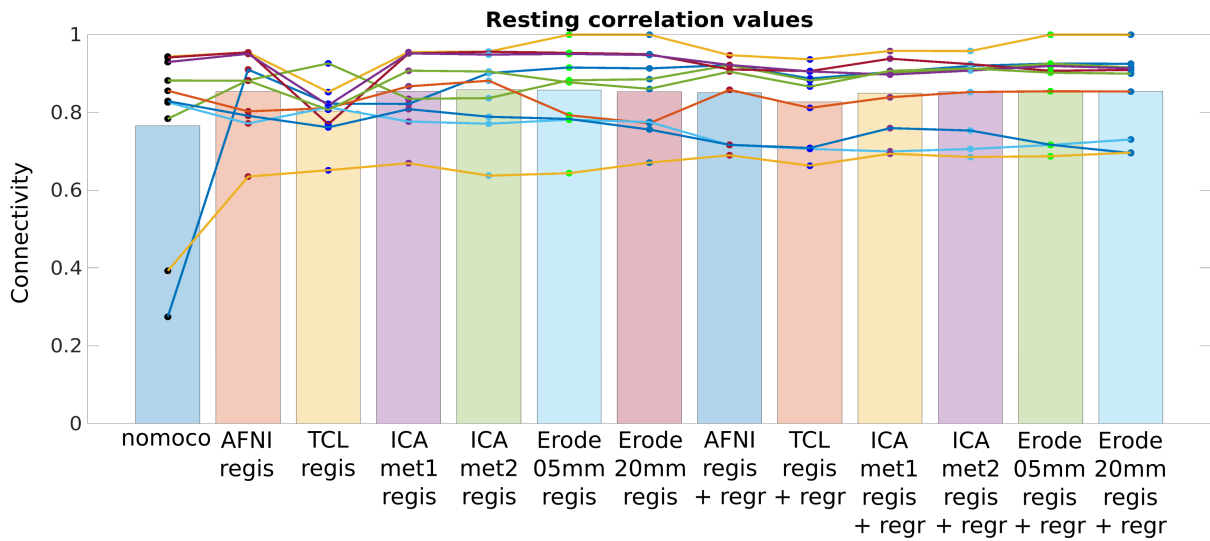


Fig. 3.14 Connectivity values generated from the *RestOnly* scan for each correction method. Each correction method is represented by a different coloured dot. Each line connecting the dots represents a different participant. The bars represent the average connectivity across participants for each method. The 'regis' terms represent registration and the 'regis+regr' represents registration and regression.

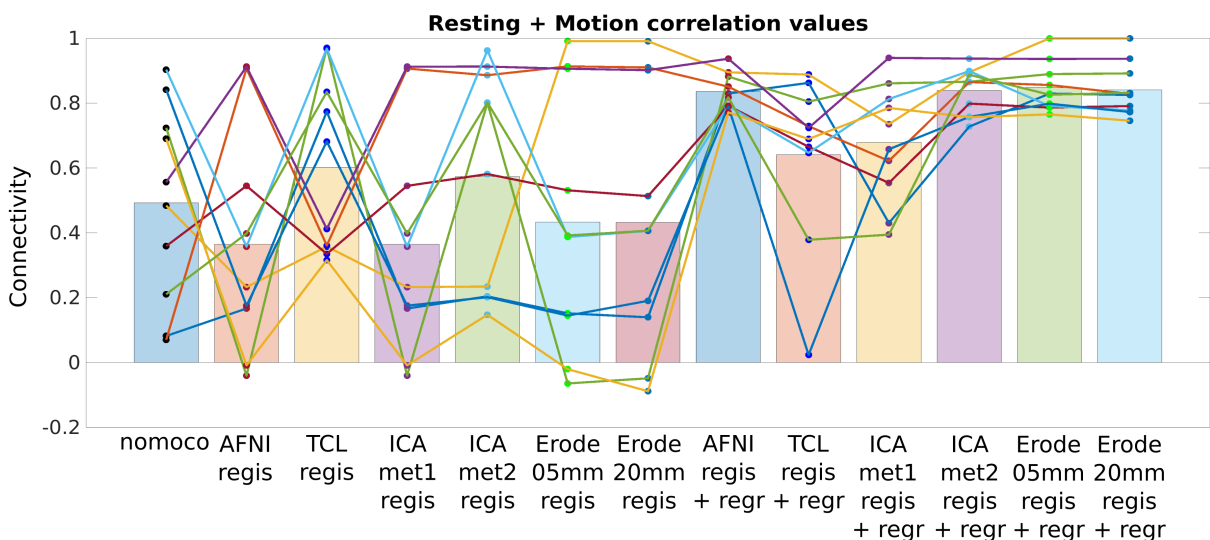


Fig. 3.15 Connectivity values generated from the *Rest+Motion* scan for each correction method. Each correction method is represented by a different coloured dot. Each line connecting the dots represents a different participant. The bars represent the average connectivity across participants for each method. The 'regis' terms represent registration and the 'regis+regr' represents registration and regression.

3.4.5.2 CBF Quantification

From Rest+ASLTag scans

Mean values of CBF across participants are displayed as a bar chart along with the values per participant (asterisks) in Figure 3.16. CBF values calculated from *registration only* methods were similar across all correction types with CBF values in the range 20 ml/100g/min to 80 ml/100g/min. Mean values for each *registration only* correction type were between 40.31 ml/100g/min and 41.68 ml/100g/min with standard deviations between 12.27 ml/100g/min and 13.26 ml/100g/min. A statistical difference was detected when comparing the VRA-based method with the Erosion 05mm method (p -value= 2.4×10^{-3}). Methods involving *registration + regression* showed a decrease in CBF value for most correction types. The camera-based and Erosion 20mm based methods showed an increase in mean CBF value but this was accompanied by an increase in standard deviation (camera: mean=67.24 ml/100g/min, stdev=29.60 ml/100g/min; Erosion 20mm: mean=45.00 ml/100g/min, stdev=38.93 ml/100g/min). Across participants, values for CBF stabilised for the ICA-based methods and spread variably for Erosion-based methods as explained by the high standard deviations detected for the Erosion methods (Erosion 05mm: mean=32.70 ml/100g/min, stdev=32.94 ml/100g/min). When compared to the VRA-based method, statistically significant differences were detected for no motion correction (p -value= 1.8×10^{-2}) and Erosion 05mm (p -value= 4.4×10^{-2}).

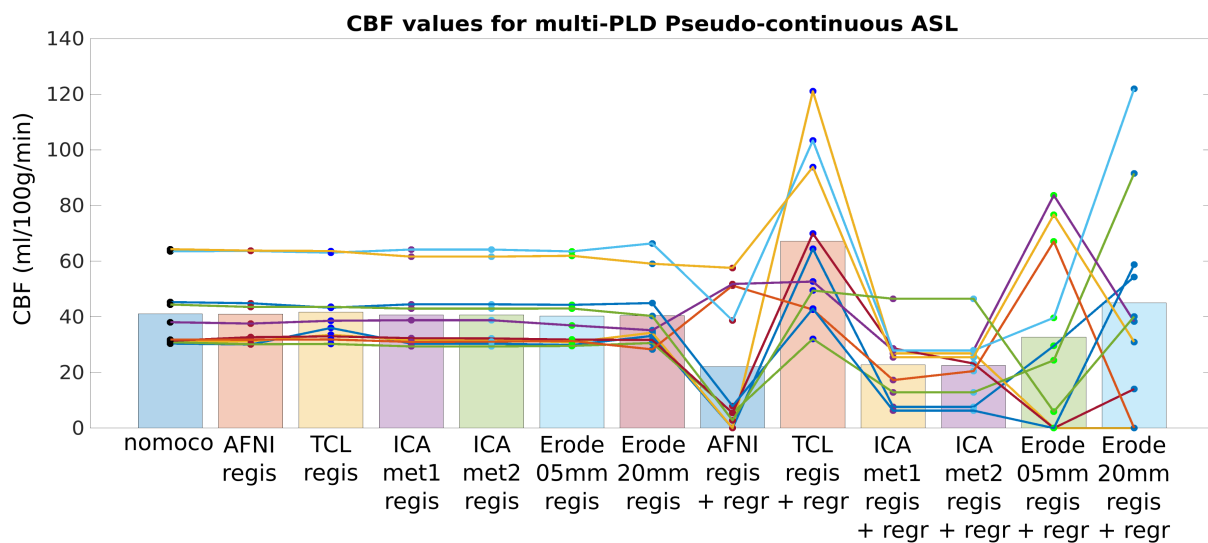


Fig. 3.16 CBF values generated from the *Rest+ASLTag* scan for each correction method. Each correction method is represented by a different coloured dot. Each line connecting the dots represents a different participant. The bars represent the average CBF across participants for each method. The 'regis' terms represent registration and the 'regis+regr' represents registration and regression.

From Rest+CO₂+ASLTag scans

Mean values of CBF across participants are displayed as a bar chart along with the values per participant (asterisks) in Figure 3.17. Values generated from *registration only* methods lie between 30-60 ml/100g/min and most involving *registration + regression* fall in the same range. The average value across participants for those involving *registration + regression* was slightly lower than those involving *registration only*. Values generated using the Erosion-

based methods involving *registration + regression* were much lower falling in the range 20-40 ml/100g/min (Erosion 05mm: mean=26.55 ml/100g/min, stdev=6.09 ml/100g/min; Erosion 20mm: mean=21.46 ml/100g/min, stdev=9.95 ml/100g/min). ICA-based methods generated higher values than the VRA-based method overall but had a greater variation (VRA: mean=34.31 ml/100g/min, stdev=4.44 ml/100g/min; ICA method 1: mean=38.75 ml/100g/min, stdev=13.22 ml/100g/min; ICA method 2: mean=38.27 ml/100g/min, stdev=12.53 ml/100g/min). When comparing the *registration only* VRA-based method to the other *registration only* methods, statistically significant differences were detected for no motion correction (p -value= 2.8×10^{-2}), ICA method 2 (p -value= 3.1×10^{-3}), Erosion 05mm (p -value= 5.1×10^{-3}) and Erosion 20mm (p -value= 2.0×10^{-4}). For the same comparison with *registration + regression* methods, statistically significant differences were detected for no motion correction (p -value= 7.8×10^{-3}), camera-based (p -value= 1.0×10^{-2}), Erosion 05mm (p -value= 1.7×10^{-3}) and Erosion 20mm (p -value= 5.9×10^{-3}).

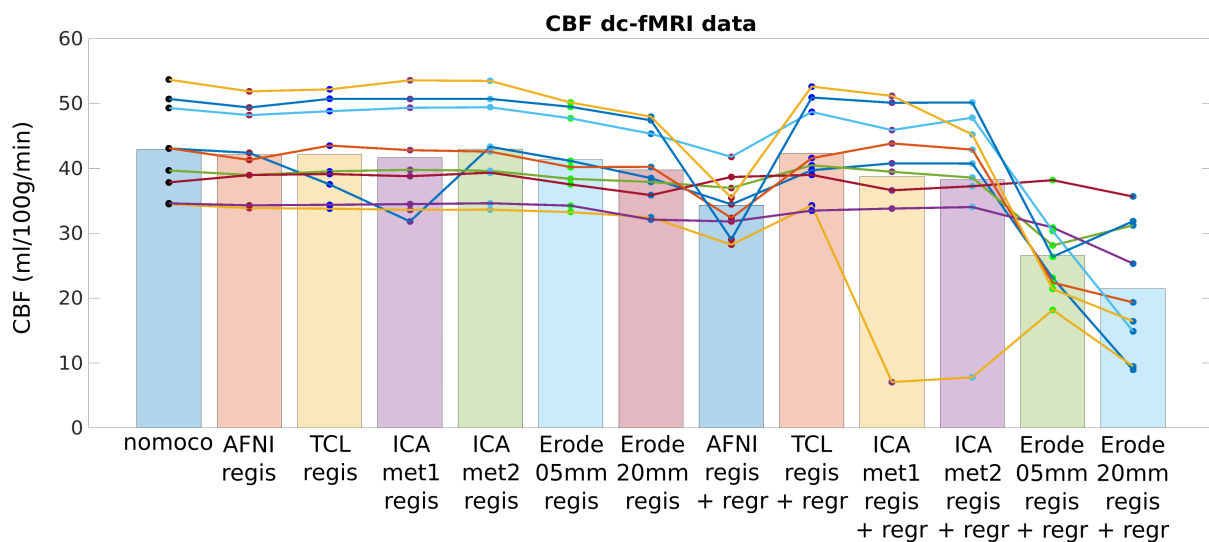


Fig. 3.17 CBF values generated from the *Rest+CO₂+ASLTag* scan for each correction method. Each correction method is represented by a different coloured dot. Each line connecting the dots represents a different participant. The bars represent the average CBF across participants for each method. The 'regis' terms represent registration and the 'regis+regr' represents registration and regression.

3.4.5.3 CVR Quantification

From Rest+CO₂ scans

Figure 3.18 shows the CVR values calculated for the *Rest+CO₂* scan. The mean value across participants is plotted as a bar for each method of correction. On the whole, values of CVR calculated using *registration only* methods were higher. A spread of CVR values is evident between participants ranging from 0.1 %BOLD/mmHg to 2.5 %BOLD/mmHg with the VRA-based *registration only* method displaying the most variable results (mean=1.19 %BOLD/mmHg,

stdev=0.78 %BOLD/mmHg). Calculated CVR values were lower when considering *registration + regression* although the ICA methods estimates were closer to that of *registration only* (ICA method 1 - *registration only*: mean=1.03 %BOLD/mmHg, stdev=0.60 %BOLD/mmHg; ICA method 1 - *registration + regression*: mean=0.79 %BOLD/mmHg, stdev=0.38 %BOLD/mmHg; ICA method 2 - *registration only*: mean=1.04 %BOLD/mmHg, stdev=0.62 %BOLD/mmHg; ICA method 2 - *registration + regression*: mean=0.80 %BOLD/mmHg, stdev=0.42 %BOLD/mmHg). Values of CVR were higher for ICA-based methods involving *registration + regression* in comparison to other methods containing *registration + regression* with p -values= 6.8×10^{-4} (ICA method 1) and 1.2×10^{-3} (ICA method 2) when compared to the VRA-based estimates. When compared to the *registration only* VRA-based methods, statistically significant differences were detected for no motion correction (p -value= 1.4×10^{-2}), camera-based (p -value= 4.7×10^{-2}), ICA method 1 (p -value= 3.3×10^{-2}), ICA method 2 (p -value= 4.0×10^{-2}), Erosion 05mm (p -value= 4.2×10^{-2}) and Erosion 20mm (p -value= 3.0×10^{-2}).

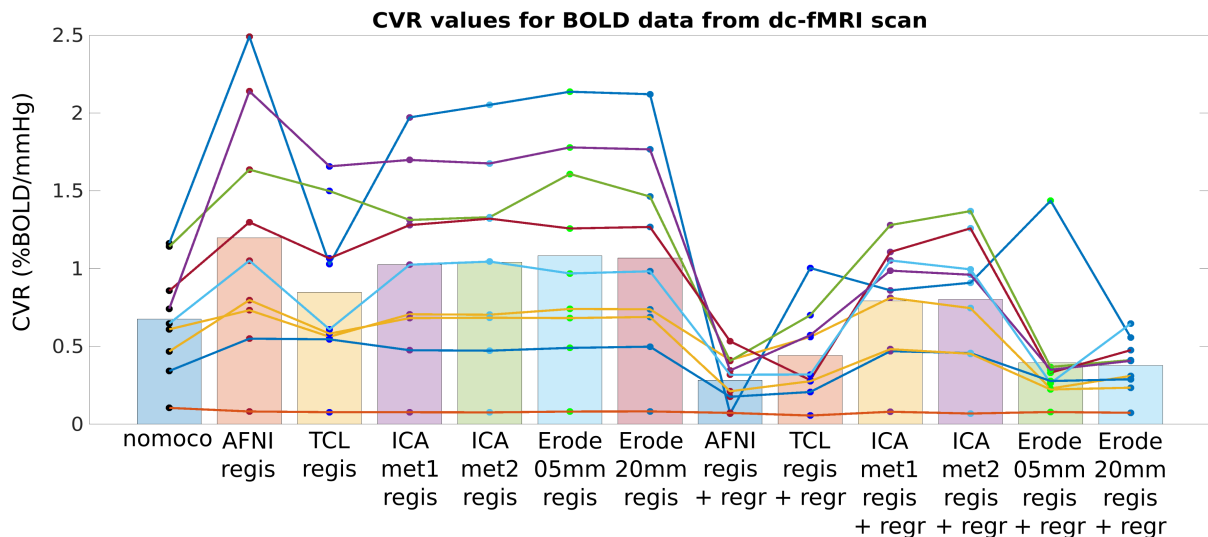


Fig. 3.18 CVR values generated from BOLD data acquired during the *Rest+CO₂* scan for each method of correction. Each correction method is represented by a different coloured dot. Each line connecting the dots represents a different participant. The bars represent the average CVR across participants for each method. The 'regis' terms represent registration and the 'regis+regr' represents registration and regression.

From *Rest+CO₂+ASLTag* scans

CVR values generated from the *Rest+CO₂+ASLTag* scan data are shown in Figure 3.19. Most values fall within the range 0.4-0.8 %BOLD/mmHg with an exception detected for the Erosion-based methods. There is no obvious difference in the average values for the methods using *registration only* and the methods using *registration + regression* and these values fell in the range 0.52-0.65 %BOLD/mmHg. No statistically significant differences were detected when comparing the VRA-based methods (*registration only* and *registration + regression*) with the other methods. A lot of variation was detected for the ICA method 2 and Erosion 05mm

methods considering *registration + regression* (ICA method 2: stdev=0.16 %BOLD/mmHg; Erosion 05mm: stdev=0.21 %BOLD/mmHg).

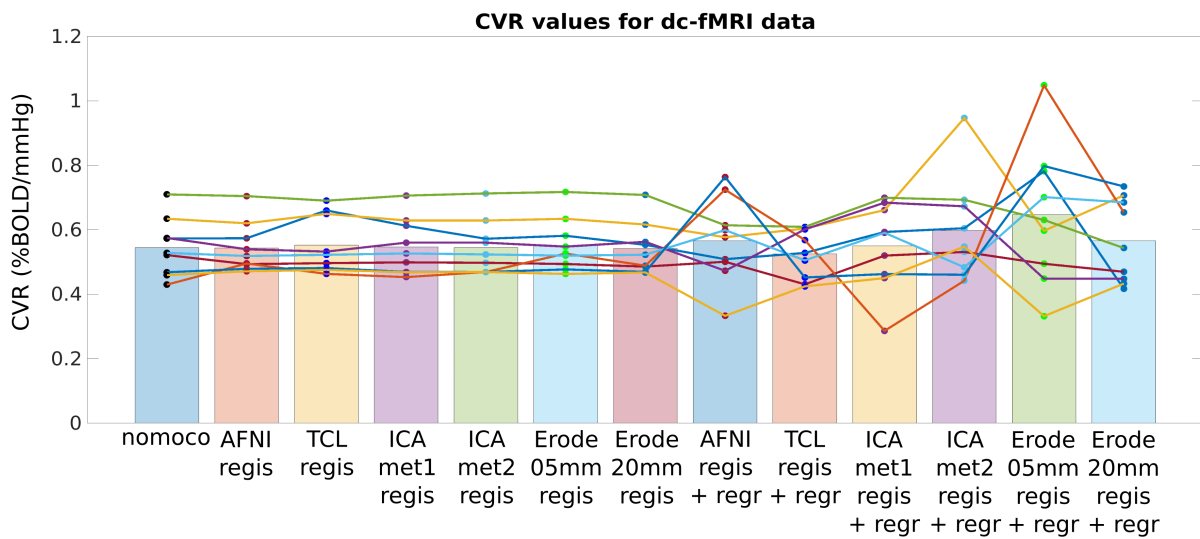


Fig. 3.19 CVR values generated from the *Rest+CO₂+ASLTag* scan for each method of correction. Each correction method is represented by a different coloured dot. Each line connecting the dots represents a different participant. The bars represent the average CVR across participants for each method. The 'regis' terms represent registration and the 'regis+regr' represents registration and regression.

From *Rest+CO₂+Motion* scans

CVR values generated from the *Rest+CO₂+Motion* scan data are shown in Figure 3.20. Most values lie within the range 0-0.8 %BOLD/mmHg with some outliers detected above this. In general, the values generated using *registration only* methods were higher than those that used *registration + regression* methods. ICA-based methods using both *registration + regression* showed values closer to that of the *registration only* methods which is similar to the *Rest+CO₂+ASLTag* results for CVR (ICA method 1 - *registration only*: mean=0.67 %BOLD/mmHg, stdev=0.35 %BOLD/mmHg; ICA method 1 - *registration + regression*: mean=0.46 %BOLD/mmHg, stdev=0.19 %BOLD/mmHg; ICA method 2 - *registration only*: mean=0.66 %BOLD/mmHg, stdev=0.33 %BOLD/mmHg; ICA method 2 - *registration + regression*: mean=0.45 %BOLD/mmHg, stdev=0.30 %BOLD/mmHg). When compared to the VRA-based estimate that considered *registration only*, the Erosion-based method that considered *registration only* was statistically different (p -value= 9.0×10^{-3}).

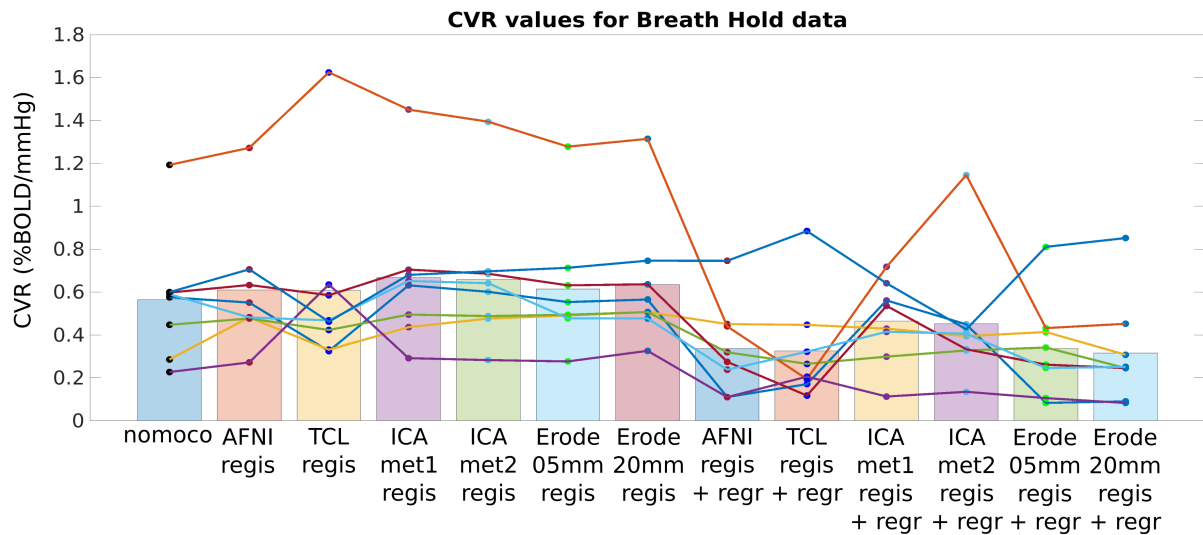


Fig. 3.20 CVR values generated from the *Rest+CO₂+Motion* scan data for each correction method. Each correction method is represented by a different coloured dot. Each line connecting the dots represents a different participant. The bars represent the average CVR across participants for each method. The 'regis' terms represent registration and the 'regis+regr' represents registration and regression.

3.4.5.4 CMRO₂ & OEF Quantification

Measures of CMRO₂ and OEF were generated using the CMRO₂ quantification pipeline.

CMRO₂

Figure 3.21 shows the CMRO₂ values calculated from the dc-fMRI data. The mean values across participants are plotted as bar plots for each correction type. Values generated using *registration only* gave higher values of CMRO₂ when compared with *registration + regression* methods. The two ICA-based methods considering *registration + regression* generated values falling between 140-180 $\mu\text{mol}/100\text{g}/\text{min}$ for most participants (ICA method 1: mean=142.68 $\mu\text{mol}/100\text{g}/\text{min}$, stdev=44.19 $\mu\text{mol}/100\text{g}/\text{min}$; ICA method 2: mean=142.12 $\mu\text{mol}/100\text{g}/\text{min}$, stdev=45.49 $\mu\text{mol}/100\text{g}/\text{min}$). The average value was lower due to two outliers with extremely low values of CMRO₂. For the VRA-based method, the average value per participant dropped below 120 $\mu\text{mol}/100\text{g}/\text{min}$ considering *registration + regression*. The Erosion-based methods that considered *registration + regression* generated values of CMRO₂ that were much lower than the VRA-based method (Erosion 05mm, $p\text{-value}=7.2 \times 10^{-3}$, Erosion 20mm, $p\text{-value}=2.5 \times 10^{-2}$) suggesting that the erosion of voxels may interfere with the quantification of CMRO₂.

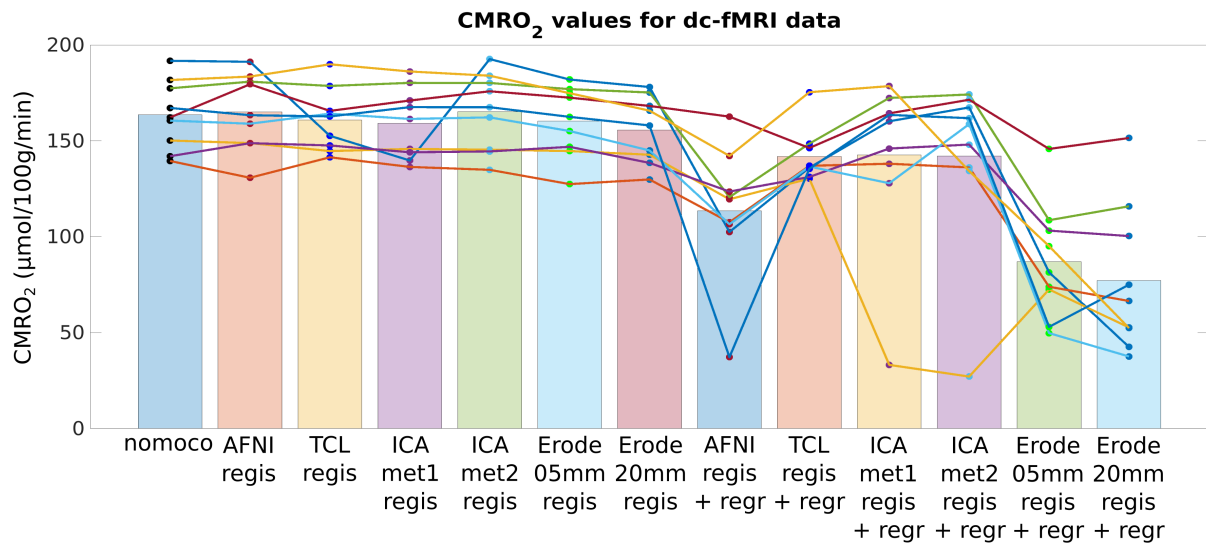


Fig. 3.21 $CMRO_2$ values generated from a dc-fMRI scan for each correction method. Each correction method is represented by a different coloured dot. Each line connecting the dots represents a different participant. The bars represent the average $CMRO_2$ across participants for each method. The 'regis' terms represent registration and the 'regis+regr' represents registration and regression.

OEF

Figure 3.22 shows the OEF values generated from a dc-fMRI scan. A drop in OEF value was observed for those methods considering *registration + regression* compared to those considering *registration only* and values generated from *registration only* were consistent across correction methods. ICA-based methods utilising *registration + regression* produced values closer to those generated using *registration only* than the other *registration + regression* methods (ICA method 1 - *registration only*: mean=159.15, stdev=18.34; ICA method 1 - *registration + regression*: mean=142.68, stdev=44.19; ICA method 2 - *registration only*: mean=165.23, stdev=19.99; ICA method 2 - *registration + regression*: mean=142.12, stdev=45.49).

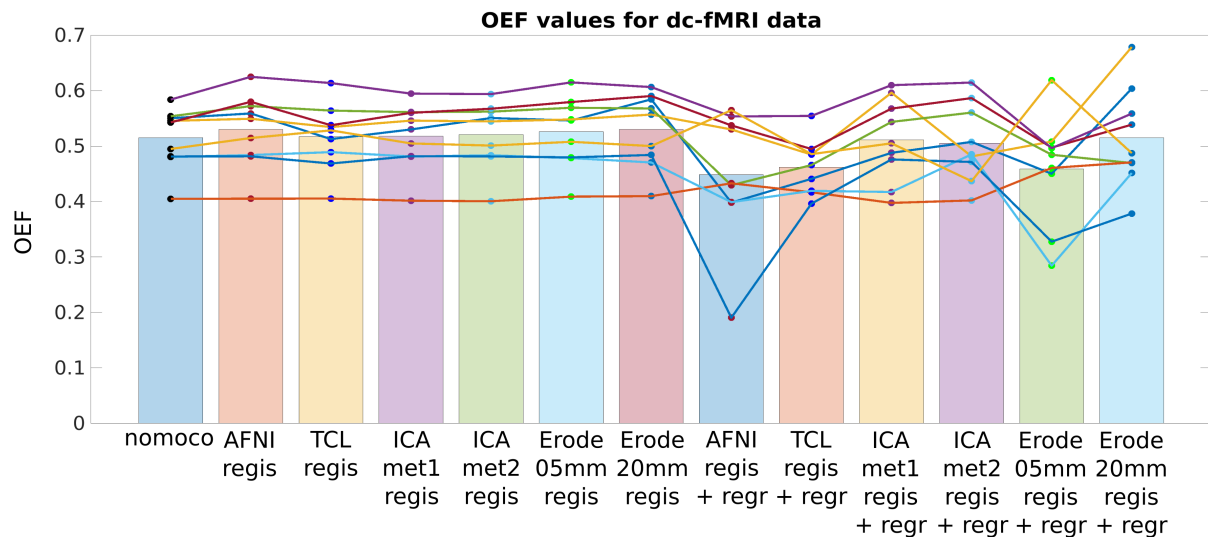


Fig. 3.22 OEF values generated from a dc-fMRI scan for each motion correction method. Each correction method is represented by a different coloured dot. Each line connecting the dots represents a different participant. The bars represent the average OEF across participants for each method. The 'regis' terms represent registration and the 'regis+regr' represents registration and regression.

3.5 Discussion

The results outlined here suggest that there is no one method of correction that works perfectly for every scan type explored. As such, the suggested method may be different depending on the desired analysis. The ICA-based methods outperformed both the camera-based and Erosion-based methods for most scan types with the strongest effect noticed in the *Rest+CO₂* scan. This scan type involved long periods of hypercapnia/hyperoxia and the CO₂ and O₂ traces were recorded for these. These traces would allow for a more accurate removal of the components within the ICA that were related to CO₂ and O₂. This would result in a more accurate estimation using the ICA-based method. This could explain why the ICA method outperformed both the camera-based and Erosion-based methods. However, one would expect a similar power detected for the *Rest+CO₂+ASLTag* scan if this was the reason. This expected result was not reflected in the data, however. The *Rest+CO₂+ASLTag* scan type included ASL tagging in addition to CO₂ which could have influenced the motion estimate and therefore explain the decrease in power.

3.5.1 Volume Registration Algorithm (VRA) based correction

The VRA-based methods resulted in relatively large values of R^2 as shown in Figures 3.11 and 3.12, especially for the *Rest+ASLTag* scan. This is significant as the R^2 values directly relate to the amount of motion that is present in the Global, GIC, or VRA-based motion parameters. Therefore, it is expected that higher R^2 values were related to a less accurate estimate of motion. Interestingly, the VRA-based method also showed relatively large R^2 values for the *RestOnly* and *Rest+Motion* scans. This result is strange as it's expected that there would be no misrepresentation

of signal as motion in scans that do not contain GICs (*RestOnly* and *Rest+Motion*). It could be the case that in these resting-state scans there was an increased amount of motion, or that accidental breath holds were present resulting in an unexpected GIC. Figure 3.12 suggests the CO_2 expired by the participant does cause a similar misrepresentation of the motion as the motion parameter estimates are similar to that of the expired CO_2 trace in some participants.

3.5.2 Camera-based correction

The camera-based methods showed large differences when compared to the VRA-based methods. This is expected as the camera is external to the scanner and estimates of motion would not be affected by the global changes induced by CO_2 or ASL tagging. This was especially noticeable for the *Rest+ASLTag* scan in Figures 3.11 and 3.12. Figure 3.12 shows that the main driver of this difference is the PLD-ramp. This is expected because longer PLD values translate to more of the tagged blood arriving at the target tissue. This would mean that the intensity change would be much larger as more signal is subtracted from the MR signal. However, when dealing with smaller motion, such as that seen within the *Rest+CO₂* and *Rest+CO₂+ASLTag* scans it seems that the camera-derived estimate overestimated the amount of motion. As a result, the registration datasets contained additional motion unrelated to the actual head motion. This was outlined in section 3.3.2.2. Therefore, the camera-derived estimates need to be treated with caution.

3.5.3 Independent Component Analysis (ICA) based correction

The ICA-based method shows less GIC variance than the other methods overall (Figure 3.12). They also shows less global signal within the motion parameters (Figure 3.11). These results suggest that there is less GIC information contained within the ICA-based estimation of motion. This is true in most scans that contained a GIC (*Rest+CO₂*, *Rest+CO₂+Motion*, *Rest+CO₂+ASLTag*), but was not true for those that did not contain a GIC (*RestOnly* and *Rest+Motion*).

The results from Figure 3.13 showed that the ICA-based estimates were similar to the VRA-based estimation for the scans that did not contain a GIC (*RestOnly* and *Rest+Motion*) which was expected. However, some participants did show lower R^2 values which could be a result of accidental breath holds from participants thus causing a GIC. For the scans that did contain a GIC (*Rest+CO₂*, *Rest+ASLTag*, *Rest+CO₂+Motion*, *Rest+CO₂+ASLTag*), the ICA-based estimates did show a difference in comparison with the VRA-based estimates. This shows that these methods are calculating different motion parameters to the VRA-based method. It was noted that the ICA method 2 showed R^2 values that were more similar to the VRA-based method than the estimates generated from ICA method 1. This was attributed to the Bonferroni correction restricting the number of components that were removed. The estimates generated for the *Rest+CO₂+Motion* had high R^2 values, especially for ICA method 2. In this scan type, the ICA method may not work as accurately due to the variation in CO_2 between participants.

The accuracy of the CO₂ trace would depend on how good the participant is at following the breath-hold challenge. Aside from this, the CO₂ trace is time-locked to motion and so the ICA would find it difficult to distinguish between motion and CO₂.

3.5.4 Erosion-based correction

Given that the Erosion-based estimates stayed consistent with the VRA-based estimate for most scan types one could draw the conclusion that erosion of edge voxels has little to no effect on the VRA-based algorithm. This, however, doesn't explain the differing results for the *Rest+ASLTag* scan type from Figure 3.11. Although a statistical difference was not found when comparing the Erosion-based methods to the VRA-based method, the spread in results for both Erosion-based methods is peculiar as all other results suggest that the Erosion-based methods should be similar to the VRA-based methods. The differences are further seen in Figure 3.12, especially for the scans that contained ASL Tagging (*Rest+ASLTag*, *Rest+CO₂+ASLTag*). Specifically focusing on the ASL Tagging, for *Rest+CO₂+ASLTag* a large difference can be seen between the VRA-based and Erosion-based 20mm methods ($p\text{-value}=3.4 \times 10^{-3}$). This suggests that ASL Tagging has a larger impact when performing a VRA with an eroded mask. As the erosion of the mask increases in size, the result seems to be more spurious across participants, resulting in an increase in R^2 . This implies that using a harsher mask does the opposite of what is expected and increases the amount of GIC present in the motion, even more so than the VRA-based estimate alone. Therefore, there may be more noise associated with the 20mm erosion masks as more voxels are eroded.

3.5.5 Quantification of Cerebrovascular Physiology

The Erosion-based methods fell short on most occasions (Figures 3.14, 3.15, 3.16, 3.17, 3.18, 3.19, 3.20, 3.21, 3.22), either agreeing with the VRA-based estimate or showing spurious results. This suggests that using a mask eroded at the edge voxels may corrupt the estimate of motion and lead to erroneous values of cerebrovascular function. Even though it was expected that excluding the areas where more issues lie (the edge voxels) would result in a better estimate of motion, it could be the case that too much (or too little) information is excluded resulting in inaccurate estimates. Additionally, the mask used may exclude the edge voxels for the initial volume, but as the volume registration progresses the edge voxels could be located at a different position in space. This is entirely possible and would therefore lead to erroneous results when the edge voxels are included in the estimation of motion. It would be desirable to allow this mask to move with the individual volumes to ensure that the edge voxels are always excluded. Doing so may improve the Erosion-based method of estimating motion. This could also explain why the Erosion-based method produces results that have a higher R^2 when looking at the regression of GICs and the global signal. The initial voxel would contain a low signal (without the signal in

those edge voxels) and the following voxels could contain a large signal as the edge voxels are now being included in the estimation, resulting in higher R^2 values.

All other methods showed a decrease in quantified value when using registration + regression (Figures 3.14, 3.15, 3.16, 3.17, 3.18, 3.19, 3.20, 3.21, 3.22), which is expected due to the removal of the motion-related signal (as well as the GIC related information in some cases). In almost all cases the ICA-based methods calculated quantified values which were greater than those calculated by the VRA-based method. This fits with the aforementioned results regarding the GIC information where there was seen to be less GIC information within the ICA-based motion estimates than for the VRA-based estimates.

3.5.5.1 Connectivity analysis

Values of connectivity varied across the different methods of correction with the values staying fairly consistent for the *RestOnly* scan type (Figure 3.14) but varying greatly for the *Rest+Motion* scan type (Figure 3.15). In the case of *Rest+Motion*, it seems that using both *registration + regression* improves the estimate of connectivity. It is important to note that asking participants to move deliberately during a BOLD scan is not a usual procedure and does lead to data that is difficult to draw conclusions from. As such these results need to be taken lightly. Such data was collected as a proof of concept to verify the accuracy of the camera-based estimate for large motion events.

3.5.5.2 CBF Quantification

A typical CBF value for healthy 20-year-old participants has been reported to be 58.1ml/100g/min and reduces every decade at a rate of 0.8ml/100g/min (Lu et al., 2011). As such a healthy range for the participants in this study would be between 50-60ml/100g/min.

From Rest+ASLTag scans

The CBF values stayed consistent across the motion correction methods that considered *registration only*. However, considering *registration + regression* caused a large variability in the CBF values. In the VRA-based, ICA-based and Erosion-based 05mm methods the values of CBF dropped when considering *registration + regression* indicating that a large amount of motion was removed in the regression stage. This was not the case for the camera-based and Erosion-based 20mm scans as the mean CBF increased. Values calculated for this scan type did not reach the expected value for this population group with most falling below 40ml/100g/min.

From Rest+CO₂+ASLTag scans

The average CBF values considering *registration only* were fairly consistent between the different motion correction methods. A drop in CBF value was detected for most methods considering *registration + regression* suggesting that the regression step is much harsher than the

registration only step (as expected). Both ICA methods were fairly consistent in the quantification when considering *registration + regression*. Only a minor drop in the average value of CBF was observed for ICA method 2. The Erosion-based methods showed a big drop in CBF value between the *registration only* and *registration + regression* steps. This is problematic as typical motion correction includes both registration and regression. The drop in CBF for the Erosion-based methods suggests that the inclusion of an eroded mask actually degrades the CBF signal. As the erosion should only be effecting the edge voxels of the brain it implies that more of the brain is being eroded than expected.

3.5.5.3 CVR Quantification

CVR measures the blood vessels ability to contract/dilate in response to an increase in demand of blood (Sleight et al., 2021). It is therefore an important metric for the measurement of cerebrovascular health.

From Rest+CO₂ scans

The VRA-based *registration only* method gave a value of CVR that was higher than most other *registration only* methods. A significant drop was seen for the camera-based *registration only* method. This is the opposite of what I hypothesised - the VRA-based method is expected to removed more signal than the camera-based method which should be reflected by a drop in CVR quantification. One explanation for this is due to the issues associated with the creation of the camera-based *registration only* datasets as these display more motion than expected (explained in depth in section 3.3.2.2). All other *registration only* methods displayed a drop in CVR value when compared to the VRA-based method, although these methods displayed similar CVR values. The opposite scenario can be seen in the *registration + regression* datasets, with the VRA-based estimation showing the lowest values of CVR. This follows the original hypothesis that more signal is removed in VRA-based methods. Additionally, this verifies that removal of signal occurs in the regression step of motion correction. Focussing only on the *registration + regression* results, the ICA-based methods show the highest values of CVR.

From Rest+CO₂+ASLTag scans

Estimated CVR values from the *registration only* methods showed similar CVR values to that of no correction. This further demonstrates that the registration step of motion correction has a very limited impact on the quantification of cerebrovascular measures. A small increase was observed in the *registration + regression* VRA-based mean estimate when compared to that of the *registration only* estimates. A similar increase was detected in the ICA-based and Erosion-based methods. Figure 3.19 shows a different trend to Figure 3.18 as the *registration + regression* step increases CVR value. This is reflected in Figure 3.11, which shows the amount of variance explained by the motion parameters on the global signal for the *Rest+CO₂+ASLTag* scan type. In this Figure, the novel motion correction estimation methods (camera-based, ICA-based and Erosion-based) displayed a similar amount of variance in the global signal to the VRA-based

method. Therefore, for this scan type, it is expected that the errors described in the hypothesis would have less of an impact.

From Rest+CO₂+Motion scans

For most participants, the estimated CVR value increased when comparing no correction to *registration only* correction. ICA-based methods showed the largest average CVR values amongst the *registration only* methods. Similarly to Figure 3.18, a drop in CVR values was seen when moving from *registration only* to *registration + regression*. This drop was smallest for the ICA-based methods. This follows the expectation that the regression step of motion correction will remove a larger amount of signal than the registration step.

3.5.5.4 CMRO₂ & OEF Quantification

A typical CMRO₂ value for a healthy 20-year-old participant is roughly 165 μmol/100g/min and is expected to decrease, with age, every decade at a rate of 2.6 μmol/100g/min (Lu et al., 2011). Thus a healthy range for CMRO₂ for the age range collected (19-32 years) would be 150-170 μmol/100g/min.

CMRO₂

Values of CMRO₂ calculated without motion correction and with *registration only* correction methods lead to similar estimations of CMRO₂. This implies that the use of registration does not affect the quantification of CMRO₂. With the addition of regression (*registration + regression*), a drop in estimated CMRO₂ was observed. This is expected as the removal of motion should affect the quantification of CMRO₂. The VRA and Erosion-based methods displayed the largest drop in estimated CMRO₂, whereas, the camera and ICA-based methods showed a smaller drop. None of the *registration + regression* methods fell within the expected CMRO₂ values for the group.

OEF

A similar trend was observed for OEF estimates as was seen for CMRO₂ estimates. The *registration only* estimates were similar to no correction and the *registration + regression* methods resulted in a drop in OEF estimation. As with CMRO₂, the ICA-based methods performed the best and only a small drop was observed between *registration only* and *registration + regression*.

3.6 Conclusion/Summary

Motion during functional imaging studies can lead to erroneous results if not dealt with correctly. Standard motion correction algorithms derive motion parameters from the data itself. These are

then used to realign individual volumes and to regress any related variance from the time series. Here, I demonstrate that although this might work well in a lot of cases, when global intensity changes (GICs) are an integral part of the experiment, this approach is prone to errors. The use of an ICA to remove signals related to the GIC resulted in motion parameters that explained less variance when regressed from the external influence on the GIC (as shown in Figure 3.12). However, this may not be enough and in some cases other methods should be incorporated to remove the GIC prior to correction of motion. For example, in multi-PLD ASL scans where a PLD-ramp drives a global signal increase, it may be better to use a temporal ICA. This is because the PLD is spatially uniform and spatial ICA may not be able to isolate the signal driving the GIC. However, at present, there are not enough time-points sampled in order to generate temporal components meaning temporal ICA is not a viable option. Additionally, the use of eroded masks in the estimation of motion is not accurate as the position of these edge voxels change with each voxel. A mask that moves with the volumes could work improve these methods and is a possible future direction for this work. Therefore, I recommend incorporating an ICA into the motion correction stage of any analysis pipeline for scans of cerebrovascular function. By avoiding the removal of variance related to imposed physiological changes caused by standard motion regression techniques, it is expected that cerebrovascular health measures will reflect the underlying physiology more accurately, however this cannot be tested without a gold standard measure.

Chapter 4

Data-driven methods for collecting cardiac information from functional MRI scans

4.1 Overview of the following two Chapters

For nearly three decades, resting state functional magnetic resonance imaging (rfMRI) has been widely used to study neural activity in the brain. Its prevalence is partly down to its ease of use as it requires no external stimulus or task, with participants only required to rest in the scanner while BOLD signals are collected. This makes it an easy experiment to setup and perform. In addition to evaluating neural activity, vascular processes can also be measured from rfMRI (Jahanian et al., 2016).

Microvasculature damage can lead to cognitive decline and dementia in an ageing population (Vikner et al., 2021). In a healthy person, the pulsatile flow generated by the contraction of the ventricles in the heart is dampened by the elastic properties of the larger arteries. As a result, the microvasculature is not subjected to high pulsatile pressure and flow (Climie et al., 2019). With increasing age, the stiffness of large arteries increases (Mitchell et al., 2004) and so these arteries may not dampen the pulse pressure as effectively. This leads to damage of the microvasculature and is thought to be particularly damaging to high flow organs such as the brain and kidneys (Mitchell, 2008). Investigating the extent of damage is therefore important to avoid the progression into cognitive decline and dementia. In MR, this is usually evaluated by measuring vasoreactivity of large intracranial vessels (Climie et al., 2019). A more direct measure of the processes that damage these vessels would be much more beneficial, however. Cardiac pulsatility is a measure of how pulsatile blood flow is in cerebral vessels in response to the pulsations of the heart. Excessive amounts of pulsatile flow can contribute to damage of the microvasculature leading to impaired function (Mitchell et al., 2011). Thus, the amount of pulsatile flow in the brain could be a vital indicator of the level of damage to microvasculature. For example, an increase in cardiac pulsatility has been observed in the brain in patients with Alzheimer's disease (Rivera-Rivera et al., 2017). Contributing factors in increased cardiac

pulsatility include hypertension and arterial stiffness. With age, the walls of systemic arteries lose elasticity resulting in an increase in vessel stiffness (Oh, 2018). Similarly, it is expected that arteries in the brain will become less elastic and stiffer with age. This would lead to a larger amount of pulsatile energy reaching the microvasculature. Other factors, such as BMI, bring about an increase in arterial stiffness (Kappus et al., 2014). Additionally, it has been suggested that an increase in mean arterial pressure (MAP) directly relates to a functional increase in arterial stiffening (Cecelja and Chowienczyk, 2010).

In rfMRI experiments, when interested in neural processes, it is important to remove effects of physiological noise. The BOLD signal is noisy and contains information related to fluctuations from physiological sources in addition to neural activity and vascular effects. Such physiological sources include cardiac-related information, respiratory information, changes in arterial CO₂ concentration, vasomotion, cerebral autoregulation and blood flow information (Murphy et al., 2013). The majority of physiological noise arises from cardiac-related noise and respiratory sources which account for around one sixth of the total signal (Bianciardi et al., 2009). Head motion also accounts for a large amount of the total signal. When combined with cardiac and respiratory noise, this can account for around 50% of the total signal (Bianciardi et al., 2009). Many studies use external physiological recordings to record cardiac and respiratory information. The former is usually recorded using a photoplethysmograph (PPG) and the latter with a respiratory bellows or nasal cannula (or mask that can record end-tidal oxygen and CO₂). These recordings are then used to separate the signal of interest (usually neuronal in origin) from the physiological noise. However, it is possible to separate any signal of interest from the ‘noise’. For example, good quality physiological recordings (and good quality recording equipment) would be required to separate cardiac-related signal from non-cardiac-related signal (Salimi-Khorshidi et al., 2014). Some data-based approaches make use of an independent component analysis (ICA) (Beckmann and Smith, 2004) to separate an rfMRI timeseries into individual components (ICs). These ICs can include components that represent various noise sources (Murphy et al., 2013). Nuisance components can then be isolated and removed from individual voxel timeseries resulting in a dataset corrected for physiological noise. This can be achieved using FMRIB’s ICA-based Xnoisifier (FIX) which is part of the FSL software package (Griffanti et al., 2014; Salimi-Khorshidi et al., 2014). FIX is an automated process that utilises ICA analysis to classify ICA components into ‘good’ and ‘bad’ components. FIX needs to be trained before it can be used to classify components. The training dataset used to train FIX is comprised of a list of ICA components that have been determined to be ‘bad’ ICA components. The components that make up the training dataset can be hand-labelled by an expert (Griffanti et al., 2017), or through an automated process. Typically, neuronal signals are labelled as ‘good’ components and all other signals are labelled as ‘bad’ components.

In the following two chapters methods to quantify cardiac pulsatility were developed. These methods make use of rfMRI data derived from the Human Connectome Project (HCP) S1200 release (Glasser et al., 2013; Van Essen et al., 2013). In Chapter 4 (this chapter) I describe the

methods I initially thought would work but did not and outline their shortcomings. Throughout the chapter the methods described build upon the previous method in some way. The final method outlined in this chapter was flawed but is improved in Chapter 5 and the results it produces are promising.

Therefore, an easy way to think of the chapter structure is Chapter 4 contains the failed methods and their reasons for failing, and Chapter 5 contains the successful methods which were derived from those in Chapter 4.

4.2 Chapter 4

4.2.1 Introduction

In this chapter, three novel methods of isolating ICA components related to the cardiac-cycle from rfMRI data are introduced. These methods were fundamentally flawed, however, and these flaws are explained throughout. During the development of these methods I learnt from these flaws and the subsequent method tried to overcome them. The final method introduced (section 4.3.8) is further built upon in Chapter 5. The novel methods work in the frequency domain and aim to determine the frequency range within which the cardiac-related information will be. Aside from introducing the novel methods, three different methods to calculate pulsatility from the cardiac-related signal were introduced and compared with each other.

4.3 Methods

4.3.1 HCP data

Data used in this study were collected by the WI-Minn Human Connectome Project in their Young Adult (22-35 years) S1200 release (Glasser et al., 2013; Van Essen et al., 2013). Over two days, participants were scanned using four different modalities: structural MRI, functional MRI, task MRI and diffusion MRI (Van Essen et al., 2013). As part of the functional session, four 15-minute resting state (rfMRI) scans were collected on a Siemens 3T ‘Connectome Skyra’ scanner with a 32-channel receive head coil. On each day, the two rfMRI scans were collected with a different phase encode direction (PE), one with a left-right (LR) PE and the other with a right-left (RL) PE. The rfMRI acquisition used a spatial resolution of 2 mm isotropic voxels (72 slices) and a TR of 0.72 s (Glasser et al., 2013; Van Essen et al., 2013). Other sequence parameters included: TE=720 ms, Flip angle=52°, FOV=208x180 mm, Matrix size=104x90. The structural session collected T1 weighted and T2 weighted images with a spatial resolution of 0.7 mm isotropic voxels (Glasser et al., 2013; Van Essen et al., 2013). For the T1w acquisition, the MR sequence parameters were as follows: TR=2400 ms, TE=2.14 ms, TI=1000 ms, Flip angle=8° and FOV=224x224 mm. The T2w MR sequence parameters were: TR=3200 ms,

TE=565 ms, Flip angle=variable and a FOV=224x224. The task and diffusion sessions were not important for this study and so will not be discussed here. Physiological monitoring was used to collect cardiac and respiratory signals for each scan using a Siemens pulse oximeter and a respiratory belt. Head motion information was collected in most scan sessions using an optical tracking camera system (Van Essen et al., 2013).

4.3.2 Processing of rfMRI Data

These pre-processing steps were carried out by the HCP and are detailed in (Glasser et al., 2013) and (Smith et al., 2013). Here, I will briefly describe the steps performed. The pipeline used, fMRIVolume (the name of the HCP pipeline), initially performed gradient-nonlinearity-induced distortion correction to reduce gradient-nonlinearity. The next step was to perform motion correction using rigid body motion registration with 6 degrees of freedom (DOF). Next, EPI image distortion correction was performed to reduce distortion in the PE direction. Finally, a non-linear registration was used to register images to MNI space. Following these pre-processing steps, rfMRI data was high pass filtered at 0.00072 Hz (a cutoff of 2000s (Smith et al., 2013)). No low-pass filtering was applied as useful neuronal signal could be present up to 0.2Hz. In total 4123 individual rfMRI datasets were analysed in this study.

4.3.3 Processing of Structural T1w Data

The processing of structural T1W data was performed by the HCP and is detailed in (Glasser et al., 2013). Here I will briefly described these steps. Structural information was pre-processed in three stages, PreFreeSurfer, FreeSurfer and PostFreeSurfer. The initial PreFreeSurfer stage included gradient-nonlinearity-induced distortion correction, alignment of repeated runs with 6-DOF rigid-body registration and averaged across repeated runs, alignment to MNI space using rigid-body 6-DOF transformation, brain extraction, readout distortion correction, boundary-based registration (BBR) of T2w to T1w, bias-field correction and registration to MNI space. The second FreeSurfer stage included downsampling of T1w images to 1 mm isotropic (using spline interpolation), FreeSurfer recon-all (stopping when white matter surfaces are generated), high resolution white matter surface generation from 0.7 mm resolution T1w image, a continuation of FreeSurfer recon-all with new white matter surfaces (stopping when Pial surfaces generated), generation of Pial surfaces from PreFreeSurfer T1w images and a continuation of FreeSurfer recon-all with new Pial surfaces. The generated Pial and white matter surfaces were used to define a grey matter (GM) ribbon as the GM voxels lie between the two surfaces. The final stage (PostFreeSurfer) included the conversion of outputs from FreeSurfer stage to standard NIFTI and GIFTI formats, generation of a final brain mask, generation of a cortical ribbon volume, generation of cortical myelin maps, normalisation of myelin maps to Conte69 group average and generation of a native surface mesh in native and MNI volume space. The structural data was used in this study to generate brain masks.

4.3.4 Processing of ICA components

The processing of ICA components was performed by (Smith et al., 2013) and is explained in detail in their paper. Here I will briefly summarise the processing steps they took. The pre-processed rfMRI data were passed through FSL's MELODIC (Beckmann and Smith, 2004) which uses an ICA to decompose datasets into different spatial and temporal components. ICA is explained in detail in Chapter 2 - Section 2.6.3. Automatic dimensionality estimation was used as this allows MELODIC to choose the optimal number of components to separate. The maximum number of components was restricted to 250.

4.3.5 Generation of Brain Masks

I generated GM masks for each participant from a GM ribbon created as part of the FreeSurfer processing stage of the structural T1w data outlined in the section 4.3.3.

4.3.6 Processing of Cardiac Data

Heart rate variability (HRV) traces were used to verify the accuracy of some of the methods introduced in this chapter. The processing performed to generate these traces is outlined in depth by (Kassinopoulos and Mitsis, 2020) but will be summarised briefly here. The PPG signal for each participant was band-pass filtered with a 2nd order Butterworth filter between 0.3 and 10 Hz. A heart rate (HR) signal was calculated (in BPM) by multiplying the inverse of the time differences between pairs of adjacent peaks by 60. This was resampled at 10 Hz (Kassinopoulos and Mitsis, 2020). This gave HRV traces for each participant.

4.3.7 Frequency Method 60-100 BPM & 50-100 BPM

These methods were the first to be attempted during this study. The underlying idea behind these methods was to identify where in the frequency domain cardiac cycles would occur. Typically, they occur at frequencies of ~ 1 Hz at rest (Murphy et al., 2013) but this frequency is dependent on the HR of the participant in question. In an ideal world, the average resting HR for each participant would be used to determine this. However, this was not available in the HCP data and therefore rough estimates had to be made. A 'window' of frequencies within which the cardiac frequency was expected to lie was defined and this will be referred to as the cardiac window. Assuming that the average resting HR for healthy adults was in the range 60-100 BPM would mean that the frequency window would lie between the values of 0.6 Hz and 1.00 Hz. The power of the signal in this window was determined by normalising each melodic FT component and calculating the mean average value within the cardiac window for each component. Components with a mean value (across their cardiac window) greater than 2.5 standard deviations from the mean of all values were determined to be cardiac-related components. This test was performed

as components with a significant amount of signal in the cardiac window would show as outliers in the test.

Initial results from this classification method showed a large number of cardiac-related components, suggesting the method was too lenient in its classification. A second concern was the definition of the cardiac window. The lower value used for the resting HR of the population (60 BPM) may have been too high and so the lower bound was changed to 50 BPM for the second attempt to capture those participants with a resting HR lower than 60BPM. However, this didn't have any affect on the leniency of the classifier in its classification.

When deciding on the frequency range to use, issues due to aliasing were ignored and it is clear now that they should have been considered. The TR of rfMRI data collected by the HCP was 0.72 s. The sampling frequency was determined by taking the inverse of the TR. This was calculated to be 1.389 Hz. Using equation 4.1 (Viessmann et al., 2019) the aliased frequency can be determined. In this equation, f_{true} represents the true frequency, f_{alias} represents the aliased frequency, f_s represents the sampling frequency and n represents the harmonic number. For a lower HR of 60 BPM, this equation states that the cardiac cycle would occur at ~ 0.398 Hz (and not 1 Hz as originally expected). Therefore, a method to isolate the cardiac-related information using average resting HR estimates will not work for this data and a new method which encompasses more of the frequency spectrum was required.

$$|f_{alias}| = f_{true} - n \cdot f_s \quad (4.1)$$

4.3.8 Frequency Method 100-400 Samples

As explained in the previous section, a method that encompasses more of the frequency spectrum would be needed to achieve the goals of this study. Therefore, the next iteration of the classification algorithm expanded the bounds of the cardiac window in an attempt to overcome any aliasing.

4.3.8.1 Definition of the Cardiac Window

To remove the influence of any neural related frequency fluctuations (Zou et al., 2008), the lower bound of this window was defined to be 0.11 Hz (or 100 frequency bins, based on the sampling rate of 1.389 Hz). This was because, typically, low-frequency fluctuations are found below 0.1 Hz. A large erroneous frequency peak was previously detected at around 0.55 Hz and was revealed to be an artefact by Power and colleagues (Power et al., 2019). To avoid this peak, the value of the upper bound was chosen to be less than 0.55 Hz. Assuming a resting HR of 110 BPM (1.83 Hz) is the maximum HR for all participants, the aliased frequency for this maximum HR is calculated to be ~ 0.440 Hz using 4.1. Then rounding this up to make the number of frequency samples a whole number would make the upper bound of this window 0.46 Hz (or 400 frequency bins).

The classification of components into cardiac or non-cardiac was completed in three stages. Each stage is outlined here and graphically represented in Figure 4.1. At each stage, the independent components (from the ICA decomposition) were assessed to determine if they were related to the cardiac cycle.

4.3.8.2 Stage One of Classification

The aim of the first stage of the classification was to determine which independent components were outliers as these were believed to be representative of cardiac components. Each component was considered separately for this step. First, the frequency data of each component was normalised by dividing by its mean. Then, the cardiac window was subdivided into smaller, sliding windows, each with a width of 0.1171Hz (equivalent to 101 frequency bins), moving in steps of 0.0058Hz (or 5 frequency bins). Within each window, the mean of the frequency data was calculated for each component. This will be referred to as the `componentMean`. This process resulted in an array containing the `componentMean` for each sliding window. Then, for each window, the average of these `componentMeans` across all components was computed. This will be referred to as the `windowMean`. A component was identified as an outlier if its `componentMean` exceeded the `windowMean` by more than 2.5 standard deviations. Components were considered preliminary cardiac components if they were an outlier in any of the windows. Components that were considered outliers in multiple windows were not treated differently to those that were outliers in only one window. The preliminary cardiac components were moved onto the second stage of classification. The components that did not meet this criterion were considered as noise.

4.3.8.3 Stage Two of Classification

The second stage of classification involved fitting a two-term Gaussian curve to the individual component frequency data within the cardiac window. A two-term Gaussian fit was used because this seemed to be the most appropriate fit when inspecting the data. Initially, the frequency data within the cardiac window was smoothed using a first order Savitzky-Golay filter with a frame length of 9. The two-term Gaussian curve was fit to the data within the cardiac window only and, as a result, only 301 points were fit. The R^2 value for each Gaussian fit was calculated and those with an R^2 greater than 0.9 were considered to be preliminary cardiac components and moved to the third and final stage of classification. The components that did not pass this stage were considered to be noise.

4.3.8.4 Stage Three of Classification

The third and final stage of classification aimed to remove erroneous Gaussian fits in order to classify more accurately. The first step was to determine which term from the two-term Gaussian fit had fit the peak of the data. This was achieved by calculating the value of the frequency

peak for each term of the Gaussian fit (for each component) and the largest absolute value was chosen to be the peak related to the cardiac cycle. This will be referred to as the cardiac peak. For all components that passed the first two stages, the median value across the cardiac peaks was calculated. From this, a median window defined as the median value ± 100 samples was generated. The cardiac peaks that were within this median window were then determined to be cardiac components. The components that did not pass all three stages were considered to be noise.

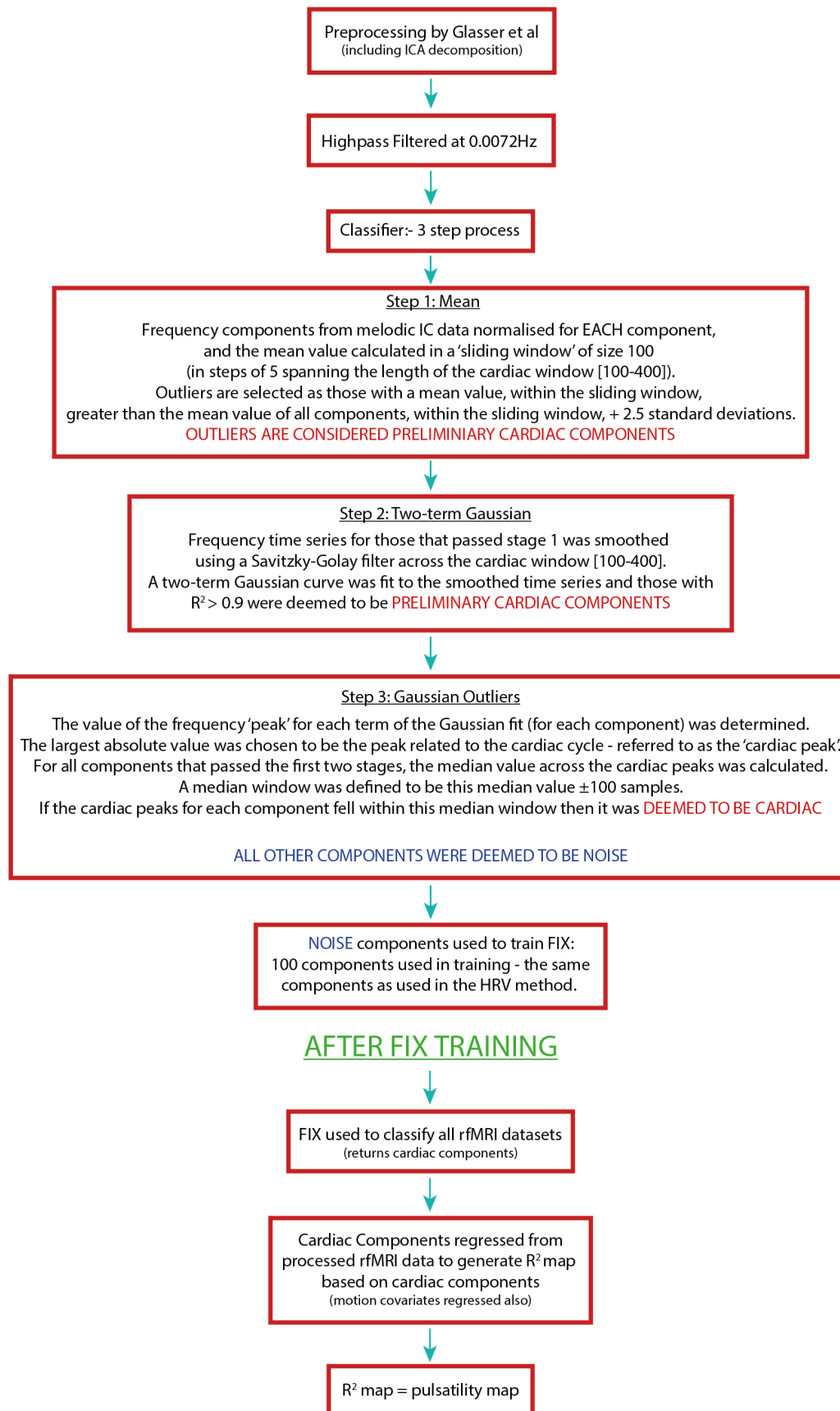


Fig. 4.1 Schematic diagram detailing the classification steps used in the 100-400 samples classifier. These steps included: Preprocessing, Mean calculation, Two-term Gaussian fitting, Gaussian Outlier estimation, Training of FIX and generation of pulsatility maps.

4.3.8.5 Calculation of Heart Rates

Calculation of HR values for each rfMRI scan was possible using the 100-400 classification method. By isolating the frequency peak for each term of the two-term Gaussian curve for each component, it was possible to determine an aliased frequency. Working backwards using equation 4.2 (Viessmann et al., 2019), a rearranged version of equation 4.1, the true frequency could be calculated and converted into a HR. Equation 4.2 results in two discrete values and therefore two HR values per component. These values were then averaged across components, resulting in two values per run. Then, the values for HR₁ and HR₂ were averaged across runs to get values of HR₁ and HR₂ for each participant.

$$f_{true} = \pm f_{alias} + n \cdot f_s \quad (4.2)$$

4.3.8.6 Regression Method

Linear regression was used to calculate pulsatility. AFNI's 3dDeconvolve (Cox, 1996; Cox and Hyde, 1997), a program that is capable of performing multiple linear regression, was used with each associated cardiac component input as a regressor in the model. Additionally, motion parameter estimates provided by the HCP were used in this model as a means of further reducing the effects of motion. The R^2 variance statistic was calculated from this regression and a map of R^2 was created. For this case, the definition of pulsatility is the variance explained by the cardiac components on the high pass data and as a result, the R^2 maps are synonymous with pulsatility.

4.3.8.7 Fast Fourier Transform (FFT) Method

An FFT was used to generate frequency information pertaining to the rfMRI data. A metric named the fractional amplitude of cardiac frequency fluctuations (fACFF) was calculated for each rfMRI scan. This metric is similar to the fractional amplitude of low-frequency fluctuations (fALFF) documented by (Zou et al., 2008). The fALFF metric is the ratio of the power in the low frequency range (0.1-0.8 Hz) to the power in the whole frequency range. Similarly, the fACFF is the ratio of the power in the cardiac frequency range to that of the whole frequency range. The cardiac frequency range was determined by defining a 'bespoke' cardiac window for each rfMRI scan. This was defined to be the mean value across the cardiac peaks ± 0.083 Hz (5 BPM). This resulted in a 0.16 Hz (10 BPM) bespoke cardiac window and this window was used to calculate fACFF. This bespoke cardiac window will be referred to as the bespoke window elsewhere in this work. The power within the bespoke window (or the amplitude of cardiac frequency fluctuations (ACFF)) was calculated by taking the square root of the power spectrum at each frequency and then averaging across the frequency window. The equation used to generate fACFF is shown in equation 4.3. This method differed from the Regression method as it didn't use the ICA components generated from the classification algorithm and instead used the bespoke windows that the algorithm produced.

$$fACFF = \frac{ACFF_{Cardiac}}{ACFF_{Whole}} \quad (4.3)$$

4.3.8.8 Bandpass Method

Bandpass regressors were generated across the ‘bespoke’ cardiac window (that was generated in section 4.3.8.7) using AFNI’s 1dBport (Cox, 1996; Cox and Hyde, 1997). This is a program designed to generate regressors that filter out frequency components within a bandpass range. The regressors were used in a linear regression (using 3dDeconvolve) to perform the bandpass filtering and calculate R^2 values per run. For this method, the definition of pulsatility is the variance explained by the bandpass regressors on the high passed data and therefore the R^2 values are directly related to pulsatility. This method differed from the Regression method as it didn’t use the ICA components generated from the classification algorithm and instead used the bespoke windows that the algorithm produced.

4.3.9 Generation of Pulsatility

Isolating the components that contained cardiac information was a useful step in the calculation of cardiac pulsatility in the microvasculature. However, knowing which components contained cardiac information is not a direct reflection of pulsatility. Sections 4.3.8.6, 4.3.8.8 & 4.3.8.7 outline the methods that were used to generate pulsatility maps. GM masks were used along with the pulsatility maps to calculate GM pulsatility values in each rfMRI scan. The median value across each participant’s repeated rfMRI scans was taken to get a value of pulsatility per participant. Pulsatility was calculated for 200 participants only to determine the accuracy of each method.

4.3.10 Correlation with physiological measures

A correlation analysis between GM median pulsatility and age, BMI, Mean Arterial Pressure (MAP), Brain Volume (BV), haematocrit and Framewise Displacement (FD) was performed. These parameters were chosen for various reasons. Age, BMI and MAP are related to arterial stiffness and so it is expected that there will be significant correlations between pulsatility and these parameters. Haematocrit and BV were chosen as they influence BOLD signal amplitudes and so should be reflected in pulsatility measures. FD was chosen as a control variable to ensure that motion correction worked as expected. MAP was calculated using equation 4.4 (Sainas, et al., 2016) where SYS is the mean systolic blood pressure and DIA is the mean diastolic blood pressure.

$$MAP = \frac{SYS + 2 \cdot DIA}{3} \quad (4.4)$$

To evaluate the statistical significance of each correlation, a statistical permutation analysis was performed. This analysis initially calculated the correlation value of the GM median pulsatility against the physiological parameter of interest. Then, the index order of the physiological vector was randomly changed and the correlation value between the GM median pulsatility and the new physiological vector was calculated. This was repeated for 10,000,000 iterations with each iteration randomly changing the index order of the physiological vector. The p-value was determined by equation 4.5, where n is the number of random correlations calculated, $corr_{rand}$ is the correlation value from the random permutation and $corr_{true}$ is the actual correlation value.

$$p - value = \frac{\sum(corr_{rand} > corr_{true})}{n} \quad (4.5)$$

4.4 Results

4.4.0.1 Classification of Components

A total of 1088 participants were classified using the 100-400 window method, with an average of 10.25 ± 4.87 classified components per participant. Figure 4.2 shows the second stage of this classification where a two-term Gaussian curve was plotted with the data and peak values were acquired. A) Displays all the components that passed stage 1 of classification and highlights the need for an accurate Gaussian plot. Some of the components that passed stage 1 show a low magnitude signal which does not represent the cardiac peak as expected. B) shows the same graph after the second classification stage. All the non-cardiac related signal has been removed, leaving the components containing signal related to cardiac fluctuations only.

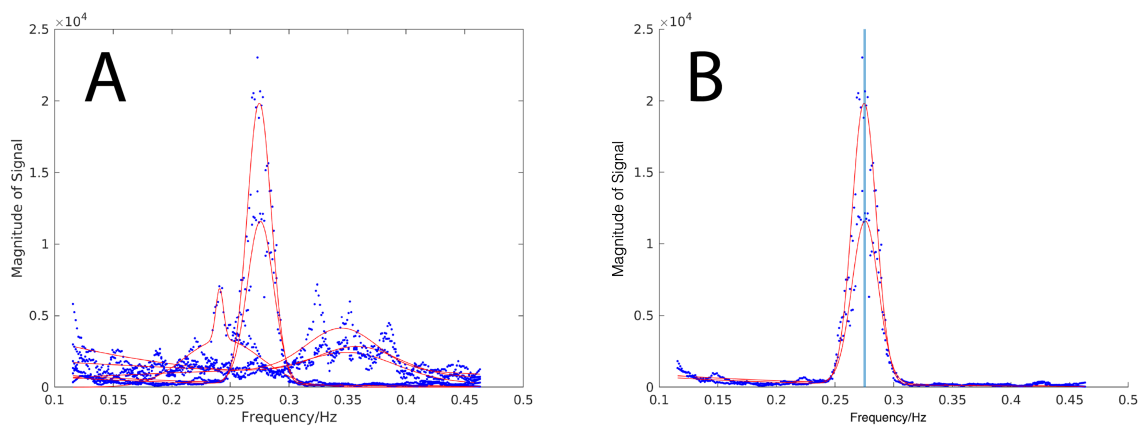


Fig. 4.2 Stage two in classification of cardiac components. A) All components surviving stage one of classification with a two-term Gaussian curve plotted. B) Two-term Gaussian curve plotted to components after noise is removed.

The components surviving all three classification steps were considered cardiac components. An example of this is shown in Figure 4.3.

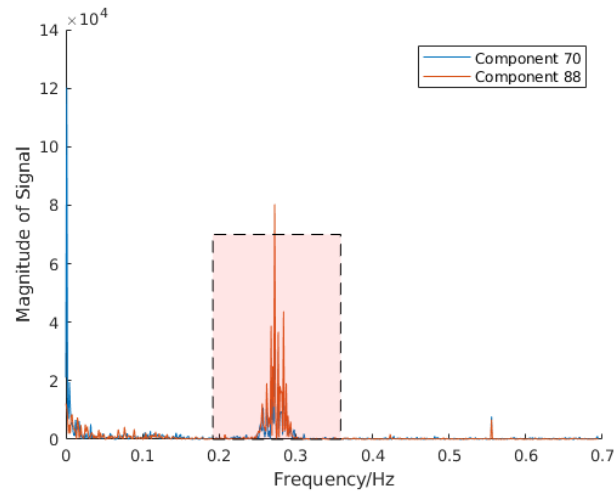


Fig. 4.3 Frequency plot of components surviving all three steps of classification the shaded area represents the bespoke cardiac window for this rfMRI scan.

4.4.0.2 Calculation of Heart Rates

Two HR values were calculated per participant. The mean value across all participants for HR₁ was 66.3 BPM while for HR₂ it was 100.32 BPM. In Figure 4.4, A) and B) are histograms of HR₁ and HR₂ respectively. Both HR values follow a normal distribution. C) shows the HR values on one graph.

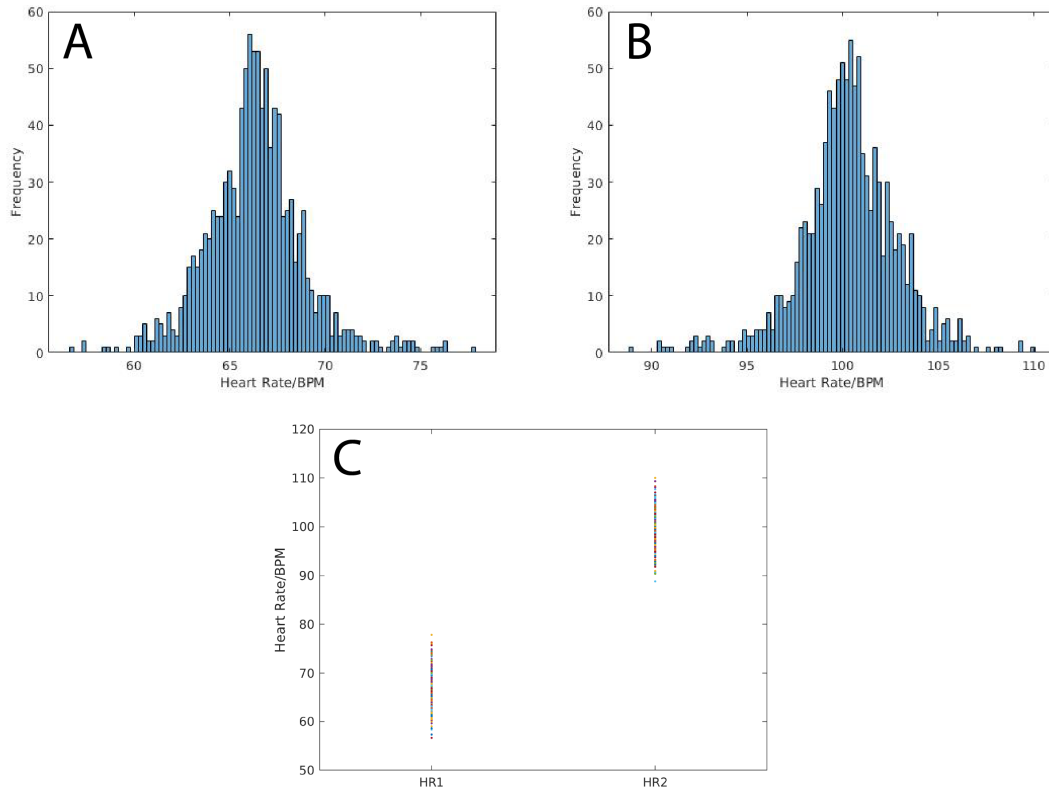


Fig. 4.4 A) Histogram showing the distribution of HR values for HR₁. B) Histogram showing the distribution of HR values in HR₂. C) HR₁ and HR₂ values plotted on one graph.

4.4.0.3 Verification of Classification

Of the 4123 rfMRI scans that were collected by the HCP, 1588 had high-quality physiological data associated with them. Calculation of HR was achieved by taking the average across the HR trace contained within the physiological data. Plots of actual HR and HR calculated from the classification script are shown in Figure 4.5. The estimation of HR values fell short around 80-90 BPM (1.333-1.500 Hz - near the sampling frequency (1.389 Hz)) and 40-50 BPM (0.667-0.833 Hz - near the Nyquist frequency (0.694 Hz)) as shown in Figure 4.5 A) and B). This suggests that the algorithm is not accurate for participants who have a HR around the sampling or Nyquist frequencies and so a new method of classification would be required to accurately classify participants with HR values near these frequencies.

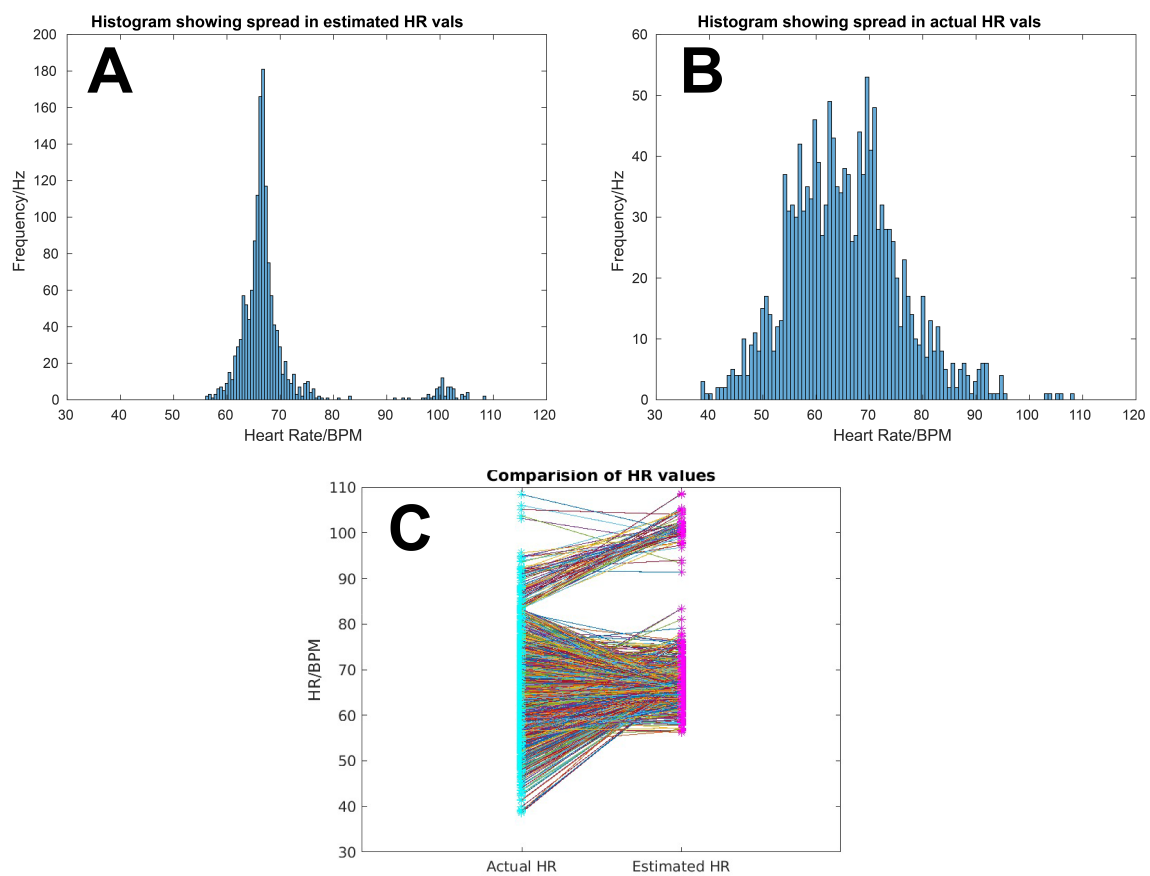


Fig. 4.5 Comparison of actual HR values and estimated HR values. A) Histogram showing the HR values estimated by classification algorithm. B) Histogram showing the actual range of heart rates. C) Plot showing the difference between the two methods with lines connecting the actual and estimated HR's.

4.4.0.4 Generating Pulsatility - Comparison between methods

All three pulsatility generating methods were used to generate pulsatility for 200 participants. Figure 4.6 shows the similarity between the three methods through a correlation analysis. All

three methods fail to show a strong correlation with each other with correlation values of 0.174 (regression vs FFT), -0.195 (regression vs bandpass) and -0.221 (FFT vs bandpass).

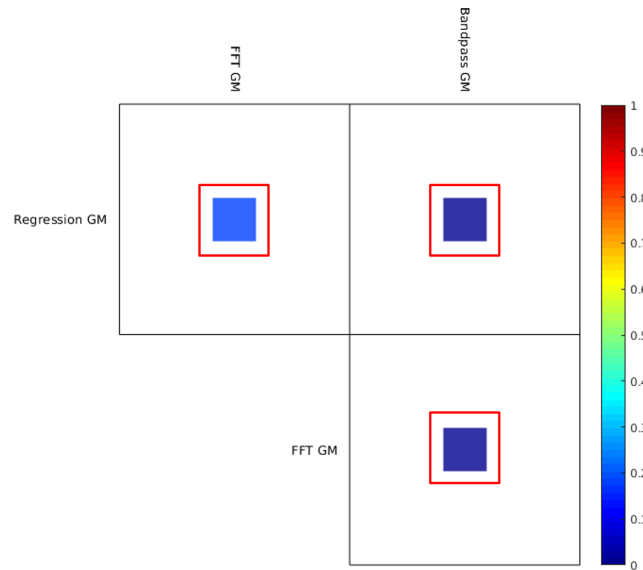


Fig. 4.6 A correlation matrix showing the similarity of the three different generating pulsatility methods used. The colour of the box represents the correlation value (see colour bar) and the size of the box represents the significance of the p-value. A larger box signifies a smaller p-value. The values highlighted in red were statistically significant ($\alpha < 0.05$).

4.4.0.5 Correlation with physiological information

Figure 4.7 shows a correlation matrix comparing the different methods with physiological information collected by the HCP. All three methods showed similar correlation values. The largest correlation was detected between the FFT method and framewise displacement (FD).

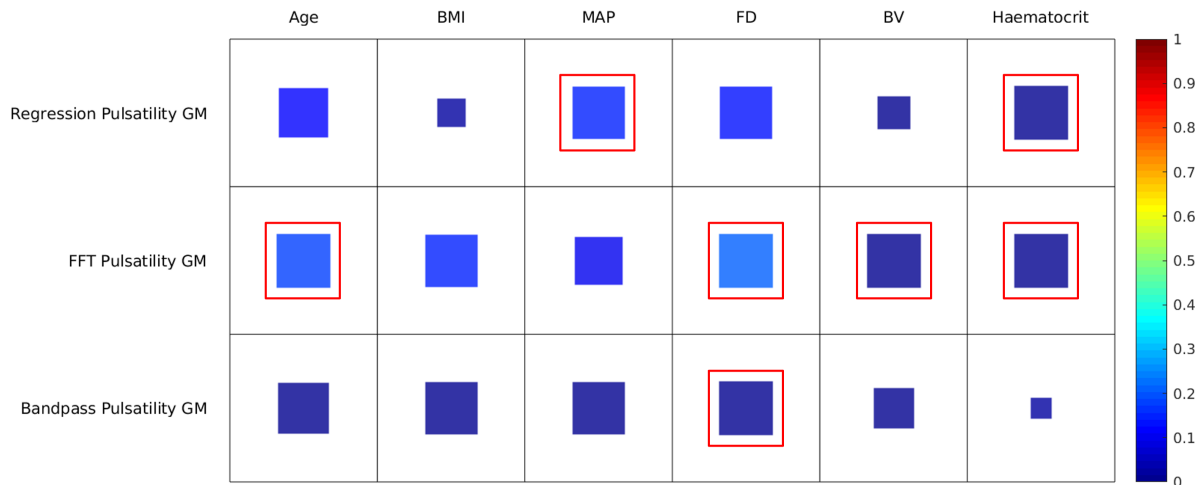


Fig. 4.7 Correlation matrix showing the correlation values for each method (Regression/FFT/Bandpass) with the associated physiological information. The colour of the box represents the correlation value (see colour bar) and the size of the box represents the significance of the p -value. A larger box signifies a smaller p -value. The values highlighted in red were statistically significant ($\alpha < 0.05$).

4.4.0.6 Iteration Problem

Evaluation of the significance of each correlation was performed using a statistical permutation analysis (as outlined in section 4.3.10). Initially, this analysis was run with 1,000 iterations although the results returned a p -value of 0. This was because none of the random permutations resulted in a correlation value greater than the actual correlation value. To account for this, more iterations were required. An analysis was run to determine the ideal number of iterations by increasing the number of iterations and calculating the p -value using equation 4.5. Additionally, I plotted these results as histograms (Figure 4.8). This Figure shows that as the number of iterations is increased, the estimated p -value also increases, which is consistent with expectations. Aside from this, it can be shown that the best estimate of the p -value was determined using 10,000,000 iterations and therefore this value of iterations was used in the subsequent p -value estimations. The data used in this analysis is introduced in Chapter 5. However, I wanted to introduce this analysis here to explain why the number of iterations used was 10,000,000.

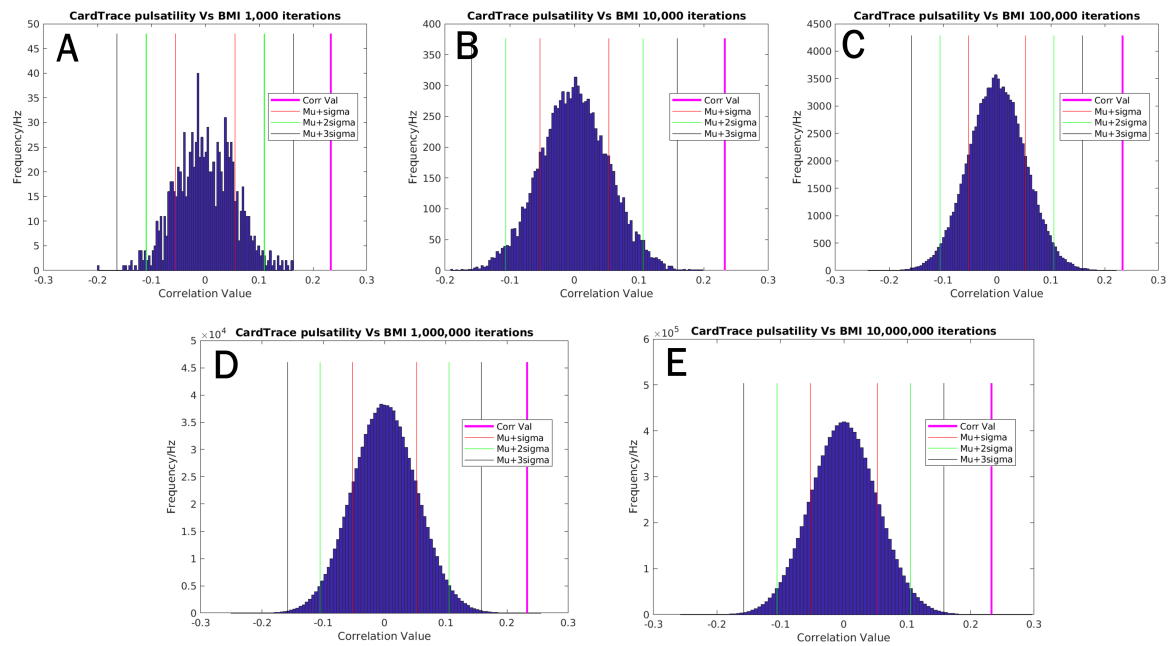


Fig. 4.8 A permutation analysis to determine the number of iterations required to calculate an accurate p -value. This data is introduced in Chapter 5. A) A histogram showing 1000 iterations. B) A histogram showing 10,000 iterations. C) A histogram showing 100,000 iterations. D) A histogram showing 1,000,000 iterations. E) A histogram showing 10,000,000 iterations.

4.5 Discussion

4.5.1 Generating Pulsatility - Comparison between methods

All three methods of generating pulsatility varied in complexity, with the regression method being the simplest. This method used ICA components that had been classified as cardiac-related as regressors in a linear regression to determine the amount of variance they could explain. The bandpass method was slightly more complex as it required the creation of a bespoke cardiac window. Using the bounds of this window, cardiac regressors were generated around the passband (defined as the upper and lower frequencies of this bespoke window). A linear regression was performed with the cardiac regressors to determine the amount of variance explained by them (and bandpass filter the data). The FFT method was the most complex as it required an FFT to be performed before the calculation of fACFF was possible. As can be seen from Figure 4.6, the three different methods fail to show high correlations with each other. This suggests that they are all evaluating different things related to the cardiac cycle. However, Figure 4.7 shows that their correlations with physiological information are all very similar.

Initially, the results showing that the three methods so not show high correlations with each other was puzzling as they are derived from the same classification algorithm. However, the regression method works by utilising the components deemed to be cardiac, whereas the bandpass and FFT methods work from the frequency windows generated from the classification

algorithm. These frequency windows should include information related to the cardiac cycle, but will also include information related to other sources of noise. As such, the bandpass and FFT methods do not isolate only the cardiac signal which could explain their differing results when compared to the regression method. It is expected that the regression method would produce more accurate measures of pulsatility as it isolates components that are cardiac-related only. However, as explained in section 4.4.0.3, there is a discrepancy in HR values determined from the classification algorithm and those that were measured by (Kassinopoulos and Mitsis, 2020), specifically around the 40-50 BPM and 80-90 BPM range. These ranges are close to the Nyquist and sampling frequencies where a large amount of aliasing would occur. Thus, the classification algorithm setup in this chapter will not produce accurate results for participants with average HR values in these ranges.

4.6 Conclusion/Summary

This chapter has outlined various methods of calculating pulsatility from rfMRI scans collected by the HCP. Classification of cardiac-related ICs was most accurately performed by the 100-400 samples Frequency Method. This algorithm was able to distinguish between ICs related to noise and those related to the cardiac cycle for most participants. However, the participants with HR values around the Nyquist and sampling frequencies (40-50 BPM and 80-90 BPM) caused issues with the algorithm due to aliasing. This is because the algorithm worked on expected frequency values and the participants who had HR values around the Nyquist and sampling frequencies would have had the frequency of the cardiac-related information shifted in the frequency domain.

Once the IC data were classified into cardiac-related and non-cardiac-related components, different methods were used to generate values of pulsatility in the microvasculature. Of these methods it was determined that the most accurate was the regression method which used a linear regression and the cardiac-related components to determine pulsatility. The other methods used bespoke cardiac windows which contained other signals not related to the cardiac cycle, thus lowering their accuracy. However, due to the aforementioned issue with participants whose HR is near the Nyquist and sampling frequencies, this method is not without its flaws. Moving forward with this work, it would be desirable to address the problem of aliasing that arises when using the regression method in HR ranges of 40-50 BPM and 80-90 BPM. To mitigate this issue, an adapted version of the regression method that avoids the problem of aliasing is needed and is introduced in chapter 5.

Chapter 5

Novel Methods for quantifying cardiac pulsatility in resting state functional images

5.1 Chapter Overview

Methods to estimate cardiac pulsatility from resting-state fMRI (rfMRI) data were introduced in the previous chapter. Although these methods failed to accurately calculate cardiac pulsatility, some did show promise. In this chapter, I will build upon these to develop two novel methods. Results showed that the estimates generated from these novel methods correlated highly with estimates from a gold standard measure of pulsatility. Comparisons were also made between the estimated pulsatility from both novel methods and physiological parameters (Age, BMI, Mean Arterial Pressure (MAP), Framewise Displacement (FD), Brain Volume (BV) and Haematocrit) using a correlation analysis. These analyses displayed similar trends to the same analysis using the gold standard.

5.2 Introduction

In the previous chapter, I introduced multiple methods of calculating cardiac pulsatility from rfMRI data. These methods, however, had flaws which affected their accuracy in calculating pulsatility. The final method discussed showed promise and this method will be built upon in this chapter. Additionally, a second, novel method of isolating ICA components related to cardiac-cycle from rfMRI data is introduced. The rfMRI data was taken from the Human Connectome Project (HCP) S1200 release (Glasser et al., 2013; Van Essen et al., 2013). Both methods isolated cardiac-related information from non-cardiac-related information using an ICA. One method (the HRV method) used a subset (~ 1588) of processed cardiac traces (HRV) (Kassinopoulos and Mitsis, 2020) to achieve this. The other method (the Frequency method) used frequency information from an ICA and the rfMRI data to classify the ICA components. The advantage of using the Frequency method over the HRV method is that it bypasses the need

for cardiac traces to be collected. This would allow for a fully data-derived cardiac classification process which is desirable. Some big data releases either have not collected cardiac traces when scanning or the quality of the traces is not good enough for training in this way. Once classified, these groups of components were then used to train FIX to calculate cardiac pulsatility for all 1200 participants in the release. The influence of age, BMI, mean arterial pressure (MAP), Brain Volume (BV) and framewise displacement (FD) on these pulsatility measures was investigated.

5.3 Methods

5.3.1 HCP data

The data used in this study is outlined in detail in 4 - section 4.3.1 but I will summarise here. The data used was collected by the WI-Minn Human Connectome Project in their Young Adult (22-35 years) S1200 release (Glasser et al., 2013; Van Essen et al., 2013). They collected data from four modalities: structural MRI, functional MRI, task MRI and diffusion MRI (Van Essen et al., 2013). Only the structural and functional MRI data was used in this study. The functional session collected four resting state (rfMRI) scans across two days. Two of these scans had a left-right phase encoding (PE) direction and the other two had a right-left PE direction. The spatial resolution is 2 mm isotropic voxels with a TR of 0.72s (Glasser et al., 2013; Van Essen et al., 2013). The TE is 33.1 ms and a flip angle of 52° was used. The structural information included T1 weighted and T2 weighted scans with a spatial resolution of 0.7 mm isotropic voxels (Glasser et al., 2013; Van Essen et al., 2013). The T1w acquisition used a TR of 2400 ms, a TE of 2.14 ms and a flip angle of 8° . The T2w acquisition used a TR of 3200 ms, a TE of 565 ms and a variable flip angle. Additionally, physiological information was collected including cardiac and respiratory signals and head motion tracking was performed (Van Essen et al., 2013).

5.3.2 Processing of Cardiac Data

Making use of cardiac traces collected by the HCP and processed by (Kassinopoulos and Mitsis, 2020) was essential for the HRV method. The processing performed on these cardiac traces is outlined in depth by (Kassinopoulos and Mitsis, 2020) and summarised in Chapter 4 - section 4.3.6. Briefly, PPG signals were band-pass filtered between 0.3 and 10 Hz. Then a HR signal was calculated (in BPM) by multiplying the inverse of the time differences between pairs of adjacent peaks by 60 and resampled at 10 Hz. This resulted in HRV traces for each participant.

5.3.3 Processing of rfMRI Data

The HCP pre-processed the rfMRI data and the steps they took are detailed in their paper (Glasser et al., 2013). These steps were briefly summarised in 4 - section 4.3.2. They used the fMRIVolume pre-processing pipeline which performs gradient-nonlinearity-induced distortion

correction, motion correction, EPI image distortion correction and non-linear registration to register images into MNI space. Following these steps, the data was high pass filtered at 0.00072 Hz (a cutoff of 2000s (Smith et al., 2013)). No low-pass filtering was applied as useful neuronal signal could be present up to 0.2Hz.

5.3.4 Processing of Structural T1w Data

Structural data was processed by the HCP and the details of this are outlined in (Glasser et al., 2013) and summarised in Chapter 4 - section 4.3.3. This data was used to generate different brain masks. The processing was completed in three stages: PreFreeSurfer, FreeSurfer and PostFreeSurfer.

5.3.5 Processing of ICA components

The processing of ICA components is explained in detail in (Smith et al., 2013) and was summarised in Chapter 4 - Section 4.3.4. Briefly, MELODIC was used to generate ICA components from the pre-processed rfMRI data. The number of components was chosen by MELODIC using Automatic dimensionality estimation. The maximum number of components was restricted to 250.

5.3.6 Generation of Brain Masks

I generated four masks for each participant, a whole brain (WB) mask, a grey matter (GM) mask, a white matter mask (WM) and a ventricle mask (Vent). The WB mask was generated from the MNI standard 2 mm Brain mask. The GM mask was generated from a GM ribbon created as part of the FreeSurfer processing stage of the structural T1w data outlined in Chapter 4 - Section 4.3.3. The WM mask was generated from the subtraction of the GM from the WB mask. The Vent mask was generated from the MNI standard 2 mm Ventricle mask. Pulsatility was calculated in the WM region as a sanity check as it is expected that there will be more pulsatility in the GM than the WM.

5.3.7 Classification of ICA Components - HRV Method

In this method, the processed HRV traces were used to determine which ICA components most resembled cardiac signal. FMRIB's ICA-based X-noiseifier (FIX), introduced in Chapter 2 - Section 2.6.4, can be used to distinguish 'good' and 'bad' components from within an ICA decomposition. In this work, the ICA components that most resembled cardiac signal were used to train FIX so that it could automatically isolate cardiac pulsatility for each rfMRI dataset. FIX was run with a threshold of 20. Initially the associated HR for each rfMRI dataset was calculated

from the HR signal (outlined in section 4.3.3) by calculating the average across this beat-to-beat HR.

5.3.7.1 Correlation of ICA & Cardiac data

The correlation value between each ICA component time series and the associated HR variability trace was calculated. This determined which ICA components had significant levels of cardiac pulsatility associated with them. An α -significance value of 0.05 was used to determine significance and this was adjusted to account for the number of components used in the correlation. Components that met this significance criteria were then deemed to be cardiac components. Using this information, 4 training datasets containing 100 (randomly selected) classified rfMRI datasets were created. The creators of FIX recommend that these training datasets are comprised of at least 10 different datasets. To increase the probability of a good classification, 100 rfMRI datasets were chosen. It was expected that a larger number of rfMRI datasets used in the training would increase the accuracy of the classifier. The rfMRI datasets used for each of the four training datasets were grouped based on their HR value: 60BPM, 70BPM, 90BPM and mixBPM, where mixBPM contained a mixture of participants chosen from the first three groups. This was to investigate whether the HR of the participants used would bias the classifier causing it to only calculate pulsatility values for the participants with a matching HR. Which would result in a reduction in the number of rfMRI datasets that could be classified. Furthermore, it could lead to the calculation of incorrect pulsatility values. The mixBPM group was used as a control to investigate how the classifier worked with a mixture of participants with different HR values. Participants with HR value around 80 BPM (1.333 Hz) were not included as this is close to the sampling frequency of 1.389 Hz. As explained in Chapter 4, aliasing was expected to cause errors in the classification for participants with HRs close to the sampling and Nyquist frequencies. Following the creation of the training datasets, FIX (Salimi-Khorshidi et al., 2014) was trained and used to determine which ICA component time series displayed large amounts of signal related to heart rate variability (HRV) for all of the 4123 rfMRI datasets.

5.3.7.2 Calculation of Pulsatility

Pulsatility was defined as the amount of variance explained by the cardiac component time series in the rfMRI BOLD time series. Calculation of pulsatility was performed on a voxel wise basis using AFNI's 3dDeconvolve (Cox, 1996; Cox and Hyde, 1997). Each associated cardiac component time series was included as an input regressor to the model. Additionally, motion parameter estimates provided by the HCP were used in the model as covariates of no interest. The R^2 variance statistic was calculated from this regression and a map of R^2 (or pulsatility) was created for each individual fMRI time series. The median pulsatility value was calculated within the three brain masks (WB, GM and WM – described fully in section 5.3.6). Figure 5.1 outlines the classification steps in a schematic diagram.

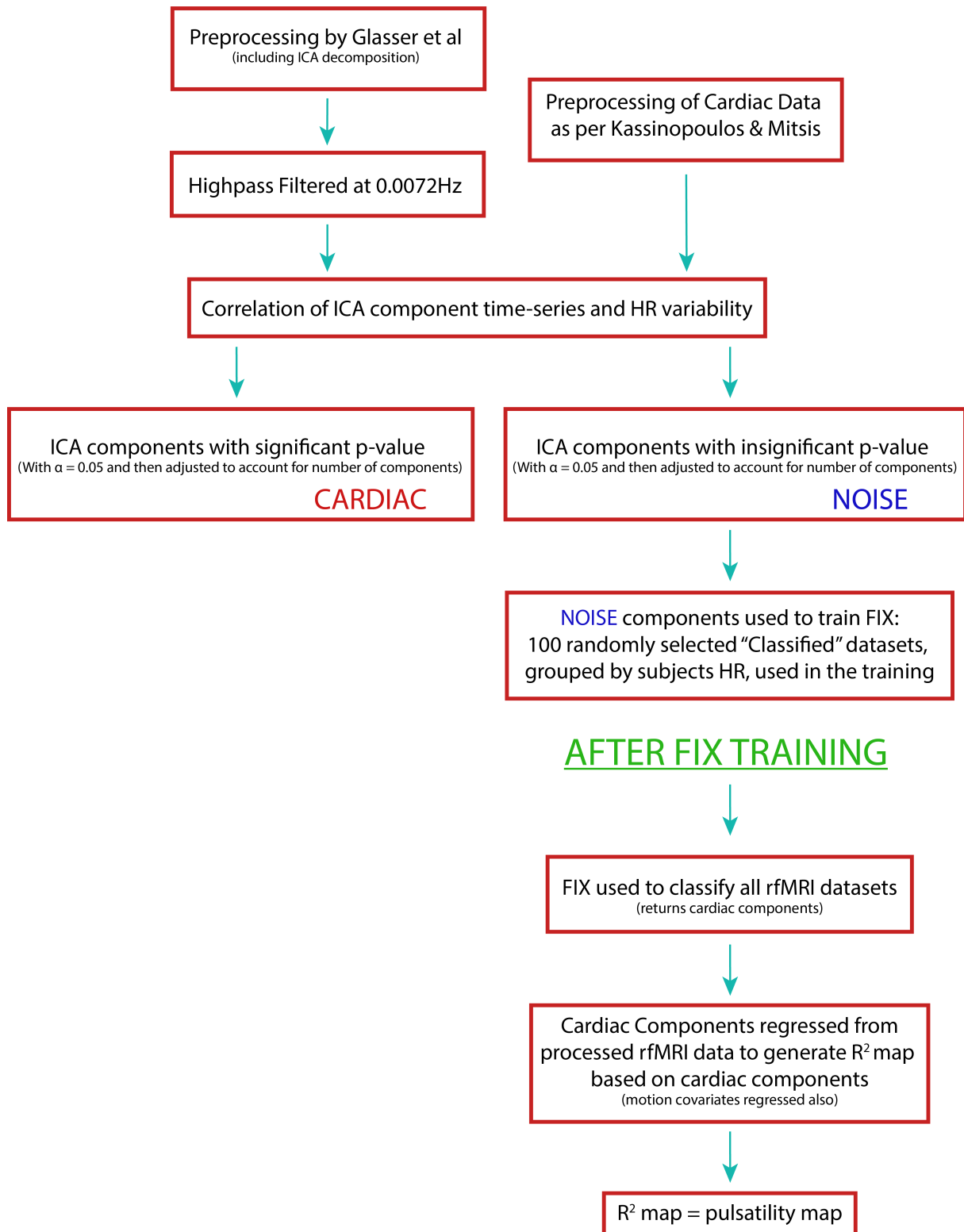


Fig. 5.1 Schematic diagram outlining the classification process for the HRV method of classification. These steps included: Preprocessing, Correlation analysis, Classification into Cardiac and Noise, Training of FIX and generation of pulsatility maps.

5.3.7.3 The relationship between HRV and Pulsatility

Blood flowing through arteries is pulsatile in nature. This pulsatile flow will affect the signal measured using fMRI. So, to measure this accurately, external equipment is used (such as a pulse oximeter). Using this independent measure, we can look for variance in the brain and assume this is related to the cardiac cycle. Therefore, these peripheral measurements (referred to as the cardiac trace) allow for the estimation of the "True" pulsatility and this is the method used to calculate the gold standard here. HRV is derived from the cardiac trace as detailed in Chapter 4 - Section 4.3.6. However, this requires good quality cardiac traces to be collected and, as such, a method of measuring HRV using fMRI is desirable. It is difficult to measure HRV using fMRI due to the lack of samples collected within a single heartbeat. The blood flowing into vessels is pulsatile in nature but is undersampled by BOLD imaging. Using fMRI, instead of sampling the whole heartbeat, an average will be collected across it. In voxels that contain a large blood signal, where there is an increase in HRV, there will be an increase in the BOLD signal for that voxel. This would also be the case for an increase in pulsatility. Therefore, from an fMRI perspective, HRV and pulsatility are coupled and voxels that show a change in HRV should also show a change in pulsatility. This is shown schematically in Figure 5.2, which was originally shown in Chapter 2 but I have placed it here as this concept is very important for understanding why I have used HRV measures to try to investigate pulsatility.

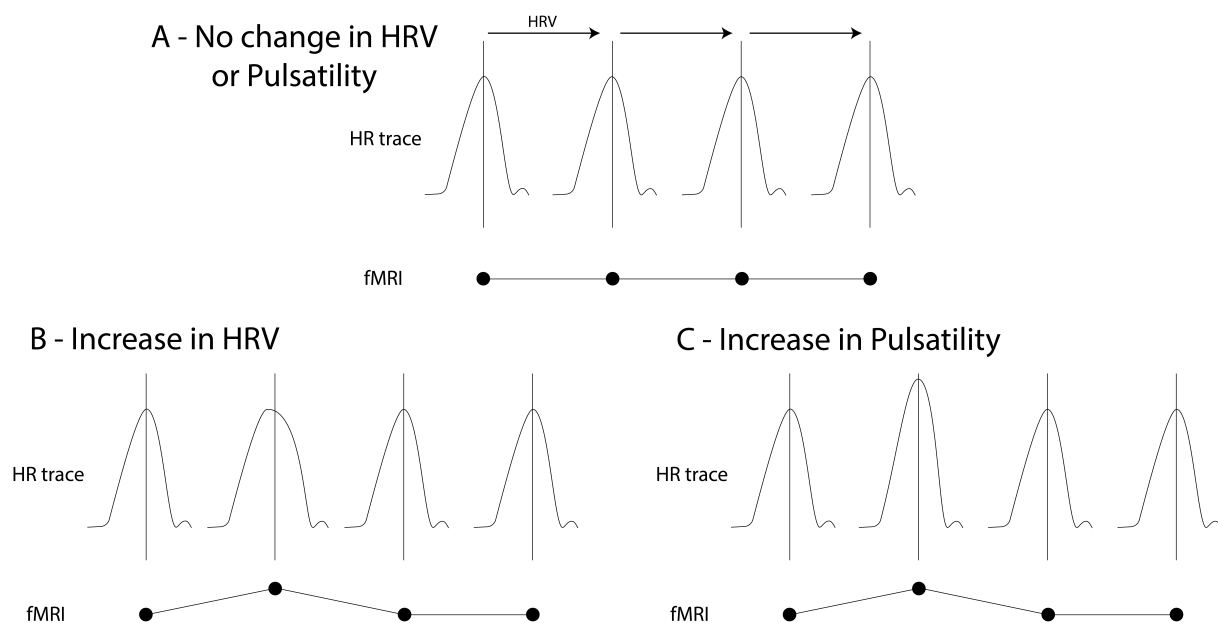


Fig. 5.2 A schematic diagram showing how closely related HRV and Pulsatility are from an fMRI perspective. A change in either HRV or Pulsatility would be reflected by the same change in fMRI and so the ability to distinguish between these two measures is difficult.

5.3.8 Classification of ICA components - Frequency Method

The Frequency method used the classification algorithm detailed in Chapter 4. The version of the algorithm used in this chapter is identical to that of Chapter 4, however the method used to calculate pulsatility is different. I will give a brief overview of this algorithm here. ICA components were classified into cardiac and non-cardiac based on their frequency content. This differs to the HRV method (detailed in section 5.3.7) as it uses frequency content rather than a comparison to an externally recorded HRV trace. Typically, cardiac cycles occur at a frequency of ~ 1 Hz at rest (Murphy et al., 2013). This frequency depends on the HR of the participant and so the definition of the upper and lower bounds of the frequency range window was crucial. The lower bound of the frequency range was chosen to be 0.11 Hz (or 100 frequency bins, based on the sampling rate of 1.389 Hz). The upper bound was chosen to be 0.46 Hz (or 400 frequency bins). This frequency range will be referred to as the cardiac window throughout the rest of this chapter. The classification algorithm then worked to classify components based on the contents of this frequency range. The algorithm worked in three stages with each aiming to build upon the last. The initial step used a smaller ‘sliding window’ of 0.0058 Hz (or 5 frequency bins) and cycled through the entire cardiac window, calculating the mean in each sliding window. Components within the sliding window with a mean value greater than the mean of all components within the sliding window ($+2.5$ standard deviations from the mean) were considered to be preliminary cardiac components. The second stage involved fitting a two-term Gaussian curve to the individual component frequency data within the cardiac window. The R^2 value for each Gaussian fit was calculated and those with an R^2 greater than 0.9 were considered to be preliminary cardiac components. The final stage of classification aimed to remove erroneous Gaussian fits in order to classify more accurately. The first step was to determine which term from the two-term Gaussian fit had fit the peak of the data. This was achieved by calculating the value of the frequency ‘peak’ for each term of the Gaussian fit (for each component) and the largest absolute value was chosen to be the peak related to the cardiac cycle. This will be referred to as the cardiac peak. Then, the median value across the cardiac peaks was calculated. From this, a median window defined as the median value ± 100 samples was generated. The cardiac peaks that were within this median window were then considered cardiac components. All components that failed these tests were considered noise components. A schematic diagram outlining these steps is shown in Figure 5.3 (this diagram is the same as found in Chapter 4).

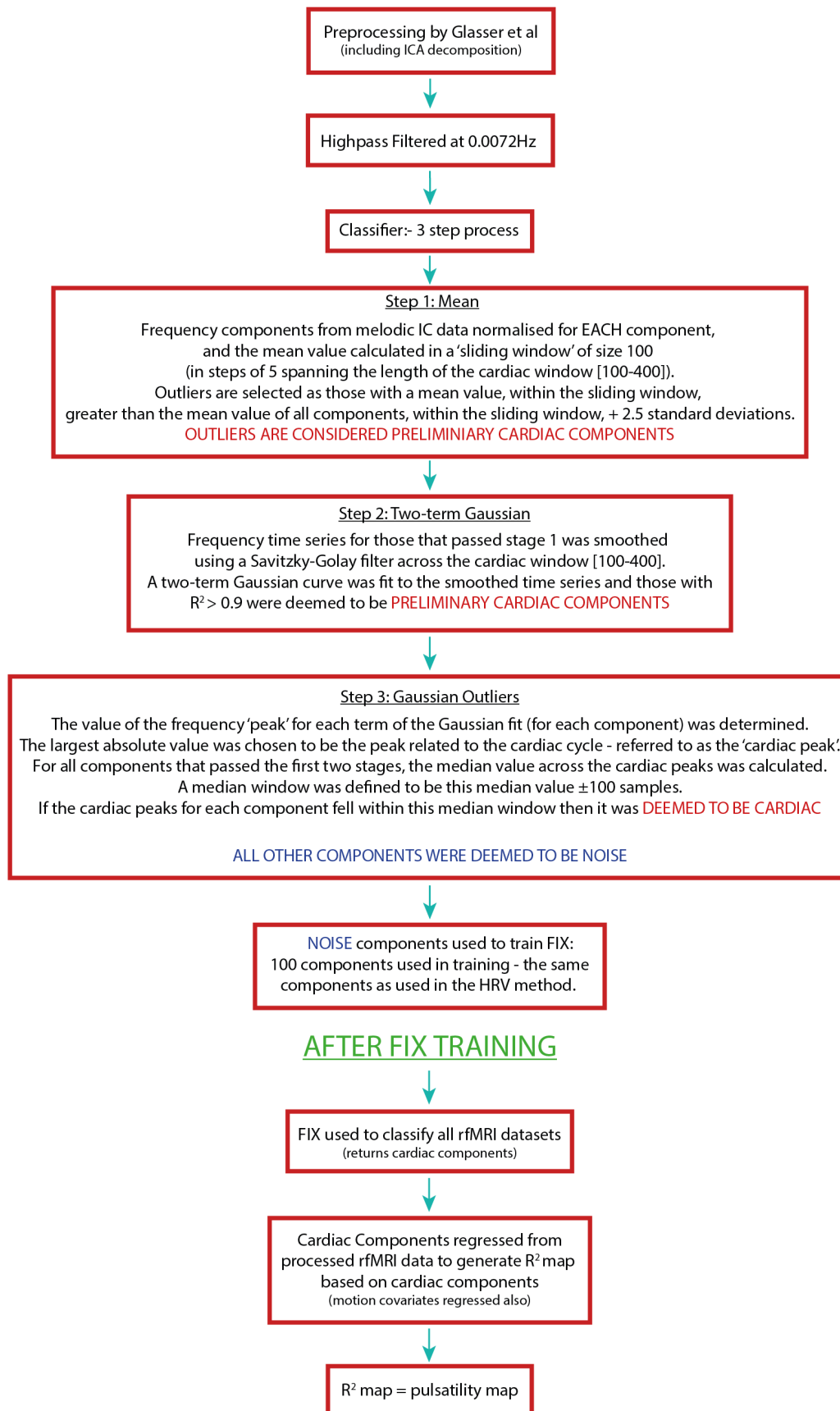


Fig. 5.3 Schematic diagram detailing the classification steps used in the 100-400 samples classifier. These steps included: Preprocessing, Mean calculation, Two-term Gaussian fitting, Gaussian Outlier estimation, Training of FIX and generation of pulsatility maps.

5.3.8.1 Calculation of Pulsatility

Using this information, 100 participants (the same participants as selected for the HRV method) were used to create four FIX training datasets. FIX was then used to determine the cardiac components for each of the 4123 rfMRI datasets. A linear regression was used to generate pulsatility maps. These were defined to be the variance explained by the cardiac component time series. Values of pulsatility were calculated for each participant by taking the median pulsatility values across the WB mask, the GM mask and the WM mask.

5.3.9 Cardiac Regressors

Regressors used by the linear regression included the MELODIC IC time series for the components considered to be cardiac. These are referred to as cardiac regressors. The baseline model included motion regressors calculated from a rigid body motion registration with 6 degrees-of-freedom. These were included in the model as regressors of no interest. Pulsatility maps and pulsatility values were calculated on a voxelwise basis.

5.3.10 Verification of pulsatility values

To verify the accuracy of the methods outlined in this chapter, pulsatility values were calculated for each of the 1588 rfMRI datasets which had useable HRV traces. To do this, the processed HRV traces were used as regressors in a linear regression from the rfMRI datasets. The outcome from the linear regression will represent the "true" pulsatility values for that participant as the cardiac was data recorded during the scan. The linear regression generated a pulsatility map and pulsatility values were created by taking the median pulsatility values across the WB mask, the GM mask and the WM mask. The values of "true" pulsatility were then compared to each method (HRV and Frequency method) in order to determine the accuracy of these methods. This comparison was achieved using a correlation between the "true" pulsatility values and the pulsatility values for each of the novel methods. Then a correlation matrix was generated and represented in a colourmap.

5.3.11 Correlation with Physiological measures

Correlation of GM median pulsatility with age, BMI, Mean Arterial Pressure (MAP), Brain Volume (BV), haematocrit and Framewise Displacement (FD) was performed. The method of doing this was detailed in Chapter 4 - Section 4.3.10 and will be briefly outlined here. The statistical significance of these correlations was evaluated using a permutation analysis where the index order of the physiological vector was randomly changed and the correlation recalculated with this new order. This was repeated so that there were 10,000,000 iterations in total. The p -value was determined from equation 4.5. Throughout this work, the level of

statistical significance was measured using an α -significance level of 0.05 (after correction for multiple comparisons).

5.4 Results

5.4.1 Verification of method accuracy - HRV method

To verify the accuracy of the pulsatility maps generated by the HRV method a comparison between the generated pulsatility and the "true" pulsatility was made. In this case, the "true" pulsatility was generated using the processed HRV traces. The desired outcome from this comparison would be a high correlation value (and significant p -value) as this would indicate an accurate calculation of pulsatility using the HRV method. Around 390 participants were involved in this comparison, as this was the number of good quality physiological traces that were analysed.

Correlation matrices were generated to determine the similarity between the "true" pulsatility values and the values generated by the HRV method. Correlation values exceeded 0.88 (associated p -value= 1.2×10^{-125}) in all cases with a maximum correlation value of 0.91 (p -value= 8.6×10^{-149}) (Figure 5.4), between the "true" GM pulsatility and that generated from the HRV method with the 60BPM training dataset. The mixBPM training dataset generated values of GM pulsatility with the lowest similarity to the "true" pulsatility with a correlation value of 0.88 (associated p -value= 1.2×10^{-125}). The high correlations with the "true" pulsatility values suggest the methods used demonstrate an accurate calculation of pulsatility and are further shown in the scatter plots included in the Appendix (Figure A.1). Further demonstrated in Figure 5.4 is the similarity of pulsatility values generated by each training dataset. The 70BPM and 90BPM methods showed the most similarity in GM pulsatility with a correlation value of 0.93 (associated p -value= 7.6×10^{-171}). However, all correlation values exceeded 0.90 (associated p -value= 4.2×10^{-146}) when comparing across methods.

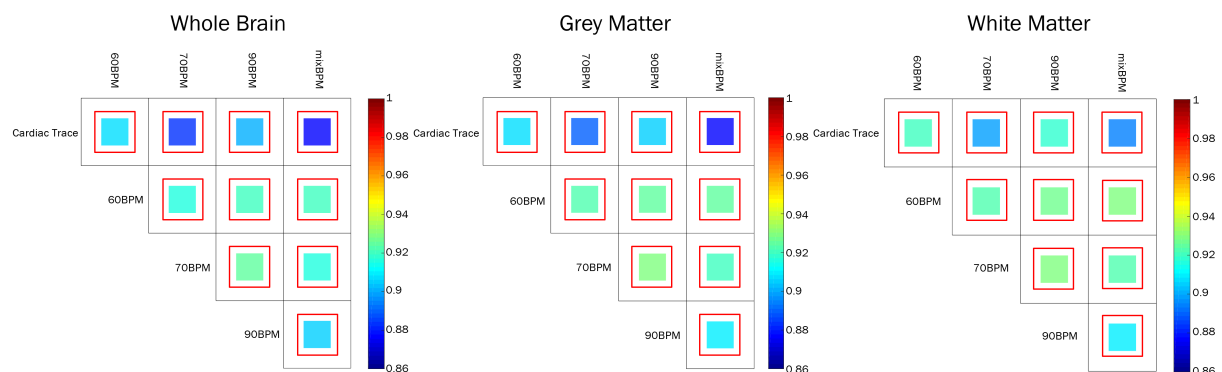


Fig. 5.4 Correlation matrix showing the similarity between "true" pulsatility values generated with the HRV trace and the different training datasets used in the HRV method. Correlation values are defined by the colourmap and the boxes scale based on the p -value. Values with a statistical significance ($\alpha < 0.05$) are enclosed in a red box.

5.4.2 Verification of method accuracy - Frequency Method

Similarly to the verification of the HRV method, correlation matrices were generated to compare the "true" pulsatility values with the Frequency method estimates for the 390 participants. These results are shown in Figure 5.5.

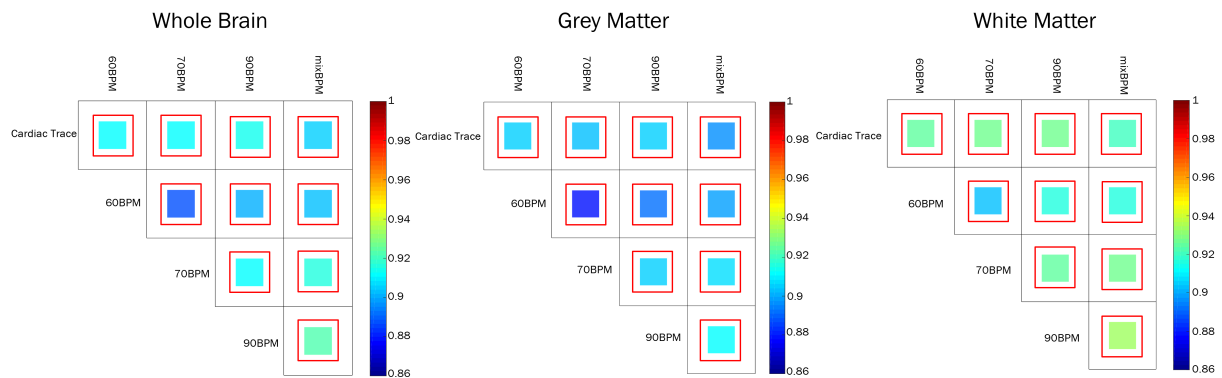


Fig. 5.5 Correlation matrix showing the similarity between "true" pulsatility values generated using HRV traces and the different training datasets used in the Frequency method. Correlation values are defined by the colourmap and the boxes scale based on the p -value. Values with a statistical significance ($\alpha < 0.05$) are enclosed in a red box.

Correlation values exceeded 0.90 (associated p -value= 3.0×10^{-140}) in all cases. Overall, the correspondance to the "true" pusatility was higher than for the HRV method. Values of correlation between training datasets (60BPM, 70BPM, 90BPM, mixBPM) did not differ by much. Scatter graphs showing the high correlations are shown in Figure A.2. The percentage difference between the gradients for the HRV and Frequency method were quantified and are shown in Figure 5.6. The HRV methods showed larger gradients. The largest difference was between the 60BPM methods. The smallest difference was between the mixBPM methods.

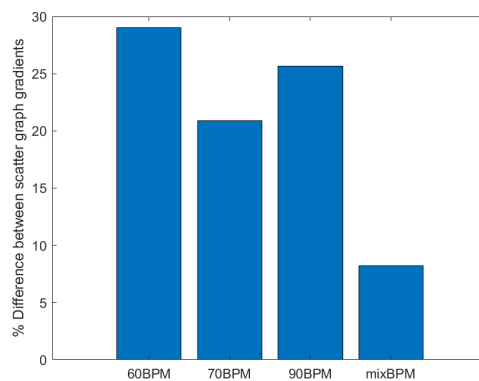


Fig. 5.6 A bar chart showing the percentage difference between the gradients of the scatter graphs (found in the Appendix - Figures A.2 & A.1) for both methods. The lower the percentage difference, the more similar the gradients are.

5.4.3 "True" Pulsatility correlations with physiological information

To further validate the methods used to calculate pulsatility, correlation values of the "true" pulsatility with different physiological parameters were calculated (Figure 5.7). Again, 390 participants were analysed here.

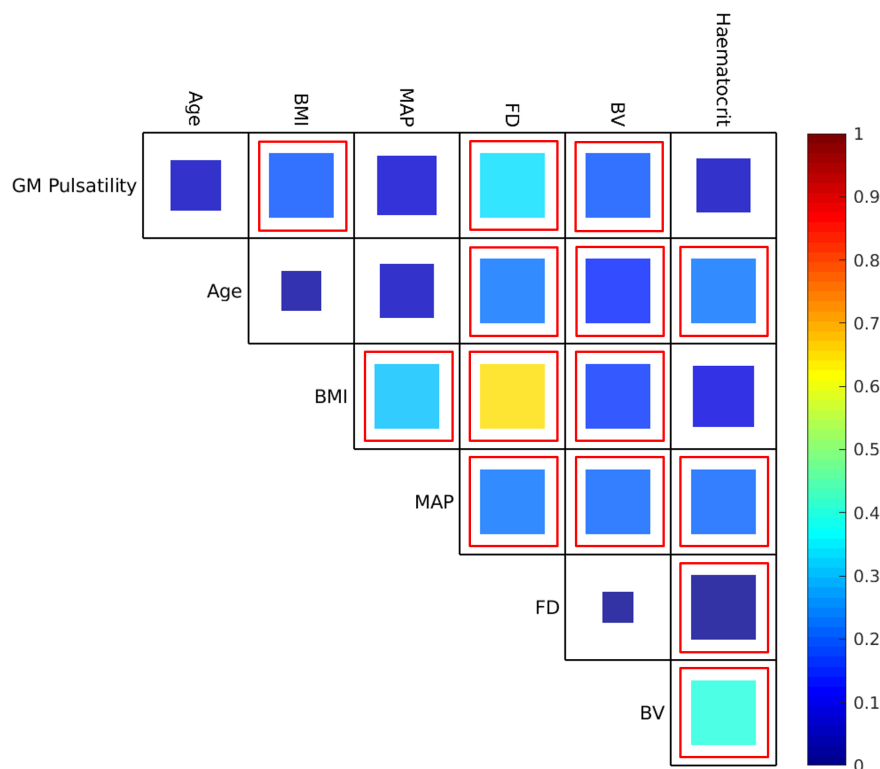


Fig. 5.7 Correlation matrix comparing "true" GM pulsatility values with different physiological parameters. The parameters in question are: Age, BMI, Mean Arterial Pressure (MAP), Frame-wise Displacement (FD), Brain Volume (BV) and Haematocrit. Correlation value is defined by the colourmap and the boxes scale depending on the p -value (smaller p -values result in larger boxes). Values with a statistical significance ($\alpha < 0.05$) are enclosed in a red box.

Overall, the correlation values were low (Figure 5.7). The greatest correlation values detected were for the comparison of GM pulsatility with BMI ($\text{corr} = 1.9 \times 10^{-1}$, $p\text{-value} = 3.7 \times 10^{-4}$) and FD ($\text{corr} = 3.3 \times 10^{-1}$, $p\text{-value} = 0$). The correlation with the least significant p -value was age vs GM pulsatility with a p -value of 3.68×10^{-1} , and the most significant was FD vs GM pulsatility with a p -value of 0. Figure 5.7 also shows the correlation values when the physiological parameters were compared with each other.

5.4.4 HRV Method Pulsatility correlations with physiological information

Correlations between HRV method estimates of pulsatility and physiological parameters are shown in Figure 5.8. This analysis included all participants. Correlation values with significant p -values were detected for all training groups following a similar trend to the results for "true" pulsatility. This similarity shows that this method is looking at cardiac-related information as

expected. The highest correlation values were detected when comparing the 60BPM estimation of pulsatility to BMI ($\text{corr}=2.2 \times 10^{-1}$, $p\text{-value}=0$), the 60BPM estimate of pulsatility to FD ($\text{corr}=3.9 \times 10^{-1}$, $p\text{-value}=0$) and the 90BPM estimate of pulsatility to BV ($\text{corr}=2.87 \times 10^{-1}$, $p\text{-value}=0$). The least significant correlation value was detected for the mixBPM estimate of pulsatility with age ($\text{corr}=1.2 \times 10^{-2}$, $p\text{-value}=7.1 \times 10^{-1}$).

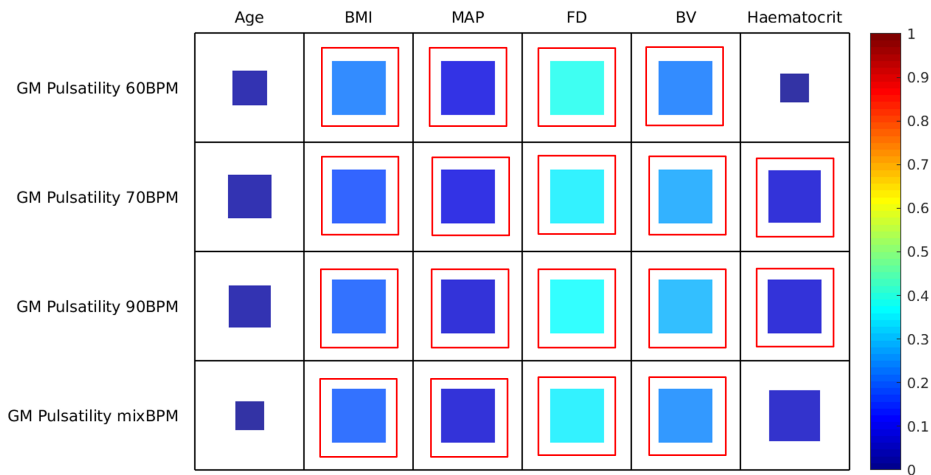


Fig. 5.8 Correlation matrix comparing GM pulsatility generated from each training dataset using the HRV method and physiological parameters. The parameters in question are: Age, BMI, Mean Arterial Pressure (MAP), Framewise Displacement (FD), Brain Volume (BV) and Haematocrit. Correlation values are absolute correlations and are defined by the colourmap, the boxes scale based on the p -value. Values with a statistical significance ($\alpha < 0.05$) are enclosed in a red box.

5.4.5 Frequency Method Pulsatility correlations with physiological information

Correlations between Frequency method estimates of pulsatility and physiological parameters are shown in Figure 5.9. Values of correlation were similar to the "true" pulsatility correlations and the HRV correlations. The most significant correlation was found between the 90BPM estimate of pulsatility and FD ($\text{corr}=3.31 \times 10^{-1}$, $p\text{-value}=0$) and the least significant correlation was found between the 60BPM estimate of pulsatility and haematocrit ($\text{corr}=3.81 \times 10^{-2}$, $p\text{-value}=2.6 \times 10^{-1}$).

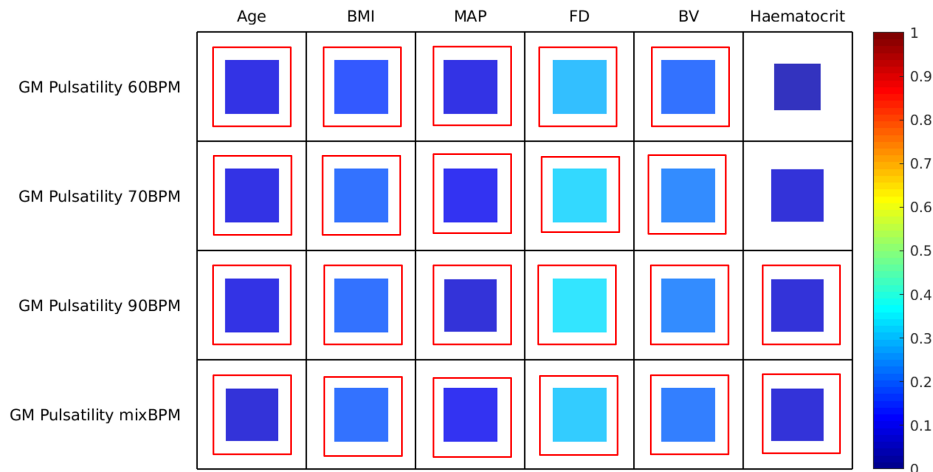


Fig. 5.9 Correlation matrix comparing GM pulsatility generated from each training dataset using the Frequency method and physiological parameters. The parameters in question are: Age, BMI, Mean Arterial Pressure (MAP), Framewise Displacement (FD), Brain Volume (BV) and Haematocrit. Correlation values are absolute correlations and are defined by the colourmap, the boxes scale based on the p -value Values with a statistical significance ($\alpha < 0.05$) are enclosed in a red box.

5.4.6 Comparisons across methods

Comparisons between GM pulsatility values calculated from both the HRV and Frequency methods are represented using a correlation matrix (Figure 5.10). Within methods, correlation values were high, all of which were greater than (or equal to) 0.8 (associated p -value= 6.37×10^{-217}). However, correlation values were lower between methods with the lowest value equal to 7.97×10^{-1} (p -value= 6.37×10^{-217}).

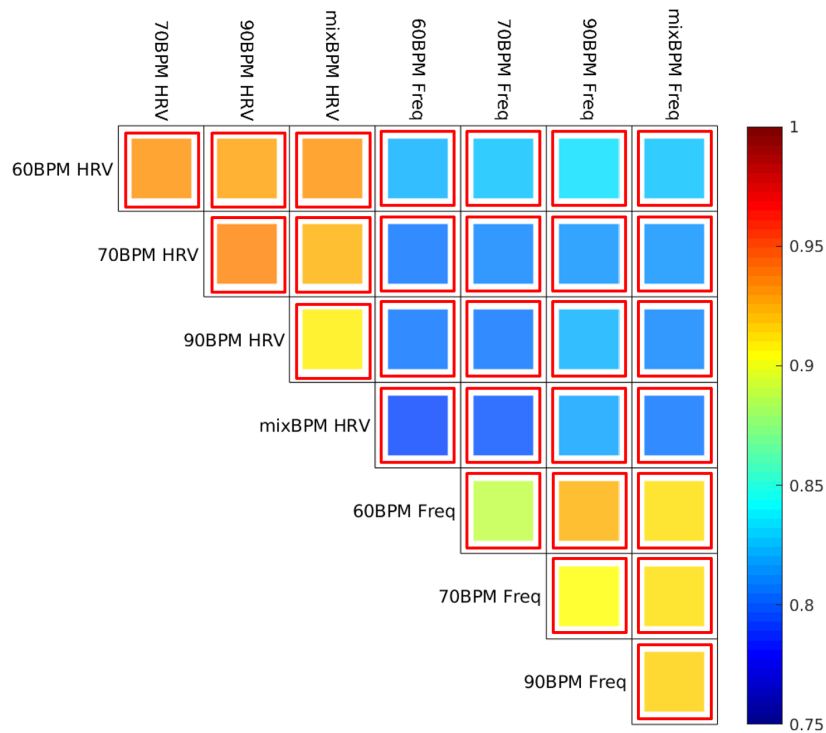


Fig. 5.10 Correlation matrix comparing the GM pulsatility calculated from both the HRV method and the Frequency Method. Correlation values are absolute correlations and are defined by the colourmap, the boxes scale based on the p -value Values with a statistical significance ($\alpha < 0.05$) are enclosed in a red box.

The number of rfMRI scans analysed by each method was dependant on how harsh the classifier was in creating the training dataset. A harsher classifier would not classify as many components as cardiac. This could mean that some rfMRI scans finish classification with no components deemed to be cardiac. Figures 5.11 and 5.12 show this in detail by displaying the number of rfMRI runs (Figure 5.11) and participants (Figure 5.12) analysed for each method used. The number of runs analysed is affected quite substantially by the harshness of the Frequency method classifier and at most 1526 runs were not classified by this method. However, as can be seen in Figure 5.12 this did not translate to a large number of unclassified participants. The reason for this difference was that at least 1 run was classified for all participants allowing a value of pulsatility to be generated. However, this may have been due to luck and may not be the case if this classifier was used on another dataset.

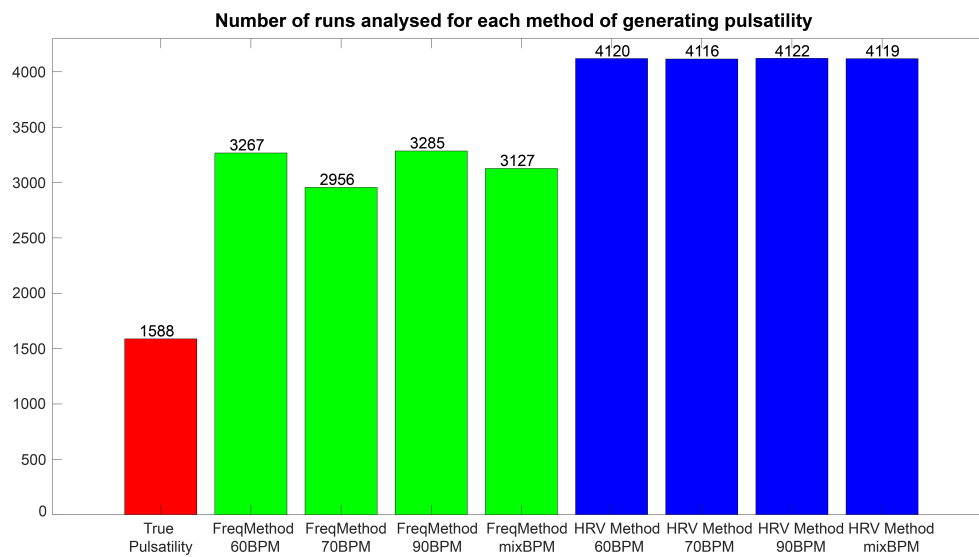


Fig. 5.11 Bar chart showing the number of 'runs' analysed for each method used to generate pulsatility. The colours represent the different methods: The red bar represents the "true" pulsatility, the green represents the estimates generated from the Frequency method and the blue represents the estimates generated from the HRV method. The number of runs is displayed above each bar.

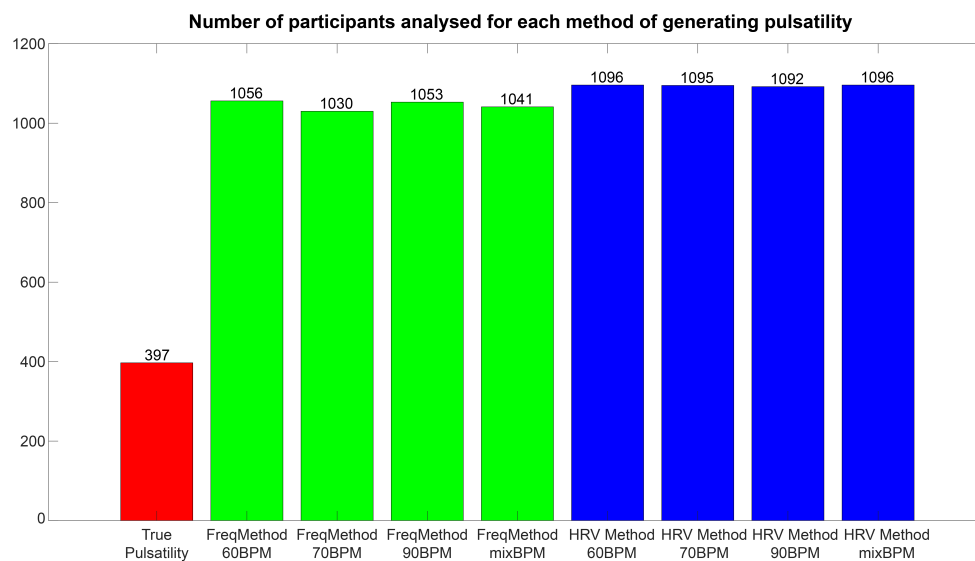


Fig. 5.12 Bar chart showing the number of participants analysed for each method used to generate pulsatility. The colours represent the different methods: The red bar represents the "true" pulsatility, the green represents the estimates generated from the Frequency method and the blue represents the estimates generated from the HRV method. The number of participants is displayed above each bar.

5.4.7 Averaged pulsatility maps

5.4.8 HRV Method

Average pulsatility maps were generated for each method (60BPM, 70BPM, 90BPM, mixBPM) and are shown in Figure 5.13. A clear structure can be seen within the GM, suggesting that this method works well. The values of pulsatility in different tissue types were compared. Bar charts showing the average pulsatility value estimated for WB, GM, WM and ventricles are shown in Figure 5.14. These results show that the largest value of average pulsatility is found when using the WB mask. The second largest pulsatility value was observed in the GM, with the third and fourth largest values found in the WM and the ventricles respectively. These trends all showed statistically significant differences with p -values less than 6.88×10^{-29} .

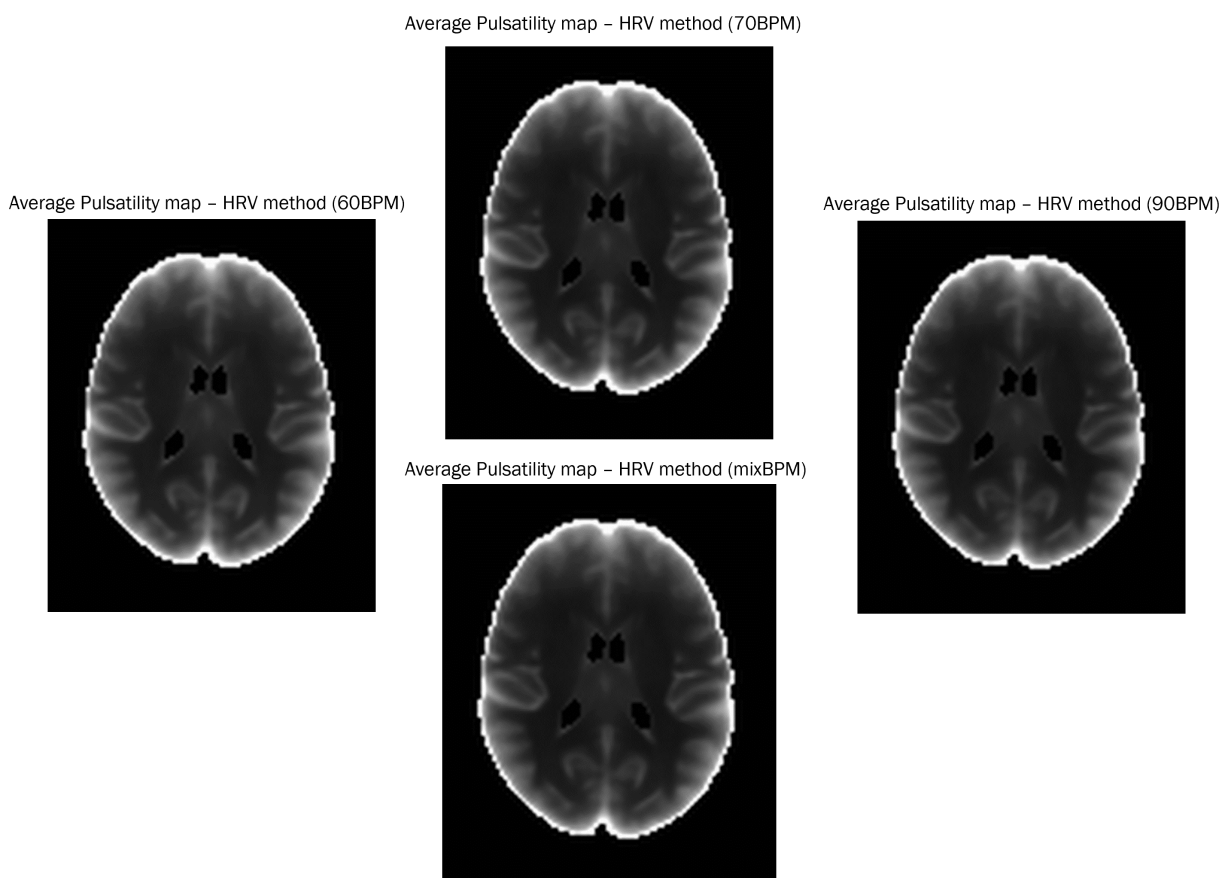


Fig. 5.13 Average Pulsatility maps for the HRV method. All four methods show very similar maps. Structure can be seen within the GM and a clear GM/WM border is evident with GM greater than WM. The white halo surrounding the brain is thought to be related to the CSF outside of the brain.

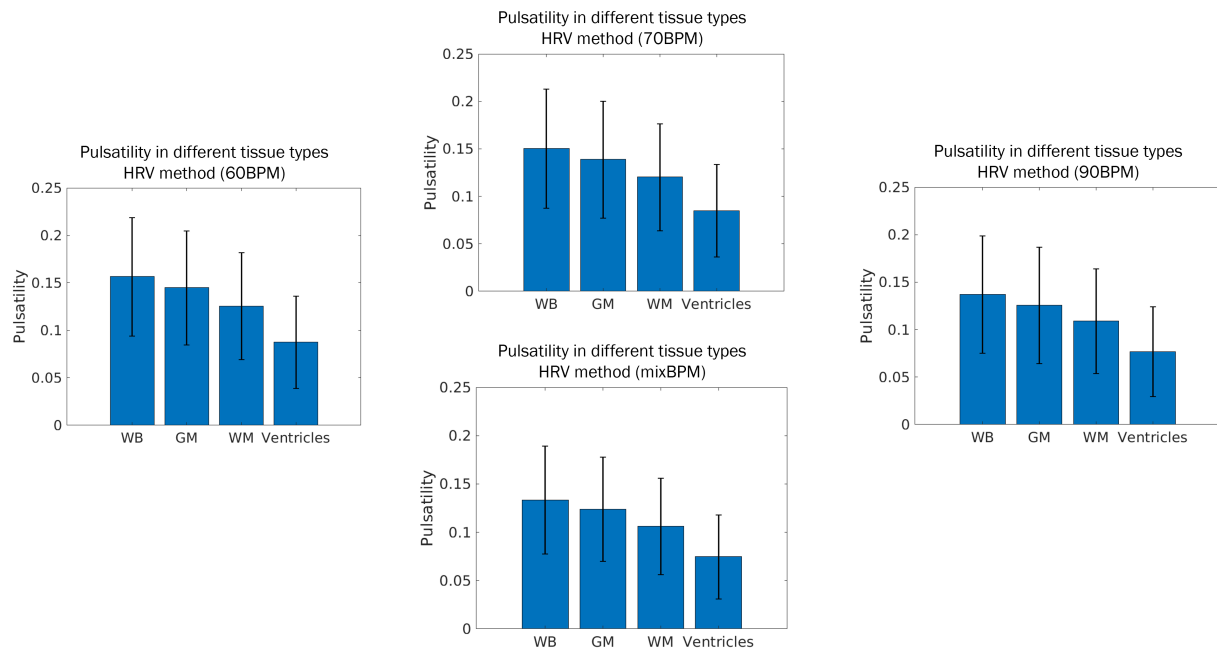


Fig. 5.14 A bar chart showing the estimated pulsatility value in different tissue types using the HRV method. Error bars are included on these bars and these tend to overlap between methods. This graph shows that there is a hierarchy of pulsatility value ranging from WB to Ventricles (with the largest pulsatility represented in the WB).

5.4.9 Frequency Method

Similarly to the HRV method, average pulsatility maps were generated for each method (60BPM, 70BPM, 90BPM, mixBPM) and these are shown in Figure 5.15. A clear structure can be seen within the GM which was also "true" for the HRV method. However, in comparison to the HRV method, these results show a slightly less obvious structure (the contrast is lower). Figure 5.16 shows average pulsatility values in the different tissue types using the Frequency method. Similar to the HRV method, these results show the estimated average pulsatility is largest using the WB mask, and decreases in magnitude in the GM, then the WM and then the ventricles. In comparison with the HRV method (5.14), the average pulsatility is lower when estimating it using the Frequency method.

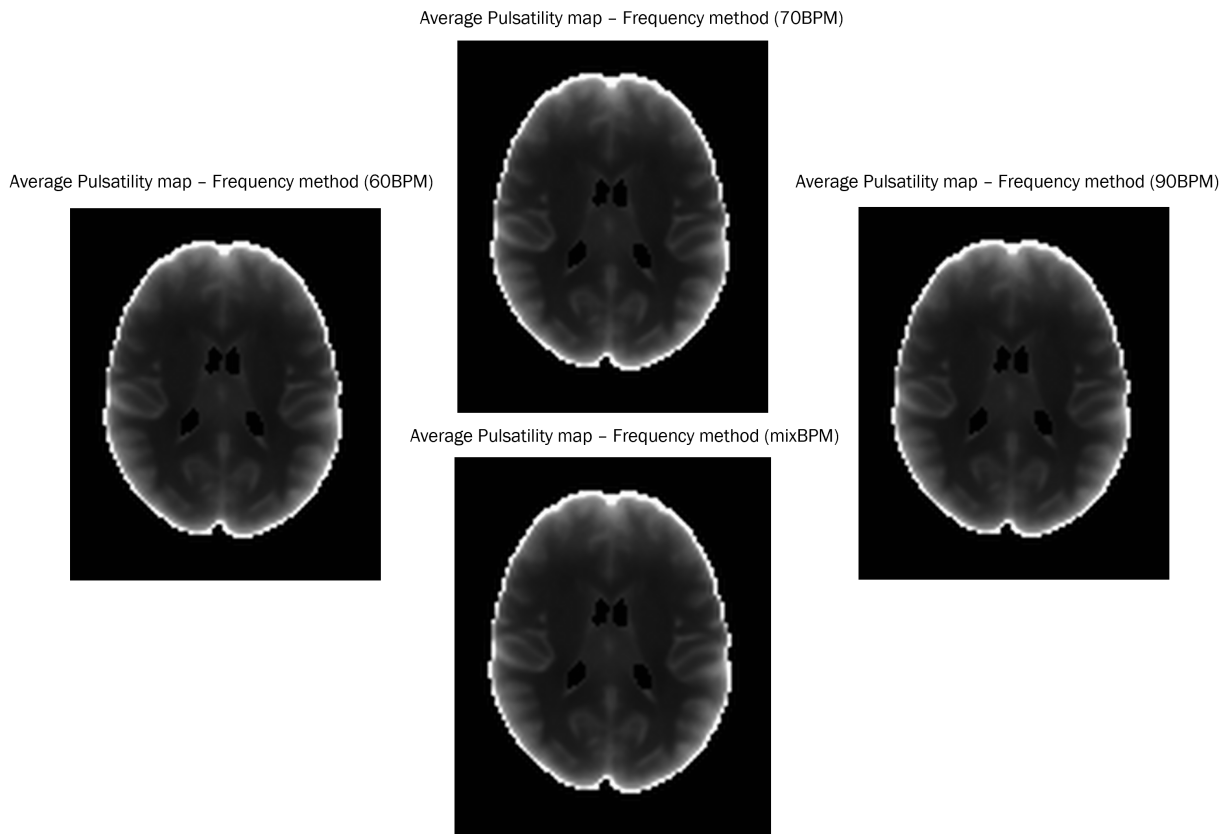


Fig. 5.15 Average Pulsatility maps for the Frequency method. All four methods show very similar maps. Structure can be seen within the GM and a clear GM/WM border is evident with GM greater than WM. The white halo surrounding the brain is thought to be related to the CSF outside of the brain.

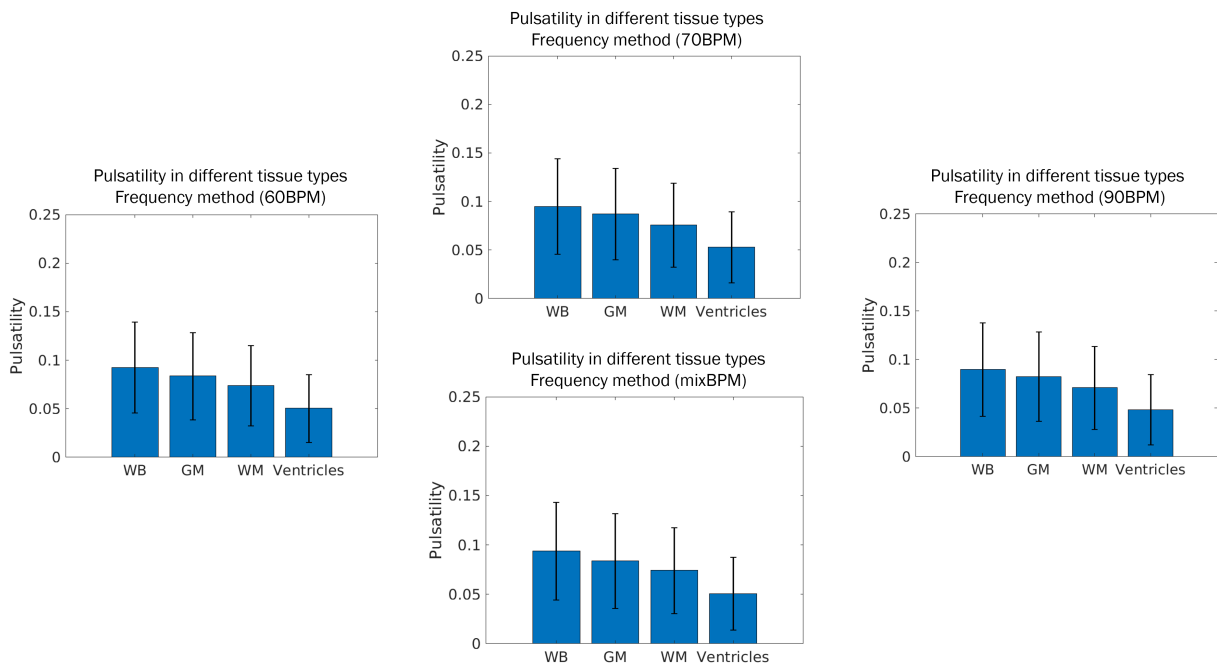


Fig. 5.16 A bar chart showing the estimated pulsatility value in different tissue types using the Frequency method. Error bars are included on these bars and these tend to overlap between methods. This graph shows that there is a hierarchy of pulsatility value ranging from WB to Ventricles (with the largest pulsatility represented in the WB).

5.4.10 "True" Pulsatility

A bar chart showing the average pulsatility (for different tissue types) estimated using the HRV trace is shown in Figure 5.17. Overall, the value of pulsatility was lower using this method when compared to the HRV and Frequency methods.

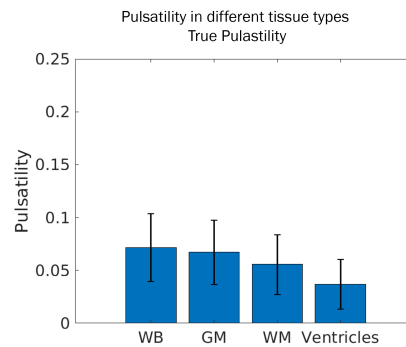


Fig. 5.17 A bar chart showing the estimated pulsatility value in different tissue types using the HRV trace ("true" pulsatility). Error bars are included on these bars and these tend to overlap between methods. This graph shows that there is a hierarchy of pulsatility value ranging from WB to Ventricles (with the largest pulsatility represented in the WB).

5.5 Discussion

Calculation of the effects of pulsatile flow on the microvasculature is an important metric in the tracking and diagnosis of cognitive decline and dementia (Mitchell et al., 2011; Rivera-Rivera et al., 2017; Vikner et al., 2021). In this study, we have presented two novel methods for the calculation of cardiac pulsatility from existing resting state datasets. The first relying on physiological recordings in a subset of participants and the second fully data driven. Both methods were compared to the "true" pulsatility values as measured using the cardiac recordings for a subset of participants (~ 390 participants). Similar values of pulsatility were measured suggesting a high accuracy for both methods with correlation values exceeding 0.88 (associated p -value= 1.2×10^{-125}) in the comparison between each method and the "true" pulsatility.

Initially, it was expected that there would be large differences in the pulsatility estimates generated from the different training datasets. One might expect that the HR values used to train the dataset would bias the classifier to detect cardiac components with similar HR's. However, these results suggest this is not the case. The values of pulsatility estimated using a classifier trained using groups of participants with different HR values (60BPM, 70BPM and 90BPM) were highly correlated with "true" pulsatility values. Furthermore these estimates also correlated highly with pulsatility values estimated using the other training datasets. This suggests that the HR value for participants used in training dataset does not bias the classifier. Figures A.1 and A.2 show scatter graphs that compare the "true" pulsatility estimates with those generated from the novel methods. Comparing these, it is clear that the gradient for those using the HRV method is

much steeper than that of the Frequency method suggesting the HRV estimates are more similar to the "true" pulsatility.

It is expected that as we age, our ability to dampen the pulse pressure from inflowing pulsatile blood decreases. This is due to the increased stiffness of vessels with advancing age (Mitchell et al., 2004) which results in damage to the microvessels within the brain. As such, it is expected that values of pulsatility will correlate highly with age. This was not the case in the results presented here as low correlations were detected. However, the HCP data is not the ideal dataset to see this relationship as the participants were young, healthy adults with a small age range (22-35). A large change in arterial stiffness and pulsatility across this age range is not expected (Reference Values for Arterial Stiffness' Collaboration, 2010).

Increases in BMI have been found to correlate with an increase in arterial stiffening (Kappus et al., 2014). Therefore, a high correlation between BMI and pulsatility was expected. BMI was one of the higher correlations observed for all methods that produced values of pulsatility and was statistically significant for each method. This supports the hypothesis that increases in BMI are associated with increases in arterial stiffness.

Motion regression was used to remove any artifacts due to motion from the time series data. However, high correlations were observed between pulsatility and framewise displacement (FD) even after motion regression. It's important to note that FD and motion are not identical. FD is an estimate of the movement of the head from one volume to another and this does not precisely represent head motion (Power et al., 2012, 2014). Additionally, it was observed that FD and BMI were strongly correlated implying that the higher the BMI, the more FD was present. The relationship between BMI and FD in the HCP dataset has been independently reported by another group (Hodgson et al., 2016) and other studies have shown a similar relationship in other datasets (Beyer et al., 2017; Ekhtiari et al., 2019). In fact, it was reported by Beyer and colleagues that losing weight (and therefore reducing BMI) resulting in a decrease in head motion during MRI (Beyer et al., 2017).

Both methods used to generate pulsatility showed promising results when compared with "true" pulsatility, which leaves the question – which method is better? Figure 5.10 compares the methods with each other to determine the similarities in their pulsatility values. Within each method, the values of pulsatility generated by each training dataset were similar with correlation values greater than 0.80 (associated p -value= 6.37×10^{-217} for lowest correlation). The values generated by the HRV method had slightly higher correlation values and all of which were greater than 0.91 (associated p -value=0). The correlations of pulsatility in WM with the "true" pulsatility were slightly higher than that of GM (Figures 5.4 & 5.5). One explanation for this could be that WM doesn't have the confounding factor of ongoing neuronal-related fluctuations that are present in GM. This, therefore, makes the GM "true" measurements noisier, even though they are larger. Thus, the correlation to the other methods is lower. The downside to the HRV method is the requirement to collect physiological traces along with the fMRI data for classifier training. This would restrict this method to studies that have good quality physiological traces in a subset

of participants. This study used only 100 physiological traces and generated accurate pulsatility maps and so this could be used for bigger studies that have larger numbers of participants. The Frequency method correlation values exceeded 0.89 (associated p -value=0) for all training datasets. The upside to this method is that it can be run on any dataset without the need for external physiological recordings. However, the number of runs analysed for each method within the Frequency method was significantly less than that of the HRV method as shown in Figure 5.11. One explanation could be the strict algorithm used to classify components in the Frequency Method which resulted in small numbers of components classified as cardiac-related for each run. This meant that FIX was unable to detect cardiac-related components based on the training data for some participants. In future, it may be necessary to make the classifying algorithm less strict to overcome this issue. The numbers classified using the HRV method stayed consistent and almost all runs resulted in the production of a measure of pulsatility. This discrepancy in the number of runs classified did not translate to a large loss in participants classified as most participants had at least one of the four runs that was classified by the Frequency Method. As such the number of participants lost was not that great as shown in Figure 5.12.

When comparing values of pulsatility in the different brain tissue types (WB, GM, WM and Ventricles), the WB returned the largest values. This was expected as this mask encompasses signal from all areas of the brain. The GM showed the second largest pulsatility values as expected. Pulsatility in the WM was attributed to cardiac-related noise. The average value of pulsatility varied across methods, with the largest values calculated using the HRV method, and the lowest values calculated using the HRV trace. It was expected that the HRV trace would show the most accurate values of pulsatility. However, only one degree of freedom is used in the estimation of the "true" pulsatility (the HRV trace), whereas the other methods contain multiple degrees of freedom as multiple cardiac components were regressed from the data. Therefore, these methods can explain more variance in the data that is related to pulsatility.

In future, it would be interesting to determine how FIX would perform using a smaller number of training datasets. If this was reducible then the number of high-quality physiological recordings required to generate measures of cardiac pulsatility using the HRV method would be significantly less. This would allow for this method to be used on other studies with smaller numbers of participants or physiological traces. Additionally, it would be useful to discover whether the FIX training datasets generated within this study can be used to classify data from other studies. The FIX recommendation is that the training dataset must be generated from a subset of the data to be classified. However, on looking through the FIX user guides, there are a small number of preset training datasets which FSL recommend to train FIX with. This implies that training datasets can be used between studies assuming the data to be classified was collected and pre-processed under the same conditions as the training data.

5.6 Conclusion

In this chapter, I have introduced two novel methods for generating measures of cardiac pulsatility in the brain that do not require HRV traces for all participants. Both methods perform well when compared with "true" measures of pulsatility (a gold standard). High correlations were observed between the "true" pulsatility values and those of the two novel methods introduced. Training datasets used to train FIX were varied by HR value but no significant difference was detected between the pulsatility values generated by each of these training datasets. This was the case for both methods and indicates that the value of HR used within the training dataset does not influence the classification of cardiac components. Since FIX is based on separating spatial components, perhaps this is not surprising. Correlations between pulsatility generated from these methods and physiological parameters were similar across the different methods. This suggests that both methods work to a similar level of accuracy. The Frequency method does not require any additional information to accompany the rfMRI data when creating training datasets and so can be implemented easily. On the other hand, the HRV method requires high quality physiological information on a subset of participants to generate training datasets. This disqualifies this method in cases where these traces are unavailable (or of a bad quality). The downside to the Frequency method was that it suffered from a large number of imaging runs that could not be classified. Although not problematic for this study, as most participants had at least one run that was classified, it is a potential shortcoming of the method. Of the two methods, the HRV method had the strongest correlation with the "true" pulsatility. This is the reason that I would recommend this method if high quality cardiac traces are available. If these high quality traces are not available, then the Frequency method does produce similar results, although these have a slightly lower correlation with the "true" pulsatility values.

Chapter 6

Discussion

Overview of Thesis

The aim of the work presented in this thesis is to improve the methods currently available to fMRI researchers attempting to measure cerebrovascular function. Gaining a better understanding of how the vascular system works within the brain enables researchers to understand how the breakdown of this system can lead to disease states, such as dementia, and discover methods to mitigate the decline of the system. Current methods used to measure cerebrovascular function include: the measurement of cerebrovascular reactivity (CVR) shown to be impaired in Alzheimer's disease and in people with mild cognitive impairment (Cantin et al., 2011; Glodzik et al., 2013); the measurement of cerebral blood flow (CBF) (Buxton, 2005; Fantini et al., 2016b) which is important in understanding brain function; and the measurement of CMRO₂ (Davis et al., 1998; Germuska et al., 2019; Hoge et al., 1999a; Merola et al., 2016; Wise et al., 2013) which is considered a direct indicator of brain health. The methods to determine these metrics all come with their own limitations and improvements can be made to the analysis pipelines that aim to address them. One such flaw in this is motion, to which fMRI and ASL are both susceptible. Attempts to compensate for this include the use of tactile feedback to reduce motion (Krause et al., 2019), prospective correction methods that correct the motion during scanning (Maclaren et al., 2012; Zahneisen and Ernst, 2016; Zaitsev et al., 2017) and retrospective correction methods that correct the motion after scanning. These methods all fall short in scans of cerebrovascular function (as demonstrated in Chapter 3 - Figure 3.2).

The vast majority of resting state fMRI (rsfMRI) studies infer connectivity between brain regions (Lee et al., 2013; Smith et al., 2013; Van Essen et al., 2013) and identify resting state networks (Lee et al., 2013; Smith et al., 2013; Van Essen et al., 2013). These investigations of functional connectivity have led to studies that aim to detect patients with Alzheimer's disease (Dai et al., 2012; Koch et al., 2012; Supekar et al., 2008), autism (Anderson et al., 2011) and studies that show it is useful in surgical planning (Bettus et al., 2010; Kokkonen et al., 2009; Liu et al., 2009; Shimony et al., 2009). However, rsfMRI can also be used to investigate

cerebrovascular function. One way was explored in Chapters 4 & 5 and uses cardiac pulsatility. By exploiting the relationship between HRV and pulsatility it was possible to make inferences about pulsatility in the brain.

Throughout this work, I have presented different methods to improve our processing pipelines in order to combat some of these issues. Namely, developing new methods to estimate motion parameters in order to generate non-erroneous estimates of motion and developing methods of isolating information pertaining to cardiac frequency fluctuations from resting state BOLD data.

Correcting Motion Registration Errors (Chapter 3)

Initial Thoughts

The first aspect that I attempted to improve upon was that of subject motion correction. Chapter 3 of this work focused on the quantification and reduction of an issue which arises in retrospective correction of motion using the conventional motion correction method in fMRI, the volume registration algorithm (VRA). Although the focus was on AFNI's implementation of the VRA, this issue is present in all variations of the VRA. The issue in question is global changes in MR signal intensity brought about by a global increase in CBF, for example. There are other ways these global changes can occur, however. Throughout this work, these changes are referred to as Global Intensity Changes (GICs) and more details about them can be found in Chapter 2 - Section 2.6.6. Initial inspection of the VRA motion parameter estimate for scans containing Global Intensity Changes (GICs) showed that they looked strikingly similar to the signal causing the GIC, indicating that signals of interest were deemed to be motion and, thus, would be removed in a motion regression step. This is shown in Chapter 3 - Figure 3.2, which shows the motion parameter estimate overlaid with the signal driving the GIC (in this case this was the CO₂ trace).

Analysis of Motion Parameters

Probing further, the estimates generated from the VRA were compared to an external motion tracker (TracInnovations, Bellarup, Denmark) through use of a linear regression with the global (average) signal in the brain. This is shown in Chapter 3 - Figure 3.11 where the R² value represents how well the motion parameter estimates fit the global (average) brain signal. The difference between the camera-based estimates and VRA-based estimates were very clear for some scan types (*Rest+CO₂+ASLTag*), indicating that this is a problem which could cause signal loss when using a VRA to correct for motion. Attempts to reduce the significance of the problem were tested using the same regression tests. The proposed methods included: ICA-based methods where ICs that most closely matched the external influence on the GIC were removed and the VRA was re-run and Erosion-based methods where a mask was eroded at the edges and used in

the VRA to exclude edge voxels from the estimation. Edge voxels contain the biggest signal change when movement is present. Therefore, the Erosion-based methods were expected to work as they removed these edge voxels from the data used to estimate motion. This would prevent the VRA from misinterpreting an increase in signal due to a GIC as motion. However, these methods produced estimates that were similar to the VRA-based estimates disproving this theory. The results showing the linear regression analyses are shown in Chapter 3 - Figures 3.11, 3.12 and 3.13. These figures all looked at how well the motion estimates fit the global signal, the external influence on the GIC and the VRA-based motion parameter estimates. From these results, it was clear that the ICA-based methods showed less GIC variance than the other methods for some scan types (Figure 3.12). It also showed less global signal within these motion estimates (Figure 3.11). However, the scans that did not contain a GIC (*RestOnly* & *Rest+Motion*) showed a similar variance to the VRA-based estimates for these scan types. This was as expected due to the lack of a GIC driving the erroneous misrepresentation of signal as motion.

The *Rest+CO₂+Motion* scan type showed high R^2 values when looking at Figure 3.13 for all correction methods. This suggests that the different correction methods produced motion parameters that were similar to the estimates generated by the VRA-based method. This was attributed to the fact that this scan type is dependent on each participant's ability to hold their breath, which meant that the magnitude of the GIC was variable between participants. This results in a less accurate estimation of the ICA components that are related to the GIC and therefore a less accurate estimate of motion. Also, the breath hold periods and motion are time-locked meaning that, when holding their breath, participants will move more. This could be because of hyperventilation in preparation for the breath hold, or that they are fidgeting more during the breath hold. Therefore, the estimation of motion during a breath hold challenge is difficult and ICA decomposition may be unable to separate motion from CO₂ effects. The Erosion-based method estimates were consistent with the VRA-based methods in most scan types. This implies that this method did not work to reduce this issue as well as expected. In fact, in some cases the use of the eroded mask resulted in a higher R^2 value, suggesting the use of a harsh mask increases the amount of GIC present in the motion estimate. This may result in more noise associated with these harsher masks. The results for the camera were trivial. On inspection of some of the camera-based *registration only* datasets (generated from the rotation and translation of the raw fMRI data with the motion parameters) an obvious amount of motion had been added to the data. This was only present with smaller amounts of motion such as that seen with the *Rest+CO₂* and *Rest+CO₂+ASLTag* scan types. This motion was not included in other *registration only* datasets. This issue was explored in Chapter 3 - Section 3.3.2.2 and arises from the noisy motion parameter estimates. As a result, the camera-based results are questionable for these scan types (*Rest+CO₂* and *Rest+CO₂+ASLTag*) and may not be trustworthy for other scan types. The camera-based estimates were very different to the VRA-based estimates. This was expected as the camera is external to the scanner and not affected by the GICs. This was especially noticeable in the *Rest+ASLTag* scan type and the driver of this difference was shown

to be the PLD-ramp (Figure 3.12). This was not surprising as a larger intensity change would be expected with increasing PLD values. This is because a longer PLD value will equate to more of the tagged blood reaching the target tissue. Therefore, a bigger subtraction from the MR signal would occur translating to a bigger GIC.

Quantification of Cerebrovascular Physiology

As well as investigating the effects of these methods on the motion parameter estimates, I also looked at how they affected the quantification of cerebrovascular physiology. In most cases, the ICA-based methods calculated quantified values that were greater than the VRA-based estimates. This was not surprising as the ICA-based method removes the signal driving the GIC before performing motion correction. As a result, a reduction in the loss of signal of interest would occur. Motion can be broken into two different things: the real motion and GIC-induced apparent motion. These methods aim to reduce the GIC-induced apparent motion. This is important when discussing the quantification of cerebrovascular physiology.

Connectivity

Connectivity analysis was performed for the *RestOnly* and the *Rest+Motion* scan types. The connectivity values were consistent for the *RestOnly* scan type across most of the motion correction methods. A slight deviation was detected for the camera-based *registration only* correction type. However, this was not the case for the *Rest+Motion* scan type as a large amount of variation was detected for these motion correction methods. As discussed earlier, this scan type involved a large motion task which is not standard practice and this could have interfered with the connectivity estimates. The *Rest+Motion* scan type was only used as a way to test the capability of the external motion tracking system and therefore the connectivity results should be treated with care. In both of these scan types there should be no GIC-induced apparent motion as there is no external GIC to introduce this. Therefore connectivity values shouldn't be affected by this apparent motion.

Cerebral Blood Flow (CBF)

Cerebral blood flow (CBF) values were calculated for some scan types as this quantity gives an indication of the amount of blood delivered to brain tissue and is an important indicator of the tissue health. It is expected that as the GIC-induced apparent motion is removed, the CBF value will increase. It is also important to consider the effects that real motion will have on CBF values. A stricter motion correction would leave less signal that could be used to quantify CBF. This would then lead to a lower CBF value. In almost all correction types, a drop in CBF value was detected with the addition of motion regression, the second stage in motion correction (*registration + regression*). The exception to this was the camera-based and Erosion-based

correction methods for the *Rest+ASLTag* scan type (Figure 3.16) which showed an increase in average CBF value. As the camera-based method is independent of the GIC's it suggests that this method removed a lot of real motion. However, when compared to the 'registration only' and 'nomoco' estimates which had average CBF values of around 40 ml/100g/min, it doesn't seem likely that the camera-based regression step would increase the CBF value to around 70 ml/100g/min (an increase of around 30 ml/100g/min). Other results from the camera-based method did show that it didn't work well for similar scan types and so the results shown for the *Rest+ASLTag* should be taken lightly. The Erosion-based correction methods also showed an increase in average CBF value which initially suggests that there was more GIC-induced apparent motion removed. However, the CBF values for each participant are very diffuse which makes the average CBF value unreliable. Therefore, conclusions cannot be drawn about the effectiveness of these correction methods for this scan type. The largest difference between the VRA-based and camera-based motion parameters was seen for the *Rest+ASLTag* scan type in all three analyses performed on the motion parameters (Figures 3.11, 3.12, 3.13).

Cerebrovascular Resistance (CVR)

Values of cerebrovascular resistance (CVR) were calculated as these allow us to understand the ability of blood vessels to contract/dilate in response to stimulus (and therefore the health of the vessels). It is expected that as the GIC-induced apparent motion is removed, the CVR value will increase. After including the regression step of motion correction, the ICA-based methods showed the largest values of CVR overall which follows the expected trend (better motion correction equates to larger CVR values). This was the case in all scan types except for the *Rest+CO₂+ASLTag* scan type where the higher values were estimated by the Erosion-based methods. Aside from this, the Erosion-based methods showed lower values of CVR in the other two scan types (*Rest+CO₂* & *Rest+CO₂+Motion*) when compared to that of the ICA methods.

Cerebral Metabolic Rate of Oxygen Consumption (CMRO₂) & Oxygen Extraction Fraction (OEF)

The cerebral metabolic rate of oxygen consumption (CMRO₂) and oxygen extraction fraction (OEF) could be estimated from the *Rest+CO₂+ASLTag* scan type. As mentioned previously, it is expected that CBF and CVR will be underestimated when there is GIC-induced apparent motion present. If every other physiological parameter was unchanging in this case then it is expected that this would lead to a reduction in CMRO₂. However, in reality, the other physiological parameters aren't going to remain constant. Therefore, it is unclear what would happen with the estimation of CMRO₂ in the case of increased apparent motion. The CMRO₂ results showed a drop in value when the regression motion correction step was included in the analysis. The camera-based and ICA-based methods showed the highest values of CMRO₂. However, none of these fell within the expected CMRO₂ range for the population suggesting the regression

step may be too harsh to allow accurate quantified values to be produced. Aside from this, the *registration only* results were similar to that of no motion correction implying that the *registration only* step does not have much of an effect on the quantification. This also suggests that the *registration only* step has a very minor effect on motion correction in general and the regression step is the driving force which removes the majority of motion. This is also true for the OEF *registration only* results as they are similar to that of no motion correction. The *registration+regression* results show a drop in OEF value when compared to the *registration only* estimates.

These results show that current retrospective motion correction methods lead to erroneous estimates of motion in scans that include GICs. I have shown that for some scan types this can be reduced by using ICA to isolate and temporarily remove the components related to the GIC prior to estimation of motion parameters. This is not the case for all scan types however and further steps, such as motion reduction techniques, should be implemented prior to the correction of motion. Such motion reduction techniques could include the use of memory foam cushions and tactile tape which could reduce the amount of motion present. These techniques were discussed briefly in the introduction to Chapter 3. Masks eroded at the edges do not produce more accurate estimates of motion when compared to the conventional techniques (VRA-based estimation). Although, this could be because the masks used in the study were in line with the initial volume. For subsequent volumes, the mask may introduce errors as the edge voxels may not be in the same location as they were in previous volumes. Therefore, a mask that moves with the subsequent volumes may improve this estimation.

Recommendations

Moving forward I would recommend that an ICA is used in the correction of motion for the following scan types: *Rest+CO₂*, *Rest+CO₂+ASLTag* and *Rest+CO₂+Motion*. This is because I have shown an improvement in motion parameter estimation in these scan types and the addition of this would not add much work to the existing analysis pipelines. For the *Rest+ASLTag* scan type, the results using an ICA weren't significantly different to the VRA-based method and therefore the use of an ICA may not add anything to the correction of motion. Finally, for the scan types that did not contain an external influence on the GIC (*RestOnly* & *Rest+Motion*) because there is no external influence on the GIC's their results were similar to that of the traditional VRA-based method. Therefore in these cases there is no reason to include any of these data-based methods.

Wider Picture

Subject motion is a source of artefact in fMRI studies due to the length of time required to collect the images. Reduction of subject motion is, therefore, important in the world of research as well

as the clinical world. In the following two sections I will outline the impact that this project could have in the research and clinical settings.

Research Impact

In all MR studies, the subject motion problem needs to be considered. This is particularly true when collecting data from groups that are less-compliant, such as children. One way of reducing motion in these groups is behavioural in nature. Showing younger children a movie clip whilst they are being scanned significantly reduced head motion compared to them looking at a fixation cross (Greene et al., 2018). The method outlined in this work is a retrospective method, meaning it is a processing method that works on the data after it has been acquired. There are many different retrospective methods used to correct data of motion. Retrospective correction can make use of motion information collected during the scan through optical tracking systems (Frost et al., 2019; Zaitsev et al., 2006), electromagnetic tracking systems (Afacan et al., 2019), and RF probes (Ooi et al., 2013, 2009). However, these rely on accurate recording of motion using these systems. Other, data-based approaches, are easier to implement as they don't require the use of external equipment. The use of fat-selective excitation as a motion navigator has been shown to estimate motion with high precision (Gallichan et al., 2015). In many cases, external motion trackers are not available and motion must be estimated from the realignment of each image to a reference image (Cox and Jesmanowicz, 1999; Woods et al., 1998). As shown in this work, the image realignment methods fall short for scans of cerebrovascular physiology where there is a GIC present, especially when CO₂ is used a stimulus. This work builds upon the existing image realignment method outlined by (Cox and Jesmanowicz, 1999) to improve it's accuracy when dealing with data that includes a GIC. By improving the accuracy of motion correction researchers will measure physiological parameters with more precision leading to a greater understanding of these physiological parameters.

Clinical Impact

The impact that motion correction has on the clinical world is enormous. Motion artefacts can make it difficult for the interpretation of MRI images which could lead to a diagnosis being missed. By reducing motion there is a chance that these missed diagnoses may not occur. In addition, more accurate physiological measures could allow certain disease states to be recognised earlier. For example, evidence suggests that impaired CVR is associated with dementia risk (Wolters et al., 2016) and stroke risk (Gupta et al., 2013). Certain patient groups will move more while being scanned such as children and patients suffering from Parkinson's disease. Current clinical practice to reduce head motion in children is to use sedation (Dong et al., 2019; Greene et al., 2018) which is costly (Slipsager et al., 2020) and can be risky (Dong et al., 2019). This also could affect the BOLD response. There is evidence suggesting that sedation suppresses the BOLD signal (Hassanzadeh et al., 2023). Other studies show that sedative agents

can affect cerebral blood flow which in turn could affect the haemodynamic response function (Di Francesco et al., 2013). Another study showed that the use of propofol (an anaesthetic agent) was not prohibitive of performing fMRI (Souweidane et al., 1999). Additionally, BOLD signal increases have been detected in response to passive listening, visual and movement tasks while patients are sedated (Ives-Deliperi and Butler, 2015). There doesn't seem to be a consensus. If head motion could be accounted for then these added costs and risks would be reduced. Therefore, by improving motion estimation and correction methods we could better understand cerebrovascular physiology. As well as this we could detect and diagnose certain diseases earlier leading to better care for patients. The work carried out in Chapter 3 aimed to achieve these goals by trying to improve methods to correct for motion in fMRI.

Quantification of Cardiac Pulsatility (Chapters 4 and 5)

In Chapters 4 and 5, I aimed to improve estimation of cardiac pulsatility, specifically from resting state data. Data taken from the Human Connectome Project (HCP) S1200 release was used to calculate values of pulsatility in the brain. Multiple attempts were made to achieve this goal, most of which worked without the use of any external recordings of cardiac signals. These methods took ICA data and attempted to isolate the cardiac-related components. Then, using these cardiac components a measure of pulsatility could be generated. The initial method looked at the frequency content of ICA information. This was used to estimate a frequency range referred to as the cardiac window. The bounds of this window were determined by estimating the range of resting heart rates (HR) for the participants in the study. The initial HR range used was 60BPM-100BPM. However, this was quickly changed to 50BPM-100BPM due to concerns that this range would overlook those with lower resting HR values. Another issue with this method was aliasing which meant that cardiac-related signals could be aliased to a frequency range outside of the cardiac window (as defined previously). Therefore, an expansion of the cardiac window was required. Additionally, the initial results from this method suggested that the algorithm was too lenient and therefore stricter tests were required.

The next iteration of this algorithm also aimed to isolate ICA components related to the cardiac cycle. However, this method differed from the previous method as it worked over a larger cardiac window: 100-400 samples (0.11Hz-0.46Hz). This method also implemented a stricter selection criteria in a three step classifier. This classifier allowed the HR of each participant to be estimated by isolating the frequency 'peak' for each term of the two-term Gaussian curve for each component. Then, the true frequency could be calculated from the aliased frequency (the frequency represented by the frequency peak) using equation 4.2. This resulted in two HR values per run which can be seen in Chapter 4 - Figure 4.4. These HR values were compared with "true" values of HR calculated from physiological data. This comparison can be seen in Chapter 4 - Figure 4.5. These results show that the classification algorithm was unable to determine the correct HR value for participants who's actual HR was around 80-90BPM (1.333-1.500Hz) and

40-50BPM (0.667-0.833Hz). These values are close to the Nyquist and sampling frequencies which shows the classification algorithm is unable to detect cardiac components accurately near to these values.

Once the classification algorithm was refined, values of pulsatility were generated in one of three methods: The regression method, the FFT method and the Bandpass method. These were outlined in detail in Chapter 4 - Sections 4.3.8.6, 4.3.8.7 and 4.3.8.8. These methods varied in complexity, the regression method was the least complex and the FFT method was the most complex. None of the three methods showed a high correlation with each other suggesting that either they are analysing different things about the cardiac cycle or that they are analysing something that has nothing to do with the cardiac cycle. The FFT and bandpass methods both worked with bespoke frequency windows taken from the full frequency spectrum whereas the regression method worked with spatial ICA component time series. As a result, the FFT and bandpass methods could be evaluating other signals that were contained within the frequency window as well as the cardiac-related information. Thus, these methods may not isolate only cardiac-related information. Therefore, the regression method was the method of choice to generate pulsatility as it was determined that this method is the most likely to isolate only cardiac-related information. This method still had flaws related to aliasing, however. This led onto Chapter 5 which fixed the issues with the classification algorithm by using FMRIB's ICA-based Xnoisifier (FIX).

The main issue with the 100-400 samples classification algorithm was the aliasing issue which meant that cardiac-related information in participants with HR value around 80-90BPM and 40-50BPM were not selected accurately. In an attempt to fix this, FIX was used to classify components based on a training dataset generated from the classification algorithm. Four training datasets were generated each of which contained participants with HR value of 60BPM, 70BPM, 90BPM and a mix of the participants in these three groups (called the mixBPM group). Each dataset contained 100 randomly selected participants. FIX was trained with these training datasets and used to classify the components for the other rfMRI runs. This method was called the Frequency Method. Additionally, a second method was used to identify which components were related to the cardiac cycle. This method used high quality HRV traces processed by Kassiopoulous and Mitsis (Kassiopoulous and Mitsis, 2020). A correlation analysis was used to determine which of the cardiac components showed a significant correlation with the processed cardiac traces and these were used to train FIX. The training datasets were created in the same way as those for the Frequency method, with the same 100 participants making up four training datasets and had each with a different HR value (60BPM, 70BPM, 90BPM, mixBPM). This method was called the HRV method. Generation of pulsatility maps followed the same method outlined in Chapter 4 - Section 4.3.8.6 and pulsatility was calculated using WB, GM, and WM masks. Additionally, the cardiac traces were used to calculate "true" pulsatility values by using them as regressors in a linear regression from the rfMRI datasets. In an ideal world, this would be the best method to produce pulsatility maps. However this relies on the availability of good

quality physiological monitoring which is not always easy to achieve. A better approach might be to collect only a select number of physiological traces and use a classifier to generate these estimates of cardiac pulsatility. However, as a sanity check the "true" pulsatility values were generated and these were compared to the values generated by both the HRV and Frequency methods.

Both methods estimated pulsatility values that correlated highly with the "true" pulsatility which shows that these methods are in fact generating valid pulsatility information. This also shows that the classification methods used work well to isolate cardiac-related data from an ICA. The values generated between training datasets also showed a high correlation and this was even true between methods. This was not what was originally expected as there was a worry that the training datasets would bias FIX to classify information related to the HR of the training dataset that trained it. However, this was not the case as shown in the highly correlated pulsatility values generated from each training dataset. This is advantageous as it allows for studies to collect cardiac traces in only a small number of participants. The method of choice would depend on a few factors. The results show that the HRV method is slightly more accurate in determining pulsatility. However, this method relies on the collection of a small number of high quality HRV traces. This is problematic for some studies that may not have collected such information or those that have low quality HRV traces. This is not the case for the Frequency method which does not need external recordings to work. However, the results also showed a discrepancy in the number of rfMRI runs analysed in comparison to the HRV method. I attributed this to the strict algorithm that classified the components in the Frequency method which may result in a lack of classification in some runs. The result is that FIX could not distinguish the cardiac-related information for similar runs which could result in less cardiac-related components classified. In this work, the number of runs did not translate to a large loss in the number of participants.

Aside from looking at the accuracy of the classifiers, I also performed correlation analyses between the pulsatility values and common physiological parameters. The reason for this was to determine if the values of pulsatility estimated by these methods correlated with these physiological parameters in the expected way (as seen with the "true" pulsatility correlations with physiological parameters). This would also allow conclusions to be drawn about the population and their current cerebro-physiological health. Significant correlation values between pulsatility and BMI as well as pulsatility and FD were observed. The former was expected as a higher BMI has been associated with increases in arterial stiffness (Kappus et al., 2014). The latter was surprising as steps were taken to correct for motion in these datasets. A relationship between BMI and FD was shown which is supported by other literature (Beyer et al., 2017; Ekhtiari et al., 2019; Hodgson et al., 2016). A significant correlation between age and pulsatility was not detected even though this correlation was expected prior to analysis. On reflection, a large correlation between age and pulsatility would be difficult to observe in this data as the participants were young adults. Overall, these methods worked well at isolating cardiac-related components from an ICA and allowed the estimation of accurate pulsatility values to be achieved. These methods

would be a viable option for any study that would like to generate measures of pulsatility in resting state fMRI datasets.

Wider Picture

The estimation of cardiac pulsatility has the potential to be an important biomarker for tracking cognitive decline from mild cognitive impairment to dementia (Mitchell et al., 2011; Rivera-Rivera et al., 2017; Vikner et al., 2021). It has been shown to correlate with hypertension in cerebral vessels (van den Kerkhof et al., 2023) and to be associated with cerebral small vessel disease (cSVD) in stroke patients (Birnefeld et al., 2019). Patients with acute ischemic stroke and transient ischemic attacks (TIA's) the pulsatility index in the middle cerebral arteries was found to be increased as the severity of intracranial arterial calcification increased (Park et al., 2012). There is evidence suggesting that the pulsatility index correlates with intracranial pressure in patients with clinical features of intracranial hypertension (Kaloria et al., 2020). It could allow for insights to be made about the glymphatic system. The work outlined in Chapters 4 and 5 introduced novel methods for the estimation of cardiac pulsatility in resting state fMRI. In the following sections I will outline the research and clinical impacts of this work.

Research Impact

Measurement of cardiac pulsatility is difficult using fMRI due to the low number of samples collected in a typical fMRI acquisition. Approaches to measure pulsatile flow do exist (Markl et al., 2016; Whittaker et al., 2022), but these only work in large arteries. Our approach works in smaller arteries and would allow us to determine cardiac pulsatility in these. In the case of arterial stiffening, it is unclear whether we would measure an increase or decrease in cardiac pulsatility in smaller vessels, but this technique could allow us to investigate this question further and potentially determine the answer.

The glymphatic system, a clearance pathway that removes solutes from the brain (Hablitz and Nedergaard, 2021; Iliff et al., 2012) is mediated by arterial pulsations (Hablitz and Nedergaard, 2021; Iliff et al., 2013; Jessen et al., 2015; Weller et al., 2008) as well as other physiological processes such as respiration and CSF pressure gradients. Arterial pulsations alter the size of perivascular spaces which send CSF into the brain (Hablitz and Nedergaard, 2021). With age, arteries stiffen and it has been suggested that the stiffening of arteries could result in a decrease in solute clearance (a reduction in the glymphatic capacity) (Hughes et al., 2015). Therefore estimation of pulsatility in these arteries could give insights to the glymphatic system. Another study demonstrated that changes in arterial pulsatility lead to the accumulation and deposition of toxic solutes in the ageing brain (Iliff et al., 2013). Iliff et al also suggested that the deposited solutes could lead to a further reduction in arterial pulsatility, causing a feedforward pathogenic cycle leading to further neurodegeneration (Iliff et al., 2013).

Clinical Impact

Blood moving through vessels in pulsatile and high pressured. Arteries allow blood to flow from the heart and around the body. These arteries have elastic walls to allow them to accommodate the pulsatile, high pressured blood flowing through them. These vessels can distend and dampen the pulsatile flow before it reaches smaller vessels which are unable to accommodate such pressures. However, in ageing and disease, these vessels can stiffen and their ability to dampen the blood flow is reduced. This can lead to damage to smaller vessels and disease states such as cSVD. Pulsatility is related to stiffness and its measurement could allow for certain disease states to be understood better. Such disease states include: Dementia (and mild cognitive decline) (Mitchell et al., 2011; Rivera-Rivera et al., 2017; Vikner et al., 2021), cSVD (Birnefeld et al., 2019), hypertension (van den Kerkhof et al., 2023), intracranial hypertension (Kaloria et al., 2020), and stroke (and TIA's) (Birnefeld et al., 2019; Park et al., 2012). Measurement of cardiac pulsatility could allow us to better understand the glymphatic system. This is important from a clinical perspective as the glymphatic system is known to play a key role in the removal of solutes in the brain (Hablitz and Nedergaard, 2021; Iliff et al., 2012). These accumulation of these solutes is characteristic of Alzheimer's disease (Hawkes et al., 2011; Weller et al., 2007) and understanding this system better could allow earlier diagnosis of Alzheimer's disease. In addition, the glymphatic system could be responsible for the prevention of other neurodegenerative diseases such as Parkinson's disease (Kylkilahti et al., 2021).

The overarching goal of this thesis was to improve current methods of measuring cerebrovascular function in fMRI. I believe that the results provided throughout this thesis prove that these methods can be improved with small changes to analysis pipelines. An ICA used as part of conventional motion correction has been shown to improve estimates of motion as well as estimates of cerebrovascular function in some scan types. As well as this, the estimation of cardiac pulsatility is possible from resting state fMRI datasets via the use of FIX, the frequency component of an ICA and a small number of high quality cardiac traces. This work will open up the possibility of evaluating cardiac pulsatility in large datasets where there was no cardiac data collected facilitating more cerebrovascular discoveries.

Future Directions

Motion Correction (Chapter 3)

The work conducted within this chapter focused on improving the conventional retrospective motion correction methods used in fMRI, namely the volume registration algorithm. Of the methods used to improve this, the Erosion-based methods did not work as well as I had initially expected. I outlined in section 6 that the reason for this could be down to the fixation of the erosion mask in a single position. So as subsequent volumes are evaluated, in extreme cases the location of the edge voxels (which are the voxels that I wanted to erode) may not be located

within the eroded section of the mask. This may be problematic as the intensity change at edge voxels is expected to be largest and so the most erroneous motion parameter estimates would originate from these voxels. Therefore, a potential improvement might be to use a mask that moves with the subsequent volumes. A potential caveat is that in order to move the eroded mask accurately, one would need to know the motion parameter from one volume to the next. Therefore, it is unclear if this would result in a feedback cycle that may end in a failure of this method.

As well as improving on the Erosion-based methods, it would be interesting to determine why all the other data based methods failed when working on the *Rest+ASLTag* scan type. Finding a method that is robust for all scans of cerebrovascular function is the ultimate goal. Although, this is a difficult feat and may not be achievable as shown by this work without the use of external recordings of motion.

Estimation of Cardiac Pulsatility (Chapters 4 & 5)

The future of this work could investigate the smallest number of training datasets required to produce accurate values of pulsatility. Reducing the number of training datasets would mean that the number of high quality cardiac traces required would be significantly reduced for a given study. This would allow this method to be more accessible for those who are unable to collect such data, or those who do not have access to this data. Further improvements could be made by examining the severity of the Frequency method classifier to understand if this explains the lack of classification by FIX in some run instances (as explained in section 6). Finally, the transferability of one FIX training dataset to another dataset could be investigated. The FSL website (which explains how to use FIX) provides training datasets that can be used with other data. This suggests that the training datasets could be applied widely thus negating the need for high quality cardiac traces. These training datasets may only work if the data to be classified is processed in the same way as the training datasets were.

References

- Afacan, O., Wallace, T. E., and Warfield, S. K. (2019). Retrospective correction of head motion using measurements from an electromagnetic tracker. *Magnetic Resonance in Medicine*, 83(2):427–437.
- Alsop, D. C., Detre, J. A., Golay, X., Gunther, M., Hendrikse, J., Hernandez-Garcia, L., Lu, H., MacIntosh, B. J., Parkes, L. M., Smits, M., van Osch, M. J., Wang, D. J., Wong, E. C., and Zaharchuk, G. (2015). Recommended implementation of arterial spin-labeled perfusion mri for clinical applications: A consensus of the ismrn perfusion study group and the european consortium for asl in dementia. *Magn Reson Med*, 73(1):102–16.
- Anderson, J. S., Nielsen, J. A., Froehlich, A. L., DuBray, M. B., Druzgal, T. J., Cariello, A. N., Cooperrider, J. R., Zielinski, B. A., Ravichandran, C., Fletcher, P. T., and et al. (2011). Functional connectivity magnetic resonance imaging classification of autism. *Brain*, 134(12):3742–3754.
- Andersson, J. L., Skare, S., and Ashburner, J. (2003). How to correct susceptibility distortions in spin-echo echo-planar images: Application to diffusion tensor imaging. *NeuroImage*, 20(2):870–888.
- Bandettini, P. A., Wong, E. C., Hinks, R. S., Tikofsky, R. S., and Hyde, J. S. (1992). Time course epi of human brain function during task activation. *Magn Reson Med*, 25(2):390–7.
- Barth, M., Breuer, F., Koopmans, P. J., Norris, D. G., and Poser, B. A. (2015). Simultaneous multislice (sms) imaging techniques. *Magnetic Resonance in Medicine*, 75(1):63–81.
- Beckmann, C. F. and Smith, S. M. (2004). Probabilistic independent component analysis for functional magnetic resonance imaging. *IEEE Trans Med Imaging*, 23(2):137–52.
- Berglund, J., van Niekerk, A., Rydén, H., Sprenger, T., Avventi, E., Norbeck, O., Glimberg, S. L., Olesen, O. V., and Skare, S. (2020). Prospective motion correction for diffusion weighted epi of the brain using an optical markerless tracker. *Magnetic Resonance in Medicine*, 85(3):1427–1440.
- Bettus, G., Bartolomei, F., Confort-Gouny, S., Guedj, E., Chauvel, P., Cozzone, P. J., Ranjeva, J. P., and Guye, M. (2010). Role of resting state functional connectivity mri in presurgical investigation of mesial temporal lobe epilepsy. *J Neurol Neurosurg Psychiatry*, 81(10):1147–54.
- Beyer, F., Kharabian Masouleh, S., Huntenburg, J. M., Lampe, L., Luck, T., Riedel-Heller, S. G., Loeffler, M., Schroeter, M. L., Stumvoll, M., Villringer, A., and et al. (2017). Higher body mass index is associated with reduced posterior default mode connectivity in older adults. *Human Brain Mapping*.
- Bianciardi, M., Fukunaga, M., van Gelderen, P., Horovitz, S. G., de Zwart, J. A., Shmueli, K., and Duyn, J. H. (2009). Sources of functional magnetic resonance imaging signal fluctuations in the human brain at rest: A 7 t study. *Magnetic Resonance Imaging*, 27(8):1019–1029.

- Billett, H. H. (1990). *Hemoglobin and Hematocrit*, chapter 151. Butterworth.
- Birnefeld, J., Wåhlin, A., Eklund, A., and Malm, J. (2019). Cerebral arterial pulsatility is associated with features of small vessel disease in patients with acute stroke and tia: A 4d flow mri study. *Journal of Neurology*, 267(3):721–730.
- Biswal, B., Zerrin Yetkin, F., Haughton, V. M., and Hyde, J. S. (1995). Functional connectivity in the motor cortex of resting human brain using echo-planar mri. *Magnetic Resonance in Medicine*, 34(4):537–541.
- Bloch, F. (1946). Nuclear induction. *Physical Review*, 70(7-8):460–474.
- Bloch, F., Hansen, W. W., and Packard, M. (1946). The nuclear induction experiment. *Physical Review*, 70(7-8):474–485.
- Borogovac, A. and Asllani, I. (2012). Arterial spin labeling (asl) fmri: Advantages, theoretical constrains and experimental challenges in neurosciences. *International Journal of Biomedical Imaging*, 2012:1–13.
- Bright, M. G. and Murphy, K. (2015). Is fmri "noise" really noise? resting state nuisance regressors remove variance with network structure. *Neuroimage*, 114:158–69.
- Buxton, R. (2009). *Introduction To Functional Magnetic Resonance Imaging*. Cambridge University Press, New York.
- Buxton, R., L.R.; F., E.C.; W., B.; S., S.; W., and R.R, E. (1998). A general kinetic model for quantatative perfusion imaging with arterial spin labelling. *MRM* 40:383-396.
- Buxton, R. B. (2005). Quantifying cbf with arterial spin labeling. *J Magn Reson Imaging*, 22(6):723–6.
- Caballero-Gaudes, C. and Reynolds, R. C. (2017). Methods for cleaning the bold fmri signal. *NeuroImage*, 154:128–149.
- Cantin, S., Villien, M., Moreaud, O., Tropres, I., Keignart, S., Chipon, E., Le Bas, J.-F., Warnking, J., and Krainik, A. (2011). Impaired cerebral vasoreactivity to co2 in alzheimer’s disease using bold fmri. *NeuroImage*, 58(2):579–587.
- Carr, H. Y. and Purcell, E. M. (1954). Effects of diffusion on free precession in nuclear magnetic resonance experiments. *Physical Review*, 94(3):630–638.
- Cecelja, M. and Chowienczyk, P. (2010). Arterial stiffening. *Hypertension*, 56(1):29–30.
- Chen, J. E. and Glover, G. H. (2015). Bold fractional contribution to resting-state functional connectivity above 0.1 hz. *NeuroImage*, 107:207–218.
- Chen, J. J. (2018). Cerebrovascular-reactivity mapping using mri: Considerations for alzheimer’s disease. *Frontiers in Aging Neuroscience*, 10.
- Chen, J. J., Wieckowska, M., Meyer, E., and Pike, G. B. (2008). Cerebral blood flow measurement using fmri and pet: a cross-validation study. *Int J Biomed Imaging*, 2008:516359.
- Cipolla, M. J. (2016). *The cerebral circulation*. Morgan & Claypool Life Sciences.
- Climie, R. E., Gallo, A., Picone, D. S., Di Lascio, N., van Sloten, T. T., Guala, A., Mayer, C. C., Hametner, B., and Bruno, R. M. (2019). Measuring the interaction between the macro- and micro-vasculature. *Front Cardiovasc Med*, 6:169.

- Cohen, A. D. and Wang, Y. (2019). Improving the assessment of breath-holding induced cerebral vascular reactivity using a multiband multi-echo asl/bold sequence. *Sci Rep*, 9(1):5079.
- Cox, R. (1996). Afni: software for analysis and visualization of functional magnetic resonance neuroimages. *Comput Biomed Res*, 29(3):162–173.
- Cox, R. and Hyde, J. (1997). Software tools for analysis and visualization of fmri data. *NMR in Biomedicine*, 10:171–178.
- Cox, R. W. and Jesmanowicz, A. (1999). Real-time 3d image registration for functional mri. *Magnetic Resonance in Medicine*, 42(6):1014–1018.
- Dai, Z., Yan, C., Wang, Z., Wang, J., Xia, M., Li, K., and He, Y. (2012). Discriminative analysis of early alzheimer’s disease using multi-modal imaging and multi-level characterization with multi-classifier (m3). *NeuroImage*, 59(3):2187–2195.
- Davis, T. L., Kwong, K. K., Weisskoff, R. M., and Rosen, B. R. (1998). Calibrated functional mri: mapping the dynamics of oxidative metabolism. *Proceedings of the National Academy of Sciences of the United States of America*, 95(4):1834–1839.
- DeYoe, E. A. and Raut, R. V. (2014). Visual mapping using blood oxygen level dependent functional magnetic resonance imaging. *Neuroimaging Clin N Am*, 24(4):573–84.
- Di Francesco, M. W., Robertson, S. A., Karunanayaka, P., and Holland, S. K. (2013). Bold fmri in infants under sedation: Comparing the impact of pentobarbital and propofol on auditory and language activation. *Journal of Magnetic Resonance Imaging*, 38(5):1184–1195.
- Dong, S., Zhu, M., and Bulas, D. (2019). Techniques for minimizing sedation in pediatric mri. *Journal of Magnetic Resonance Imaging*, 50(4):1047–1054.
- Ekhtiari, H., Kuplicki, R., Yeh, H.-w., and Paulus, M. P. (2019). Physical characteristics not psychological state or trait characteristics predict motion during resting state fmri. *Scientific Reports*, 9(1).
- Elster, A. D. (1993). Gradient-echo mr imaging: Techniques and acronyms. *Radiology*, 186(1):1–8.
- Essig, M., Shiroishi, M. S., Nguyen, T. B., Saake, M., Provenzale, J. M., Enterline, D., Anzalone, N., Dörfler, A., Rovira, A., Wintermark, M., and Law, M. (2013). Perfusion mri: the five most frequently asked technical questions. *AJR Am J Roentgenol*, 200(1):24–34.
- Fantini, S., Sassaroli, A., Tgavalekos, K. T., and Kornbluth, J. (2016a). Cerebral blood flow and autoregulation: current measurement techniques and prospects for noninvasive optical methods. *Neurophotonics*, 3(3):031411.
- Fantini, S., Sassaroli, A., Tgavalekos, K. T., and Kornbluth, J. (2016b). Cerebral blood flow and autoregulation: Current measurement techniques and prospects for noninvasive optical methods. *Neurophotonics*, 3(3):031411.
- Fierstra, J., Sobczyk, O., Battisti-Charbonney, A., Mandell, D. M., Poublanc, J., Crawley, A. P., Mikulis, D. J., Duffin, J., and Fisher, J. A. (2013). Measuring cerebrovascular reactivity: what stimulus to use? *J Physiol*, 591(23):5809–21.
- Finn, E. S., Huber, L., and Bandettini, P. A. (2021). Higher and deeper: Bringing layer fmri to association cortex. *Progress in Neurobiology*, 207:101930.

- Frost, R., Wighton, P., Karahanoğlu, F. I., Robertson, R. L., Grant, P. E., Fischl, B., Tisdall, M. D., and van der Kouwe, A. (2019). Markerless high-frequency prospective motion correction for neuroanatomical mri. *Magnetic Resonance in Medicine*, 82(1):126–144.
- Gallichan, D., Marques, J. P., and Gruetter, R. (2015). Retrospective correction of involuntary microscopic head movement using highly accelerated fat image navigators (3d fatnavs) at 7t. *Magnetic Resonance in Medicine*, 75(3):1030–1039.
- Germuska, M., Chandler, H., Stickland, R., Foster, C., Fasano, F., Okell, T., Steventon, J., Tomassini, V., Murphy, K., Wise, R., and et al. (2019). Dual-calibrated fmri measurement of absolute cerebral metabolic rate of oxygen consumption and effective oxygen diffusivity. *NeuroImage*, 184:717–728.
- Germuska, M., Merola, A., Murphy, K., Babic, A., Richmond, L., Khot, S., Hall, J. E., and Wise, R. G. (2016). A forward modelling approach for the estimation of oxygen extraction fraction by calibrated fmri. *Neuroimage*, 139:313–323.
- Glasser, M. F., Sotiropoulos, S. N., Wilson, J. A., Coalson, T. S., Fischl, B., Andersson, J. L., Xu, J., Jbabdi, S., Webster, M., Polimeni, J. R., Van Essen, D. C., Jenkinson, M., and Consortium, W. U.-M. H. (2013). The minimal preprocessing pipelines for the human connectome project. *Neuroimage*, 80:105–24.
- Glodzik, L., Randall, C., Rusinek, H., and de Leon, M. J. (2013). Cerebrovascular reactivity to carbon dioxide in alzheimer’s disease. *Journal of Alzheimer’s Disease*, 35(3):427–440.
- Glover, G. H. (2011). Overview of functional magnetic resonance imaging. *Neurosurg Clin N Am*, 22(2):133–9, vii.
- Gohel, S. R. and Biswal, B. B. (2015). Functional integration between brain regions at rest occurs in multiple-frequency bands. *Brain Connectivity*, 5(1):23–34.
- Gorelick, P. B., Scuteri, A., Black, S. E., DeCarli, C., Greenberg, S. M., Iadecola, C., Launer, L. J., Laurent, S., Lopez, O. L., Nyenhuis, D., and et al. (2011). Vascular contributions to cognitive impairment and dementia. *Stroke*, 42(9):2672–2713.
- Greene, D. J., Koller, J. M., Hampton, J. M., Wesevich, V., Van, A. N., Nguyen, A. L., Hoyt, C. R., McIntyre, L., Earl, E. A., Klein, R. L., and et al. (2018). Behavioral interventions for reducing head motion during mri scans in children. *NeuroImage*, 171:234–245.
- Griffanti, L., Douaud, G., Bijsterbosch, J., Evangelisti, S., Alfaro-Almagro, F., Glasser, M. F., Duff, E. P., Fitzgibbon, S., Westphal, R., Carone, D., and et al. (2017). Hand classification of fmri ica noise components. *NeuroImage*, 154:188–205.
- Griffanti, L., Salimi-Khorshidi, G., Beckmann, C. F., Auerbach, E. J., Douaud, G., Sexton, C. E., Zsoldos, E., Ebmeier, K. P., Filippini, N., Mackay, C. E., Moeller, S., Xu, J., Yacoub, E., Baselli, G., Ugurbil, K., Miller, K. L., and Smith, S. M. (2014). Ica-based artefact removal and accelerated fmri acquisition for improved resting state network imaging. *Neuroimage*, 95:232–47.
- Griswold, M. A., Jakob, P. M., Heidemann, R. M., Nittka, M., Jellus, V., Wang, J., Kiefer, B., and Haase, A. (2002). Generalized autocalibrating partially parallel acquisitions (grappa). *Magnetic Resonance in Medicine*, 47(6):1202–1210.
- Grubb, R. L., Raichle, M. E., Eichling, J. O., and Ter-Pogossian, M. M. (1974). The effects of changes in paco₂ on cerebral blood volume, blood flow, and vascular mean transit time. *Stroke*, 5(5):630–639.

- Gupta, A., Chazen, J., and Hartman, M. (2013). Cerebrovascular reserve and stroke risk in patients with carotid stenosis or occlusion: A systematic review and meta-analysis. *Journal of Vascular Surgery*, 57(6):1720.
- Hablitz, L. M. and Nedergaard, M. (2021). The glymphatic system. *Current Biology*, 31(20).
- Hahn, E. L. (1950a). Nuclear induction due to free larmor precession. *Physical Review*, 77(2):297–298.
- Hahn, E. L. (1950b). Spin echoes. *Physical Review*, 80(4):580–594.
- Hanon, O., Haulon, S., Lenoir, H., Seux, M.-L., Rigaud, A.-S., Safar, M., Girerd, X., and Francoise, F. (2005). Relationship between arterial stiffness and cognitive function in elderly subjects with complaints of memory loss. *Stroke*, 36(10):2193–2197.
- Hassanzadeh, E., Hornak, A., Hassanzadeh, M., Warfield, S. K., Pearl, P. L., Bolton, J., Suarez, R., Stone, S., Stufflebeam, S., and Ailion, A. S. (2023). Comparison of fmri language laterality with and without sedation in pediatric epilepsy. *NeuroImage: Clinical*, 38:103448.
- Hawkes, C. A., Härtig, W., Kacza, J., Schliebs, R., Weller, R. O., Nicoll, J. A., and Carare, R. O. (2011). Perivascular drainage of solutes is impaired in the ageing mouse brain and in the presence of cerebral amyloid angiopathy. *Acta Neuropathologica*, 121(4):431–443.
- Henson, R., Buechel, C., Josephs, O., and Friston, K. (1999). The slice-timing problem in event-related fmri. *NeuroImage*, 9:125.
- Hodgson, K., Poldrack, R. A., Curran, J. E., Knowles, E. E., Mathias, S., Göring, H. H., Yao, N., Olvera, R. L., Fox, P. T., Almasy, L., and et al. (2016). Shared genetic factors influence head motion during mri and body mass index. *Cerebral Cortex*.
- Hoge, R. D., Atkinson, J., Gill, B., Crelier, G. R., Marrett, S., and Pike, G. B. (1999a). Linear coupling between cerebral blood flow and oxygen consumption in activated human cortex. *Proceedings of the National Academy of Sciences*, 96(16):9403–9408.
- Hoge, R. D., Atkinson, J., Gill, B., Crelier, G. R., Marrett, S., and Pike, G. B. (1999b). Linear coupling between cerebral blood flow and oxygen consumption in activated human cortex. *Proceedings of the National Academy of Sciences*, 96(16):9403–9408.
- Huettel, S., Song, A., and McCarthy, G. (2014). *Functional Magnetic Resonance Imaging*. Sinauer.
- Hughes, T. M., Craft, S., and Lopez, O. L. (2015). Review of ‘the potential role of arterial stiffness in the pathogenesis of alzheimer’s disease’. *Neurodegenerative Disease Management*, 5(2):121–135.
- Iliff, J. J., Wang, M., Liao, Y., Plogg, B. A., Peng, W., Gundersen, G. A., Benveniste, H., Vates, G. E., Deane, R., Goldman, S. A., and et al. (2012). A paravascular pathway facilitates csf flow through the brain parenchyma and the clearance of interstitial solutes, including amyloid β . *Science Translational Medicine*, 4(147).
- Iliff, J. J., Wang, M., Zeppenfeld, D. M., Venkataraman, A., Plog, B. A., Liao, Y., Deane, R., and Nedergaard, M. (2013). Cerebral arterial pulsation drives paravascular csf–interstitial fluid exchange in the murine brain. *The Journal of Neuroscience*, 33(46):18190–18199.
- Ives-Deliperi, V. L. and Butler, J. T. (2015). Functional mapping in pediatric epilepsy surgical candidates: Functional magnetic resonance imaging under sedation with chloral hydrate. *Pediatric Neurology*, 53(6):478–484.

- Jahanian, H., Christen, T., Moseley, M. E., Pajewski, N. M., Wright, C. B., Tamura, M. K., and Zaharchuk, G. (2016). Measuring vascular reactivity with resting-state blood oxygenation level-dependent (bold) signal fluctuations: A potential alternative to the breath-holding challenge? *Journal of Cerebral Blood Flow & Metabolism*, 37(7):2526–2538.
- James, N. L., Milijasevic, Z., Ujhazy, A., Edwards, G., Jermyn, K., Mynard, J. P., and Celermajer, D. S. (2019). The common carotid artery provides significant pressure wave dampening in the young adult sheep. *IJC Heart & Vasculature*, 23:100343.
- Jandackova, V. K., Scholes, S., Britton, A., and Steptoe, A. (2016). Are changes in heart rate variability in middle-aged and older people normative or caused by pathological conditions? findings from a large population-based longitudinal cohort study. *Journal of the American Heart Association*, 5(2).
- Jenkinson, M., Bannister, P., Brady, M., and Smith, S. (2002). Improved optimization for the robust and accurate linear registration and motion correction of brain images. *NeuroImage*, 17(2):825–841.
- Jenkinson, M., Bijsterbosch, J., Chappell, M., and Winkler, A. (2020). *Short introduction to the general linear model for neuroimaging*. Independently published.
- Jenkinson, M. and Smith, S. (2001). A global optimisation method for robust affine registration of brain images. *Medical Image Analysis*, 5(2):143–156.
- Jessen, N. A., Munk, A. S., Lundgaard, I., and Nedergaard, M. (2015). The glymphatic system: A beginner's guide. *Neurochemical Research*, 40(12):2583–2599.
- Jezzard, P. and Balaban, R. S. (1995). Correction for geometric distortion in echo planar images from b0 field variations. *Magnetic Resonance in Medicine*, 34(1):65–73.
- Jezzard, P., Matthews, P., and Smith, S. (2003). *Functional Magnetic Resonance Imaging: An Introduction to Methods*. OUP Oxford.
- Kalaria, N., Panda, N. B., Bhagat, H., Kalaria, N., Soni, S. L., Chauhan, R., Chhabra, R., and Jangra, K. (2020). Pulsatility index reflects intracranial pressure better than resistive index in patients with clinical features of intracranial hypertension. *Journal of Neurosciences in Rural Practice*, 11:144–150.
- Kappus, R. M., Fahs, C. A., Smith, D., Horn, G. P., Agiovlasitis, S., Rossow, L., Jae, S. Y., Heffernan, K. S., and Fernhall, B. (2014). Obesity and overweight associated with increased carotid diameter and decreased arterial function in young otherwise healthy men. *Am J Hypertens*, 27(4):628–34.
- Kassinopoulos, M. and Mitsis, G. D. (2020). Physiological noise modelling in fmri based on the pulsatile component of photoplethysmograph. *bioRxiv*.
- Kastrup, A., Krüger, G., Neumann-Haefelin, T., and Moseley, M. E. (2001). Assessment of cerebrovascular reactivity with functional magnetic resonance imaging: Comparison of co2 and breath holding. *Magnetic Resonance Imaging*, 19(1):13–20.
- Kety, S. S. and Schmidt, C. F. (1948). The effects of altered arterial tensions of carbon dioxide and oxygen on cerebral blood flow and cerebral oxygen consumption of normal young men 1. *Journal of Clinical Investigation*, 27(4):484–492.
- Koch, W., Teipel, S., Mueller, S., Benninghoff, J., Wagner, M., Bokde, A. L., Hampel, H., Coates, U., Reiser, M., Meindl, T., and et al. (2012). Diagnostic power of default mode network resting state fmri in the detection of alzheimer's disease. *Neurobiology of Aging*, 33(3):466–478.

- Kokkonen, S. M., Nikkinen, J., Remes, J., Kantola, J., Starck, T., Haapea, M., Tuominen, J., Tervonen, O., and Kiviniemi, V. (2009). Preoperative localization of the sensorimotor area using independent component analysis of resting-state fmri. *Magn Reson Imaging*, 27(6):733–40.
- Krause, F., Benjamins, C., Eck, J., Luehrs, M., van Hoof, R., and Goebel, R. (2019). Active head motion reduction in magnetic resonance imaging using tactile feedback. *bioRxiv*.
- Kwong, K. K., Belliveau, J. W., Chesler, D. A., Goldberg, I. E., Weisskoff, R. M., Poncelet, B. P., Kennedy, D. N., Hoppel, B. E., Cohen, M. S., Turner, R., and et al. (1992). Dynamic magnetic resonance imaging of human brain activity during primary sensory stimulation. *Proc Natl Acad Sci U S A*, 89(12):5675–9.
- Kylkilahti, T. M., Berends, E., Ramos, M., Shanbhag, N. C., Töger, J., Markenroth Bloch, K., and Lundgaard, I. (2021). Achieving brain clearance and preventing neurodegenerative diseases—a glymphatic perspective. *Journal of Cerebral Blood Flow & Metabolism*, 41(9):2137–2149.
- Lacolley, P., Regnault, V., and Laurent, S. (2020). Mechanisms of arterial stiffening. *Arteriosclerosis, Thrombosis, and Vascular Biology*, 40(5):1055–1062.
- Lee, M. H., Smyser, C. D., and Shimony, J. S. (2013). Resting-state fmri: a review of methods and clinical applications. *AJNR Am J Neuroradiol*, 34(10):1866–72.
- Lewis, L. D., Setsompop, K., Rosen, B. R., and Polimeni, J. R. (2018). Stimulus-dependent hemodynamic response timing across the human subcortical-cortical visual pathway identified through high spatiotemporal resolution 7t fmri. *NeuroImage*, 181:279–291.
- Liu, H., Buckner, R. L., Talukdar, T., Tanaka, N., Madsen, J. R., and Stufflebeam, S. M. (2009). Task-free presurgical mapping using functional magnetic resonance imaging intrinsic activity. *J Neurosurg*, 111(4):746–54.
- London, G. M. and Pannier, B. (2010). Arterial functions: how to interpret the complex physiology. *Nephrology Dialysis Transplantation*, 25(12):3815–3823.
- Lowe, M. J. and Sorenson, J. A. (1997). Spatially filtering functional magnetic resonance imaging data. *Magnetic Resonance in Medicine*, 37(5):723–729.
- Lu, H., Xu, F., Rodrigue, K. M., Kennedy, K. M., Cheng, Y., Flicker, B., Hebrank, A. C., Uh, J., and Park, D. C. (2011). Alterations in cerebral metabolic rate and blood supply across the adult lifespan. *Cereb Cortex*, 21(6):1426–34.
- Maclaren, J., Herbst, M., Speck, O., and Zaitsev, M. (2012). Prospective motion correction in brain imaging: A review. *Magnetic Resonance in Medicine*, 69(3):621–636.
- Markl, M., Schnell, S., Wu, C., Bollache, E., Jarvis, K., Barker, A., Robinson, J., and Rigsby, C. (2016). Advanced flow mri: Emerging techniques and applications. *Clinical Radiology*, 71(8):779–795.
- Mckeown, M. J., Makeig, S., Brown, G. G., Jung, T.-P., Kindermann, S. S., Bell, A. J., and Sejnowski, T. J. (1998). Analysis of fmri data by blind separation into independent spatial components. *Human Brain Mapping*, 6(3):160–188.
- Merola, A., Murphy, K., Stone, A. J., Germuska, M. A., Griffeth, V. E., Blockley, N. P., Buxton, R. B., and Wise, R. G. (2016). Measurement of oxygen extraction fraction (oef): An optimized bold signal model for use with hypercapnic and hyperoxic calibration. *NeuroImage*, 129:159–174.

- Mitchell, G. F. (2008). Effects of central arterial aging on the structure and function of the peripheral vasculature: implications for end-organ damage. *J Appl Physiol (1985)*, 105(5):1652–60.
- Mitchell, G. F., Parise, H., Benjamin, E. J., Larson, M. G., Keyes, M. J., Vita, J. A., Vasan, R. S., and Levy, D. (2004). Changes in arterial stiffness and wave reflection with advancing age in healthy men and women: the framingham heart study. *Hypertension*, 43(6):1239–45.
- Mitchell, G. F., van Buchem, M. A., Sigurdsson, S., Gotal, J. D., Jonsdottir, M. K., Kjartansson, O., Garcia, M., Aspelund, T., Harris, T. B., Gudnason, V., and Launer, L. J. (2011). Arterial stiffness, pressure and flow pulsatility and brain structure and function: the age, gene/environment susceptibility–reykjavik study. *Brain*, 134(Pt 11):3398–407.
- Moreton, F. C., Dani, K. A., Goutcher, C., O’Hare, K., and Muir, K. W. (2016). Respiratory challenge mri: Practical aspects. *NeuroImage: Clinical*, 11:667–677.
- Mullinger, K. J., Mayhew, S. D., Bagshaw, A. P., Bowtell, R., and Francis, S. T. (2013). Poststimulus undershoots in cerebral blood flow and bold fmri responses are modulated by poststimulus neuronal activity. *Proceedings of the National Academy of Sciences*, 110(33):13636–13641.
- Murphy, K., Birn, R. M., and Bandettini, P. A. (2013). Resting-state fmri confounds and cleanup. *Neuroimage*, 80:349–59.
- Murphy, K., Harris, A. D., and Wise, R. G. (2011). Robustly measuring vascular reactivity differences with breath-hold: normalising stimulus-evoked and resting state bold fmri data. *Neuroimage*, 54(1):369–79.
- Nichols, W. W., Nichols, W. W., and McDonald, D. A. (2011). *McDonald’s blood flow in arteries: Theoretic, experimental, and clinical principles*. Hodder Arnold.
- Ogawa, S., Lee, T. M., Kay, A. R., and Tank, D. W. (1990). Brain magnetic resonance imaging with contrast dependent on blood oxygenation. *Proceedings of the National Academy of Sciences*, 87(24):9868–9872.
- Ogawa, S., Tank, D. W., Menon, R., Ellermann, J. M., Kim, S. G., Merkle, H., and Ugurbil, K. (1992). Intrinsic signal changes accompanying sensory stimulation: functional brain mapping with magnetic resonance imaging. *Proc Natl Acad Sci U S A*, 89(13):5951–5.
- Oh, Y. S. (2018). Arterial stiffness and hypertension. *Clin Hypertens*, 24:17.
- Ooi, M. B., Aksoy, M., Maclaren, J., Watkins, R. D., and Bammer, R. (2013). Prospective motion correction using inductively coupled wireless rf coils. *Magnetic Resonance in Medicine*, 70(3):639–647.
- Ooi, M. B., Krueger, S., Thomas, W. J., Swaminathan, S. V., and Brown, T. R. (2009). Prospective real-time correction for arbitrary head motion using active markers. *Magnetic Resonance in Medicine*, 62(4):943–954.
- Palta, P., Sharrett, A. R., Wei, J., Meyer, M. L., Kucharska-Newton, A., Power, M. C., Deal, J. A., Jack, C. R., Knopman, D., Wright, J., and et al. (2019). Central arterial stiffness is associated with structural brain damage and poorer cognitive performance: The aric study. *Journal of the American Heart Association*, 8(2).
- Papaioannou, T. G., Protogerou, A. D., Stergiopoulos, N., Vardoulis, O., Stefanadis, C., Safar, M., and Blacher, J. (2014). Total arterial compliance estimated by a novel method and all-cause mortality in the elderly: The proteger study. *AGE*, 36(3).

- Park, K.-Y., Chung, P.-W., Kim, Y. B., Moon, H.-S., Suh, B.-C., and Yoon, W. T. (2012). Increased pulsatility index is associated with intracranial arterial calcification. *European Neurology*, 69(2):83–88.
- Payne, S. (2016). *Cerebral autoregulation control of blood flow in the brain*. Springer International Publishing.
- Phillips, A. A., Chan, F. H., Zheng, M. M., Krassioukov, A. V., and Ainslie, P. N. (2016). Neurovascular coupling in humans: Physiology, methodological advances and clinical implications. *J Cereb Blood Flow Metab*, 36(4):647–64.
- Pinto, J., Chappell, M. A., Okell, T. W., Mezue, M., Segerdahl, A. R., Tracey, I., Vilela, P., and Figueiredo, P. (2019). Calibration of arterial spin labeling data—potential pitfalls in post-processing. *Magnetic Resonance in Medicine*, 83(4):1222–1234.
- Power, J. D., Barnes, K. A., Snyder, A. Z., Schlaggar, B. L., and Petersen, S. E. (2012). Spurious but systematic correlations in functional connectivity mri networks arise from subject motion. *Neuroimage*, 59(3):2142–54.
- Power, J. D., Mitra, A., Laumann, T. O., Snyder, A. Z., Schlaggar, B. L., and Petersen, S. E. (2014). Methods to detect, characterize, and remove motion artifact in resting state fmri. *Neuroimage*, 84:320–41.
- Power, J. D., Silver, B. M., Dubin, M. J., Martin, A., and Jones, R. M. (2019). Distinctions among real and apparent respiratory motions in human fmri data. *bioRxiv*.
- Powers, W. J. (2016). 3 - cerebral blood flow and metabolism: Regulation and pathophysiology in cerebrovascular disease. In Grotta, J. C., Albers, G. W., Broderick, J. P., Kasner, S. E., Lo, E. H., Mendelow, A. D., Sacco, R. L., and Wong, L. K., editors, *Stroke (Sixth Edition)*, pages 28–46.e7. Elsevier, London, sixth edition edition.
- Pruessmann, K. P., Weiger, M., Scheidegger, M. B., and Boesiger, P. (1999). Sense: Sensitivity encoding for fast mri. *Magnetic Resonance in Medicine*, 42(5):952–962.
- Purcell, E. M., Torrey, H. C., and Pound, R. V. (1946). Resonance absorption by nuclear magnetic moments in a solid. *Physical Review*, 69(1-2):37–38.
- Pusey, E., Yoon, C., Anselmo, M. L., and Lufkin, R. B. (1988). Aliasing artifacts in mr imaging. *Computerized Medical Imaging and Graphics*, 12(4):219–224.
- Rabi, I. I., Zacharias, J. R., Millman, S., and Kusch, P. (1938). A new method of measuring nuclear magnetic moment. *Physical Review*, 53(4):318–318.
- Rajendra Acharya, U., Paul Joseph, K., Kannathal, N., Lim, C. M., and Suri, J. S. (2006). Heart rate variability: A review. *Medical & Biological Engineering & Computing*, 44(12):1031–1051.
- Reardon, M. and Malik, M. (1996). Changes in heart rate variability with age. *Pacing and Clinical Electrophysiology*, 19(11):1863–1866.
- Reference Values for Arterial Stiffness' Collaboration (2010). Determinants of pulse wave velocity in healthy people and in the presence of cardiovascular risk factors: 'establishing normal and reference values'. *Eur Heart J*, 31(19):2338–50.
- Rivera-Rivera, L. A., Schubert, T., Turski, P., Johnson, K. M., Berman, S. E., Rowley, H. A., Carlsson, C. M., Johnson, S. C., and Wieben, O. (2017). Changes in intracranial venous blood flow and pulsatility in alzheimer's disease: A 4d flow mri study. *J Cereb Blood Flow Metab*, 37(6):2149–2158.

- Safo, M. K. and Kato, G. J. (2014). Therapeutic strategies to alter the oxygen affinity of sickle hemoglobin. *Hematology/Oncology Clinics of North America*, 28(2):217–231.
- Sainas, G., Milia, R., Palazzolo, G., Iba, G., Marongui, E., Roberto, S., Pinna, V., Ghiani, G., Tocco, F., and Crisafulli, a. (2016). Mean blood pressure assessment during post-exercise: Results from two different methods of calculation. *Journal of Sports Science and Medicine*, 15:424–433.
- Salimi-Khorshidi, G., Douaud, G., Beckmann, C. F., Glasser, M. F., Griffanti, L., and Smith, S. M. (2014). Automatic denoising of functional mri data: combining independent component analysis and hierarchical fusion of classifiers. *Neuroimage*, 90:449–68.
- Satterthwaite, T. D., Elliott, M. A., Gerraty, R. T., Ruparel, K., Loughhead, J., Calkins, M. E., Eickhoff, S. B., Hakonarson, H., Gur, R. C., Gur, R. E., and Wolf, D. H. (2013). An improved framework for confound regression and filtering for control of motion artifact in the preprocessing of resting-state functional connectivity data. *Neuroimage*, 64:240–56.
- Schmithorst, V. J., Hernandez-Garcia, L., Vannest, J., Rajagopal, A., Lee, G., and Holland, S. K. (2013). Optimized simultaneous asl and bold functional imaging of the whole brain. *Journal of Magnetic Resonance Imaging*, 39(5):1104–1117.
- Scouten, A., Papademetris, X., and Constable, R. (2006). Spatial resolution, signal-to-noise ratio, and smoothing in multi-subject functional mri studies. *NeuroImage*, 30(3):787–793.
- Shimony, J. S., Zhang, D., Johnston, J. M., Fox, M. D., Roy, A., and Leuthardt, E. C. (2009). Resting-state spontaneous fluctuations in brain activity: a new paradigm for presurgical planning using fmri. *Acad Radiol*, 16(5):578–83.
- Singer, J., Trollor, J. N., Baune, B. T., Sachdev, P. S., and Smith, E. (2014). Arterial stiffness, the brain and cognition: A systematic review. *Ageing Research Reviews*, 15:16–27.
- Sladky, R., Friston, K. J., Tröstl, J., Cunnington, R., Moser, E., and Windischberger, C. (2011). Slice-timing effects and their correction in functional mri. *NeuroImage*, 58(2):588–594.
- Sleight, E., Stringer, M. S., Marshall, I., Wardlaw, J. M., and Thrippleton, M. J. (2021). Cerebrovascular reactivity measurement using magnetic resonance imaging: A systematic review. *Frontiers in Physiology*, 12.
- Slipsager, J. M., Ellegaard, A. H., Glimberg, S. L., Paulsen, R. R., Tisdall, M. D., Wighton, P., van der Kouwe, A., Marner, L., Henriksen, O. M., Law, I., and et al. (2019). Markerless motion tracking and correction for pet, mri, and simultaneous pet/mri. *PLOS ONE*, 14(4).
- Slipsager, J. M., Glimberg, S. L., Højgaard, L., Paulsen, R. R., Wighton, P., Tisdall, M. D., Jaimes, C., Gagoski, B. A., Grant, P. E., van der Kouwe, A., and et al. (2021). Comparison of prospective and retrospective motion correction in 3d-encoded neuroanatomical mri. *Magnetic Resonance in Medicine*, 87(2):629–645.
- Slipsager, J. M., Glimberg, S. L., Sjøgaard, J., Paulsen, R. R., Johannesen, H. H., Martens, P. C., Seth, A., Marner, L., Henriksen, O. M., Olesen, O. V., and et al. (2020). Quantifying the financial savings of motion correction in brain mri: A model-based estimate of the costs arising from patient head motion and potential savings from implementation of motion correction. *Journal of Magnetic Resonance Imaging*, 52(3):731–738.
- Smith, S. M., Beckmann, C. F., Andersson, J., Auerbach, E. J., Bijsterbosch, J., Douaud, G., Duff, E., Feinberg, D. A., Griffanti, L., Harms, M. P., Kelly, M., Laumann, T., Miller, K. L., Moeller, S., Petersen, S., Power, J., Salimi-Khorshidi, G., Snyder, A. Z., Vu, A. T., Woolrich, M. W., Xu, J., Yacoub, E., Ugurbil, K., Van Essen, D. C., Glasser, M. F., and Consortium, W. U.-M. H. (2013). Resting-state fmri in the human connectome project. *Neuroimage*, 80:144–68.

- Snell, R. S. (2011). *Clinical neuroanatomy*. LWW.
- Soares, J. M., Magalhães, R., Moreira, P. S., Sousa, A., Ganz, E., Sampaio, A., Alves, V., Marques, P., and Sousa, N. (2016). A hitchhiker's guide to functional magnetic resonance imaging. *Frontiers in Neuroscience*, 10.
- Souweidane, M., Kim, K., McDowall, R., Ruge, M., Lis, E., Krol, G., and Hirsch, J. (1999). Brain mapping in sedated infants and young children with passive-functional magnetic resonance imaging. *Pediatric Neurosurgery*, 30(2):86–92.
- Sun, Z. (2015). Aging, arterial stiffness, and hypertension. *Hypertension*, 65(2):252–256.
- Supekar, K., Menon, V., Rubin, D., Musen, M., and Greicius, M. D. (2008). Network analysis of intrinsic functional brain connectivity in alzheimer's disease. *PLoS Computational Biology*, 4(6).
- Tucker, W. D., Arora, Y., and Mahajan, K. (2017). *Anatomy, blood vessels*. StatPearls Publishing.
- van den Kerkhof, M., van der Thiel, M. M., Postma, A. A., van Oostenbrugge, R. J., Kroon, A. A., Jansen, J. F., and Backes, W. H. (2023). Hypertension correlates with stronger blood flow pulsatility in small perforating cerebral arteries assessed with 7 tesla magnetic resonance imaging. *Hypertension*, 80(4):802–810.
- Van Essen, D., Ugurbil, K., Auerbach, E., Barch, D., Behrens, T., Bucholz, R., Chang, A., Chen, L., Corbetta, M., Curtiss, S., and et al. (2012). The human connectome project: A data acquisition perspective. *NeuroImage*, 62(4):2222–2231.
- Van Essen, D. C., Smith, S. M., Barch, D. M., Behrens, T. E., Yacoub, E., Ugurbil, K., and Consortium, W. U.-M. H. (2013). The wu-minn human connectome project: an overview. *Neuroimage*, 80:62–79.
- van Zijl, P. C., Hua, J., and Lu, H. (2012). The bold post-stimulus undershoot, one of the most debated issues in fmri. *NeuroImage*, 62(2):1092–1102.
- Viessmann, O., Moller, H. E., and Jezzard, P. (2019). Dual regression physiological modeling of resting-state epi power spectra: Effects of healthy aging. *Neuroimage*, 187:68–76.
- Vikner, T., Eklund, A., Karalija, N., Malm, J., Riklund, K., Lindenberger, U., Backman, L., Nyberg, L., and Wahlin, A. (2021). Cerebral arterial pulsatility is linked to hippocampal microvascular function and episodic memory in healthy older adults. *J Cereb Blood Flow Metab*, 41(7):1778–1790.
- Weller, R. O., Djuanda, E., Yow, H.-Y., and Carare, R. O. (2008). Lymphatic drainage of the brain and the pathophysiology of neurological disease. *Acta Neuropathologica*, 117(1):1–14.
- Weller, R. O., Subash, M., Preston, S. D., Mazanti, I., and Carare, R. O. (2007). Symposium: Clearance of a β from the brain in alzheimer's disease: Perivascular drainage of amyloid- β peptides from the brain and its failure in cerebral amyloid angiopathy and alzheimer's disease. *Brain Pathology*, 18(2):253–266.
- Whittaker, J. R., Fasano, F., Venzi, M., Liebig, P., Gallichan, D., Möller, H. E., and Murphy, K. (2022). Measuring arterial pulsatility with dynamic inflow magnitude contrast. *Frontiers in Neuroscience*, 15.
- Williams, D. S., Detre, J. A., Leigh, J. S., and Koretsky, A. P. (1992). Magnetic resonance imaging of perfusion using spin inversion of arterial water. *Proc Natl Acad Sci U S A*, 89(1):212–6.

- Wise, R. G., Harris, A. D., Stone, A. J., and Murphy, K. (2013). Measurement of cerebral blood flow and absolute cerebral metabolic rate of oxygen: MRI-based methods using interleaved and combined hypercapnia and hyperoxia. *Neuroimage*, 83:135–47.
- Wolters, F. J., de Bruijn, R. F., Hofman, A., Koudstaal, P. J., and Ikram, M. A. (2016). Cerebral vasoreactivity, apolipoprotein e, and the risk of dementia. *Arteriosclerosis, Thrombosis, and Vascular Biology*, 36(1):204–210.
- Wong, E. C. (2014). An introduction to ASL labeling techniques. *J Magn Reson Imaging*, 40(1):1–10.
- Woods, R. P., Grafton, S. T., Holmes, C. J., Cherry, S. R., and Mazziotta, J. C. (1998). Automated image registration: I. general methods and intrasubject, intramodality validation. *Journal of Computer Assisted Tomography*, 22(1):139–152.
- Zahneisen, B. and Ernst, T. (2016). Homogeneous coordinates in motion correction. *Magn Reson Med*, 75(1):274–9.
- Zaitsev, M., Akin, B., LeVan, P., and Knowles, B. R. (2017). Prospective motion correction in functional MRI. *Neuroimage*, 154:33–42.
- Zaitsev, M., Dold, C., Sakas, G., Hennig, J., and Speck, O. (2006). Magnetic resonance imaging of freely moving objects: Prospective real-time motion correction using an external optical motion tracking system. *NeuroImage*, 31(3):1038–1050.
- Zou, Q. H., Zhu, C. Z., Yang, Y., Zuo, X. N., Long, X. Y., Cao, Q. J., Wang, Y. F., and Zang, Y. F. (2008). An improved approach to detection of amplitude of low-frequency fluctuation (ALFF) for resting-state fMRI: fractional ALFF. *J Neurosci Methods*, 172(1):137–41.

Appendix A

Additional Figures and Tables

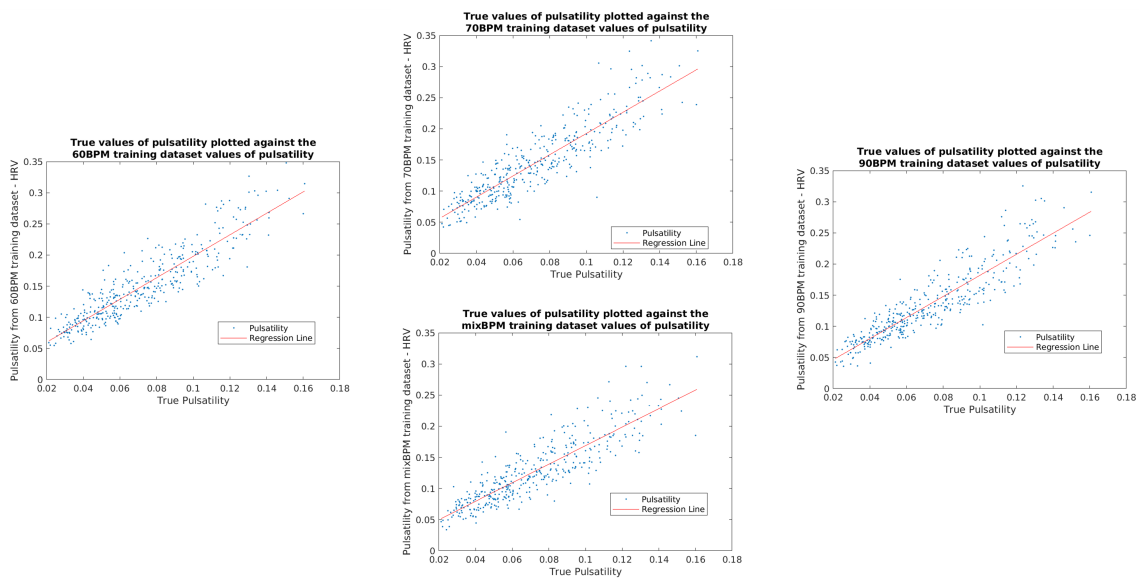


Fig. A.1 Scatter Graphs showing the positive correlation between the pulsatility values estimated from the HRV method and the True pulsatility values.

Correlation between training datasets WB - Frequency Method (Fig 5.4 in Thesis)						p-value between training datasets WB - Frequency Method (Fig 5.4 in Thesis)					
	True Pulsatility	60BPM	70BPM	90BPM	mi6BPM		True Pulsatility	60BPM	70BPM	90BPM	mi6BPM
True Pulsatility	1.00E+00	9.11E-01	9.12E-01	9.13E-01	9.05E-01		1.00E+00	3.33E-152	2.57E-153	1.25E-154	2.23E-147
60BPM		1.00E+00	8.88E-01	9.01E-01	9.04E-01		60BPM	1.00E+00	9.63E-134	1.41E-143	3.95E-146
70BPM			1.00E+00	9.11E-01	9.15E-01		70BPM		1.00E+00	1.23E-152	1.07E-156
90BPM				1.00E+00	9.22E-01		90BPM			1.00E+00	1.65E-163
mi6BPM					1.00E+00		mi6BPM				1.00E+00

Correlation between training datasets GM - Frequency Method (Fig 5.4 in Thesis)						p-value between training datasets GM - Frequency Method (Fig 5.4 in Thesis)					
	True Pulsatility	60BPM	70BPM	90BPM	mi6BPM		True Pulsatility	60BPM	70BPM	90BPM	mi6BPM
True Pulsatility	1.00E+00	9.05E-01	9.02E-01	9.06E-01	8.96E-01		1.00E+00	2.62E-147	7.00E-145	1.18E-147	2.97E-140
60BPM		1.00E+00	8.73E-01	8.92E-01	8.96E-01		60BPM	1.00E+00	5.22E-128	4.96E-137	9.35E-142
70BPM			1.00E+00	9.04E-01	9.07E-01		70BPM		1.00E+00	1.37E-146	1.04E-148
90BPM				1.00E+00	9.12E-01		90BPM			1.00E+00	1.08E-153
mi6BPM					1.00E+00		mi6BPM				1.00E+00

Correlation between training datasets WM - Frequency Method (Fig 5.4 in Thesis)						p-value between training datasets WM - Frequency Method (Fig 5.4 in Thesis)					
	True Pulsatility	60BPM	70BPM	90BPM	mi6BPM		True Pulsatility	60BPM	70BPM	90BPM	mi6BPM
True Pulsatility	1.00E+00	9.25E-01	9.27E-01	9.28E-01	9.19E-01		1.00E+00	6.63E-166	4.97E-169	3.33E-169	1.73E-160
60BPM		1.00E+00	9.04E-01	9.15E-01	9.17E-01		60BPM	1.00E+00	5.36E-146	5.65E-156	1.05E-157
70BPM			1.00E+00	9.25E-01	9.27E-01		70BPM		1.00E+00	2.64E-166	1.23E-168
90BPM				1.00E+00	9.33E-01		90BPM			1.00E+00	5.22E-176
mi6BPM					1.00E+00		mi6BPM				1.00E+00

												Lowest correlation value
												Highest correlation value
												Statistically significant

Fig. A.4 Tables showing the correlation and p -values for the comparison between the Frequency method and the ‘true’ pulsatility. The values highlighted in yellow signify the lowest correlation value and those in green signify the highest correlation value. The values highlighted in red signify statistically significant p -values.

